INTERFEROMETRY IN PERTURBED MEDIA

Reciprocity Theorems, Deconvolution Interferometry, and Imaging of Borehole Seismic Data.

by

Ivan Vasconcelos

A thesis submitted to the Faculty and the Board of Trustees of the Colorado School of Mines in partial fulfillment of the requirements for the degree of Doctor of Philosophy (Geophysics).

Golden, Colorado

Date _____

Signed: _____
Ivan Vasconcelos

Approved: _____
Dr. Roel K. Snieder
Professor of Geophysics
Thesis Advisor

Approved: _____
Dr. Ilya Tsvankin
Professor of Geophysics
Thesis Co-advisor

Golden, Colorado

Date _____

_____
Dr. Terence K. Young
Professor and Head,
Department of Geophysics

ABSTRACT

Interferometry recovers the impulse response of waves propagating between two sensors as if one of them acts as a source. The primary focus of this thesis is on providing a framework for interferometry based on perturbation theory that can be used for the direct reconstruction of the portion of the data that is of interest for imaging and inversion methodologies. I derive general reciprocity theorems in perturbed acoustic media. These theorems show that the wavefield perturbations are extracted from cross-correlating the perturbations detected by one receiver with unperturbed waves sensed by another. Apart from applications to interferometry, the representation theorems presented here can also be used for inverse-scattering and time-lapse monitoring. I also present a theory describing interferometry by deconvolution, based on a series expansion of deconvolved waves in the wavefield perturbations. This expansion is used to give a scattering-based interpretation of the physics of deconvolution interferometry. Deconvolution interferometry, like its correlation counterpart, also retrieves the impulse response between the receivers, but with boundary conditions that are different than those of the original measurement. Interferometry by deconvolution is particularly important for recovering the impulse response from noise records excited by a long and complicated source-time function. As an application of deconvolution interferometry in exploration geophysics, I elaborate on the use of this method for processing seismic-while-drilling data, while comparing to more standard practices. Interferometry by deconvolution yields wide-band images from drilling noise without requiring an independent estimate of the drill-bit excitation. This concept is applied to borehole measurements of drilling noise at the San Andreas Fault Observatory at

Depth (SAFOD) to provide a broadside depth image of the San Andreas Fault system. This image displays the localized subsurface structure of the San Andreas Fault and of another major blind fault. Finally, the representation theorems in perturbed media are used to develop an interferometry method that targets the interference of specific arrivals in the data. This *target-oriented interferometry* method can be used to reconstruct primary reflections from internal multiples. The interference of internal multiples can be used to image subsalt structures using borehole receiver arrays placed beneath salt. I test this method both on numerical experiments and on field data from deep-water Gulf of Mexico.

Para Michele, Bernardo, Beth and Barbara.

"*Firmitas, Utilitas, Venustas.*"

Vitruvius, *De Architectura.*

TABLE OF CONTENTS

LIST OF FIGURES

ACKNOWLEDGMENTS

More than just a document that describes the outcome of intense years of apprenticeship and scientific work, my thesis carries the flavor of true fulfillment. The education that has been provided to me during these years extends far beyond academic knowledge, and this was only possible with the dedication of many outstanding individuals who sometimes did not even realize what they were doing for me. After my so-called "Heiland Lecture" for the Department of Geophysics, one of the faculty comments was that my acknowledgements sounded like the Oscar ceremony. I do not expect this Acknowledgements section to be any shorter, so feel free to skip to other Sections.

First, I would like to begin by acknowledging my instructors throughout these years. When thinking of pursuing a Ph.D. degree, Prof. Liliana Diogo, Marta Mantovani, Renato Prado and Marcelo Assumpção of the University of São Paulo provided much needed encouragement. Prof. Ilya Tsvankin brought me for a visit to CWP during my last semester as an undergraduate, in the Fall of 2003. Because of Ilya's patient and diligent guidance, I had no doubt in pursuing my doctorate degree at CWP. Ilya Tsvankin has passed on to me more than just "Everything you have always wanted to know about Seismic Anisotropy, but were afraid to ask."; much of my scientific rigor and critical sense has spawned from Ilya's teachings. Vladimir Grechka has also taught me about anisotropy, but more than that, he has been a counselor and a friend. The same is true for Ken Larner, I thank Ken for setting my standards on scientific communication. John Stockwell has always provided interesting scientific discussions and amusing stories (he also spent many hours fixing all sorts of computer

bugs in my early days at CWP). At the day of my first comprehensive examination, John Scales planted the seed that made me want to give my research the broadest possible. During the final portions of my thesis work, Paul Sava taught me about migration and kindly invited me to many cups of coffee. Thanks to Jon Leydens for many fulfilling discussions on writing cool papers and enjoy doing it.

The friends I have had over the past few years have many times given me much joy, and brought me true wealth of human experience. Alison Malcolm was the first to receive me in Golden. Alison was my tutor in the CWP ways, and, along with Scott, she never ceased to amuse me with highly analytical humor. Mark Vrijlandt, Kjetil Jansen, and David Eckert have been, and remain, my ultimate "partners in crime". Tammy Gipprich was an outstanding dance partner. Matthew Reynolds... there's just too much to tell. Neal and Amy Dannemiller were the party masters. Ton Evers and Roberto Aguilera are a nonstop party. Kasper and Ludmila van Wijk practically housed and fed me during the 2004 Eurocup. Alex and Adrianne Grêt took me in for a number of sleep-overs in Boulder. Xiaoxia Xu asks the questions you would have never thought of by yourself. Huub Douma and Matt Haney always kept me sharp on a vast array of the most inappropriate jokes. Carlos Pacheco always reminded me to laugh at myself (even when I thought it wasn't funny). Tanja Wojak, Coralie Genty and Lotta Johansson have become adopted sisters. Kurang Mehta taught me to handle my everyday work with diligence and tranquility. Jyoti Behura enlightened me countless times with his keen intelligence. Yaping Zhu's kindness soothed me during several moments of graduate distress. Katie Baker, Stephanie Aleixo, Adriana Citali and Chris Dobo made me feel at home in Houston. CWP has been a family away from home over these years. I owe many, many thanks to Michelle Szobody, a person CWP could simply not be without. Likewise, Barbara McLenon not only made

sure my papers came out decent, but she also brought joy to many early mornings at CWP. Rodrigo, Simone, Rafael, and Julinha Fuck, along with Gabi Melo, for being my Brazilian family away from Brazil. Pat, Mel, Amy and Steve Kirk deserve my very special thanks for not only having given me a home, but also for their love and encouragement.

This thesis would not nearly be what it is if it were not for Prof. Roel Snieder. As far as science is concerned, Roel never failed to provide me with inspiration, especially in the moments when it was most needed. Prof. Snieder shaped the scientist I am today, and will forever serve as role model to me. With his companionship and sense of humor, Roel became a close friend for life.

I owe practically all of my character and accomplishments to those who supported, encouraged and loved me over these years. The countless, never-ending efforts of Michele and Bernardo, my parents, made me into the person and the professional I am today. My mother taught me about courage, determination, and above all, how to be a rebel. My father's unconditional support of my curiosity sparkled the scientist in me. The love and respect given by my parents forged the principles that rule my life and my work. My sister Beth never ceased to have faith in me, and for that reason I am profoundly thankful to her. She taught me the values of kindness, joy and confidence. I also thank Rodrigo Hengler, my sister Bia, my niece Barbara and my brother Cesar for their unconditional care and support.

It was during my doctorate that, thanks to the Kirk family, I met Barbara Fontanals. With her ever lively and sweet ways, Barbarita was there by my side throughout the most challenging times in the pursuit of my Ph.D. Her love and patience filled my graduate days with much comfort and happiness. Her presence and support are true gifts, without which this thesis would not have been possible.

I am deeply thankful to Gloria and Javier for including me in the family with true parent love, for letting me participate in $^{+}D_2$, and for their help with many Spain-related issues. Many thanks to Javi for introducing me to Patxaran, to Sergio for the "meriendas" we shared together, and to both of them for letting me take over their home office. My love and my appreciation also go to Tia Nu for being the grandmother I had never had, and for lighting countless candles to secure the success of my PhD (it must have taken a lot of candles...). Thanks to Paco for many early morning walks full of joy and simplicity. And thanks to Gordito for just being cute.

Finally, I thank my committee members, Dr. Tom Davis, Dr. Mike Batzle, Dr. Paul Martin and Dr. Luis Tenorio for their guidance, and for revising this thesis.

Chapter 1

INTRODUCTION

The inference of waves recorded at two observation points can be used to extract waves that propagate between these points. *Interferometry* is the general term I use to refer to the methods by which we can manipulate recorded wavefields to extract waves that propagate between the receivers as if one of them acts as a source. In the field of exploration geophysics, Claerbout (1968) was the first to note that the autocorrelation of recorded transmission responses yields the reflection response in 1D media. He referred to this approach as *daylight imaging* (Claerbout, 1968; Rickett and Claerbout, 1999), by comparing it to the manner by which human eyesight works. This analogy with human vision can be associated to some of the first formal proofs of the concepts of *interferometry* in multidimensions, which rely on the cross-correlation diffuse waves recorded by two sensors to extract the impulse response between them (Lobkis and Weaver, 2001; Weaver and Lobkis, 2004). Diffuse-wave correlations (e.g., Weaver and Lobkis, 2004; Larose et al., 2006) rely on the physical principle of *equipartioning*, which states that at the observation points, after averaging over time, waves travel in all directions with the same amount of energy. This condition is necessary for the reconstruction of the medium's full impulse response from correlations of the recorded data.

In the context of interferometry, the medium's impulse response is formally defined by the Green's functions describing waves that propagate between the two sensors. Thus, interferometry is also referred to as *Green's function retrieval* (e.g., Weaver

and Lobkis, 2004; Wapenaar et al., 2006). Along with the diffuse-wave theory (e.g., Weaver and Lobkis, 2004), other derivations are based on *representation theorems* (e.g., Wapenaar et al., 2004; Wapenaar et al., 2006; Snieder, 2007; Snieder et al., 2007) also demonstrate the results of interferometry. These representations theorems (also called Greens's theorems) come from general reciprocity theorems (de Hoop, 1988; Fokkema and van den Berg, 1993; Wapenaar et al., 2006) which relate two arbitrarily different wave states in one and the same space. The representation theorems used to describe interferometry are akin to those used in the derivation of the Kirchhoff-Helmholtz integral (e.g., Bleistein et al., 2001) that is commonly used in seismic imaging methods (e.g., Bleistein et al., 2001; Biondi, 2006). For systems that are invariant in time reversal, the representation theorems state that the impulse response between two sensors can be extracted from cross-correlating waves excited by sources distributed over a closed surface that surrounds the receiver. This source configuration produces waves propagating at all directions at the receiver locations, being thus similar in concept to the physics of equipartioned diffuse waves.

There are examples of applications of interferometry in the fields of exploration seismology (e.g., Schuster, 2001; Schuster et al., 2004; Bakulin and Calvert, 2004; Mehta et al., 2007b), ultrasonics (e.g., Malcolm et al., 2004; van Wijk, 2006), ocean acoustics (Roux et al., 2004; Sabra et al., 2004), global earth seismology (e.g., Shapiro et al., 2005; Sabra et al., 2005a), structural engineering (Snieder and Şafak, 2006; Thompson and Snieder, 2006) and helioseismology (e.g., Rickett and Claerbout, 1999). In exploration seismology, Schuster and co-workers have provided interferometric imaging applications for reverse vertical-seismic profile (VSP) data (e.g. Schuster et al., 2004; Yu and Schuster, 2006), increasing dramatically the illumination area in these experiments. Bakulin and Calvert (2004,2006) use time-reversal arguments

to design *Virtual Sources* with interferometry that eliminate the influence of highly heterogeneous overburden in VSP data. Mehta et al. (2007b,c) extended the *Virtual Source* method of Bakulin and Calvert (2006) to multiple removal and time-lapse applications. Shapiro et al. (2005) and Sabra et al. (2005a) rely on the incoherent excitation produced by ocean waves hitting the coast to extract surface waves propagating between sensors and use them for surface-wave tomography. These are only some of the examples of interferometry applications I cite in this thesis. My work offers perturbation-based and deconvolution interferometry as tools to treat yet another subset of physical problems related to scattering-based imaging and monitoring temporal changes in the medium. I give examples of applications in fault and subsalt imaging, and imaging with coherent noise such as drilling noise.

This thesis consists on the compilation of five stand-alone research articles that are intrinsically related. One of the ways in which I establish the relationship between the research work in these articles is simply by cross-referencing the chapters, whenever appropriate. Apart from citations, this Introduction sets a general framework for these papers, providing a "map" to guide the readers through both the content and the broader context of each article.

As discussed above, the most central concept in this manuscript is that of *interferometry*. To understand the meaning of this term[1] in a fundamental way, let us first review the conventional approach to describing natural phenomena in mathematical physics (which include geophysical applications). A general mathematical construction to describe a physical phenomenon postulates a conceptual model $\mathfrak{M}$ (Figure 1.1) to describe a Material State. This Material State is typically represented by *model* parameters associated with physical material quantities such as mass, thermal con-

[1] I follow the terminology introduced by Schuster (2001).

Figure 1.1. A common mathematical concept of a physical system. The solid arrows denote a *forward modeling* scheme, where a measurement $\mathfrak{D}$ is predicted from a given material state $\mathfrak{M}$ by means of a theoretical framework $\mathfrak{T}$. The dotted arrows represent an *inversion*, where the theory is used to infer the material state from observations.

ductivity or resistivity, for example. On the other end of the mathematical physics constructions lies the Measurement $\mathfrak{D}$ (Figure 1.1) of a physical quantity such as pressure, temperature or electric potential. The Material State $\mathfrak{M}$ and the Measurements $\mathfrak{D}$ are linked by a formal and reproducible deductive system (e.g., that of *Principia Mathematica*; Whitehead and Russell, 1910, 1912, 1913) in the form of a Theory $\mathfrak{T}$ (Figure 1.1). This conceptual construction can be used to predict the data that would be acquired for a known model, this is commonly referred to as *forward modeling* or simply as *modeling* (this is illustrated by the solid arrow in Figure 1.1). The concept in Figure 1.1 can also be used to infer the Material States from a given Measurement by means of *inversion* (e.g., Tarantola, 1987). Interferometry methods use the mathematical physics concept in Figure 1.1 differently from the more conventional forward or inverse approaches. By manipulating the Theory $\mathfrak{T}$ (Figure 1.2), interferometry can be used to reconstruct a pseudo-measurement $\mathfrak{D}_r$ from actual measurements $\mathfrak{D}_a$, with no knowledge of the Material State $\mathfrak{M}$ (e.g., Wapenaar et al., 2006; Snieder et al., 2007).

Although my objective in this thesis is more mundane than the discussion of

Figure 1.2. The general concept of *interferometry* as treated by this manuscript. Based on a set of theories $\mathfrak{T}$, the acquired measurements $\mathfrak{D}_a$ are used to *reconstruct* a pseudo-measurement $\mathfrak{D}_r$.

the principles of mathematical physics, it is worth noting two important issues regarding the concept illustrated by Figure 1.1. First, it is important to note that the Material parameters only have meaning in the context of a proposed model and Theory set. The monograph by Tarantola (2006) provides a thorough discussion on the meaning of physical measurements and parameters. Second, Gödel (1930) showed that a mathematical statement that cannot be proved is not necessarily false, nor it is guaranteed that a proven mathematical statement is true. This means that the mathematical representation of physical phenomena expresses a limited perception of the natural world which cannot be logically proven to be true. Wigner (1960) discusses the complex role of mathematics in describing different levels of human phenomenological perception. Following standard scientific practice, in this thesis I present theory and experiments that communicate my intuition on particular aspects of wave propagation. More specifically, through the method of interferometry I describe how seismological measurements can be used to recover a pseudo-acquisition thatdiffers from the originally recorded data, and give examples of applications in exploration geophysics.

Interferometry can be used reconstruct a pseudo-acquisition from recorded mea-

surements without knowledge of model parameters (Figure 1.2). The objective of geophysics, however, is the understanding of the subsurface, i.e., of the model. So how can interferometry be used to gain insight about the Earth's subsurface that cannot be gained by the original measurements? The limitations of the acquired data $\mathfrak{D}_a$ (Figure 1.2) in terms of number of sources and sensors, spatial distribution, etc., along with the approximations in the theory dictate which portion of $\mathfrak{M}$ can be inferred by means of inversion (Figure 1.1). In this context, the interferometrically reconstructed data $\mathfrak{D}_r$ can be used to recover a portion of the model space of $\mathfrak{M}$ that is different from that recovered by the inversion of $\mathfrak{D}_a$. For example, seismic imaging methods (e.g., Bleistein et al., 2001; Biondi, 2006) typically assume that the data contains only single-scattered waves, and cannot handle multiply-scattered waves. With interferometry, I use seismic imaging techniques based on single-scattering to image waves scattered multiple times within the subsurface (Chapter 6), this results in an image with illumination properties that are different than what would have been obtained with the same data using standard processing techniques.

It may sound like "new data" is "created" from observed data by interferometry, but no such thing really happens. The data reconstructed by interferometry contains all of the same information present in the original measurements. The idea of interferometry is akin to that of reshuffling poker cards, where each card represents a set of information contained in the observed data. One may then be inclined to think that this presents a contradiction to the discussion in the previous paragraph, where I state that interferometric data can be used to infer portions of the model space which the original measurements cannot estimate. What happens in practice is that the approximate theories used to infer models typically consider only a subset of the data, i.e., they look at some of the cards in our information deck in a predetermined

order. Once interferometry reshuffles the information in the data, the same approximate theories have access to data features that are ignored in the original experiment. The example of imaging internal multiples with interferometry given in the previous paragraph illustrates this concept.

The focus on perturbation theory is a fundamental aspect of my research in interferometry that makes it unique with respect to other published work in the field. As I show in this thesis, the perturbation approach plays a key role in formally connecting the result of interferometry to the scattering and monitoring problems. The theory I present here targets the interferometric reconstruction of wavefield perturbations, which are the desired input for many existing techniques in imaging (e.g., Bleistein et al. 2001; Weglein et al., 2003; Biondi, 2006), data processing (e.g., Weglein et al., 2003; Malcolm et al., 2004) and inversion (e.g., Tarantola, 1987; Bleistein et al., 2001; Weglein et al., 2003). Other approaches in interferometry (see citations in Chapters 2 through 6) result in the reconstruction of the full wavefields. I discuss this with further detail below.

Although centered on theory and applications of interferometry, this thesis also deals with other topics such as perturbation and scattering theory, passive and active seismic imaging, and imaging of fault zones and subsalt environments. The two first papers (Chapters 2 and 3) provide the theoretical background for the applications presented in Chapters 4 through 6. The articles were not all directed to a single scientific community, so there are subtle differences in the language and discourse focus between one Chapter and another. Much of the general language and scientific writing standards I employ in these texts is inspired by Gopen and Swan (1990) and Penrose and Katz (1998). In this Chapter, I provide brief descriptions of the other Chapters, highlighting the connections between their contents. More detailed descrip-

tions of the context of each article can be found in the corresponding Introduction sections of each Chapter.

As mentioned above, in the theoretical papers (Chapters 2 and 3) I use perturbation theory (e.g., Schrödinger, 1950; Lipmann, 1956; Rodberg, 1967). The main reason for using perturbation theory in my derivations is its use in the description of scattering problems (e.g., Lipmann, 1956; Rodberg, 1967). We use scattering-based arguments to connect the theory we present in Chapters 2 and 3 with the seismic applications in Chapters 4 through 6, in a manner analogous as that presented by de Hoop (1996), Weglein et al. (2003), and Malcolm et al. (2007). In Chapter 2, I manipulate the acoustic wave equations that describe waves in unperturbed and perturbed media to derive reciprocity theorems of the convolution- and correlation-type (de Hoop, 1988; Fokkema and van den Berg, 1993). The theoretical framework I use in Chapter 2 relies in a general domain representation (Figure 1.3) first introduced by de Hoop (1988) and used by Fokkema and van den Berg (1993). The use of this domain representation allows for the derivations of theories that account for arbitrary complexity in medium and geometry parameters. The reciprocity theorems in Chapter 2 provide explicit relations between wavefields (unperturbed and perturbed) and the wavefield perturbations. Next I derive representation theorems using the Green's functions and discuss how they can be used to extract only the wavefield perturbations that propagate between the receivers from recorded data using interferometry. The extraction of the wavefield perturbations is important because they are the input to most seismic imaging methods (e.g., Bleistein et al., 2001; Biondi et al., 2006). Going beyond interferometric imaging, in Chapter 2 I discuss the application of the representation theorems in perturbed media for monitoring medium changes and inverse-scattering imaging. I describe interferometry in Chapter 2 by means of

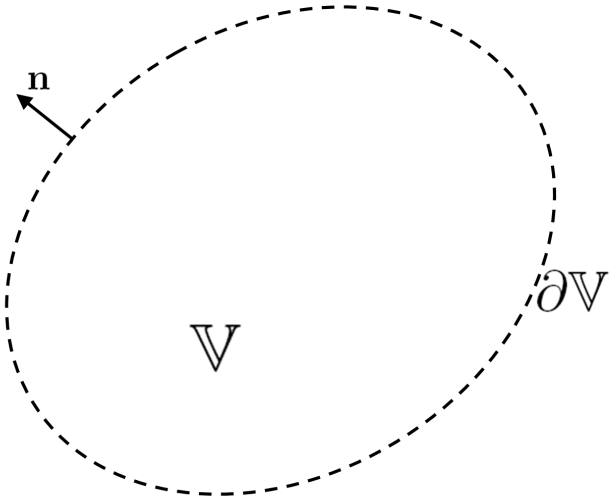

Figure 1.3. The domain representation used to derive reciprocity theorems. $\mathbb{V}$ is an arbitrary volume bounded by $\partial\mathbb{V}$ with normal unit vectors $\mathbf{n}$.

cross-correlations, which relates to other descriptions of interferometry (e.g., Lobkis and Weaver, 2001; Wapenaar et al., 2002; Wapenaar et al., 2006; Snieder et al., 2007; see Chapter 2 for a more detailed discussion).

Interferometry extracts the response between two given receivers as if one of them acts as a source. When waves are excited by transient noise sources, the response reconstructed by correlation-based interferometry carries an average of the power spectra of the excitations (Snieder et al., 2006a; Wapenaar and Fokkema, 2006; Chapter 3). If the excitation is described by a long and complicated time series, extracting the Earth's impulse response from the result of cross-correlation interferometry is complicated due to the imprint of the source power spectra. Such complicated excitations can be found in passive experiments as in seismic-while-drilling (e.g., Rector and Marion, 1991; Poletto and Miranda, 2004) or turbine monitoring, for instance; waveforms incoming from the subsurface can also constitute a complicated and incoherent exci-

tation (e.g., Trampert et al., 1993; Snieder and Şafak, 2006; Mehta et al., 2007c,d). As an alternative to cross-correlations, in Chapter 3 I provide a theory that describes deconvolution interferometry in acoustic media of arbitrary complexity. This theory is based on a series expansion of deconvolved waves with respect to small wavefield perturbations. Using the results of Chapter 2, I study how deconvolution interferometry can be used to extract the impulse response propagating between receivers for arbitrarily complicated excitation. In Chapter 3, I provide a scattering-based physical analysis of deconvolution interferometry, and explain how this method yields a pseudo-experiment with different boundary conditions from the original recordings. Using a simple model of a homogeneous medium with a single reflector, I use the stationary-phase method (Bleistein and Handelsman, 1975) to illustrate the result of deconvolution interferometry. I illustrate the concepts in Chapter 3 with simple numerical examples.

Chapters 2 and 3 together present a set of tools that can be used for interferometry in perturbed media, both in the context of imaging (by associating scattering to perturbation theory) and in monitoring changes in the medium. While Chapter 2 provides representation theorems that can be used for imaging/inversion and for correlation interferometry, Chapter 3 offers the physics of deconvolution interferometry that can be used for imaging waves excited by long and complicated source-time functions. Throughout my derivations, I assume that the reader is familiar with commonly referred topics of mathematical physics such as the wave equation, Fourier integral transformations and their associated properties, and the Gauss divergence theorem (e.g., see Courant and Hilbert, 1989).

I discuss applications for the theory presented in Chapters 2 and 3 in Chapters 4 through 6. In Chapter 4, I describe the application of deconvolution interferometry

to the recordings of drill-bit noise. The majority of methods that treat seismic-while-drilling (SWD) data require independent measurements (called *pilot records*) of the drill-bit excitation to extract the Earth's impulse response (e.g., Rector and Marion, 1991; Poletto et al., 2004; Haldorsen et al., 1994). Deconvolution interferometry can be of particular use for processing SWD when pilot records are not available or if they provide a poor representation of the drill-bit signal. In Chapter 4 I illustrate, with a numerical example, the how deconvolution interferometry can be used to image drill-bit noise passively recorded by subsalt borehole receiver arrays. With a heuristic extension of the theory in Chapter 3 to the case of elastic wave propagation, I analyze multicomponent field records of drill-bit noise from the Pilot borehole of the San Andreas Fault Observatory at Depth (SAFOD) at Parkfield, CA (e.g., http://www.icdp-online.de/sites/sanandreas/index/index.html; Chavarria et al., 2003). In both the numerical and field data examples, I provide comparisons between the results of deconvolution- and correlation-based interferometry.

The geophysical characterization of the San Andreas fault zone is important to the understanding of the local dynamics of transcurrent plate boundaries (Turcotte and Schubert, 2001) and their associated seismicity. In particular, the dynamics of the San Andreas fault (SAF) is crucial in characterizing the seismogenic risk of highly populated areas in CA that lie near the fault zone. Figure 1.4 shows a satellite image of the SAF by Palmdale, CA, where of the urbanized area lies next to the fault. The SAFOD drill-bit data, whose processing I discuss in Chapter 4, is part of a comprehensive set of data on the San Andreas fault zone at Parkfield, CA. These data include not just passive (Oye et al., 2004; Nadeau et al., 2004) and active (Hole et al., 2001; Catchings et al., 2003; Chavarria et al., 2003) seismic records, but also surface gravity (Roecker et al., 2004) and resistivity surveys (Unsworth et al., 2000;

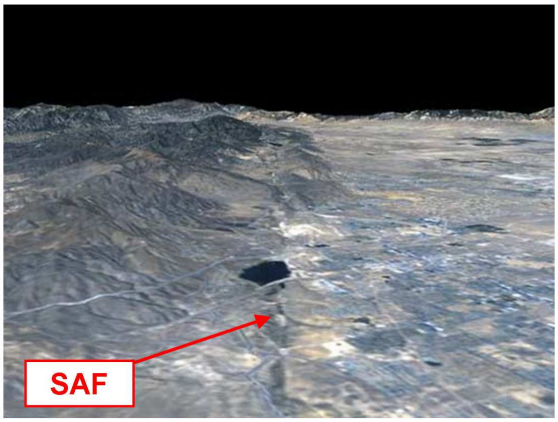

Figure 1.4. Perspective view of a satellite image of the San Andreas Fault (SAF) at Palmdale, CA. The image is overlaid on a 3D topographic model. The image perspective is the same of an observer looking toward the South East direction. The SAF zone is marked by the linear feature in the center of the image (indicated by the red arrow). The city of Palmdale can be seen in the right-hand side of the image. (Courtesy of the NASA Visible Earth project, http://visibleearth.nasa.gov)

Unsworth and Bedrosian, 2004), and well information in the form of logs (Boness and Zoback, 2004, 2006) and rock samples in the form of cores and washed cuttings (Solum et al., 2004, 2006). In Chapter 5, I provide an interpretation of the results of the deconvolution interferometry of the SAFOD Pilot Hole SWD data (Chapter 4) along with the imaging of active-shot seismic data recorded in the SAFOD Main Hole. We compare the results obtained by the joint interferometric and active-shot imaging with previous measurements at Parkfield to arrive at a geological interpretation of the images I obtain.

In Chapter 6 I propose yet another application of the perturbation-based interferometry presented in Chapter 2. This application consists in the interferometry of waves that are excited by sources at the Earth's surface that reflect multiple times

within the subsurface and are recorded by borehole sensors. Using the theory in Chapter 2, I show that the interference of multiple reflections can be used to reconstruct primary reflections that propagate between the borehole receivers. These primary waves can be used in algorithms designed for standard seismic exploration experiments (e.g., Bleistein et al., 2001; Biondi, 2006) to image structures that lie above the receiver array. Because the interferometry method I describe in Chapter 6 targets the imaging of a chosen portion of the subsurface surrounding a borehole receiver array, I refer to it as *target-oriented interferometry*. This target-oriented interferometry methodology relies on a wavefield separation procedure to separate unperturbed waves from wavefield perturbations in the recorded data. I describe target-oriented interferometry and compare it to other existing interferometry methods in Chapter 6. With the same numerical model used in Chapter 4, I generate a synthetic experiment that demonstrates that target-oriented interferometry can be designed to use internal multiples for imaging subsalt features from borehole arrays located below these structures. Finally I test these concepts on field data from deep-water Gulf of Mexico, where I demonstrate the effects of target-oriented interferometry on the recorded data as well as on the final images.

With Chapters 4 and 6 I address the potential importance of using interferometry in imaging off-shore subsalt environments. A large portion of significant significant oilfields in Gulf of Mexico, Brazil, West Africa, North Sea and in the Mediterranean are set in salt-rich geological environments with high structural complexity. In many cases, surface seismic in these environments is compromised by strong spatial variations and complexity in medium parameters around the salt bodies. In Chapters 4 and 6 I promote interferometry techniques for subsalt borehole seismic data that can overcome, in a localized portion of the subsurface, some of the issues encountered by

surface seismic in imaging subsalt structures.

In this thesis, the concept described by Figure 1.2 is the foundation of the interferometry theories I discuss in Chapters 2 and 3. With the different numerical and field interferometric imaging examples in Chapters 3 through 6 I demonstrate how the data remapping achieved with interferometry (Figure 1.2) can be used to obtain subsurface images that cannot be obtained from the original recorded data with existing processing techniques.

Chapter 2

REPRESENTATION THEOREMS AND GREEN'S FUNCTION RETRIEVAL IN PERTURBED ACOUSTIC MEDIA[1]

2.1 Summary

Representation theorems describe important general properties of wave propagation. We provide general representation theorems for perturbed acoustic media in the form of convolution- and correlation-type theorems. Our results differ from previous derivations because we provide explicit integral relations between wavefields and wavefield perturbations which alone do not satisfy the acoustic wave equations. Using Green's functions to describe perturbed and unperturbed waves in two distinct wave states, we provide expressions based in our representation theorems that are applicable to remote sensing experiments. When medium perturbations are localized and away from the observation points, we show that by cross-correlating wavefield perturbations recorded at a given receiver with unperturbed waves at another, we generate a pseudo-experiment where only wavefield perturbations propagate from one receiver to the other as if one of them were a source. This application has been validated by numerical examples and seismic field experimentation. In another application, our representation theorems in perturbed media, along with inverse scattering methods, can be used to directly estimate medium perturbations from remotely acquired data.

[1]Submitted to Physical Review E.

2.2 Introduction

Representation theorems, also referred to as reciprocity theorems, have long been used to describe important properties of wave propagation phenomena. Lord Rayleigh (1878) used a local form of an acoustic representation theorem to demonstrate source-receiver reciprocity. Time-domain reciprocity[2] theorems were later generalized to relate two wave states with different field, material and source properties in absorbing, heterogeneous media (de Hoop, 1988). Fokkema and van den Berg (1993) provide an in-depth analysis of frequency-domain acoustic representation theorems, discussing many applications that follow from these theorems.

Fokkema and van den Berg (1993) show that acoustic representation theorems can be used for modeling wave propagation, for boundary and domain imaging, and for estimation of the medium properties. In the field of exploration seismology, an important application of convolution-type representation theorems lies in removing multiple reflections caused by the Earth's free-surface (e.g., Fokkema and van den Berg, 1993; Berkhout and Verschuur, 1997). These approaches rely on the convolution of single-scattered waves to create multiples (according to the description given by the convolution-type representation theorems), which are then subtracted from the recorded data. Other approaches for the elimination of multiples from seismic data rely on the inverse scattering methods (e.g., Weglein et al., 2003; Malcolm et al., 2007). The inverse-scattering based methodologies are typically used separately from the representation theorem approaches (Fokkema and van den Berg, 1993; Berkhout and Verschuur, 1997) in predicting multiples.

In particular, recent forms of reciprocity theorems have been derived for the Green's functions (e.g., Wapenaar et al., 2002; Wapenaar and Fokkema, 2006; Wape-

[2]We use the terms *representation theorems* and *reciprocity theorems* interchangeably.

naar et al., 2006), showing that the cross-correlations of waves recorded by two receivers can be used to obtain the waves that propagate between these receivers as if one of them behaves as a source. These results coincide with other studies based on cross-correlations of diffuse waves in a medium with an irregular boundary (Lobkis and Weaver, 2001), caused by randomly distributed uncorrelated sources (Weaver and Lobkis, 2001; Wapenaar et al., 2002; Shapiro et al., 2005), or present in the coda of the recorded signals (Snieder, 2004). An early analysis by Claerbout (1968) shows that the reflection response in a 1D medium can be reconstructed from the autocorrelation of recorded transmission responses. This result was later extended for cross-correlations in heterogeneous 3D media by Wapenaar et al. (2004), who used one-way representation theorems in their derivations. Green's function retrieval by cross-correlations has found applications in the fields of global (e.g., Shapiro et al., 2005; Sabra et al., 2005a) and exploration seismology (e.g., Schuster et al., 2004; Willis et al. 2006; Bakulin and Calvert, 2006), ultrasonics (e.g., Fink, 1997; Malcolm et al., 2004; vanWijk, 2006), helioseismology (e.g., Rickett and Claerbout, 1999), structural engineering (Snieder and Şafak, 2006; Thompson and Snieder, 2006) and ocean acoustics (Roux et al., 2004; Sabra et al., 2005b).

Although the correlation-based Green's function retrieval has been proven for special cases by methods other than representation theorems (e.g., Lobkis and Weaver, 2001; Weaver and Lobkis, 2004; Bakulin and Calvert, 2006), the derivations based on reciprocity theorems have provided for generalizations beyond lossless acoustic wave propagation. The extension to elastic wave propagation was shown by Wapenaar (2004) using representation theorems. Snieder (2006), derived representation theorems for the diffusion equation, showing that the reconstruction of the Green's functions by wavefield correlations does not require time-reversal to hold. More gen-

eral forms of representation theorems have been derived by Wapenaar et al. (2006) and by Snieder et al. (2007) which include a wide range of differential equations such as the acoustic, elastodynamic, and electromagnetic wave equations, as well as the diffusion, advection and Schrödinger equations, among others.

In this paper, we derive representation theorems for acoustic perturbed media. Although previous derivations of representation theorems account for arbitrary medium parameters that are different between two wave states (e.g., de Hoop, 1988; Fokkema and van den Berg, 1993; Wapenaar et al., 2006), they do not explicitly consider the special case of perturbed media. In perturbed media, there are special relations between the unperturbed and perturbed wave states (e.g., in terms of the physical excitation) that make the representation theorems in such media differ in form with respect to their more general counterparts (Fokkema and van den Berg, 1993; Wapenaar et al., 2006). We discuss some of these differences in this manuscript. Another important aspect of studying representation theorems in perturbed media lies in retrieving wavefield perturbations from cross-correlations, in a manner analogous to that discussed by Wapenaar et al. (2006) and Snieder et al. (2007). This is important because from the representation theorems in Wapenaar et al. (2006) and Snieder et al. (2007) it is only possible to reconstruct wavefield quantities. As we show in this paper, wavefield perturbations by themselves do not satisfy the wave equations and thus their retrieval does not follow directly from the general formulation presented by Wapenaar et al. (2006) and Snieder et al. (2007).

We first derive general forms of convolution- and correlation-type representation theorems by manipulating the perturbed and unperturbed wave equations for two wave states. In the Section that follows, we rewrite our representation theorems in terms of the Green's functions for unperturbed and perturbed waves in the two

states. Finally, we discuss two applications of the Green's function forms of our representation theorems in perturbed acoustic media. In one application, we describe the physical cases in which the cross-correlation of wavefield perturbations at an observation point with unperturbed waves at another yields wavefield perturbations that propagate between the two observation points as if a source were placed in one of them. Another application covers the use of representation theorems in perturbed media to estimate medium perturbations. This application involves the combination of our reciprocity theorems and inverse scattering methods (Weglein et al., 2004; Malcolm et al., 2007).

2.3 Representation theorems in convolution and correlation form

We start by defining acoustic wave states in a domain $\mathbb{V}$, bounded by $\partial\mathbb{V}$ (Figure 2.1; de Hoop, 1988; Fokkema and van den Berg, 1993). The outward pointing vector normal to $\partial\mathbb{V}$ is represented by $\mathbf{n}$. We define two wave states, which we denote by the superscripts A and B, respectively. Each wave state is defined in an unperturbed medium with compressibility $\kappa_0(\mathbf{r})$ and density $\rho_0(\mathbf{r})$; as well as in a perturbed medium described by the material properties $\kappa(\mathbf{r})$ and $\rho(\mathbf{r})$. The acoustic wavefield equations for state A in an unperturbed medium are, in the frequency-domain,

$$\begin{aligned} \nabla p_0^A(\mathbf{r},\omega) \,-\, i\omega\rho_0(\mathbf{r})\mathbf{v}_0^A(\mathbf{r},\omega) \quad &= 0 \\ \nabla\cdot\mathbf{v}_0^A(\mathbf{r},\omega) \,-\, i\omega\kappa_0(\mathbf{r})p_0^A(\mathbf{r},\omega) \quad &= q^A(\mathbf{r},\omega)\,, \end{aligned} \tag{2.1}$$

where $p^A(\mathbf{r},\omega)$ and $\mathbf{v}^A(\mathbf{r},\omega)$ represent pressure and particle velocity, respectively. The quantity $q^A(\mathbf{r},\omega)$ describes the source distribution in terms of volume injection rate

density. Similar equations describe waves in state A in a perturbed medium:

$$\begin{aligned} \nabla p^A(\mathbf{r},\omega) \; - \; i\omega\rho(\mathbf{r})\mathbf{v}^A(\mathbf{r},\omega) \quad &= 0 \\ \nabla \cdot \mathbf{v}^A(\mathbf{r},\omega) \; - \; i\omega\kappa(\mathbf{r})p^A(\mathbf{r},\omega) \quad &= q^A(\mathbf{r},\omega) \; , \end{aligned} \tag{2.2}$$

with perturbed pressure and particle velocity given by $p^A(\mathbf{r},\omega)$ and $\mathbf{v}^A(\mathbf{r},\omega)$, respectively. The acoustic field equations that describe wave propagation in state B follow by replacing the superscript A by B in equations 2.2 and 2.1. Note that the source distribution $q^A(\mathbf{r},\omega)$ is the same for both the unperturbed (equation 2.1) and perturbed (equation 2.2) cases. We assume that no external volume forces are present by setting the right-side of the vector equations in equations 2.1 and 2.2 equal to zero. The perturbed pressure for either wave state is given by $p = p_0 + p_S$, where the subscript S indicates the wavefield perturbation caused by medium changes. According to equations 2.1 and 2.2, particle velocities in unperturbed and perturbed media are given by $\mathbf{v} = (i\omega\rho)^{-1}p$ and $\mathbf{v}_0 = (i\omega\rho_0)^{-1}p_0$, respectively. Thus, for small perturbations in density (i.e., $\rho_0/\rho \approx 1$), $\mathbf{v} = \mathbf{v}_0 + \mathbf{v}_S$, where $\mathbf{v}_S = (i\omega\rho)^{-1}p_S$. The perturbations in compressibility can be arbitrarily large. For brevity, in this paper we assume that perturbations only occur in compressibility, thus $\rho = \rho_0$. Despite this assumption, our derivations are equally valid for small perturbations in density.

To derive Rayleigh's reciprocity theorem (Rayleigh, 1878; de Hoop, 1988; Fokkema and van den Berg, 1993) we insert the equations of motion and stress-strain relations for states A and B (equations 2.1 and 2.2) in

$$\mathbf{v}_0^B \cdot \mathbf{E}_0^A \; + \; p_0^A E_0^B - \mathbf{v}_0^A \cdot \mathbf{E}_0^B \; - \; p_0^B E_0^A \; ; \tag{2.3}$$

where $\mathbf{E}$ and E represent the equation of motion and the stress-strain relation in

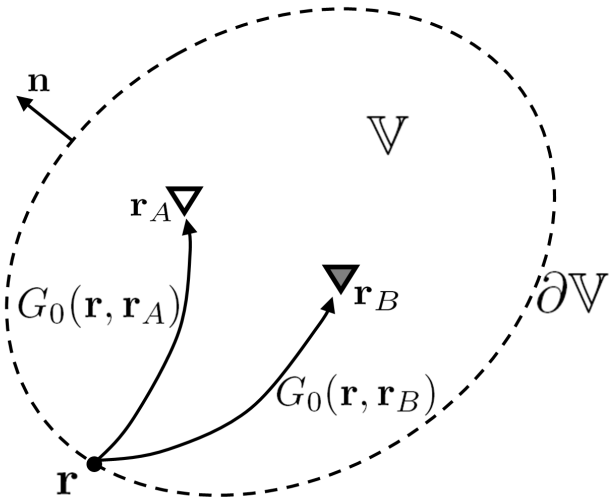

Figure 2.1. Illustration of the domain used in the representation theorems. The domain consists of a volume $\mathbb{V}$, bounded by $\partial\mathbb{V}$. The unit vector normal to $\partial\mathbb{V}$ is represented by $\mathbf{n}$. The wave states A and B are represented by receivers placed at $\mathbf{r}_A$ (white triangle) and $\mathbf{r}_B$ (grey triangle), respectively. The solid arrows denote the stationary paths of unperturbed waves G_0, propagating between the receivers and an arbitrary point $\mathbf{r}$ on $\partial\mathbb{V}$.

equation 2.1, respectively. The subscripts in equation 2.3 indicate that equations and field parameters (p and $\mathbf{v}$) are considered in the unperturbed case. The superscripts indicate whether equations and field parameters pertain to state A or B. For brevity, we omit the parameter dependence on $\mathbf{r}$ and ω. From equation 2.3 we isolate the *interaction quantity* $\nabla \cdot (p_0^A \mathbf{v}_0^B - p_0^B \mathbf{v}_0^A)$ (de Hoop, 1988). Next, we integrate the result of equation 2.3 over the domain $\mathbb{V}$ and apply Gauss' divergence theorem. This results in

$$\oint_{\mathbf{r}\in\partial\mathbb{V}} \left[p_0^A \mathbf{v}_0^B \; - \; p_0^B \mathbf{v}_0^A\right] \cdot d\mathbf{S} = \int_{\mathbf{r}\in\mathbb{V}} \left[p_0^A q_0^B \; - \; p_0^B q_0^A\right] dV \; ; \tag{2.4}$$

which is commonly referred as a reciprocity theorem of the convolution type (Rayleigh, 1878; de Hoop, 1988; Fokkema and van den Berg, 1993), because the frequency-domain products of field parameters represent convolutions in the time domain. A correlation-type reciprocity theorem (de Hoop, 1988; Fokkema and van der Berg, 1993) can be derived from isolating the interaction quantity $\nabla \cdot (p_0^A \mathbf{v}_0^{B*} + p_0^{B*} \mathbf{v}_0^A)$ from

$$\mathbf{v}_0^{B*} \cdot \mathbf{E}_0^A \; + \; p_0^A E_0^{B*} + \mathbf{v}_0^A \cdot \mathbf{E}_0^{B*} \; + \; p_0^{B*} E_0^A \; , \tag{2.5}$$

where * denotes complex conjugation. Subsequent volume integration and application of the divergence theorem yields

$$\oint_{\mathbf{r}\in\partial\mathbb{V}} \left[p_0^A \mathbf{v}_0^{B*} \; + \; p_0^{B*} \mathbf{v}_0^A\right] \cdot d\mathbf{S} = \int_{\mathbf{r}\in\mathbb{V}} \left[p_0^A q_0^{B*} \; + \; p_0^{B*} q_0^A\right] dV \; , \tag{2.6}$$

where complex conjugates represents time-domain cross-correlations of field parameters. For this reason, equation 2.6 is a representation theorem of the correlation type (de Hoop, 1988; Fokkema and van den Berg, 1993). Convolution- and correlation-type representation theorems for the perturbed wave states (e.g., equation 2.2) can be expressed simply by removing the subscript $_0$ from equations 2.3 though 2.6. In equa-

tion 2.6 we assume that κ_0 and ρ_0 are real quantities (i.e.; the medium is lossless). In the next Section we review the application of such theorems for retrieving the Green's functions of arbitrary media (Wapenaar et al., 2002; Wapenaar and Fokkema, 2006).

The theorems in equations 2.4 and 2.6 hold when the material properties in states A and B are the same. General reciprocity theorems that account for arbitrarily different source and material properties between two wave states have been derived by de Hoop (1988) and Fokkema and van den Berg (1993). Here, we further develop the representation theorems of de Hoop (1988) and Fokkema and van den Berg (1993) for the special case of perturbed acoustic media. First, we consider

$$\mathbf{v}_0^B \cdot \mathbf{E}^A \; + \; p^A E_0^B - \mathbf{v}^A \cdot \mathbf{E}_0^B \; - \; p_0^B E^A \; , \tag{2.7}$$

which involves the equations and field parameters for state B in an unperturbed medium (e.g., equation 2.1), along with equations and field parameters for state A in a perturbed medium (equation 2.2). From equation 2.7 we isolate the interaction quantity $\nabla \cdot (p^A \mathbf{v}_0^B - p_0^B \mathbf{v}^A)$. After separating this quantity, we integrate equation 2.7 over $\mathbb{V}$ and apply Gauss' theorem. Next, given that $p = p_0 + p_s$ and $\mathbf{v} = \mathbf{v}_0 + \mathbf{v}_S$, we use the result in equation 2.4, which gives

$$\oint_{\mathbf{r} \in \partial \mathbb{V}} \left[p_S^A \mathbf{v}_0^B \; - \; p_0^B \mathbf{v}_S^A \right] \cdot d\mathbf{S} = \int_{\mathbf{r} \in \mathbb{V}} p_S^A q_0^B dV \; + \; \int_{\mathbf{r} \in \mathbb{V}} i\omega(\kappa_0 - \kappa) p^A p_0^B dV \; , \tag{2.8}$$

which is a convolution-type representation theorem for perturbed media. This expression is a new form of representation theorem because it relates the wavefields p_0^B and $\mathbf{v}_0^B$ with the wavefield perturbations p_S^A and $\mathbf{v}_S^A$. Previous derivations of representation theorems (e.g., de Hoop, 1988; Fokkema and van den Berg, 1993; Wapenaar and Fokkema, 2006). Previously derived reciprocity theorems provide, for two arbi-

trary wave states, relations between field parameters that satisfy wave equations (e.g., equations 2.1 and 2.2). Wavefield perturbations such as p_S^A and $\mathbf{v}_S^A$, by themselves, do not satisfy the wave equations for perturbed media (e.g., equation 2.2). Although equation 2.8 accounts for compressibility changes only, it can be modified to include density perturbations. Such modification involves adding, to the right-hand side of the equation, a third volume integral whose integrand is proportional to $(\rho_0 - \rho)$ and the wavefields $\mathbf{v}^A$ and $\mathbf{v}_0^B$ (Fokkema and van den Berg, 1993).

The correlation-type counterpart of equation 2.8 can be derived from the interaction quantity $\nabla \cdot (p^A \mathbf{v}_0^{B*} + p_0^{B*} \mathbf{v}^A)$, which can be isolated from

$$\mathbf{v}_0^{B*} \cdot \mathbf{E}^A \; + \; p^A E_0^{B*} + \mathbf{v}^A \cdot \mathbf{E}_0^{B*} \; + \; p_0^{B*} E^A \; . \tag{2.9}$$

After performing the same steps as in the derivation of equation 2.8 we obtain

$$\oint_{\mathbf{r} \in \partial \mathbb{V}} \left[p_S^A \mathbf{v}_0^{B*} \; + \; p_0^{B*} \mathbf{v}_S^A \right] \cdot d\mathbf{S} = \int_{\mathbf{r} \in \mathbb{V}} p_S^A q_0^{B*} dV \; - \; \int_{\mathbf{r} \in \mathbb{V}} i\omega(\kappa_0 - \kappa) p^A p_0^{B*} dV \; , \tag{2.10}$$

which is a correlation-type representation theorem for perturbed acoustic media. Again, we assume that both κ and κ_0 are real (i.e., no attenuation takes place). As with its convolution counterpart (equation 2.8), equation 2.10 is novel because it provides a relation between the wavefield perturbations in state A and the unperturbed waves in state B. Density perturbations can be included in equation 2.10 in a manner analogous to that discussed for equation 2.8 (de Hoop, 1988; Fokkema and van den Berg, 1993). By interchanging the superscripts in equations 2.7 and 2.9 we derive convolution- and correlation-type representation theorems that relate the perturbations p_S^B and $\mathbf{v}_S^B$ to p_0^A and $\mathbf{v}_0^A$. These theorems have the same form as the ones in equations 2.8 and 2.10, except A is interchanged with B in equation 2.8, and

with $B*$ in equation 2.10.

Since the source term $q^A(\mathbf{r},\omega)$ is the same both in the unperturbed and perturbed cases, it follows from equations 2.1 and 2.2 that

$$\begin{aligned} \nabla p_0^A(\mathbf{r},\omega) \,-\, i\omega\rho_0(\mathbf{r})\mathbf{v}_0^A(\mathbf{r},\omega) \quad &= \nabla p^A(\mathbf{r},\omega) \,-\, i\omega\rho(\mathbf{r})\mathbf{v}^A(\mathbf{r},\omega) \\ \nabla\cdot\mathbf{v}_0^A(\mathbf{r},\omega) \,-\, i\omega\kappa_0(\mathbf{r})p_0^A(\mathbf{r},\omega) \quad &= \nabla\cdot\mathbf{v}^A(\mathbf{r},\omega) \,-\, i\omega\kappa(\mathbf{r})p^A(\mathbf{r},\omega)\;. \end{aligned} \tag{2.11}$$

These relations can be used to derive others representation theorems in perturbed media. To derive a convolution-type theorem, we first consider the combination

$$\begin{aligned} \mathbf{v}_0^B\cdot\mathbf{R}^A \,+\, p_0^A R^B \quad &-\mathbf{v}_0^A\cdot\mathbf{R}^B \,-\, p_0^B R^A \\ &+ \\ \mathbf{v}^B\cdot\mathbf{R}^A \,+\, p^A R^B \quad &-\mathbf{v}^A\cdot\mathbf{R}^B \,-\, p^B R^A\;, \end{aligned} \tag{2.12}$$

where $\mathbf{R}$ and R are the vector and scalar relations in equation 2.11; the superscripts indicate whether they pertain to wave state A or B. Equation 2.12 is subject to volume integration and to the application of the theorem of Gauss. This equation is then simplified by using the identities $p = p_0 + p_s$ and $\mathbf{v} = \mathbf{v}_0 + \mathbf{v}_S$. In simplifying equation 2.12, we also use the convolution-type representation theorem in equation 2.8 as shown, and with interchanged A and B superscripts. These steps result in

$$\oint_{\mathbf{r}\in\partial\mathbb{V}} \left[p_S^A\mathbf{v}_S^B \,-\, p_S^B\mathbf{v}_S^A\right]\cdot d\mathbf{S} = \int_{\mathbf{r}\in\mathbb{V}} i\omega(\kappa-\kappa_0)\left[p_S^A p_0^B - p_0^A p_S^B\right] dV\;. \tag{2.13}$$

Because the the frequency-domain products in integrands translate to convolutions in the time domain, this integral theorem is of the convolution type. The convolution-type representation theorem in equation 2.13 relates wavefield perturbations from

both wave states over the surface $\partial\mathbb{V}$ with wavefield perturbations, unperturbed waves, and the medium perturbation $(\kappa - \kappa_0)$ within the volume $\mathbb{V}$. Equation 2.13 can be extended to include small density perturbations by adding a extra volume integral with the integrand proportional to $(\rho - \rho_0)\left[\mathbf{v}_S^A \mathbf{v}_0^B - \mathbf{v}_0^A \mathbf{v}_S^B\right]$ (e.g., Fokkema and van den Berg, 1993).

A correlation-type theorem of the same form as equation 2.13 can be derived from modifying the relations in equation 2.12 to account for the time-reversed wave state $B*$ (e.g., equations 2.3 and 2.5). Again, we integrate the result over $\mathbb{V}$, use Gauss' divergence theorem, and simplify it by representing perturbed wavefields in terms of unperturbed waves and wavefield perturbations. Using the theorem in equation 2.10 as is, and with A interchanged with $B*$, we obtain

$$\oint_{\mathbf{r}\in\partial\mathbb{V}} \left[p_S^A \mathbf{v}_S^{B*} + p_S^{B*} \mathbf{v}_S^A\right] \cdot d\mathbf{S} = \int_{\mathbf{r}\in\mathbb{V}} i\omega(\kappa - \kappa_0)\left[p_0^A p_S^{B*} - p_S^A p_0^{B*}\right] dV \ , \qquad (2.14)$$

which is the correlation-type counterpart of the theorem in equation 2.13. This theorem can be extended to include small density perturbations in a manner analogous to that described for equation 2.13. Like the representation theorems in equations 2.8 and 2.10, equations 2.13 and 2.14 provide relations between wavefield perturbations and wavefields that satisfy the acoustic wave equations.

2.4 Representation theorems for the Green's functions

In this Section, we rewrite the representation theorems for perturbed acoustic media derived in the previous Section in terms of the Green's functions. We focus the discussion on the role of Green's functions in the representation theorems in equations 2.10 and 2.14 because of the applicability of these theorems to remote sensing experiments (treated in the next Section). The Green's function forms of the

theorems in equations 2.4 and 2.6 are treated by others (e.g., Wapenaar et al., 2002; Wapenaar and Fokkema, 2006; Draganov et al., 2006). The convolution theorem in equation 2.4 leads to the well-known acoustic source-receiver reciprocity relation (e.g., Rayleigh, 1878; Fokkema and van den Berg, 1993; Wapenaar and Fokkema, 2006). From the correlation-type theorem in equation 2.6, Wapenaar et al. (2004) and Wapenaar and Fokkema (2006) show that the surface integration of the cross-correlated Green's function results in the causal and acausal Green's functions that propagate between two receivers. We discuss this with in more detail below.

We introduce the Green's functions, in the frequency domain, by setting

$$q^{A,B} = \delta(\mathbf{r} - \mathbf{r}_{A,B}) \, , \tag{2.15}$$

where the positions $\mathbf{r}_{A,B}$ denote the wave states A and B, respectively. This choice for q allows for expressing the field quantity p in terms of the Green's functions G, i.e.,

$$p^{A,B}(\mathbf{r}, \omega) = G(\mathbf{r}, \mathbf{r}_{A,B}, \omega) = G_0(\mathbf{r}, \mathbf{r}_{A,B}, \omega) \, + \, G_S(\mathbf{r}, \mathbf{r}_{A,B}, \omega) \, , \tag{2.16}$$

where the subscripts $_0$ and $_S$ stand, respectively, for unperturbed waves and wavefield perturbations. Note that these are the Green's functions for sources of the volume injection rate type. The derivation below can also be reproduced using volume injection sources (e.g., Wapenaar and Fokkema, 2006). It follows from equations 2.16 and 2.2 that $\mathbf{v}^{A,B} = (i\omega\rho)^{-1}\nabla G(\mathbf{r}, \mathbf{r}_{A,B}, \omega)$. Substituting the Green's functions (equa-

tion 2.16) for the wavefields p and $\mathbf{v}$ in equation 2.10 gives

$$\begin{aligned}\int_{\mathbf{r}\in\mathbb{V}} G_S(\mathbf{r},\mathbf{r}_A)\delta(\mathbf{r}-\mathbf{r}_B)dV &= \oint_{\mathbf{r}\in\partial\mathbb{V}} \frac{1}{i\omega\rho}\left[G_S(\mathbf{r},\mathbf{r}_A)\nabla G_0^*(\mathbf{r},\mathbf{r}_B)\right]\cdot d\mathbf{S} \\ &- \oint_{\mathbf{r}\in\partial\mathbb{V}} \frac{1}{i\omega\rho}\left[G_0^*(\mathbf{r},\mathbf{r}_B)\nabla G_S(\mathbf{r},\mathbf{r}_A)\right]\cdot d\mathbf{S} \\ &+ \int_{\mathbf{r}\in\mathbb{V}} i\omega(\kappa_0-\kappa)G(\mathbf{r},\mathbf{r}_A)G_0^*(\mathbf{r},\mathbf{r}_B)dV\ ; \quad (2.17)\end{aligned}$$

for brevity we omit the dependence on ω. The volume integral on the left-hand side yields $G_S(\mathbf{r}_B,\mathbf{r}_A)$, which describes causal wavefield perturbations that propagate from $\mathbf{r}_B$ to $\mathbf{r}_A$ as if the observation point at $\mathbf{r}_B$ acts as a source. The wavefields ∇G can be expressed in terms G. If the medium at and around $\partial\mathbb{V}$ is smooth, the normal derivatives of G (right-hand side of equation 2.17) are approximately given by multiplying each wave constituent in the Green's function by $\pm i\omega c^{-1}(\mathbf{r})|cos\ \alpha(\mathbf{r})|$ (Wapenaar and Fokkema, 2006); with $c(\mathbf{r}) = [\kappa(\mathbf{r})\rho(\mathbf{r})]^{-\frac{1}{2}}$ the local acoustic wavespeed at $\partial\mathbb{V}$ and $\alpha(\mathbf{r})$ the local angle between a given ray-geometrical arrival and $\mathbf{n}$ (Figure 2.1). The minus and plus signs indicate inward and outward propagating waves, respectively. When the medium outside $\mathbb{V}$ is heterogeneous, and depending on the shape of $\partial\mathbb{V}$, the correlation products between in- and out-going waves from the two wave states contribute to the surface integral on the right-hand side of equation 2.17 (Draganov et al. 2003, 2006; Wapenaar and Fokkema, 2006).

With the purpose of deriving relations that allow the experimental extraction of $G_S(\mathbf{r}_B,\mathbf{r}_A)$ from sources over $\partial\mathbb{V}$, we assume that the medium at and outside $\partial\mathbb{V}$ is homogeneous with wavespeed c and mass density ρ. In this case we can write, in equation 2.17, ∇G in terms of G by multiplying each wave constituent by $i\omega c^{-1}(\mathbf{r})|cos\ \alpha(\mathbf{r})|$. Next, assuming far-field propagation and that ∇G is parallel to $\mathbf{n}$ (i.e., that the surface is locally smooth and perpendicular to incoming waves)

at $\partial\mathbb{V}$ we set $(\nabla G)\cdot\mathbf{n} = i\omega c^{-1}G$. We rely on these assumptions in all subsequent equations. Thus, we can simplify equation 2.17 to

$$\begin{aligned} G_S(\mathbf{r}_B,\mathbf{r}_A) &= \frac{2}{\rho c}\oint_{\mathbf{r}\in\partial\mathbb{V}} G_S(\mathbf{r},\mathbf{r}_A)G_0^*(\mathbf{r},\mathbf{r}_B)dS \\ &+ i\omega\int_{\mathbf{r}\in\mathbb{V}}(\kappa_0-\kappa)G(\mathbf{r},\mathbf{r}_A)G_0^*(\mathbf{r},\mathbf{r}_B)dV\ . \end{aligned} \tag{2.18}$$

This equation shows that the causal wavefield perturbation $G_S(\mathbf{r}_B,\mathbf{r}_A)$ is obtained from the surface integral of the cross-correlation of wavefield perturbations at $\mathbf{r}_A$ with unperturbed waves at $\mathbf{r}_B$. Along with this surface integral, a volume integral is necessary to recover $G_S(\mathbf{r}_B,\mathbf{r}_A)$. Using the Green's function form of the representation theorem in equation 2.10 with interchanged superscripts A by $B*$, we obtain $G_S^*(\mathbf{r}_B,\mathbf{r}_A)$:

$$\begin{aligned} G_S^*(\mathbf{r}_B,\mathbf{r}_A) &= \frac{2}{\rho c}\oint_{\mathbf{r}\in\partial\mathbb{V}} G_0(\mathbf{r},\mathbf{r}_A)G_S^*(\mathbf{r},\mathbf{r}_B)dS \\ &- i\omega\int_{\mathbf{r}\in\mathbb{V}}(\kappa_0-\kappa)G_0(\mathbf{r},\mathbf{r}_A)G^*(\mathbf{r},\mathbf{r}_B)dV\ . \end{aligned} \tag{2.19}$$

The relations in equations 2.18 and 2.19 are similar in form to expressions for the retrieval of the impulse response from diffuse-wave correlation (e.g., Lobkis and Weaver, 2001; Malcolm et al., 2004; Larose et al., 2006) and from correlations of deterministic wavefields (e.g., Wapenaar, 2004; Snieder, 2004; Wapenaar and Fokkema, 2006). In these studies, the cross-correlation of recorded waves leads to a superposition of causal and acausal wavefields G or G_0. This points to two important differences between equations 2.18 and 2.19 and previous expressions for Green's function retrieval. The first difference is that here we obtain the wavefield perturbations G_S, which by themselves do not satisfy the acoustic wave equations (e.g., equation 2.2),

from cross-correlating G_S with G_0. Second, the proper manipulation of unperturbed waves G_0 and perturbations G_S in the integrands of equations 2.18 and 2.19 allow for the separate retrieval of causal and acausal $G_S(\mathbf{r}_B, \mathbf{r}_A)$ in the frequency-domain.

The retrieval of $G_0(\mathbf{r}_B, \mathbf{r}_A)$ from cross-correlation of the recorded $G_0(\mathbf{r}, \mathbf{r}_{A,B})$ or $G(\mathbf{r}_B, \mathbf{r}_A)$ with $G(\mathbf{r}, \mathbf{r}_{A,B})$ only requires a surface integration (e.g., Wapenaar, 2004; Wapenaar and Fokkema, 2006). Apart from surface integration, the retrieval of $G_S(\mathbf{r}_B, \mathbf{r}_A)$ from equations 2.18 or 2.19 also requires a volume integration. The evaluation of the volume integral requires, apart from knowledge of the wavefields G and G_0 within $\mathbb{V}$, the values of the medium perturbations $(\kappa_0 - \kappa)$. Having only sources over $\partial\mathbb{V}$, and with no knowledge about the model perturbations, the reconstruction of $G_S(\mathbf{r}_B, \mathbf{r}_A)$ from equations 2.18 and 2.19 is incomplete. As we discuss in the next Section, there are cases in which the volume integrals in equations 2.18 and 2.19 can be neglected. Here, we provide insight into the physical meaning of the volume integrals in these equations.

The volume integrals in equation 2.18 account for medium perturbations that lie in the path of unperturbed waves $G_0(\mathbf{r}, \mathbf{r}_B)$. To illustrate this concept, we use the example in Figure 2.2. In this example, we assume that the medium perturbations are confined to a defined subvolume $\mathbb{P}$. This causes the integrand of the volume integral in equation 2.18 (as well as in equation 2.19) to be nonzero only for $\mathbf{r} \in \mathbb{P}$. In Figure 2.2, the indicated source position $\mathbf{r}$ is a stationary source position that gives the dominant contribution to direct waves propagating from $\mathbf{r}_B$ to $\mathbf{r}_A$ (Snieder et al., 2006; Chapter 3). The solid arrow in the Figure represents the stationary path of $G_0(\mathbf{r}, \mathbf{r}_B)$, while the dotted arrow denotes the stationary path of $G_S(\mathbf{r}_B, \mathbf{r}_A)$. The stationary path of $G(\mathbf{r}, \mathbf{r}_A)$, for the desired arrival (dotted arrow inFigure 2.2), is given by the combination of the two paths shown in Figure 2.2. Along the path shown in Figure 2.2

(dotted arrow), $G_S(\mathbf{r}_B, \mathbf{r}_A)$ is only influenced by perturbations that lie between $\mathbf{r}_B$ and $\mathbf{r}_A$. The same perturbations influence the waves in $G_S(\mathbf{r}, \mathbf{r}_A)$ (present in the integrands in equation 2.18), but these waves are also perturbed by medium changes in the path from $\mathbf{r}$ to $\mathbf{r}_B$. In this case, the portion of the stationary path of $G_S(\mathbf{r}, \mathbf{r}_A)$ that is influenced by perturbations between $\mathbf{r}$ to $\mathbf{r}_B$ coincides with the stationary path of $G_0(\mathbf{r}, \mathbf{r}_B)$ (solid arrow) in Figure 2.2. Thus, the volume integral in equation 2.18 acts as *secondary sources* within $\mathbb{P}$ that are proportional to the perturbation $(\kappa_0 - \kappa)$, placed along a perturbation path defined by $G(\mathbf{r}, \mathbf{r}_A)G_0^*(\mathbf{r}, \mathbf{r}_B)$. These secondary sources cancel the contribution of medium perturbations along the solid arrow (the path of $G_0(\mathbf{r}, \mathbf{r}_B)$) in Figure 2.2 that are encoded in $G_S(\mathbf{r}, \mathbf{r}_A)$ (e.g., within the surface integral in equation 2.18). This cancelation ensures that the wavefield perturbations in the recovered $G_S(\mathbf{r}_B, \mathbf{r}_A)$ correspond to the medium perturbations sensed only by waves that propagate from $\mathbf{r}_B$ to $\mathbf{r}_A$.

Although we use the example of Figure 2.2 to discuss the volume integral in equation 2.18, the integral accounts for perturbations in the paths of all waves in $G_0(\mathbf{r}, \mathbf{r}_B)$ (apart from the arrows in Figure 2.2) and for arbitrary source positions $\mathbf{r}$ (not just for stationary source positions). In other words, even though the argument above, for simplicity, relies on geometrical concepts (e.g., stationary-phase) the interpretation of the volume integral holds for finite-bandwidth signals and for media of arbitrary scattering strength. This follows from the fact that there are no high-frequency or weak perturbations assumptions behind equation 2.18. Furthermore, this interpretation is not restricted to medium configurations as in Figure 2.2; the medium perturbations can be arbitrarily distributed within $\mathbb{V}$. Although we focus in the interpretation above on the volume integral in equation 2.18, a similar interpretation holds for the volume integral in equation 2.19. In equation 2.19, the volume integral compensates

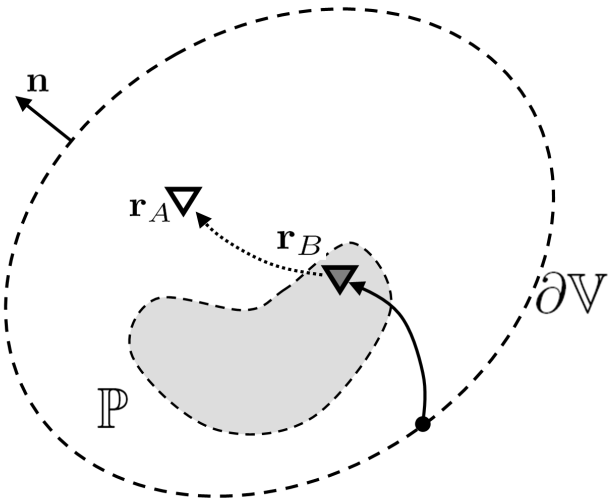

Figure 2.2. A schematic interpretation of the function of the volume integral in retrieving $G_S(\mathbf{r}_B, \mathbf{r}_A)$ (equation 2.18). Medium perturbations are restricted to the volume $\mathbb{P}$. The solid arrow indicates the stationary paths unperturbed waves in $G_0(\mathbf{r}, \mathbf{r}_B)$, while the dotted arrow denotes perturbed waves in $G_S(\mathbf{r}_B, \mathbf{r}_A)$. The path defined by the two arrows combined is also a stationary path to waves in $G_S(\mathbf{r}, \mathbf{r}_A)$. Note that the medium gets perturbed along a portion of the path of $G_0(\mathbf{r}, \mathbf{r}_B)$. Here, the position $\mathbf{r}$ is a stationary source position that contributes to the direct wave that travels from $\mathbf{r}_B$ to $\mathbf{r}_A$.

the effects of medium perturbations in the path of all unperturbed waves in $G_0(\mathbf{r}, \mathbf{r}_A)$. When medium perturbations also occur in densities ($\rho \neq \rho_0$; equations 2.1 and 2.2), the corresponding volume integrals (see discussion in previous Section) play the same role as the volume integrals that account for perturbations in compressibility (equations 2.18 and 2.19).

Equations 2.18 and 2.19 provide representation relations obtained from impulsive physical sources (e.g., equation 2.15). The results in this paper can be extended to transient excitations (Snieder et al. 2006; Wapenaar and Fokkema, 2006) of the type $W(\mathbf{r}, \omega)$, such that the recorded data is, for example, given by $p^A(\mathbf{r}, \omega) = W(\mathbf{r}, \omega) G(\mathbf{r}, \mathbf{r}_A, \omega)$ (and likewise for $\mathbf{r}_B$). In that case the results in equations 2.18 and 2.19 are multiplied by $\langle |W(\mathbf{r}, \omega)|^2 \rangle$, an arbitrarily chosen average of the power spectrum of the excitation (Snieder et al. 2006; Wapenaar and Fokkema, 2006). The results of equations 2.18 and 2.19 can also be extended to accommodate mutually active uncorrelated noise sources (e.g., Weaver and Lobkis, 2001; Derode et al., 2003; Shapiro et al., 2005; Snieder et al., 2006) by following the same steps described by Wapenaar and Fokkema (2006).

Finally, we turn our attention to the representation theorem in equation 2.14. Using the Green's functions as defined in equation 2.16, along with the same assumptions used to derive equations 2.18 and 2.19, we express equation 2.14 as

$$\begin{aligned} \frac{2}{\rho c} \oint_{\mathbf{r} \in \partial \mathbb{V}} G_S(\mathbf{r}, \mathbf{r}_A) G_S^*(\mathbf{r}, \mathbf{r}_B) dS &= i\omega \int_{\mathbf{r} \in \mathbb{V}} (\kappa - \kappa_0)\, G_0(\mathbf{r}, \mathbf{r}_A) G_S^*(\mathbf{r}, \mathbf{r}_B) dV \\ &- i\omega \int_{\mathbf{r} \in \mathbb{V}} (\kappa - \kappa_0)\, G_S(\mathbf{r}, \mathbf{r}_A) G_0^*(\mathbf{r}, \mathbf{r}_B) dV \ . \end{aligned} \tag{2.20}$$

This equation relates the surface integral of cross-correlated wavefield perturbations

to a volume integral whose integrand is proportional to the medium perturbation and cross-correlations between unperturbed waves and wavefield perturbations. Note that equation 2.20 does not depend on the source term q (equation 2.15); the same holds for the representation theorem in equation 2.14. Although not immediately applicable for the reconstruction of the Green's function as equations 2.18 or 2.19, equation 2.20 is suitable for other purposes in remote sensing experiments. These purposes are discussed in the next Section.

2.5 Applications to remote sensing experiments

As we discuss in the previous Section, equations 2.18 and 2.19 retrieve $G_S(\mathbf{r}_B, \mathbf{r}_A)$: the wavefield perturbations that propagate between $\mathbf{r}_B$ and $\mathbf{r}_A$, as if the observation point at $\mathbf{r}_B$ acts as a source. This result is of particular interest for remote sensing experiments where physical sources exist only on the surface $\partial\mathbb{V}$ (Figure 2.3), or when the excitation is caused by uncorrelated noise sources of unknown locations randomly distributed within $\mathbb{V}$. In such cases, equations 2.18 and 2.19 can be used to retrieve the wavefield perturbation between receivers within the volume $\mathbb{V}$, which in turn can be used to image the perturbed medium. We refer to the retrieval of impulse response between receivers by the term *interferometry*, borrowing the terminology from the field of exploration geophysics, where it is referred to as *seismic interferometry* (Schuster, 2001). We use the term *interferometric imaging* when referring to the imaging[3] of the impulse response reconstructed by interferometry.

The main issue in using equations 2.18 and 2.19 for interferometry is that the medium perturbations $(\kappa_0 - \kappa)$ (as well as field quantities) must be known for the

[3]By *imaging* we refer to imaging based on linear mapping procedures as described by Biondi (2006), as well as inverse imaging methods (e.g., Tarantola, 1987; Bleistein et al., 2001; Weglein et al., 2003).

volume integral in the equations to be evaluated. This is a problem for interferometry because it typically relies only on the observation, at the points $\mathbf{r}_A$ and $\mathbf{r}_B$, of waves excited by sources on $\partial\mathbb{V}$ (e.g., Weaver and Lobkis, 2001; Wapenaar et al. 2004; Wapenaar and Fokkema, 2006). This problem can be overcome by assuming that medium perturbations are restricted to a perturbation volume $\mathbb{P}$ that does not include the observation points $\mathbf{r}_A$ and $\mathbf{r}_B$ (Figure 2.3). In this case, there is a subset of sources $\mathbf{r}$ (Figure 2.3) on a portion $\partial\mathbb{V}_1$ of $\partial\mathbb{V}$ for which the stationary paths of unperturbed waves in $G_0(\mathbf{r},\mathbf{r}_B)$ are not affected by the medium perturbations within $\mathbb{P}$ (e.g., solid arrow in Figure 2.3). For these sources, the stationary wave paths in $G_S(\mathbf{r},\mathbf{r}_A)$ that are affected by the medium perturbations are the same as those in $G_S(\mathbf{r}_B,\mathbf{r}_A)$. Because of this, the contribution of the volume integral in equation 2.18 for $\mathbf{r}\in\partial\mathbb{V}_1$ is negligible, hence,

$$G_S(\mathbf{r}_B,\mathbf{r}_A)\approx\frac{2}{\rho c}\int_{\mathbf{r}\in\partial\mathbb{V}_\mathbf{1}} G_S(\mathbf{r},\mathbf{r}_A)G_0^*(\mathbf{r},\mathbf{r}_B)dS\ , \tag{2.21}$$

Equation 2.21 only recovers a portion of the waves in $G_S(\mathbf{r}_B,\mathbf{r}_A)$ (dotted arrow in Figure 2.3) that arise from stationary source regions on the surface segment $\partial\mathbb{V}_1$ (e.g., in the vicinity the source position $\mathbf{r}$ in Figure 2.3; Snieder et al. 2006;Chapter 3). The volume integral in equation 2.18 cannot be neglected in the cases when (i) $\mathbf{r}_B$ is inside $\mathbb{P}$ (e.g., Figure 2.2), (ii) when the medium is perturbed over the entire support of $\mathbb{V}$ or (iii) when we consider sources for which wave paths in $G_0(\mathbf{r},\mathbf{r}_B)$ are affected by perturbations in $\mathbb{P}$.

According to equation 2.21, by cross-correlating unperturbed waves measured at $\mathbf{r}_B$ with wavefield perturbations at $\mathbf{r}_A$ and integrating over sources at $\partial\mathbb{V}_1$, we obtain wavefield perturbations that propagate from $\mathbf{r}_B$ to $\mathbf{r}_A$ as if a source were placed at $\mathbf{r}_B$. This makes equation 2.21 suitable for interferometry. Chapter 3 use stationary-phase analysis to validate of equation 2.21 for the special case of a homogeneous

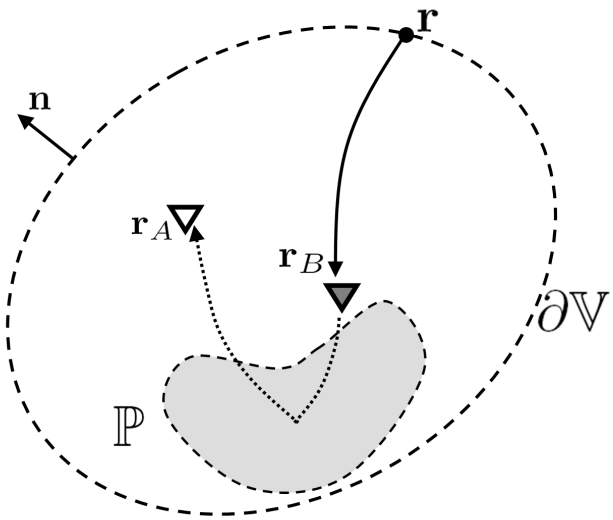

Figure 2.3. Application of the representation theorem in equation 2.18 in interferometric imaging experiments. As in Figure 2.2, solid and dotted arrows represent stationary paths of unperturbed and perturbed waves, respectively. The medium perturbation is restricted to the volume $\mathbb{V}$. Both receivers, at $\mathbf{r}_A$ (white triangle) and $\mathbf{r}_B$ (grey triangle), are outside the perturbation volume $\mathbb{V}$. The stationary paths indicated by the arrows contribute to the reconstruction of waves scattered by the perturbations within $\mathbb{P}$.

medium with a single reflector. In equation 2.21, the truncation of the surface integral from equation 2.18 can lead to a nonzero error in the retrieval of $G_S(\mathbf{r}_B, \mathbf{r}_A)$. If the medium and/or its perturbations are heterogeneous, this error may manifest in the form of amplitude distortions (e.g., caused by apparent absorption) or by the introduction of spurious arrivals (Snieder et al., 2006; Wapenaar, 2006;Chapter 3). The volume integral in equation 2.19 can be neglected by considering sources $\mathbf{r} \in \partial\mathbb{V}_2$, for which the wave paths in $G_0(\mathbf{r}, \mathbf{r}_A)$ are not affected by medium perturbations in $\mathbb{P}$. This reasoning is analogous to that we used to approximate equation 2.21 from equation 2.18.

Equation 2.20 can also be applied to remote sensing experiments. The application, however, is not the same as that of equations 2.18 and 2.19. Instead of recovering the wavefield perturbations $G_S(\mathbf{r}_B, \mathbf{r}_A)$, equation 2.20 can be used to estimate the medium perturbations $(\kappa_0 - \kappa)$ inside $\mathbb{V}$ (right-hand side of the equation) from wavefield perturbations measured at $\mathbf{r}_A$ and $\mathbf{r}_B$ for $\mathbf{r} \in \partial\mathbb{V}$. To do this, we assume that we know, apart from $G_S(\mathbf{r}, \mathbf{r}_A)$ from $\mathbf{r} \in \partial\mathbb{V}$, the unperturbed medium parameters κ_0 as well as the unperturbed waves observed at $\mathbf{r}_A$ and $\mathbf{r}_B$ excited by $\mathbf{r} \in \partial\mathbb{V}$. This means that the left-hand side of equation 2.20 is a known quantity. Furthermore, since κ_0 and G_0 for $\mathbf{r} \in \partial\mathbb{V}$ are known, it is possible to model the unperturbed waves inside $\mathbb{V}$. Within the integrand in the right-hand side of equation 2.20, the wavefield perturbations G_S can be expressed in terms of the corresponding unperturbed wavefields G_0 and of $(\kappa_0 - \kappa)$ by means of a scattering series (e.g., Lippmann, 1956; Rodberg, 1967; de Hoop, 1996). When using a scattering series formulation, the only unknown quantities in equation 2.20 are the medium perturbations $(\kappa_0 - \kappa)$. These perturbations can be estimated by solving the integral expression in equation 2.20. Inverse scattering methods, with the examples of the Lippmann-Schwinger based ap-

proach of Weglein et al. (2003) or the hybrid Bremmer-Lippmann method of Malcolm et al. (2007), can in principle be used to invert equation 2.20 for the perturbations $(\kappa_0 - \kappa)$. The numerical implementation of such inverse scattering methods is involved and yields approximate results (Malcolm et al., 2007). Although we do not provide a detailed treatment of the Green's function forms of the convolution-type theorems from the previous Section (equations 2.8 or 2.13), these can be employed for the estimation of the medium perturbations in an analogous manner as we describe here for equation 2.14.

2.6 Discussion and conclusion

By manipulating the acoustic wave equations for unperturbed and perturbed media we derive convolution- and correlation-type representation theorems for perturbed acoustic media. These theorems differ from previous forms of reciprocity theorems (e.g., de Hoop, 1988; Fokkema and van den Berg, 1993) because they provide explicit relations between the wavefields and wavefield perturbations. Unlike wavefield parameters (e.g., de Hoop, 1988; Fokkema and van den Berg, 1993), the wavefield perturbations by themselves do not satisfy the perturbed wave equations. We extend our reciprocity theorems for perturbed media to the special case of the Green's functions.

With the Green's function form of the correlation-type representation theorems, we show that by cross-correlating wavefield perturbations measured at one receiver with unperturbed waves recorded by another we obtain the wavefield perturbations that propagate between the receivers as if one of the receivers were a source. This concept relates to previous work in the field of Green's function retrieval from diffuse-wave correlation (e.g., Weaver and Lobkis, 2001; Malcolm et al., 2004; Larose et al.,

2006) and from correlation of deterministic wavefields (Wapenaar, 2004; Snieder, 2004; Wapenaar and Fokkema, 2006). These studies show that cross-correlations can be used to recover a superposition of the causal and acausal parts of the wavefields G or G_0 (i.e., unperturbed or perturbed). Our expressions recover the wavefield perturbations G_S, which do not satisfy the wave equations for G, separately from its acausal counterpart G_S^*. For systems that are invariant under time reversal, Green's function retrieval by wavefield cross-correlations require only a surface integration (Larose et al., 2006; Wapenaar and Fokkema, 2006; Snieder et al., 2007), whereas the retrieval of the perturbations G_S from correlations of wavefield perturbations with unperturbed wavefields requires an additional volume integral. We show that this volume integral accounts for medium perturbations that lie in the path of unperturbed waves that propagate from sources at the surface $\partial\mathbb{V}$ to the receiver that acts as a pseudo-source.

The extraction of wavefield perturbations G_S that propagate between receivers as if one of them acts as a source is a useful tool for remote sensing experiments. When medium perturbations are localized within a volume $\mathbb{P}$ that does not contain the observation points, the wavefield perturbations propagating between receivers can be obtained from only the surface integral of cross-correlated perturbations and unperturbed wavefields (i.e., the volume integral can be neglected). In this case, the correlation-type theorems we propose can be applied to *interferometry* (the term is borrowed from Schuster, 2001). We have proposed direct applications of the interferometric retrieval of wavefield perturbations as proposed in this paper (e.g., Chapter 3; Chapter 6). In Chapter 6, the retrieval of wavefield perturbations according to the formulation in this paper is used to image salt structures in the Earth's subsurface from the interference of multiply scattered waves measured inside a deep borehole in

off-shore Gulf of Mexico. Chapter 3 use the concepts developed here to interpret the physical meaning of their deconvolution-based interferometry approach. Their deconvolution interferometry method (based partly on equations 2.18 and 2.21) has been validated with numerical experiments Chapters 3 and 4. Using field measurements of the noise generated by a well being drilled, in Chapters 4 and 5 we also apply the concepts presented in this paper.

As suggested in Chapter 6, the interferometric retrieval of wavefield perturbations we describe here can be used for targeting the imaging of particular portions of the medium. They refer to this as *target-oriented interferometry* (Chapter 6). Such an application has also been implicitly proposed by Bakulin and Calvert (2006) and by Mehta et al. (2007), in the so-called *Virtual Source* method. With this method (Bakulin and Calvert, 2006; Mehta et al., 2007a), transmission and reflection responses can be regarded as unperturbed waves and wavefield perturbations, respectively. This points out to the relationship between the results we present here and those of Wapenaar et al. (2004), that show that the reflection response between receivers can be obtained from cross-correlations between reflection and transmission responses measured by these receivers. Although most of the examples cited come from the field of geophysics, our results are immediately applicable to other fields in acoustics such as physical oceanography, laboratory and medical ultrasonics, and non-destructive testing.

Another important potential use for the exact form of the correlation-type reciprocity theorems that retrieve the wavefield perturbations that propagate between two receivers lies in the calculation of the so-called *Fréchet derivatives* (Tarantola, 1987; Hettlich, 1998; Sava and Biondi, 2004). The Fréchet derivatives consist in the partial derivatives of the wavefield perturbations with respect to the medium perturbations,

which can be directly derived from the theorems we provide here. These derivatives are important for the computation of sensitivity kernels used in full-waveform inversion (e.g., Tarantola, 1987), in inverse imaging (Hettlich, 1998) or in linearized forms of wave-equation based tomography (Sava and Biondi, 2004).

From correlation- and convolution-type representation theorems in perturbed media, we suggest the application of estimating the medium perturbations by combining theorems presented here with inverse scattering theory (Weglein et al., 2003; Malcolm et al., 2007). This type of approach can be potentially used for inverse imaging of the wavefield perturbations (e.g., Tarantola, 1987; Weglein et al., 2003), as well as for the targeting the extraction of a particular desired subset of the wavefield perturbations (Malcolm et al., 2007). In this context, the use of our expressions can be simplified through linearizing the wavefield perturbations on the medium changes. This would yield, for example, a *Born* approximation (e.g., Snieder, 1990; Bleistein et al., 2001; Weglein et al., 2003) of the theorems presented here.

Apart from imaging applications, we expect that our results (both in terms of retrieving wavefield perturbations and for estimating medium perturbations) can be used for monitoring temporal changes in the medium. In geoscience, this could be applied to remotely monitoring the depletion of aquifer or hydrocarbon reservoirs; or monitoring the injection of CO_2 for carbon sequestration. In material sciences, our results can be used to monitor material integrity with respect, for example, to temporal changes in temperature. The detection of earthquake damage is a potential application in the field of structural engineering. Within medical imaging applications, our expressions can be tailored, for instance, to observe tumor evolution from ultrasonic measurements.

The theory we present here assumes lossless media. In light of the work of Snieder

(2007), who shows that Green's function retrieval can be accomplished in attenuative acoustic media, we believe that our discussions regarding the retrieval of wavefield perturbations can be extended to absorbing media by following steps analogous to those in Snieder (2007). Furthermore, since Green's function retrieval by cross-correlations has been shown to hold for a wide class of differential equations (Wapenaar et al., 2006; Snieder, 2006; Snieder et al., 2007), the representation theorems for perturbed media presented here can be potentially extended to describe other physical phenomena, such as perturbations in electromagnetic wave propagation, diffusion, advection and quantum scattering.

2.7 Acknowledgements

This research was financed by the NSF (grant EAS-0609595) and by the sponsors of the Consortium for Seismic Inverse Methods for Complex Structures at the Center for Wave Phenomena. We thank Huub Douma (Princeton University) for a thorough review of the paper and for exciting discussions and suggestions.

Chapter 3

INTERFEROMETRY BY DECONVOLUTION – THEORY AND NUMERICAL EXAMPLES[1]

3.1 Summary

Interferometry allows us to synthesize data recorded at any two receivers into waves that propagate between these receivers as if one of them behaves as a source. This is typically accomplished by cross-correlations. Based on perturbation theory and representation theorems, we show that interferometry can also be done by deconvolutions for arbitrary media and multidimensional experiments. This is important for interferometry applications where the excitation is described by a complicated function. First, we derive a series expansion that proves that interferometry can be accomplished by deconvolution before source integration. This method, unlike using cross-correlations, yields only causal scattered waves that propagate between the receivers. We provide an analysis in terms of singly and multiply scattered waves. Because deconvolution interferometry shapes the zero-offset trace in the interferometric shot gather into a band limited spike centered at time equal zero, spurious arrivals are generated by the method. Here, we explain the physics behind these spurious arrivals and demonstrate the they usually do not map onto coherent structures in the image domain. We also derive an interferometry method that does deconvolution after source integration that is associated with existing interferometry techniques. Decon-

[1]Submitted to Physical Review E.

volution after source integration yields both causal and acausal scattering responses, and it also introduces spurious events. Finally, we illustrate the main concepts of deconvolution interferometry and its differences with the correlation-based approach through stationary-phase analysis and with numerical examples.

3.2 Introduction

The main objective of seismic interferometry is to obtain the impulse response between receivers, without any knowledge about model parameters (Lobkis and Weaver, 2001; Weaver and Lobkis, 2004a; Wapenaar et al., 2004a). Typically, interferometry is implemented using by cross-correlations of recorded data (Curtis et al., 2006; Larose et al., 2006). Many of the formal proofs and arguments surrounding interferometry are based on cross-correlations. Proofs based on correlation-type representation theorems state the validity of interferometry for acoustic waves (Lobkis and Weaver, 2001; Weaver and Lobkis, 2004b), for elastic media (Wapenaar et al, 2004a and b, Draganov et al., 2006), and also for attenuative (Snieder, 2007) and perturbed media (Chapter 2). Other proofs of interferometry based on time-reversal were offered by Fink (2006), and by Bakulin and Calvert (2006) in their Virtual-Source methodology. Schuster et al. (2004) and Yu and Schuster (2006) use correlation-based interferometry imbedded within an asymptotic migration scheme to do interferometric imaging. Similarly, Snieder (2004) Sabra et al. (2004) and Snieder et al. (2006a) rely on the stationary-phase method to explain results from interferometry.

The field of interferometry expands beyond exploration seismology. There are examples of interferometry applications in many other fields such as ultrasonics (Malcolm et al., 2004; van Wijk, 2006), helioseismology (Rickett and Claerbout, 1999), global seismology (Shapiro et al., 2005; Sabra et al., 2005). Curtis et al. (2006) and

Larose et al. (2006) give comprehensive interdisciplinary reviews of interferometry. As the understanding of interferometry progresses, finding more applications to the method is inevitable. For example, reservoir engineering may soon benefit from interferometry, as Snieder (2006) recently found that the principles of interferometry also hold for the diffusion equation. In an even more general framework, interferometry can be applied to a wide class of partial differential equations, with the examples of the Schrödinger or the advection equation (Wapenaar et al., 2006; Snieder et al., 2007). These findings might bring possibilities for interferometry within quantum mechanics, meteorology or mechanical engineering, for instance.

Our goal in this paper is to gain insight into interferometry from yet another point of view. Although interferometry is typically done by correlations, it is almost natural to wonder if it could be accomplished by deconvolutions. This issue was in fact raised by Curtis et al. (2006) as one of the standing questions within interferometry. We claim that interferometry can indeed be accomplished by deconvolutions for arbitrary, multidimensional media. In fact, there are already successful examples of deconvolution interferometry. Trampert et al. (1993) used deconvolution to extract the SH-wave propagator matrix and to estimate attenuation. Snieder and Şafak (2006) recovered the elastic response of a building using deconvolutions, and were able to explain their results using 1D normal-mode theory. Mehta and Snieder (2006) obtained the near-surface propagator matrix using deconvolutions from the recording of a teleseismic event in a borehole seismometer array.

In his early paper that spawned much of today's work on interferometry, Claerbout (1968) originally suggested the use of deconvolution to retrieve the Earth's 1D reflectivity response. He then turned to correlation because it tends to be a more stable operation. Loewenthal and Robinson (2000) showed that the deconvolution

of dual wavefields can be used to change the boundary conditions of the original experiment to generate only up-going scattered waves at the receiver locations and to recover reflectivity. In a series of papers on free-surface multiple suppression, Amundsen and co-workers use inverse deconvolution-like operators designed to remove the free-surface boundary condition (e.g., Amundsen, 2001; Holvik and Amundsen, 2005). The topics of multiple suppression and interferometry are intrinsically related, precisely due to the manipulation of boundary conditions. This is explicitly pointed out by Berkhout and Verschuur (2006), by Mehta et al. (2006) and by Snieder et al. (2006b). Consequently, previous work on deconvolution-based multiple suppression is also related to the practice of interferometry. Since we seek to shed light on the physics behind deconvolution interferometry, we hope to bring yet another piece to the puzzle that connects interferometry and other geophysical applications. These applications may be the manipulation of boundary conditions for multiple suppression, passive and active imaging, time-lapse monitoring and others.

Using a combination of perturbation theory and representation theorems (as in Chapter 2), we first review interferometry by correlations. In our discussion on correlation-based interferometry, we restrict ourselves to key aspects which help understanding the meaning of deconvolution interferometry. In the Section that follows, we go through a derivation in which we represent deconvolution interferometry by a series similar in form to the Lippmann-Schwinger scattering series (Rodberg et al., 1967; Weglein et al., 2003). We first analyze the meaning of series terms of leading-order in the scattered wavefield, to then discuss the role of the higher-order terms of the deconvolution interferometry series. Next, we also demonstrate that interferometry can be accomplished by deconvolution after integration over sources, and compare the outcome of this method with deconvolution before source integration and with

cross-correlation interferometry. Finally, using a single-layer model we illustrate the main concepts of deconvolution interferometry, while comparing it to its correlation-based counterpart. This is done by a stationary-phase analysis of the most prominent terms in deconvolution interferometry, and with a synthetic data example.

Although it is not our intention here to discuss a specific use for interferometry by deconvolution, we point out the this method will be of most use for interferometry applications that require the suppression of the source function. The paper Chapter 4 is dedicated to a specific application of deconvolution interferometry, providing both numerical and field data examples in drill-bit seismic imaging. In particular, an important component of the broad-side imaging of the San Andreas fault at Parkfield presented Chapter 5 would not have been possible without deconvolution interferometry (Chapter 4). Apart from drill-bit seismics, a complicated source signal may be generated by the Earth itself. In the examples by Trampert et al. (1993), Snieder and Şafak (2006) and Mehta and Snieder (2006), deconvolution is necessary to suppress the incoming Earth signal, which contains arrivals of different modes, multiply scattered waves, etc. In the method by Loewenthal and Robinson (2000) the purpose of deconvolution is to collapse all down-going waves into a spike at zero time, leaving only the up-going Earth response. These are but examples of applications where deconvolution interferometry plays an important role.

3.3 Theory of interferometry

In this section we describe the theory of deconvolution interferometry through a perturbation theory approach. We begin by reviewing interferometry by cross-correlation in perturbed media. Next, we cover the derivation of deconvolution interferometry before summation over sources. Since such a derivation is done by a

series expansion, we interpret the physical significance of the most prominent terms of the deconvolution interferometry series. On the following subsection, we discuss yet another option for interferometry where deconvolution is done after the summation over sources. Finally, we illustrate the physical significance of the the most prominent terms of the deconvolution interferometry series by providing an asymptotic analysis of these terms for a simplified toy model.

3.3.1 Review of interferometry by cross-correlations

Let the frequency-domain wavefield $u(\mathbf{r}_A, \mathbf{s}, \omega)$ recorded at $\mathbf{r}_A$ be the superposition of the unperturbed and scattered Green's functions $G_0(\mathbf{r}_A, \mathbf{s}, \omega)$ and $G_S(\mathbf{r}_A, \mathbf{s}, \omega)$, respectively, convolved with a source function $W(\mathbf{s}, \omega)$ associated with an excitation at $\mathbf{s}$, hence

$$u(\mathbf{r}_A, \mathbf{s}, \omega) = W(\mathbf{s}, \omega) \left[G_0(\mathbf{r}_A, \mathbf{s}, \omega) + G_S(\mathbf{r}_A, \mathbf{s}, \omega) \right] . \tag{3.1}$$

Although here and throughout the text we call G_S the *scattered wavefield*, formally G_S represents a wavefield perturbation. In our derivations, we rely on perturbation theory (Weglein et al., 2003; Chapter 2), such that the quantities G_0 and u (or its impulsive version, G), respectively, represent background and perturbed wavefields that satisfy the equation for acoustic (Chapter 2), elastic (Wapenaar et al., 2004a) and possibly attenuative waves (Snieder, 2007a), and may contain higher-order scattering and inhomogeneous waves. Both the background medium and the medium perturbation can be arbitrarily heterogenous and anisotropic. Also, $W(\mathbf{s}, \omega)$ may be a complicated function of frequency, and may vary as a function of $\mathbf{s}$.

The cross-correlation of the wavefields measured at $\mathbf{r}_A$ and $\mathbf{r}_B$ (equation 6.1) thus gives

$$C_{AB} = |W(\mathbf{s})|^2 \, G(\mathbf{r}_A, \mathbf{s}) G^*(\mathbf{r}_B, \mathbf{s}) \, ; \tag{3.2}$$

where * denotes complex-conjugation. From equation 4.2, it follows that the cross-correlation C_{AB} depends on the power spectrum of $W(\mathbf{s})$. Note that we choose to omit the frequency dependence of equation 4.2 for the sake of brevity; we do the same with all of the other equations in this paper. Following the principle of interferometry (Lobkis and Weaver, 2001; Wapenaar et al, 2006), we integrate the cross-correlations in equation 4.2 over a surface Σ that includes all sources $\mathbf{s}$, giving

$$\oint_{\Sigma} C_{AB} \, d\mathbf{s} \; = \; \langle |W(\mathbf{s})|^2 \rangle \, [G(\mathbf{r}_A, \mathbf{r}_B) \; + \; G^*(\mathbf{r}_A, \mathbf{r}_B)] \; ; \tag{3.3}$$

where $\langle |W(\mathbf{s})|^2 \rangle$ is the source average of the power spectra (Snieder et al., 2007), and $G(\mathbf{r}_A, \mathbf{r}_B)$ and $G^*(\mathbf{r}_A, \mathbf{r}_B)$ are the causal and acausal Green's functions for an excitation at $\mathbf{r}_B$ and receiver at $\mathbf{r}_A$. Note that for equation 6.2 to hold G corresponds to the *pressure* response in acoustic media (e.g., Wapenaar and Fokkema, 2006). If G is the *particle velocity* response, the plus sign on the right-hand side of equation 6.2 is replaced by a minus sign (e.g., Wapenaar and Fokkema, 2006). Equation 6.2 has been derived by many other authors (e.g., Wapenaar et al., 2004b; Draganov et al., 2006) and it is not our intention here to restate it. Instead, we highlight the importance of the $\langle |W(\mathbf{s})|^2 \rangle$ term in equation 6.2.

The source average $\langle |W(\mathbf{s})|^2 \rangle$ may be a complicated function of frequency (or time), hence

recovering the response between the receivers at $\mathbf{r}_A$ and $\mathbf{r}_B$ through equation 6.2 can be difficult. In the interferometry literature, most authors suggest deconvolving the power spectrum average $\langle |W(\mathbf{s})|^2 \rangle$ after the integration in equation 6.2 (Wapenaar et al., 2004a; Snieder et al., 2006; Fink, 2006). This assumes that an independent estimate of the source function is available. Indeed, in some applications such an estimate can be obtained (Mehta et al., 2007). There are many cases in which independent estimates of the source function are not a viable option. The second part of this paper (Chapter 4) deals with a specific drill-bit seismic examples for which independent estimates of the source function are not available, and the correlation-based interferometry (equation 6.2) does not provide acceptable results. In the next two Sections we provide alternative interferometry methodologies that recover the impulse response between the receivers without the requirement of having independent estimates of the power spectrum of the source function.

In this paper we focus on understanding the physical meaning of interferometry by deconvolution, and its differences with its correlation-based counterpart. To do so it is necessary to review some of the physics behind cross-correlation interferometry in perturbed media. Thus, for the moment, it is convenient to assume a source function that is independent of the source position $\mathbf{s}$ ($W(\mathbf{s}) = W$) in equations 6.1, 4.2 and 6.2. Combining equations 6.1 and 4.2, we can expand C_{AB} into four terms:

$$\begin{aligned} C_{AB} &= u(\mathbf{r}_A, \mathbf{s}) u^*(\mathbf{r}_B, \mathbf{s}) \\ &= \underbrace{u_0(\mathbf{r}_A, \mathbf{s}) u_0^*(\mathbf{r}_B, \mathbf{s})}_{C_{AB}^1} + \underbrace{u_S(\mathbf{r}_A, \mathbf{s}) u_0^*(\mathbf{r}_B, \mathbf{s})}_{C_{AB}^2} + \\ &+ \underbrace{u_0(\mathbf{r}_A, \mathbf{s}) u_S^*(\mathbf{r}_B, \mathbf{s})}_{C_{AB}^3} + \underbrace{u_S(\mathbf{r}_A, \mathbf{s}) u_S^*(\mathbf{r}_B, \mathbf{s})}_{C_{AB}^4}, \end{aligned} \tag{3.4}$$

where $u_0 = WG_0$ and $u_S = WG_S$ (see equation 6.1). The four terms, namely C_{AB}^1

through C^4_{AB}, can be inserted into equation 6.2, giving

$$\oint_{\Sigma} \left[C^1_{AB} + C^2_{AB} + C^3_{AB} + C^4_{AB} \right] d\mathbf{s} = |W|^2 \left[G_0(\mathbf{r}_A, \mathbf{r}_B) + G_S(\mathbf{r}_A, \mathbf{r}_B) + \right. \\ \left. + G_0^*(\mathbf{r}_A, \mathbf{r}_B) + G_S^*(\mathbf{r}_A, \mathbf{r}_B) \right]. \qquad (3.5)$$

Each of the four integrals on the left-hand side of equation 3.5 has a different physical meaning. With the use of representation theorems, in Chapter 2 we analyze how each integral in equation 3.5 relates to the terms in the right-hand side of the equation. Note that for imaging purposes, we want to use only the u_S terms in equation 3.5. The first integral relates to the unperturbed terms in the right-hand side of equation 3.5 to give,

$$\oint_{\Sigma} u_0(\mathbf{r}_A, \mathbf{s}) u_0^*(\mathbf{r}_B, \mathbf{s})\, d\mathbf{s} = |W|^2 \left[G_0(\mathbf{r}_A, \mathbf{r}_B) + G_0^*(\mathbf{r}_A, \mathbf{r}_B) \right]. \qquad (3.6)$$

The relationship in equation 3.6 is not surprising because the unperturbed wavefields u_0 satisfy the unperturbed wave equation. Consequently, interferometry of the unperturbed wavefields on the left-hand side of equation 3.6 must yield the causal and acausal unperturbed wavefields between $\mathbf{r}_B$ and $\mathbf{r}_A$ (right-hand side of equation 3.6). A less obvious relationship between the terms in equation 3.5 (Chapter 2) is that the dominant contribution to the causal scattered wavefield between $\mathbf{r}_B$ and $\mathbf{r}_A$ comes from the correlation between the unperturbed wavefield at $\mathbf{r}_B$ and the scattered wavefield at $\mathbf{r}_A$, that is,

$$\int_{\sigma_1} u_S(\mathbf{r}_A, \mathbf{s}) u_0^*(\mathbf{r}_B, \mathbf{s})\, d\mathbf{s} \approx |W|^2 \, G_S(\mathbf{r}_A, \mathbf{r}_B)\,; \qquad (3.7)$$

where σ_1 is a portion of Σ that yields stationary contributions to $G_S(\mathbf{r}_A, \mathbf{r}_B)$. In

Chapter 2 we show that this relationship holds for most types of experiments in exploration seismology (surface seismic, many VSP experiments, etc.). Equation 6.3 is an approximate relationship because it neglects the influence of a volume integral that provides a correction for medium perturbations that sit in the stationary paths of the unperturbed waves that propagate from the sources $\mathbf{s}$ to the receiver at $\mathbf{r}_B$ (Chapter 2). In the context of seismic imaging, the extraction of $G_S(\mathbf{r}_A, \mathbf{r}_B)$ is the objective of interferometry. Equation 6.3 is not only important for the separation of the scattered waves that propagate between $\mathbf{r}_B$ and $\mathbf{r}_A$, but also because it can be used to show that deconvolution interferometry is capable of recovering the response between any two receivers.

An important requirement for the successful application of interferometry is that there must be waves propagating at all directions at each receiver location. Many authors refer to this condition as *equipartioning* (Weaver and Lobkis, 2004; Larose et al, 2006), while others simply mention the necessity of having many sources closely distributed around a closed surface integral, such as in equation 6.2. In real-life exploration experiments, however, it is impossible to surround the subsurface with sources. As a consequence we end up with only a partial source integration, instead of the closed surface integration necessary for equation 6.2 to hold. As was pointed out by Snieder et al. (2006) for simplified 1D models, truncation of the surface integral may lead to the introduction of spurious events in the final interferometric gathers. This holds for general 3D models as well, and it can be easily verified provided that

$$\int_{\sigma_1} C_{AB}\, d\mathbf{s} + \int_{\sigma_2} C_{AB}\, d\mathbf{s} = |W|^2 \left[G(\mathbf{r}_A, \mathbf{r}_B) + G^*(\mathbf{r}_A, \mathbf{r}_B)\right] , \tag{3.8}$$

where σ_1 and σ_2 are surface segments of Σ, such that $\sigma_1 \cup \sigma_2 = \Sigma$. Now, suppose that in an actual field experiment we could only acquire data with waves excited over

the surface σ_1 (such as in equation 6.3). Then, as we can see from equation 3.8, the integration over all available sources (the integral over σ_1) results in the desired response (right-hand side of equation 3.8) minus the integral over σ_2. In this case, if the integral over σ_2 is non-zero (i.e., there are stationary contributions associated with sources placed over σ_2), then the data synthesized from interferometry over σ_1 would contain spurious events associated the missing sources over σ_2. Although this at first glance may seem like a practical limitation of the method of interferometry, in reality the lack of primary sources in the subsurface is somewhat compensated by multiple scattering, or by reflections below the region of interest (Wapenaar, 2006; Halliday et al., 2007). In field experiments, some of the desired system equipartioning may be achieved with longer recording times, making up for some of the missing sources over σ_2. Because this is a model-dependent problem, it is impossible in practice to pre-determine what the influence of missing sources will be, and to what extent longer recording times make up for these sources.

3.3.2 Deconvolution before summation over sources

As we have seen in the previous Section, the cross-correlation of the wavefields $u(\mathbf{r}_A, \mathbf{s})$ and $u(\mathbf{r}_B, \mathbf{s})$ contains the power spectrum of the excitation function (equation 4.2). Instead deconvolution of $u(\mathbf{r}_A, \mathbf{s})$ with $u(\mathbf{r}_B, \mathbf{s})$ gives

$$D_{AB} = \frac{u(\mathbf{r}_A, \mathbf{s})}{u(\mathbf{r}_B, \mathbf{s})} = \frac{u(\mathbf{r}_A, \mathbf{s})\, u^*(\mathbf{r}_B, \mathbf{s})}{|u(\mathbf{r}_B, \mathbf{s})|^2} = \frac{G(\mathbf{r}_A, \mathbf{s})\, G^*(\mathbf{r}_B, \mathbf{s})}{|G(\mathbf{r}_B, \mathbf{s})|^2}, \tag{3.9}$$

Now the source function $W(\mathbf{s})$ (equation 6.1) is canceled by the deconvolution process. Although no multidimensional deconvolution interferometry approach has been presented to date, it is intuitive to proceed with the integration

$$\oint_{\Sigma} D_{AB}\, d\mathbf{s} \;=\; \oint_{\Sigma} \frac{G(\mathbf{r}_A, \mathbf{s})\, G^{*}(\mathbf{r}_B, \mathbf{s})}{\left|G(\mathbf{r}_B, \mathbf{s})\right|^2}\, d\mathbf{s}\,, \tag{3.10}$$

to mimic the procedure of interferometry by cross-correlation (equation 6.2). The existing proofs for the validity of interferometry by cross-correlation (equation 6.2) are not immediately applicable to interferometry by deconvolution. For example, the use of representation theorems (e.g., Wapenaar et al., 2004a; Wapenaar et al., 2006; Chapter 2) is unpractical for the spectral ratio of wavefields. Also, stationary-phase evaluation of the integral in equation 3.10 for a specified model (such as in Snieder et al., 2006) is compromised by the presence of $|G(\mathbf{r}_B, \mathbf{s})|^2$ in the numerator. Despite being zero-phase, $|G(\mathbf{r}_B, \mathbf{s})|^2$ contains cross-terms between unperturbed and scattered wavefields (see below) which make the denominator in equation 3.10 a highly oscillatory function that cannot be accounted for by the stationary-phase method (Bleistein and Handelsman, 1975).

Our solution to evaluating the integral in equation 3.10 is to expand the denominator in a power series, which then allows us to give a physical interpretation to deconvolution interferometry. The next two Sections cover the derivations of this series expansion and the subsequent interpretation of its physical significance.

Contributions to first-order in the scattered wavefield.

We focus our discussion on the terms that make the most prominent contributions to the deconvolution interferometry integral in equation 3.10. First, we rewrite the deconvolution in equation 4.11 as

$$D_{AB} = \frac{C_{AB}}{|G(\mathbf{r}_B,\mathbf{s})|^2} = \frac{1}{|G(\mathbf{r}_B,\mathbf{s})|^2}\left[G_0(\mathbf{r}_A,\mathbf{s})G_0^*(\mathbf{r}_B,\mathbf{s}) + G_S(\mathbf{r}_A,\mathbf{s})G_0^*(\mathbf{r}_B,\mathbf{s}) + \right.$$

$$\left. + G_0(\mathbf{r}_A,\mathbf{s})G_S^*(\mathbf{r}_B,\mathbf{s}) + G_S(\mathbf{r}_A,\mathbf{s})G_S^*(\mathbf{r}_B,\mathbf{s})\right]; \tag{3.11}$$

where we explicitly identify the relationship between deconvolution and the cross-correlation of $G(\mathbf{r}_B,\mathbf{s})$ with $G(\mathbf{r}_B,\mathbf{s})$, here denoted by C_{AB}. As in equation 3.4, the numerator in equation 4.11 yields four terms as shown in the right-hand side of equation 3.11. The next step in our derivation is to express $|G(\mathbf{r}_B,\mathbf{s})|^{-2}$ as

$$\frac{1}{|G(\mathbf{r}_B,\mathbf{s})|^2} = \frac{1}{\left[G_0(\mathbf{r}_B,\mathbf{s}) + G_S(\mathbf{r}_B,\mathbf{s})\right]\left[G_0^*(\mathbf{r}_B,\mathbf{s}) + G_S^*(\mathbf{r}_B,\mathbf{s})\right]}; \tag{3.12}$$

which shows that the numerator in equation 3.10 contains the power spectra of the unperturbed and scattered wavefields, as well as cross-terms between these two wavefields. If we assume the wavefield perturbations to be small ($|G_S|^2 << |G_0|^2$), the last term in the denominator of equation 3.12 can be dropped, hence

$$|G(\mathbf{r}_B,\mathbf{s})|^{-2} \approx \frac{1}{|G_0(\mathbf{r}_B,\mathbf{s})|^2\left[1 + \frac{G_0(\mathbf{r}_B,\mathbf{s})\,G_S^*(\mathbf{r}_B,\mathbf{s})}{|G_0(\mathbf{r}_B,\mathbf{s})|^2} + \frac{G_S(\mathbf{r}_B,\mathbf{s})\,G_0^*(\mathbf{r}_B,\mathbf{s})}{|G_0(\mathbf{r}_B,\mathbf{s})|^2}\right]}, \tag{3.13}$$

By inspecting the denominator, it follows that equation 3.13 can be expanded in a power series in $G_S/G_0 + G_S^*/G_0^*$. From this expansion, taking terms only up to first order in the wavefield perturbations gives

$$|G(\mathbf{r}_B,\mathbf{s})|^{-2} \approx \frac{1}{|G_0(\mathbf{r}_B,\mathbf{s})|^2}\left[1 - \frac{G_S(\mathbf{r}_B,\mathbf{s})}{G_0(\mathbf{r}_B,\mathbf{s})} - \frac{G_S^*(\mathbf{r}_B,\mathbf{s})}{G_0^*(\mathbf{r}_B,\mathbf{s})}\right]. \tag{3.14}$$

After inserting equation 3.14 into the integral in equation 3.10 and keeping only the terms which are linear in the wavefield perturbations G_S, we get

$$\begin{aligned}\oint_\Sigma D_{AB}\,d\mathbf{s} &= \underbrace{\oint_\Sigma \frac{G_0(\mathbf{r}_A,\mathbf{s})G_0^*(\mathbf{r}_B,\mathbf{s})}{|G_0(\mathbf{r}_B,\mathbf{s})|^2}\,d\mathbf{s}}_{D_{AB}^1} + \underbrace{\oint_\Sigma \frac{G_S(\mathbf{r}_A,\mathbf{s})G_0^*(\mathbf{r}_B,\mathbf{s})}{|G_0(\mathbf{r}_B,\mathbf{s})|^2}\,d\mathbf{s}}_{D_{AB}^2} \\ &- \underbrace{\oint_\Sigma \frac{G_S(\mathbf{r}_B,\mathbf{s})G_0(\mathbf{r}_A,\mathbf{s})G_0^*(\mathbf{r}_B,\mathbf{s})}{G_0(\mathbf{r}_B,\mathbf{s})}\,d\mathbf{s}}_{D_{AB}^3}.\end{aligned} \tag{3.15}$$

Equation 4.12 shows that, to leading order in the scattered wavefield, the deconvolution integral in equation 3.10 can be represented by the integrals D_{AB}^1 through D_{AB}^3. In fact, equation 4.12 is a Born-like approximation (e.g., Weglein et al., 2003) of equation 3.10. In contrast with the term $|G(\mathbf{r}_B,\mathbf{s})|^2$ in equation 3.10, the term $|G_0(\mathbf{r}_B,\mathbf{s})|^2$ in equation 4.12 does not contain cross-terms between unperturbed and scattered wavefields. Therefore, $|G_0(\mathbf{r}_B,\mathbf{s})|^2$ is a slowly-varying zero-phase function of $\mathbf{s}$. This means that only the numerators determine the stationary contributions to the integrals in the right-hand side of equation 4.12. This property allows the direct comparison between the phases of the integrands in equations 4.12 and the terms in equation 3.5.

Physical insights into deconvolution interferometry come from observing that the integrands of the D_{AB}^1 and D_{AB}^2 terms (equation 4.12) have the same phase as the C_{AB}^1 and C_{AB}^2 terms in equations 3.4 and 3.5. Based on these observations, and on equation 3.6 (Chapter 2), we can conclude that D_{AB}^1 provides the causal and acausal

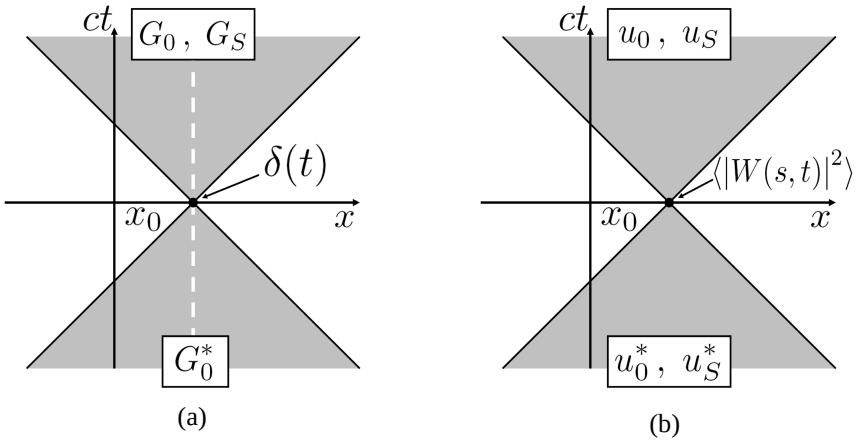

Figure 3.1. Representation of the wavefields that result from (a) deconvolution and (b) correlation interferometry. We refer to this representation as *light cones*. The medium is 1D with a wavespeed c. x_0 is the location of the pseudo-source. The grey-shaded areas represent the regions where the wavefields are nonzero. Away from these areas the wavefields are equal to zero. The wavefield produced by deconvolution interferometry in (a) is zero also along the dashed white line, for $t \neq 0$. In the time-domain, the excitation in (a) is given by $\delta(t)$, while in (b) it is given by $\langle|W(s,t)|^2\rangle$. The white text boxes indicate what type of wavefields propagate in the causal and acausal light cones of (a) and (b).

unperturbed wavefield that propagates from $\mathbf{r}_B$ to $\mathbf{r}_A$. More importantly, since the integrand of D^2_{AB} and C^2_{AB} have the same phase, the term D^2_{AB} gives the causal scattered waves that are excited at $\mathbf{r}_B$ and recorded at $\mathbf{r}_A$.

In the process of deriving equation 4.12 from equations 3.10, 3.11 and 3.14, the terms that carry the same phase as C^3_{AB} and C^4_{AB} cancel with the products of C^1_{AB} and C^2_{AB} with the G^*_S/G^*_0 term. This cancelation implies that interferometry by deconvolution does not recover the acausal scattering response between the two receivers. Note that the acausal scattered waves are attenuated in deconvolution interferometry even for a closed surface integral (equation 4.12), or for an equipartioned system. This is a difference with what is obtained with interferometry by cross-correlation, which does recover the acausal scattering response between the receivers (equation 6.2).

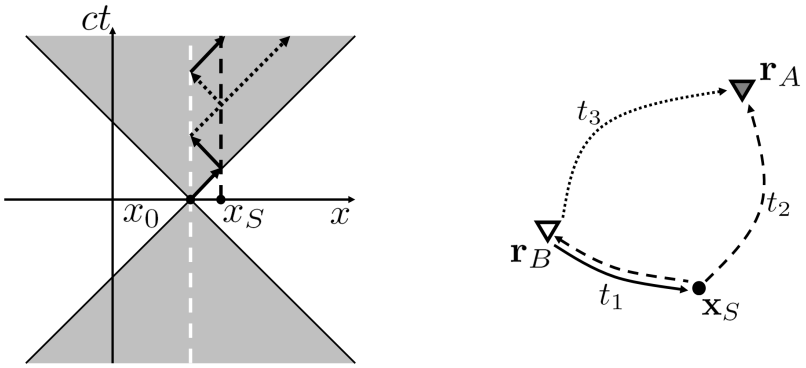

Figure 3.2. Illustrations of the *free point* boundary condition in deconvolution interferometry. (a) provides an interpretation of the free point boundary condition for 1-dimensional media with wavespeed c, using the light cone representation (as in Figure 3.1a). x_0 is the location of the pseudo-source (and of the free point) and x_S is the location of a point scatterer. The arrows represent waves, excited by the source in x_0, propagating in the medium. Waves denoted with solid arrows propagate with opposite polarity with respect to waves represented by dotted arrows. The wavefield is equal to zero at the dashed white line, and the black vertical line indicates the region of influence of the medium perturbation at x_S. (b) illustrates the free point boundary condition in a 3D inhomogeneous acoustic medium. The pseudo-source, located at $\mathbf{r}_B$, is shown with the white triangle. The receiver is represented by the grey triangle at $\mathbf{r}_A$. The medium perturbation is a point scatterer at $\mathbf{x}_S$, here denoted by the black circle. The solid arrow depicts a direct wave excited at $\mathbf{r}_B$. This wave is scattered at $\mathbf{x}_S$ and propagates toward $\mathbf{r}_A$ and $\mathbf{r}_B$, as shown by the dashed arrows. The dotted arrow denotes a free point scattered wave that is recorded at $\mathbf{r}_A$. Waves represented by dashed and dotted arrows have opposite polarity. t_1 through t_3 are the traveltimes of waves that propagate from $\mathbf{r}_B$ to $\mathbf{x}_S$, $\mathbf{x}_S$ to $\mathbf{r}_A$, and $\mathbf{r}_B$ to $\mathbf{r}_A$, respectively.

The term D^3_{AB} has no counterpart in correlation interferometry. In a zero-offset interferometric experiment, that is $\mathbf{r}_A = \mathbf{r}_B$, the integrands of D^3_{AB} and D^2_{AB} have the same phase. In that case, the stationary traveltimes that come from integrating D^3_{AB} are the same as the ones coming from D^2_{AB}. These traveltimes correspond to scattered waves for a zero-offset experiment at $\mathbf{r}_B$. Given that D^3_{AB} and D^2_{AB} have opposite sign (equation 4.12), their contributions cancel when $\mathbf{r}_A = \mathbf{r}_B$. As the offset between the two receivers increases, the stationary traveltimes from D^3_{AB} and D^2_{AB} become increasingly different. As we shall discuss in more detail in Section 3.3.4, the stationary traveltimes from D^3_{AB} at finite offsets does not correspond to physical events for real wavefields excited at $\mathbf{r}_B$ and recorded at $\mathbf{r}_A$. Because of this we refer to terms such as D^3_{AB} as *spurious events*. Next, we explain the origin of the spurious arrivals in deconvolution interferometry.

Indeed, setting $\mathbf{r}_A = \mathbf{r}_B$ in equation 3.10 yields, in the time domain, a delta function at zero time. In deconvolution interferometry, scattered waves must cancel at zero-offset. This is a boundary condition imposed on the interferometric experiment where we excite waves at $\mathbf{r}_B$ and record them at $\mathbf{r}_A$. The consequence of this boundary condition is the creation of spurious events such as D^3_{AB} that cancel scattered waves that arrive at zero-offset with finite traveltimes. Note that these spurious arrivals are different from the ones that may result from the truncation of the surface integral (equation 3.8), and exist even for a closed surface of sources or in an equipartioned system (equation 4.12). Truncation of the surface integral in deconvolution interferometry will have the same effect as in interferometry by cross-correlation (see previous Section).

In Figure 3.1, we summarize the physical meaning of deconvolution interferometry and compare it to the correlation-based approach. The type of wavefield

representation in Figure 3.1 comes from the theory of special relativity (Ohanian and Ruffini, 1994). According to the causality principle, no wave in Figure 3.1 can move faster than the medium wavespeed c (which for the sake of argument we assume to be constant). Hence, an excitation that occurs at x_0 and $t = 0$ influences only the causal grey-shaded regions in Figure 3.1, and it is influenced by the acausal grey-shaded regions. In special relativity theory, these grey-shaded areas are called *light cones*: the causal grey-shaded regions are the *future light cones*, while the acausal ones are the *past light cones*. From equation 4.11, it follows that $D_{BB} = 1$ (i.e., when $\mathbf{r}_A = \mathbf{r}_B$). In this case, deconvolution interferometry yields $G(\mathbf{r}_B, \mathbf{r}_B) = 1$ in the frequency domain, which translates to

$$G(\mathbf{r}_B, \mathbf{r}_B, t) = \delta(t) \tag{3.16}$$

in the time domain. Hence, in deconvolution interferometry, the time-domain excitation is given by $\delta(t)$ (Figure 3.1a). This excitation influences all of the causal light cone of interferometry by deconvolution, except at $x = x_0$ for $t > 0$, where the wavefield is zero (equation 4.15). Likewise, the condition given by equation 4.15 states that the pseudo-source in deconvolution interferometry is influenced by all events of the past light cone, except for the ones at $x = x_0$ and $t < 0$. The pseudo-source in deconvolution interferometry generates the unperturbed impulse response $G_0(x, x_0, t)$ and the impulsive scattered waves $G_S(x, x_0, t)$, as indicated in the future light cone of Figure 3.1a. This pseudo-source, obtained by deconvolution, is influenced only by unperturbed waves in its past light cone, which pertain to impulsive wavefield $G_0^*(x, x_0, t)$. This observation holds for terms from the deconvolution interferometry series (after the expansion of equation 3.10) of any order in the scattered wavefield, as we demonstrate in the next Section.

In correlation interferometry (Figure 3.1b), the excitation at $t = 0$ is given

by $\langle |W(s,t)|^2 \rangle$, where $s = x_0$ for the pseudo-source synthesized by interferometry. This excitation generates the unperturbed wavefield $u_0(x, x_0, t)$ and the perturbation $u_S(x, x_0, t)$ in the future light cone in Figure 3.1b. The acausal waves in $u_0^*(x, x_0, t)$ and $u_S^*(x, x_0, t)$ present in the past light cone of correlation interferometry influence the excitation at $x = x_0$ and $t = 0$. Therefore, unlike in deconvolution interferometry (Figure 3.1b), x_0 is influenced by the acausal scattered waves in correlation interferometry (Figure 3.1b). Note that $u_0(x, x_0, t)$ and $u_S(x, x_0, t)$ (and their acausal counterparts) are not impulsive. Another difference with the deconvolution approach is that correlation interferometry influences $x = x_0$ for $t > 0$, and is influenced by waves at $x = x_0$ for $t < 0$ (Figure 3.1b). Although the light cone representations in Figure 3.1 are valid for one-dimensional homogeneous media, it can be generalized to higher dimensions (Ohanian and Ruffini, 1994) and to inhomogeneous media. These generalizations, however, are not necessary to our discussion on the physics of interferometry.

Finally, we rely on Figure 3.2 to summarize the physics of the extra boundary condition imposed by deconvolution interferometry (equation 4.15). From this condition (equation 4.15), it follows that $G(\mathbf{r}_B, \mathbf{r}_B, t) = 0$ when $t \neq 0$, which is represented by the dashed white line in Figures 3.1a and 3.2a. If G is the *pressure* response, we refer to this boundary condition in the interferometric experiment as the *free point* boundary condition. We use this term because the physical meaning of this boundary is analogous to that of a *free surface* boundary condition (where pressure is equal to zero), but instead it only applies to a *point* in space (in this case, $\mathbf{r}_B$). When G stands for the *particle velocity* response, the condition in equation 4.15 has the effect of *clamping* the point $\mathbf{r}_B$, so that it cannot move for $t \neq 0$. In that case, we refer to equation 4.15 as the *clamped point* boundary condition. Throughout this paper, we

use the term *free point* when referring to the condition given by equation 4.15, since in previous equations G is represents pressure waves (e.g., equations 6.2 and 3.6). The boundary condition imposed by deconvolution interferometry in elastic media is different than that we discuss here, as shown Chapter 4.

The effect of the free point boundary condition in a 1D homogeneous medium is illustrated by Figure 3.2a. The medium is perturbed by a scatterer at x_S. According to our interpretation of Figure 3.1a, the medium perturbations occurs at $t = 0$, so the black dashed line in Figure 3.2a shows that the medium perturbation only influences the future light cone in Figure 3.2a. Starting at $x = x_0$ and $t = 0$, the arrows in Figure 3.2a describe the path of a wave that propagates toward the scatterer at x_S, bounces off the scatterer to be then scattered again at the free point at $x = x_0$. This wave keeps on scattering infinite times between x_S and x_0. As in the free surface boundary condition, the free point at x_0 reflects waves with a reflection coefficient equal to -1. Note that the waves in Figure 3.2a change polarity at each bounce off the free point at x_0.

The extension of the free point concept to 3D inhomogeneous media is shown in Figure 3.2b. In this example, deconvolution interferometry is conducted for receivers at $\mathbf{r}_A$ and $\mathbf{r}_B$, as in equation 3.10. The receiver at $\mathbf{r}_B$ acts as a pseudo-source (white triangle in the Figure). The medium perturbation is the point scatterer at $\mathbf{x}_S$. The pseudo-source at $\mathbf{r}_B$ sends a direct wave (solid arrow in Figure 3.2b), with traveltime t_1 toward the scatterer. After this direct wave scatters at $\mathbf{x}_S$, it propagates back to $\mathbf{r}_B$ and toward $\mathbf{r}_A$ (dashed arrows), where it is recorded. This recorded singly scattered wave corresponds to the D_{AB}^2 term in equation 4.12, with traveltime $t = t_1 + t_2$. When it arrives at $\mathbf{r}_B$, the wave backscattered at $\mathbf{x}_S$ scatters once more because of the free point boundary condition. The free-point scattered wave (dotted arrow) then

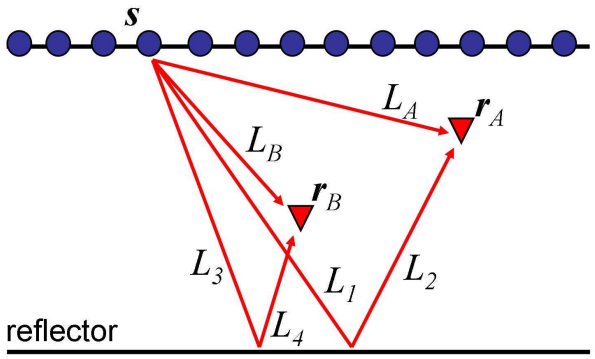

Figure 3.3. A simple model gain intuitive understanding about the physical meaning of the terms in equation 4.12. Receivers are imbedded in an acoustic homogeneous space containing a single reflector, bounded by a perfectly absorbing surface. Only direct and single-scattered waves are considered. Sources are depicted by circles on the surface, the two receivers are represented by triangles. L_A, L_B and L_1 through L_4 are the lengths of the ray segments. The reflection coefficient r is constant with respect to both position and incidence angle.

travels directly to $\mathbf{r}_A$, where it is recorded at $t = 2t_1 + t_3$. This arrival corresponds to the D^3_{AB} term in equation 4.12. When $\mathbf{r}_A = \mathbf{r}_B$, $t_2 = t_1$ and $t_3 = 0$, and the singly scattered and free-point scattered waves have the same traveltime. This agrees with our previous discussion on the phase of the terms in equation 4.12. For a fixed $\mathbf{r}_B$ and varying $\mathbf{r}_A$, the traveltime of the free-point scattered wave is only controlled by t_3, since t_1 stays constant. Note that t_3 is also the traveltime of the direct wave that travels from $\mathbf{r}_B$ to $\mathbf{r}_A$, which is in turn given by the D^1_{AB} term in equation 4.12. Since the term D^3_{AB} is controlled by the direct wave traveltime t_3 for a fixed $\mathbf{r}_B$, it has the same moveout as the direct wave in an interferometric shot gather with a pseudo-source at $\mathbf{r}_B$. Figure 3.2b illustrates only one of the many free point scattered waves produced by deconvolution interferometry.

Although the presence of spurious events such as D^3_{AB} (equation 4.12) may appear to be a problem for imaging interferometric gathers that result from deconvolution, we

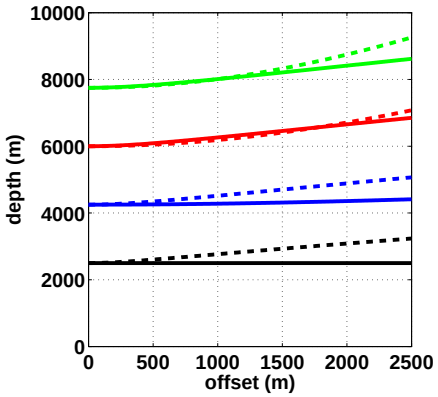

Figure 3.4. Depths obtained by shot-profile migration of stationary traveltimes of deconvolution interferometry terms with varying receiver-to-receiver offset. Black lines correspond to the terms that are of leading order in the scattered wavefield (see previous Section). The black solid line represents migrated depths from traveltimes associated to the D^2_{AB} term (equation 4.12); whereas the black dashed line pertains to the D^3_{AB} term (also equation 4.12). The curves colored in blue, red and green are associated respectively to terms which are quadratic, cubic and quartic with respect to scattered waves. For a given order in the scattered waves, we show only the two terms that have strongest amplitude. Of the blue curves, the solid curve relates to the $T_1^{2^{nd}}$ in equation 3.19 and the dashed one pertains to $T_2^{2^{nd}}$ (equation 3.20). The imaged depths computed from the $T_1^{3^{rd}}$ (equation 3.21) and $T_2^{3^{rd}}$ (equation 3.22) stationary traveltimes are shown by the solid and dashed red lines, respectively. Although the quartic terms related to the green curves are not explicitly shown in the text, they come from the deconvolution interferometry series in equation 3.18 for n equal to 3 and 4.

show in the Sections to come that these spurious events typically are not mapped onto coherent reflectors. What is most important is that interferometry by deconvolution is capable of successfully recovering the causal scattering response between any two receivers, as shown by the D^2_{AB} term.

Higher-order terms

In the previous section we limited our analysis to the terms of first order in G_S. Here, we analyze the higher-order terms. The full deconvolution series resulting from the expansion of equation 3.11 is

$$D_{AB} = \frac{C_{AB}}{\left|G_0(\mathbf{r}_B,\mathbf{s})\right|^2}\sum_{n=0}^{\infty}\left(-\frac{G_S(\mathbf{r}_B,\mathbf{s})}{G_0(\mathbf{r}_B,\mathbf{s})}-\frac{G_S^*(\mathbf{r}_B,\mathbf{s})}{G_0^*(\mathbf{r}_B,\mathbf{s})}\right)^n. \tag{3.17}$$

As shown in Appendix A, a physical analysis of the terms in equation 3.17 allows us to simplify it to

$$D_{AB} \approx \frac{G(\mathbf{r}_A,\mathbf{s})}{G_0(\mathbf{r}_B,\mathbf{s})}+\frac{C_{AB}}{\left|G_0(\mathbf{r}_B,\mathbf{s})\right|^2}\sum_{n=1}^{\infty}(-1)^n\left(\frac{G_S(\mathbf{r}_B,\mathbf{s})}{G_0(\mathbf{r}_B,\mathbf{s})}\right)^n. \tag{3.18}$$

In this equation, the first term yields physical unperturbed and scattered waves that propagate between $\mathbf{r}_B$ and $\mathbf{r}_A$, while the second term accounts for the effect of the free point boundary condition in deconvolution interferometry. The objective of the simplification in equation 3.18 is to keep only the terms that have non-zero phase which bring the most prominent contributions to the series in equation 3.17. The approximation that leads to equation 3.18 involves neglecting terms from equation 3.17 which are zero-phase or that yield arrivals with negligible amplitudes (see Appendix A). Note that the acausal terms proportional to $(G_S^*/G_0^*)^n$ in equation 3.17 are not present in equation 3.18 because they cancel in the $n \to \infty$ limit (see Appendix A). This cancellation determines that the point x_0 in Figure 3.1a is not influenced by acausal scattered waves (see discussion in Section 3.3.2). The first term in equation 3.18 gives the terms D_{AB}^1 and D_{AB}^2 in equation 4.12. The term D_{AB}^3 is obtained by the product of C_{AB}^1 and the first term of the sum in equation 3.18. It is important to note that terms of a given order in the scattered wavefield come from different values of n in equation 3.18. Let us take, for example,

$$T_1^{2^{nd}} = -\,G_S(\mathbf{r}_A,\mathbf{s})\,G_0^*(\mathbf{r}_B,\mathbf{s})\left(\frac{G_S(\mathbf{r}_B,\mathbf{s})}{G_0(\mathbf{r}_B,\mathbf{s})}\right) \tag{3.19}$$

and

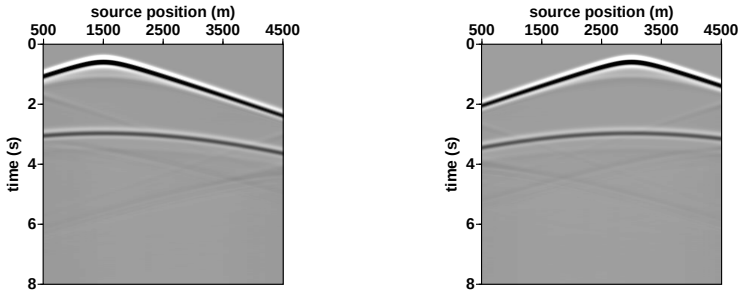

(a) (b)

Figure 3.5. Common receiver gathers for receivers placed at (a) 1500 m and at (b) 3000 m.

$$T_2^{2^{nd}} \;=\; G_0(\mathbf{r}_A,\mathbf{s})\,G_0^*(\mathbf{r}_B,\mathbf{s})\left(\frac{G_S(\mathbf{r}_B,\mathbf{s})}{G_0(\mathbf{r}_B,\mathbf{s})}\right)^2 \tag{3.20}$$

where T_i^o represents a given term T_i from equation 3.18 of order o in the scattered wavefield G_S. $T_1^{2^{nd}}$ and $T_2^{2^{nd}}$ are the most prominent terms which are of second-order in the scattered wavefield, where $T_1^{2^{nd}}$ comes from $n = 1$ while $T_2^{2^{nd}}$ comes from $n = 2$. When $\mathbf{r}_A = \mathbf{r}_B$, $T_1^{2^{nd}}$ and $T_2^{2^{nd}}$ will give rise to arrivals with twice the traveltimes of $G_S(\mathbf{r}_A,\mathbf{r}_B)$. Since these two terms have opposite polarity (equations 3.19 and 3.20), their contributions cancel. Likewise the terms

$$T_1^{3^{rd}} \;=\; G_S(\mathbf{r}_A,\mathbf{s})\,G_0^*(\mathbf{r}_B,\mathbf{s})\left(\frac{G_S(\mathbf{r}_B,\mathbf{s})}{G_0(\mathbf{r}_B,\mathbf{s})}\right)^2 \tag{3.21}$$

and

$$T_2^{3^{rd}} \;=\; -\,G_0(\mathbf{r}_A,\mathbf{s})\,G_0^*(\mathbf{r}_B,\mathbf{s})\left(\frac{G_S(\mathbf{r}_B,\mathbf{s})}{G_0(\mathbf{r}_B,\mathbf{s})}\right)^3 \tag{3.22}$$

result in traveltimes that are three times those of $G_S(\mathbf{r}_A,\mathbf{r}_B)$ when $\mathbf{r}_A = \mathbf{r}_B$. $T_1^{3^{rd}}$ and $T_2^{3^{rd}}$ are the most prominent terms from the series in equation 3.18 which are

of third-order in the wavefield perturbations. They come respectively from setting $n = 2$ and $n = 3$ in equation 3.18. The phase of of any the higher-order terms in deconvolution interferometry (second term in equation 3.18; e.g., equations 3.19 through 3.22) can be physically explained by the interactions of the free point at $\mathbf{r}_B$ (equations 3.10 and 4.15) with the waves scattered by the medium perturbation. In the example of Figure 3.2b, the higher-order spurious multiples arise from multiple scattering between the scatterer at $\mathbf{x}_S$ and the free point at $\mathbf{r}_B$.

As we demonstrate with our numerical example, some of these higher-order spurious terms (such as in equations 3.19 through 3.22) may be present in the deconvolution interferometry integrand. Hence, it is important to understand to what extent these terms present a challenge to the proper imaging from interferometry by deconvolution. We investigate this in the next Sections.

3.3.3 Deconvolution after summation over sources

Using the deconvolution approach described by equation 3.10 is not the only option for doing interferometry without independent estimates of the source function. The deconvolution of $u(\mathbf{r}_A, \mathbf{s})$ and $u(\mathbf{r}_B, \mathbf{s})$ is equal to

$$D_{AB} = \frac{u(\mathbf{r}_A, \mathbf{s})\; u^*(\mathbf{r}_B, \mathbf{s})}{u(\mathbf{r}_A, \mathbf{s})\; u^*(\mathbf{r}_B, \mathbf{s})} = \frac{C_{AB}}{C_{BB}}, \tag{3.23}$$

where C_{BB} is the auto-correlation of $u(\mathbf{r}_B, \mathbf{s})$. In the previous Section we summed this result over all sources. Interferometry can be done as in the previous Section, or we can first integrate over sources, and then compute the spectral ratio

$$\frac{\oint_\Sigma C_{AB}\, d\mathbf{s}}{\oint_\Sigma C_{BB}\, d\mathbf{s}} = \frac{G(\mathbf{r}_A, \mathbf{r}_B) + G^*(\mathbf{r}_A, \mathbf{r}_B)}{\oint_\Sigma C_{BB}\, d\mathbf{s}}. \tag{3.24}$$

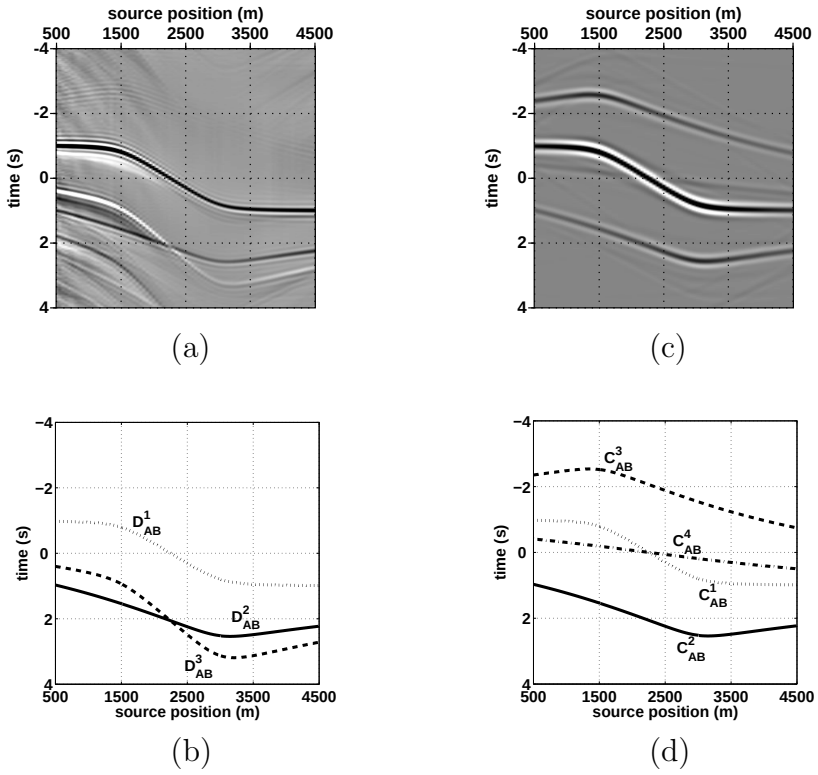

Figure 3.6. Deconvolution and cross-correlation gathers for the first and last receivers, whose lateral positions are, respectively, 1500 and 3000 m. (a) displays the deconvolution gather obtained from deconvolving the modeled common-receiver gathers, whereas (b) shows ray-theoretical traveltimes for the terms in equation 4.12, computed according to integrands in equation 4.12 in Section 3.3.4. Analogous to (a), (c) is the cross-correlation gather generated from source-by-source correlation of the two receiver gathers. (d) shows the asymptotic traveltimes corresponding the phase of the integrands in equation 3.5.

The ratio on the left-hand side of the equation cancels the contribution of the wavelet $\langle |W(\mathbf{s})|^2 \rangle$ (equation 6.2). No independent estimate of the source function is required. Other authors have suggested approaches similar to the one in equation 3.24. The pilot-trace approach used in drill-bit seismology (e.g., Poletto and Miranda, 2004; Rector and Marion, 1991) uses auto-correlations of the accelerometer recordings or geophone data to build a deconvolution operator (Chapter 4). The Virtual Source method (Bakulin and Calvert, 2006; Schuster and Zhou, 2006) also relies on a deconvolution analogous to the one in equation 3.24.

As we did with the cross-correlation in equation 3.4, we can expand C_{BB} and integrate it over sources, giving:

$$\oint_{\Sigma} C_{BB}\, d\mathbf{s} \;=\; \oint_{\Sigma} C^1_{BB}\, d\mathbf{s} \;+\; \oint_{\Sigma} C^2_{BB}\, d\mathbf{s} \;+\; \oint_{\Sigma} C^3_{BB}\, d\mathbf{s} \;+\; \oint_{\Sigma} C^4_{BB}\, d\mathbf{s} \tag{3.25}$$

From the integration of the four terms on the right-hand side of equation 3.25, we can write

$$\frac{1}{\oint_{\Sigma} C_{BB}\, d\mathbf{s}} \;=\; \frac{1}{\left[\left|G_0(\mathbf{r}_B, \mathbf{r}_B)\right|^2 \;+\; \oint_{\Sigma} C^2_{BB}\, d\mathbf{s} \;+\; \oint_{\Sigma} C^3_{BB}\, d\mathbf{s} \;+\; \left|G_S(\mathbf{r}_B, \mathbf{r}_B)\right|^2 \right]}\,; \tag{3.26}$$

where the denominator contains zero-phase terms (the power spectra), as well as the causal and acausal zero-offset scattered wavefield $u_S(\mathbf{r}_B, \mathbf{r}_B)$. Using the weak perturbation approximation ($|G_0|^2 >> |G_S|^2$), we can approximate

$$\left[\oint_{\Sigma} C_{BB}\, d\mathbf{s}\right]^{-2} \approx \frac{1}{|G_0(\mathbf{r}_B,\mathbf{r}_B)|^2 \left[1 + \frac{1}{|G_0(\mathbf{r}_B,\mathbf{r}_B)|^2}\oint_{\Sigma} C_{BB}^2\, d\mathbf{s} + \frac{1}{|G_0(\mathbf{r}_B,\mathbf{r}_B)|^2}\oint_{\Sigma} C_{BB}^3\, d\mathbf{s}\right]} \tag{3.27}$$

which gives us an expression of the same form as equation 3.13. Hence, we can expand equation 3.27 in a power series of the same form as in our previous discussions (see equations 3.13, 3.14 and 3.17). Considering only the very first term of the series expansion, it gives

$$\frac{\oint_{\Sigma} C_{AB}\, d\mathbf{s}}{\oint_{\Sigma} C_{BB}\, d\mathbf{s}} \approx \frac{G(\mathbf{r}_A,\mathbf{r}_B) + G^*(\mathbf{r}_A,\mathbf{r}_B)}{|G_0(\mathbf{r}_B,\mathbf{r}_B)|^2}\,. \tag{3.28}$$

This expression shows that deconvolving the integral over C_{AB} by the integral over C_{BB} recovers both the causal and acausal response at $\mathbf{r}_A$ for waves excited at $\mathbf{r}_B$. This response is scaled by the power spectrum of the zero-offset unperturbed wavefield. Note that equation 3.28 is approximate. Other terms of the series expansion of equation 3.27 yield cross-correlations and convolutions between causal and acausal $u(\mathbf{r}_A,\mathbf{r}_B)$ and $u_S(\mathbf{r}_B,\mathbf{r}_B)$. Since, after Chapter 2,

$$\int_{\sigma_1} C_{BB}^2\, d\mathbf{s} = \int_{\sigma_1} G_S(\mathbf{r}_B,\mathbf{s}) G_0^*(\mathbf{r}_B,\mathbf{s})\, d\mathbf{s} \approx G_S(\mathbf{r}_B,\mathbf{r}_B)\,, \tag{3.29}$$

and

$$\int_{\sigma_1} C_{BB}^3\, d\mathbf{s} = \int_{\sigma_1} G_0(\mathbf{r}_B,\mathbf{s}) G_S^*(\mathbf{r}_B,\mathbf{s})\, d\mathbf{s} \approx G_S^*(\mathbf{r}_B,\mathbf{r}_B)\,. \tag{3.30}$$

Other terms arising from the expansion of equation 3.27 are bound to be small because not only they are products between G and G_S terms, but also because they are divided by $|G_0(\mathbf{r}_B,\mathbf{r}_B)|^{2n}$ (with $n = 2, 3, 4, \ldots$).

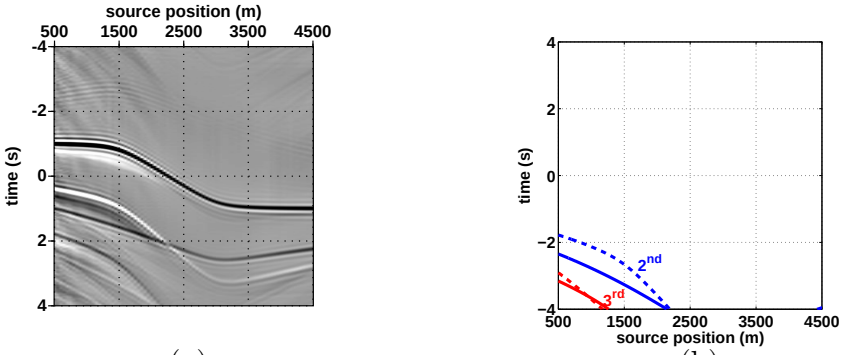

(a) (b)

Figure 3.7. Deconvolution interferometry terms which are nonlinear in the scattered wavefield. The left panel shows the integrand of the deconvolution interferometry integral (equation 3.10),computed from finite-difference modeling (same as in Figure 3.6a). In (b), the traveltimes corresponding to the second order terms $T_1^{2^{nd}}$ and $T_2^{2^{nd}}$ (equations 3.19 and 3.20) are shown respectively with solid and dashed blue curves; while the solid and dashed red curves come from $T_1^{3^{rd}}$ and $T_2^{3^{rd}}$ (equations 3.21 and 3.22), respectively. The curves in (a) correspond to the curves of the same color and type in Figure 3.4.

3.3.4 Example: asymptotic analysis of deconvolution interferometry

In Section 3.3.2 we discussed some of the physics behind the terms in deconvolution interferometry based on their integral representation. Here we illustrate the ideas in the previous Sections using asymptotics. We use these asymptotic methods to investigate the spurious arrivals in imaging gathers produced by deconvolution interferometry (see Section 3.3.2). Although it is necessary to restrict this type of analysis to simple models, the observations provide useful insight into the physics of our problem. Snieder et al. (2006) used the same kind of asymptotic analysis to study the terms arising from interferometry by cross-correlations (e.g., equation 3.4). They also characterized spurious multiples that come from a limited source integration (see discussion concerning equation 3.8). Since our approach is analogous to that in Snieder et al. (2006), we do not reproduce all steps in their derivation. Some of these steps are reproduced in Appendix B.

The toy model we use is that of a single reflector in a homogeneous medium (Figure 3.3). The unperturbed wavefields $u_0(\mathbf{r}_{A,B}, \mathbf{s})$ consist of the direct waves while $u_S(\mathbf{r}_{A,B}, \mathbf{s})$ are the single-reflected waves. We use the far-field acoustic Green's functions in equation B.1 to represent the ray-geometric arrivals in Figure 3.3. If we rewrite the term D^1_{AB} in equation 4.12 according to equation B.1 we get

$$D^1_{AB} \;=\; \frac{1}{(4\pi L_B)^2} \int \frac{e^{ik(L_A - L_B)}}{L_A L_B} dxdy \;, \tag{3.31}$$

where the integral over $\mathbf{s}$ (equation 4.12) has been converted to the integration over the lateral coordinates x and y (representing the surface plane). The stationary-phase evaluation (see Appendix A) of the integral in equation 3.31 gives

$$D^1_{AB} \;=\; \frac{nc}{32\pi^2\, L_B^2\, cos\psi}\, \frac{G_0(\mathbf{r}_A, \mathbf{r}_B)}{(-i\omega)}\,; \tag{3.32}$$

with the acoustic wavespeed c, and n representing sources per unit area (Snieder et la., 2006). A straight raypath connecting $\mathbf{r}_A$, $\mathbf{r}_B$ and the surface determines the stationary source position that gives equation 3.32. The angle defined between this stationary ray and the vertical defines the angle ψ. $G_0(\mathbf{r}_A, \mathbf{r}_B)$ is the unperturbed Green's function, in this case a direct wave, propagating from $\mathbf{r}_B$ to $\mathbf{r}_A$. Equation 3.32 is consistent with our interpretation of the term D^1_{AB} in Section 3.3.2. The $(-i\omega)^{-1}$ in equation 3.32 indicates that after interferometry it is necessary to perform a time-domain differentiation to obtain the Green's function (Snieder et al., 2006). This is a correction factor commonly found in interferometry (e.g., Wapenaar et al., 2004a; van Wijk et al., 2006): it compensates for the source integration, and it depends on which type of Green's function is considered (Wapenaar et al, 2004b). Although for simplicity we have not explicitly kept the $i\omega$ factors in the integrals in previous Sections, the exact forms of those expressions also have $i\omega$ factors (Chapter 2).

The term D^2_{AB} of equation 4.12 for our model reduces with equation B.1 to the integral

$$D^2_{AB} \;=\; \frac{r}{(4\pi L_B)^2} \int \frac{e^{ik(L_1+L_2-L_B)}}{(L_1+L_2)\, L_B} dxdy\;, \tag{3.33}$$

which is has a form similar to that of equation 3.31. This integral can also be evaluated with the stationary phase method, giving

$$D^2_{AB} \;=\; \frac{nc}{32\pi^2\, L_B^2\, cos\psi}\; \frac{G_S(\mathbf{r}_A, \mathbf{r}_B)}{(-i\omega)}\,; \tag{3.34}$$

where r is the constant reflection coefficient at the interface in Figure 3.3. The

stationary source point that results in equation 3.34 is associated with a raypath that starts at the surface, passes through $\mathbf{r}_B$, specularly reflects off the interface and is recorded at $\mathbf{r}_A$. Since the stationary raypaths that give equations 3.32 and 3.34 are different, the corresponding values of the obliquity factor $cos\psi$ are also different. The stationary-phase evaluation of D^2_{AB} (equation 3.33) results in $G_S(\mathbf{r}_A, \mathbf{r}_B)$: a causal singly reflected wave excited at $\mathbf{r}_B$ and recorded at $\mathbf{r}_A$.

Next, we consider the asymptotic behavior of the D^3_{AB} term (equation 4.12). Using the Green's functions in equation B.1, D^3_{AB} is given by

$$D^3_{AB} = -\frac{r}{(4\pi L_B)^2} \int \frac{e^{ik[(L_3+L_4-L_B)-(L_A-L_B)]}}{(L_3+L_4)\, L_A L_B^2} dxdy\ . \tag{3.35}$$

If $\mathbf{r}_A = \mathbf{r}_B$, the phase of the integrand in equation 3.35 is the same as in equation 3.33, so the resulting stationary-phase evaluation of D^3_{AB} is proportional to $G_S(\mathbf{r}_B, \mathbf{r}_B)$. This supports the physical interpretation of D^3_{AB} provided in Section 3.3.2, where we argue that for $\mathbf{r}_A = \mathbf{r}_B$ the terms D^3_{AB} and D^1_{AB} have the same phase and give the zero-offset scattered-wave traveltimes. For $\mathbf{r}_A \neq \mathbf{r}_B$, D_{AB} is not associated to any stationary paths that would exist for a real excitation placed at $\mathbf{r}_B$ without the free point boundary condition (equation 4.15).

The main objective in studying the spurious terms such as D^3_{AB} is to determine their influence in imaging data from deconvolution interferometry. Hence, we proceed with a numerical asymptotic analysis of the spurious arrivals. Once we specify a model such as the one in Figure 3.3, we compute the ray-based traveltimes of each spurious arrival for all source positions, according to equation 3.18. From the maxima of the phases of each spurious event, we determine their corresponding stationary traveltime and source position. We did this for a fixed position $\mathbf{r}_B$ as a function of a laterally-varying $\mathbf{r}_A$. Given the receiver positions, stationary traveltimes and model

parameters, we predict the migrated depth of any given term (e.g., D^2_{AB}) through common-shot migration (Bleistein et al., 2001). The result of this analysis is shown in Figure 3.4. The geometry and model parameters used in the computations in Figure 3.4 are the same as in the numerical model we discuss in the next Section. For these computations, $\mathbf{r}_A$ and $\mathbf{r}_B$ are kept at the same constant depth level.

Only the term D^2_{AB} represents physical scattered waves in Figure 3.4. As expected, D^2_{AB} is mapped at the same depth for all offsets, as shown by the solid black line in the Figure. On the other hand, the spurious terms in Figure 3.4 map to depths that increase with increasing offset. This suggests that when a sufficiently large range of offsets is used, most spurious events interfere destructively when imaged. The only exception is the term $T_1^{2^{nd}}$, whose mapped depth varies slowly with offset. We suspect that this might be because the phase of $T_1^{2^{nd}}$ is equivalent to twice the phase of the integrand of D^2_{AB} (equation 4.12), thus representing artifact multiples arising from convolving $u_S(\mathbf{r}_A, \mathbf{r}_B)$ with itself.

If only a short offset aperture is available (e.g., in the offset range 0 to 500 m in Figure 3.4), the spurious multiples may add constructively in the final image. We argue that even if spurious events in Figure 3.4 map to image they will not be very prominent because they are of higher order in the scattered wavefield. In addition, these terms should cancel close to zero-offset because of the free point boundary condition imposed by deconvolution interferometry (see discussion in Section 3.3.2). This boundary condition requires the zero-offset wavefield to be zero at finite times (see Section 3.3.2). Indeed, solid and dashed lines of a common color in Figure 3.4 pertain to terms that have opposite polarity.

Note that at zero-offset (Figure 3.4), 2^{nd}-order spurious events map at twice the depth of the physical reflector relative to the receivers (receiver depth is 750 m);

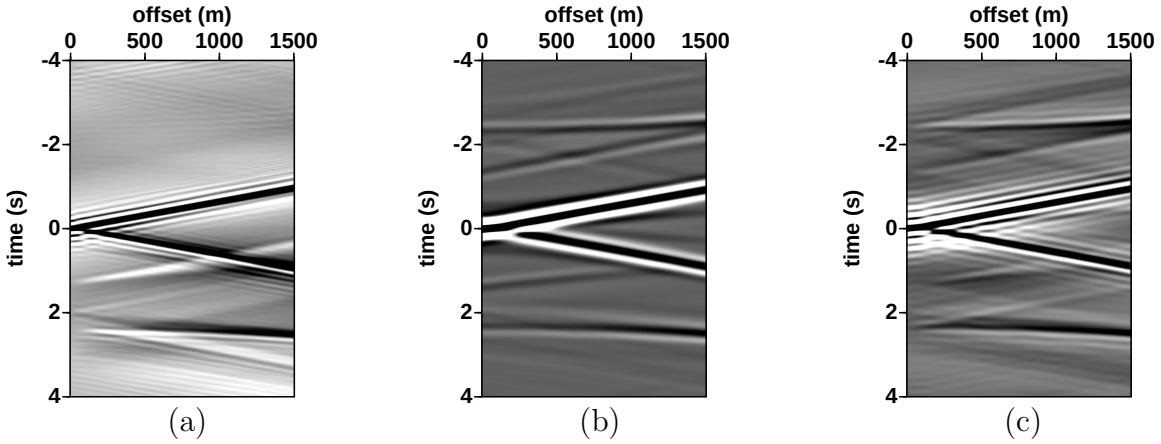

Figure 3.8. Pseudo-shot (interferometric) gathers with the shot positioned at the receiver at 1500 m. The gather in (a) is obtained by deconvolution before stacking (equation 3.10), (b) is generated by cross-correlations (equation 6.2) and (c) is given by deconvolution after summation over sources (equation 3.24). Source integration of the gathers in Figures 3.6a and c yield the last trace in (a) and (b), respectively.

3^{rd}-order events map at three times that depth, and so on. This observation relates to the remarks made about the zero-offset traveltimes expected for the higher-order terms in Section 3.3.2.

3.4 Numerical example

The model we use is composed of a water layer with a wavespeed of 1500 m/s. A flat, horizontal interface was placed at 2500 m depth. The contrast at the interface is produced by a velocity step from 1500 to 2200 m/s, with a constant background density of 1000 kg/m^3. The receivers were positioned in a horizontal line at 750 m depth, starting at lateral position $x = 1500$ m and ending at 3000 m, with increments of 25 m. The source line was also horizontal at a depth of 400 m, ranging from $x = 500$ m to 4500 m, with increments of 50 m. The data was modeled by 2D acoustic finite-

differencing with absorbing boundary conditions. Figure 3.5 shows that the data consists of direct and single-reflected waves. As in the previous Section, we refer to these waves as $u_0(\mathbf{r}_{A,B}, \mathbf{s})$ and $u_S(\mathbf{r}_{A,B}, \mathbf{s})$, respectively.

First, we use the data in Figure 3.5 to analyze the integrands in equations 6.2 and 3.10. The deconvolution of the wavefield in Figure 3.5a with the wavefield in Figure 3.5b yields Figure 3.6a, while the cross-correlation yields Figure 3.6c. The deconvolution gather (Figure 3.6a) displays causal term D^2_{AB}, while both causal (C^2_{AB}) and acausal (C^3_{AB}) contributions are present in the cross-correlation gather (Figure 3.6c). This confirms our claim that deconvolution interferometry gives mostly causal scattering contributions (see Section 3.3.2). The term C^4_{AB} also does not have a corresponding term in the deconvolution gather, as was predicted by equation 4.12. Also, the waveforms in Figure 3.6a are sharper than those in Figure 3.6c because deconvolution suppresses the source function. We use a *water-level regularization* method to do deconvolutions. For a brief discussion on this method see Appendix A in Chapter 4.

The arrival times predicted with perturbation theory (bottom plots in Figure 3.6) provide an accurate representation of the modeled results in the top panels of Figure 3.6. In particular, the deconvolution series (equation 3.18, Figure 3.6b) describes well the most prominent terms in deconvolution interferometry (equation 3.10, Figure 3.6a). As predicted by theory, the terms D^2_{AB} and D^3_{AB} have opposite polarity. The extrema of the curves in Figure 3.6 are stationary source positions. Thus, the stationary traveltime of each term is the time associated to the extremum of its curve in Figure 3.6. The stationary traveltimes from D^1_{AB} and C^1_{AB} are $t = \pm 1$ s, representing causal and acausal direct waves. D^2_{AB} and C^2_{AB} result in a stationary time of approximately 2.5 s, which coincides with the traveltime of a causal single-scattered

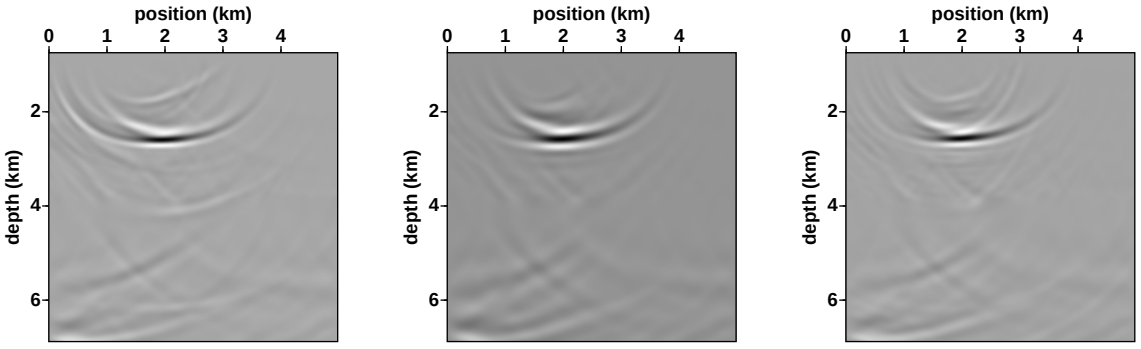

(a) (b) (c)

Figure 3.9. Shot-profile wave-equation migrated images of the virtual shot gathers in Figure 3.8. In this figure, (a), (b) and (c) are the images obtained from migrating the gathers in Figure 3.8a, b and c, respectively. The true depth of the target interface is 2500 m. The shot is placed at 1.5 km and receivers cover a horizontal line from 1.5 to 3.0 km.

wave. In previous Sections we showed that the stationary traveltimes given by D^2_{AB} and D^3_{AB} only coincide when $\mathbf{r}_A = \mathbf{r}_B$. Since in Figure 3.6 $\mathbf{r}_A \neq \mathbf{r}_B$, the stationary time of D^3_{AB} is different from that of D^2_{AB}.

There are other events present in the lower left-hand corner of Figure 3.6a which are not present in Figure 3.6b. These events are described by higher-order terms of the deconvolution series (equation 3.18). Figure 3.7 shows how the events are described by terms of second and third order in the scattered wavefield. The events corresponding to third-order terms have considerably smaller amplitude than the ones related to second-order terms. Second-order terms are in turn weaker than the leading-order terms (Figure 3.6a). A decrease in the power of the events with increasing order in the perturbed wavefield is expected, given the form of equation 3.18. These examples confirm the accuracy of the deconvolution series in describing the character of the integrand in deconvolution interferometry (equation 3.10).

The integration over sources (e.g., equations 6.2 and 3.10) corresponds to the horizontal stack of the plots in Figures 3.6a and c. Stacking, for example, Figure 3.6c results in a single trace that represents a wavefield excited at a lateral position of 1500 m and recorded at 3000 m. We create an interferometric shot gather with a pseudo-shot placed at 1500 m by computing and stacking all of the deconvolution and cross-correlation gathers (Figures 3.6a and c) for the receiver fixed at 1500 m but varying the lateral position of the other receiver from 1500 to 3000 m. The interferometric shot gathers are shown in Figure 3.8.

All gathers in Figure 3.8 show both causal and acausal direct waves. Only the gathers produced from cross-correlation (Figure 3.8b) and deconvolution after stack (Figure 3.8c) show causal and acausal reflections, agreeing with equations 6.2 and 3.28. The interferometric gather produced from deconvolution interferometry (Figure 3.8a) indeed only shows the causal scattered wave. The first-order term D^3_{AB} (equation 4.12) can be seen in Figure 3.8a with opposite polarity and slower moveout compared to the physical reflection. The reflection and the D^3_{AB} spurious events converge at zero-offset where they cancel. As observed in Figure 3.8a, this is due to the effect of the free point boundary condition (equation 4.15) imposed by the deconvolution of wavefields before source integration (see Section 3.3.2). As in Figure 3.8a, the zero-offset trace of the gather in Figure 3.8c consists of a band-limited spike at 0 s. This can be verified by setting $C_{AB} = C_{BB}$ in equation 3.24. In contrast to Figure 3.8a, Figure 3.8c does not contain the spurious events produced by the free point boundary condition present when deconvolving the wavefields before source integration. There are other events which are related to the truncated source integration (see Section 3.3.1). These are, for example, the upward-sloping linear events appearing between the direct arrivals and the reflections in all three gathers.

The images obtained by shot-profile migration of the gathers in Figure 3.8 are shown in Figure 3.9. The shot-profile migration was done by wavefield extrapolation, with a split-step Fourier extrapolator. The reflector is placed at the correct depth in all three images. Also, all three images are remarkably similar, despite the differences between the gathers in Figure 3.8. The similarity between the images comes from the fact that the spurious events in deconvolution interferometry have a negligible effect in images made from offset-dependent data. Based on Figure 3.4, we argue in Section 3.3.4 that the spurious events produced by deconvolution interferometry typically do not map onto coherent reflectors. This justifies the absence of spurious reflectors in Figure 3.9a. In Figure 3.9, we can also appreciate the effect of deconvolution (Figures 3.9a and c) in compressing the waveform relative to cross-correlation (Figure 3.9b).

3.5 Discussion and conclusions

By representing recorded wavefields as a superposition of direct and scattered wavefields, we derived a series expansion yielding terms that follow from performing deconvolution interferometry on receiver gathers before summing over sources. This derivation suggests that interferometry by deconvolution before stacking over sources gives only the causal scattered wavefield as if one of the receivers acted as a source. Because deconvolution interferometry requires the zero-offset wavefield to be zero at nonzero times, it generates spurious events to cancel scattered arrivals at zero-offset. We refer to this condition as the *free point* boundary condition at the pseudo-source location. With a simple model we illustrate this by using asymptotic approximations to the terms in deconvolution interferometry using the stationary-phase method. We also argue that interferometry can also be accomplished by deconvolution after sum-

mation over sources, which would yield terms analogous to correlation-based interferometry.

Numerical examples with impulsive source data showed that deconvolution interferometry can successfully retrieve the causal response between two receivers. This response can be used to build interferometric shot gathers which in turn can be imaged. Imaging of deconvolution interferometric shot gathers proved to practically eliminate the spurious arrival generated by the deconvolution method. Indeed, our numerical asymptotic analysis suggests that the deconvolution-related spurious events add destructively in the imaging of offset-variable data. It may be possible to create a reverse-time imaging scheme that results in an image free of spurious artifacts. We believe this could be done from the proper manipulation of boundary conditions in numerical modeling by the finite-difference method (Biondi, 2006). Although our assessment of the spurious events is model dependent, we believe that our observations also hold for more complicated models (see Part II of this article).

Ideally, we want interferometry to give us the best possible representation of the impulse response between two given receivers. Cross-correlation interferometry yields an accurate representation of the waves propagating between the receivers, but it requires an estimate of the power spectrum of the wavelet for it to give an impulsive response. Deconvolution interferometry yields an impulsive response, but it does so at the cost of generating artifacts. Another option is to design an inverse filter to do interferometry (Sheiman, personal communication, 2006). For example, the inverse filter may require the zero-offset trace in the pseudo-shot with a pre-determined band-limited pulse. This inverse filter does not require any knowledge about the model, and its output would be described the deconvolution series discussed here. If there is some knowledge about the model, the inverse filter may be designed to replicate an

estimate of a desired wavefield (e.g., Amundsen, 2001). In this case, the output of the inverse filter will approximate an impulsive version of cross-correlation interferometry. We associate the form of the deconvolution interferometry series to that of scattering series such as the Lippman-Schwinger series (Rodberg et al., 1967; Weglein et al. 2003). Forward and inverse scattering series serve, for instance, as the basis to methodologies in imaging and multiple suppression (Weglein et al., 2003). In analogy to scattering-based approaches, it is possible to express the deconvolution interferometry series in forward and inverse forms as well. Hence, an inverse deconvolution interferometry series may be designed for the imaging of pseudo-shots generated by deconvolution interferometry.

The results we present here are consistent with previous deconvolution interferometry results. Although there is no explicit source integration in the work of Snieder and Şafak (2006) and of Mehta et al. (2007a), their results agree with our representation of deconvolution interferometry before integration over sources. In the 1D models, such as used by Snieder and Şafak (2006) and Mehta et al. (2007a), the excitation produced by teleseismic events was naturally in the stationary path between the receivers. This excludes the need for a full 3D source integration as in equation 3.10. Moreover, we argue that the application commonly referred to as *receiver function* (e.g., Shen et al. 1998, Mehta et al., 2007b) in global seismology is a direct application of deconvolution interferometry. With the same type of 1D layered model as in Snieder and Şafak (2006) and of Mehta et al. (2007a), the receiver functions consist on the deconvolution of a radial receiver component with the vertical component of the same receiver. This, in interferometry terms, yields a zero-offset trace that corresponds to an excitation in the vertical direction whose wavefield is recorded in the radial direction. Also, like in Snieder and Şafak (2006) and Mehta et

al. (2007a), no source integration is required because in the 1D model all incoming waves are in the stationary wave-path.

It is important to point out other perhaps less obvious relationships between our work and that of other authors. With an elegant derivation and examples, Loewenthal and Robinson (2000) show that deconvolutions between measured dual wavefields (e.g., particle velocity and pressure) can be used for model-independent redatuming and for recovering reflectivity. Their derivation, in fact, is a proof of the application of deconvolution interferometry for dual wavefields. Amundsen (2001) designs deconvolution-type inverse operators to strip the influence of the water layer in marine data, at the same time performing free-surface multiple attenuation and estimating reflectivity. In a companion paper, Holvik and Amundsen (2005) use representation theorems of the same type as discussed in Section 3.3.1 along with deconvolution for elastic wavefield decomposition and multiple elimination. These papers are intimately related to deconvolution interferometry as we propose it. We advocate that the proper choice and manipulation of the wavefield pair u_0 and u_S give rise to different applications, with the example of dual wavefields by Loewenthal and Robinson (2001) or the boundary-condition approach by Amundsen (2001) and Holvik and Amundsen (2005). We also use these examples to highlight the potential of deconvolution-based interferometry in recovering data with amplitudes consistent with the subsurface reflectivity function.

There are other important potential applications for deconvolution interferometry. As we summarized in Figure 3.1, deconvolution interferometry gives only causal wavefield perturbations, while unperturbed waves are present at both positive and negative times. For an ideal source coverage, the subtraction of the acausal wavefield from deconvolution interferometry from its causal response results only in wave-

field perturbations. This idea may be useful for processing data from time-lapse experiments, as well as for pre-processing procedures such as direct- or surface-wave suppression. In the context of imaging, we highlight that in the cross-correlation imaging condition (Claerbout, 1985; Sava, 2006), the correlation serves the purpose of reproducing a zero-offset pseudo-shot experiment placed on top of a reflector (after extrapolating data to the reflector position). This is a direct application of the concept of correlation interferometry (e.g., Wapenaar and Fokkema). We believe that deconvolution interferometry can also be used to impose deconvolution imaging conditions (e.g., Muijs et al., 2007) that help to construct images whose amplitudes are an estimate of subsurface reflectivity (Bleistein et al., 2001).

Our goal here was to demonstrate the feasibility of using deconvolutions to recover the impulse response between receivers. Nonetheless, deconvolution interferometry has proven to be an important tool for interferometric imaging from complicated excitation. The Earth itself may be the cause of complicated source functions, as in the case of Snieder and Şafak (2006) and of Mehta et al. (2007a). When using internal multiples for imaging, we found deconvolution interferometry to be necessary (Chapters 4 and 5). In other applications the complicated character of the excitation may be related to the source itself. One such example is drill-bit seismology. When independent measures of the drill-bit stem noise are not available, deconvolution interferometry is necessary. This is the focus of the next part of this manuscript (Chapter 4). Here, we highlight the physical differences between three interferometric methods: 1) deconvolution before source integration, 2) cross-correlations and 3) deconvolution after source integration. The comparison between methods 1) and 2) serves the purpose of providing the reader with information that allows one to relate the new content in this manuscript to much of the existing literature about inter-

ferometry. The understanding of the methods 2) and 3) provides the basis for the discussion about the specific use of deconvolution interferometry in drill-bit seismic imaging, which is the subject of the second part of our study (Chapter 4).

3.6 Acknowledgements

We thank the NSF (grant EAS-0609595) and the sponsors of the consortium for Seismic Inverse Methods for Complex Structures for their financial support. We are grateful to Kurang Mehta (CWP), Rodney Calvert and Jon Sheiman (both Shell) for insightful discussions and suggestions throughout this project. I.V. thanks Art Weglein for a private lecture on the inverse scattering series that inspired many of the ideas in this paper.

Chapter 4

INTERFEROMETRY BY DECONVOLUTION – APPLICATION TO DRILL-BIT SEISMIC IMAGING[1]

4.1 Summary

In the practice of Seismic-While-Drilling (SWD), the goal is to determine the subsurface impulse response from drill-bit noise records. Most of the existing SWD technologies rely on pilot sensors and/or models to predict the drill-bit source function, which is then removed from the data. Deconvolution interferometry successfully recovers the impulse response between receivers from drill-bit noise without the need for an independent estimate of the drill-bit source function. We give a general review of current SWD methods in the context of cross-correlation interferometry, followed by a comparison of these methods with deconvolution interferometry. Unlike other SWD processing methods, interferometry does not require knowledge about the drill-bit position. We heuristically extend the concept of interferometry by deconvolution to multi-component data in elastic media. In elastic media, the radiation pattern of the interferometric pseudo-source are influenced by the radiation properties of the bit. This dependence is a function of the medium properties and of the distance between the bit and the recording sensors. Interferometry by deconvolution is of most use to SWD applications where pilot records are absent or provide unreliable estimates of the bit excitation. With a numerical SWD subsalt example, we show that decon-

[1]Submitted to Geophysics.

volution interferometry provides an impulsive image of the subsurface that cannot be obtained by correlations without an estimate of the source autocorrelation. This numerical example also illustrates the potential of SWD and deconvolution interferometry for passive imaging in deep-water subsalt environments. Finally, we validate the use of deconvolution interferometry in processing field SWD data acquired at the San Andreas Fault Observatory at Depth (SAFOD). Since no pilot records were available for these data, deconvolution outperforms correlation in obtaining an interferometric image of the San Andreas Fault zone at depth.

4.2 Introduction

The recording of drilling noise can be used for seismic imaging (Rector and Marion; 1991). In the majority of seismic-while-drilling applications (e.g., Poletto and Miranda, 2004) the data acquisition and imaging geometries fall under the category of reverse VSP (RVSP) experiments, where knowledge of the position of the drill-bit is required. With the autocorrelogram migration method, Schuster et al. (2004) and Yu et al. (2004) recognized that interferometry could be applied to SWD data without any knowledge of the drill bit position. Recently, Poletto and Petronio (2006) used interferometry to characterize fault zones ahead of a tunnel being drilled.

Interferometry is a proven methodology for the recovery of the impulse response between any two receivers from measurements of uncorrelated noise. This can be accomplished in diffuse fields by cross-correlating the data recorded by two receivers (Lobkis and Weaver, 2001; Larose et al., 2006). Wapenaar (2004) and Wapenaar et al. (2004) provided general proofs that cross-correlations of deterministic wavefields excited by uncorrelated noise result in the impulse response between receivers for arbitrary media. When the measured data is excited by correlated noise sources,

the result from cross-correlation interferometry contains the source power spectrum (Snieder et al., 2006a; Wapenaar and Fokkema, 2006; Chapter 3). In the specific case of SWD applications, the drill-bit noise signal (and its power spectrum) is a long and complicated source-time function with a narrow band signature (Poletto and Miranda, 2004). Hence, the extraction of an impulsive response from the application of cross-correlation interferometry to SWD data requires an additional processing step. This is the removal of the source signature (Wapenaar and Fokkema, 2006).

As shown by Chapter 3, interferometry can also be accomplished by deconvolution. One advantage of deconvolution interferometry over its correlation counterpart is that it removes the source function without the need for an extra processing step. The main objective of this paper is to validate deconvolution interferometry as a method to recover impulsive signals from drill-bit noise without the need for an independent estimate of the drill-bit excitation function.

There are many existing examples of successful applications of SWD technology. Most of the SWD methods rely on the so-called pilot sensors to independently estimate the drill-bit excitation (Rector and Marion, 1991; Haldorsen et al. 1994; Poletto and Miranda, 2004). Without relying on pilot records, Miller et al. (1990) design multichannel weighting deconvolution filters based on statistical assumptions about the source function. The monograph by Poletto and Miranda (2004) provides a comprehensive description of pilot deconvolution technologies. Some pilot-based SWD methods deconvolve the bit excitation directly from the recorded data (e.g., Haldorsen et al., 1994) while most methodologies rely on cross-correlations (e.g., Rector and Marion, 1991; Poletto and Miranda, 2004). There is a close connection between correlation-based SWD methods and cross-correlation interferometry, which we highlight in this paper. Pilot-based SWD technologies can be elaborate; the more

sophisticated pilot recordings may use dual-field sensors (Poletto et al., 2004) or accelerometers mounted close to the drill-bit (Poletto and Miranda, 2004). Recognizing that pilot records are imperfect estimates of the drill-bit excitation, Poletto et al. (2000) present a statistical technique that further optimizes pilot deconvolution. We promote the use of deconvolution interferometry for the cases where pilot signals are absent or provide poor estimates of the drill-bit excitation. As described by Poletto and Miranda (2004), examples of data for which pilot deconvolution can be unsuccessful are those excited by deep drilling wells, deviated wells, or when the drill-bit is below strong geologic contrasts (e.g., below salt).

The majority of SWD experiments constitute RVSP geometries (Rector and Marion, 1991; Poletto and Miranda, 2004). Drilling noise has also been used for imaging ahead of the drill-bit (i.e., "Look-Ahead" VSP) as shown by Armstrong et al. (2000) and Malusa et al. (2002). Armstrong et al. (2000) showed examples of drill-bit imaging in the deep-water Gulf of Mexico. Most SWD experiments are conducted onshore with roller-cone drill-bits (Poletto and Miranda, 2004). Deep-water offshore applications of SWD technology, such as described by Armstrong et al. (2000), are rare. One of the reasons why deep-water offshore SWD is uncommon is that pilot records yield poor representations of the bit excitation in these conditions (Poletto and Miranda, 2004). With the numerical experiment in this paper we demonstrate the potential of interferometry by deconvolution for treating passive recordings of drilling noise in deep-water subsalt environments.

We first review SWD methods based on correlations and pilot deconvolution in the context of interferometry. Next, we describe the role of deconvolution interferometry (Chapter 3) in extracting the impulse response between receivers from drilling noise. Within this description, we discuss the applications of the concepts presented

by Chapter 3 to elastic media, and elaborate on how the drill-bit radiation properties influence the recovered elastic response. With a numerical example using the *Sigsbee* salt model, we compare the performance of deconvolution and correlation interferometry in passive drill-bit imaging. Finally, we present the results of using deconvolution interferometry for the imaging of the San Andreas Fault zone from SWD data acquired at Parkfield, CA.

4.3 Drill-bit seismic imaging and deconvolution interferometry

In this section we compare existing method for processing seismic-while-drilling data with deconvolution interferometry.

4.3.1 The practice of seismic-while-drilling

The frequency-domain wavefield measured at $\mathbf{r}_A$ excited by a working drill-bit at $\mathbf{s}$ is given by

$$u(\mathbf{r}_A, \mathbf{s}, \omega) = W(\mathbf{s}, \omega)\, G(\mathbf{r}_A, \mathbf{s}, \omega)\,, \tag{4.1}$$

where $G(\mathbf{r}_A, \mathbf{s}, \omega)$ is the impulse response between $\mathbf{s}$ and $\mathbf{r}_A$, and $W(\mathbf{s}, \omega)$ is the drill-bit excitation function. For brevity, we omit the dependence on the angular frequency ω in subsequent equations. As in most exploration imaging experiments, the objective of drill-bit seismology is to image the subsurface from its impulse response, G, which needs to be obtained from equation 6.1. The main issue for successful imaging from drill-bit noise is removing the imprint of the source function W (Rector and Marion, 1991; Haldorsen et al., 1994; Poletto and Miranda, 2004). The first complication imposed by drill-bit excitation is that the source is constantly active; in other words, the source pulse is as long as the total recording time of the data. Additionally, the

drill-bit is a source of coherent noise that is dominated by specific vibrational modes associated with the drilling process (Poletto, 2005a). These strong drilling-resonant modes give the time-domain drill-bit signature a predominantly monochromatic character. Apart from the coherent vibrations, weaker random vibrations that occur during drilling make the drill-bit signal wide-band (Poletto, 2005a). We illustrate these issues in our subsalt example, where we provide a numerical model for the drill-bit excitation.

Current interferometric approaches to processing drill-bit noise records rely on correlations (e.g., Schuster et al.; 2004, Yu et al., 2004; Poletto and Miranda, 2004). The cross-correlation of wavefields measured at $\mathbf{r}_A$ and $\mathbf{r}_B$ is, in the frequency domain, given by

$$\begin{aligned} C_{AB} &= u(\mathbf{r}_A, \mathbf{s})\, u^*(\mathbf{r}_B, \mathbf{s}) \\ &= |W(\mathbf{s})|^2\, G(\mathbf{r}_A, \mathbf{s})\; G^*(\mathbf{r}_B, \mathbf{s})\,; \end{aligned} \tag{4.2}$$

where * stands for complex conjugation. It follows from this expression that the cross-correlation is influenced by the power spectrum of the drill-bit source function. In the time domain, the power spectrum in equation 4.2 corresponds to the autocorrelation of the drill-bit source-time function. This autocorrelation, despite being zero phase, is similar in character to the excitation $W(\mathbf{s}, t)$: a long, complicated waveform with a monochromatic appearance.

In the majority of drill-bit processing methods presented to date, the removal of the drill-bit source function in equation 6.1 (or of its autocorrelation, equation 4.2) relies on an independent estimate of the drill-bit excitation. This estimate typically comes in the form of the so-called *pilot record* or *pilot trace* (e.g., Rector and Marion, 1991; Poletto and Miranda, 2004). The pilot records are the data acquired by accelerometers placed in the rig/drill-stem structure. The most common form of pilot

sensor mount is at the top of the drill-string. Pilot sensors may also consist of *dual-wavefield* sensors that measure displacement and strain waves (Poletto et al., 2004). The positioning and the type of sensors used in acquiring pilot records depends on the specific SWD application. Poletto and Miranda (2004) provide a detailed explanation of the different types of pilot sensor technologies and their applications.

Within the literature on SWD, there are different descriptions of the signal acquired by the pilot sensors. Most of these descriptions are based on deterministic physical models for wave propagation in the rig/stem/bit system (Rector, 1992; Rector and Hardage, 1992; Haldorsen et al., 1994; Poletto and Miranda, 2004). Poletto et al. (2000) and Poletto and Miranda (2004) propose a statistical approach for the description of the drill bit signal. Since for the purpose of deconvolution interferometry we do not require a particular description of the pilot signal, it is convenient to express it in the general form

$$P(\mathbf{r}_d, \mathbf{s}) = W(\mathbf{s})\; T_d(\mathbf{r}_d, \mathbf{s})\,; \tag{4.3}$$

T_d is the transfer function of the drill-stem and rig assembly, and $\mathbf{r}_d$ is the location of the pilot sensor in the assembly. This transfer function includes reflection and transmission coefficients of the rig/stem/bit system, drill-string multiples, etc (Poletto and Miranda, 2004). The autocorrelation of the pilot signal in equation 4.3 gives

$$C_{PP} = |W(\mathbf{s})|^2 \;\; |T_d(\mathbf{r}_d, \mathbf{s})|^2 \;. \tag{4.4}$$

From this autocorrelation, and with additional knowledge about T_d, it is possible to design a filter $\mathcal{F}$, of the form

$$\mathcal{F}\left(C_{PP}\right) \approx \frac{1}{\left|W(\mathbf{s})\right|^2}\,. \tag{4.5}$$

We use the notation $\mathcal{F}\left(C_{PP}\right)$ to indicate that $\mathcal{F}$ is a function of the autocorrelation C_{PP}. The deterministic (Rector, 1992; Rector and Hardage, 1992; Haldorsen et al., 1994; Poletto and Miranda, 2004) or statistical (Poletto et al., 2000; Poletto and Miranda, 2004) descriptions of T_d aim to remove its influence (equation 4.3) in the design of the filter $\mathcal{F}$. We present $\mathcal{F}$ as an approximation of $|W(\mathbf{s})|^{-2}$ in equation 4.5 because the theories that are used to eliminate the influence of T_d are approximate (e.g., Rector and Hardage, 1992; Poletto and Miranda, 2004). Multiplying the filter $\mathcal{F}$ (equation 4.5) by the cross-correlation in equation 4.2 gives

$$\mathcal{F}\, C_{AB} \approx G(\mathbf{r}_A, \mathbf{s})G^*(\mathbf{r}_B, \mathbf{s})\,. \tag{4.6}$$

According to this equation, $\mathcal{F}$ removes the power spectrum of the drill-bit excitation from the correlation in equation 4.2. The application of $\mathcal{F}$ is what is referred to as *pilot deconvolution* (Poletto and Miranda, 2004). The SWD RVSP methods rely on the cross-correlations of geophone data (equation 6.1) with the pilot signal (equation 4.3) to determine the time delay of waves that propagate between the drill-bit and the receivers (e.g. Rector and Marion, 1991; Poletto and Miranda, 2004). Note that for these methods it is necessary to know the drill-bit position $\mathbf{s}$. Although the most common applications of SWD RVSP correlate pilot and geophone signals (equation 4.2 correlates geophone signals), the removal of the drill-bit source function is done by pilot deconvolution in a manner analogous to the one presented here.

Following the principles of interferometry (e.g., Lobkis and Weaver, 2001; Wapenaar and Fokkema, 2006), the source average of the cross-correlations in equation 4.2

gives

$$\oint_{\Sigma} C_{AB}\, d\mathbf{s} \;=\; \langle |W(\mathbf{s})|^2 \rangle \left[G(\mathbf{r}_A, \mathbf{r}_B) \;+\; G^*(\mathbf{r}_A, \mathbf{r}_B) \right] ; \tag{4.7}$$

the integration is done over a closed surface Σ that includes all sources $\mathbf{s}$ (Chapter 3). According to equation 6.2, the source average of the cross-correlations gives the superposition of the causal and acausal impulse responses between $\mathbf{r}_A$ and $\mathbf{r}_B$. This response is shaped by the source average of the excitation spectrum $\langle |W(\mathbf{s})|^2 \rangle$. When using the noise from a single drill-bit, source integration reduces to a line integral, rather than an integration over a surface. This is not necessarily an issue for interferometry from drill-bit noise for two reasons. The first reason is that the desired response (right-hand side of equation 6.2) is obtained if the drill-bit samples the stationary source points that give rise to the target arrivals (Snieder et al., 2006a; Wapenaar and Fokkema, 2006). The second reason is that the long recording times employed in drill-bit acquisition can help sampling multiply scattered waves. These waves may make up for some of the missing sources that are required by the integration in equation 6.2 (Wapenaar, 2006; Chapter 3), depending on the scattering properties of the medium.

The processing of SWD data with correlation interferometry as in equation 6.2 does not require knowledge of the drill-bit position $\mathbf{s}$. This was observed by Schuster et al. (2004), who, along with the companion paper by Yu et al. (2004), first proposed the use of interferometry by correlation for imaging from drill-bit noise. Although not explicitly referring to interferometry, Poletto and Miranda (2004) promote the stack of cross-correlations over long listening times. In the context of drilling, listening times in the order of days translate to varying the drill-bit position $\mathbf{s}$. Hence, in general, the stack of long listening times mentioned by Poletto and Miranda (2004) is equivalent to an integration over $\mathbf{s}$ (equation 6.2).

The term $\langle|W(\mathbf{s})|^2\rangle$ in equation 6.2 plays the same role $|W(\mathbf{s})|^2$ in equation 4.2. The average of the excitation power spectra constitutes, in the time domain, a long zero-phase waveform with a monochromatic character. The removal of this waveform can also be achieved using the pilot record (equation 4.3). Poletto and Miranda (2004) recognize that pilot deconvolution can be done before or after stacking over long time records (which is equivalent to stacking over $\mathbf{s}$). From integrating the pilot autocorrelation (equation 4.4) over sources $\mathbf{s}$ we get

$$\oint_{\Sigma} C_{PP}\, d\mathbf{s} \;=\; \langle|W(\mathbf{s})|^2\rangle\langle|T_d(\mathbf{r}_d,\mathbf{s})|^2\rangle\,. \tag{4.8}$$

$\langle|T_d(\mathbf{r}_d,\mathbf{s})|^2\rangle$ is the source average of the transfer function T_d (equation 4.3). Given that a model that describes T_d is available (e.g., Rector and Hardage, 1992; Poletto and Miranda, 2004), the result of integral in equation 4.9 can be used to build a filter such as

$$\mathcal{F}_{av}\left(\langle C_{PP}\rangle\right) \;\approx\; \frac{1}{\langle|W(\mathbf{s})|^2\rangle}\,; \tag{4.9}$$

where $\langle C_{PP}\rangle$ is the source average represented by the integral in equation 4.9. Applying the filter $\mathcal{F}_{av}$ to the integral in equation 6.2 gives

$$\mathcal{F}_{av}\left[\oint_{\Sigma} C_{AB}\, d\mathbf{s}\right] \approx\; G(\mathbf{r}_A,\mathbf{r}_B) \;+\; G^{*}(\mathbf{r}_A,\mathbf{r}_B)\,; \tag{4.10}$$

where the influence of the drill-bit source signature is removed. This is a general representation of pilot deconvolution for the correlation-based interferometry of drill-bit noise records. After pilot deconvolution, interferometry by correlations of SWD data yields the causal and acausal impulse response for waves excited at $\mathbf{r}_B$ and recorded at $\mathbf{r}_A$. Poletto and Miranda (2004) give a comprehensive review of pilot deconvolution

methods. Note that the filtering of equation 6.2 by $\mathcal{F}_{av}$ involves deconvolving the source integral of C_{AB} by the source integral of C_{PP}. This approach is similar in concept to deconvolution interferometry after source integration described by Chapter 3.

There are a number of different approaches to processing SWD data. Most of them rely on cross-correlation (e.g. Rector and Marion; Poletto and Miranda, 2004). Some of these correlation-based processing techniques (e.g., RVSP techniques) require knowledge of the drill-bit position $\mathbf{s}$, and apply pilot deconvolution in a manner similar to that in equations 4.5 and 4.6. Another approach to treating drilling noise records is to use a source average of the cross-correlations (Poletto and Miranda, 2004; Schuster et al., 2004; Yu et al., 2004) as in equations 6.2 through 4.10. Although we describe SWD processing by the correlation of recordings made by geophones at two arbitrary locations $\mathbf{r}_A$ and $\mathbf{r}_B$, some SWD applications rely on correlations between pilot and geophone signals (Poletto and Miranda, 2004). Methods based on pilot trace correlations are affected by the drill-bit source function in the same way it affects methods based on geophone correlations. Therefore, the pilot deconvolution discussion above also applies to SWD processing by correlating pilot and geophone traces (Poletto and Miranda, 2004). The majority of SWD technologies rely on the acquisition of pilot records to remove the drill-bit source function.

4.3.2 Deconvolution interferometry

We present interferometry by deconvolution as an alternative to processing drill-bit noise records. A detailed description of the method and physics of deconvolution interferometry is given by Chapter 3. Here, we rely on the key concepts of that work to highlight the differences between interferometry by deconvolution and other

techniques in SWD data processing. We extend the physical interpretation of deconvolution interferometry given by Chapter 3 heuristically to elastic media for the special case of single-scattered waves. This extension is necessary for the discussion on the processing of the SAFOD SWD data.

Consider the deconvolution of the wavefield measured at $\mathbf{r}_A$ (equation 6.1) with the wavefield recorded at $\mathbf{r}_B$, given by

$$\begin{aligned} D_{AB} &= \frac{u(\mathbf{r}_A,\mathbf{s})}{u(\mathbf{r}_B,\mathbf{s})} = \frac{u(\mathbf{r}_A,\mathbf{s})\,u^*(\mathbf{r}_B,\mathbf{s})}{\left|u(\mathbf{r}_B,\mathbf{s})\right|^2} \\ &= \frac{G(\mathbf{r}_A,\mathbf{s})\,G^*(\mathbf{r}_B,\mathbf{s})}{\left|G(\mathbf{r}_B,\mathbf{s})\right|^2}\,. \end{aligned} \tag{4.11}$$

This deconvolution cancels the drill-bit source spectrum $|W(s)|^2$, present in cross-correlation (equation 4.2). Note that this cancelation occurs without the need for an independent estimate of $W(\mathbf{s})$. The next step in deconvolution interferometry is to mimic its correlation-based counterpart (see equation 6.2) and integrate equation 4.11 over all sources $\mathbf{s}$. The impulsive wavefields G are taken as a superposition of an unperturbed wavefields G_0 and wavefield perturbations G_S (Chapter 3). The perturbations G_S can be interpreted as the waves scattered by the medium (Chapter 3; Weglein et al., 2003). In this context, in Chapter 3 we expand the deconvolution in equation 4.11 into a power series over $G_S(\mathbf{r}_B,\mathbf{s})/G_0(\mathbf{r}_B,\mathbf{s})$. After integrating over

$\mathbf{s}$ and keeping the terms that are linear in the scattered waves G_S, we get

$$\begin{aligned}
\oint_\Sigma D_{AB}\, d\mathbf{s} &= \underbrace{\oint_\Sigma \frac{G_0(\mathbf{r}_A,\mathbf{s})G_0^*(\mathbf{r}_B,\mathbf{s})}{|G_0(\mathbf{r}_B,\mathbf{s})|^2}\, d\mathbf{s}}_{D^1_{AB}} \\
&+ \underbrace{\oint_\Sigma \frac{G_S(\mathbf{r}_A,\mathbf{s})G_0^*(\mathbf{r}_B,\mathbf{s})}{|G_0(\mathbf{r}_B,\mathbf{s})|^2}\, d\mathbf{s}}_{D^2_{AB}} \\
&- \underbrace{\oint_\Sigma \frac{G_S(\mathbf{r}_B,\mathbf{s})G_0(\mathbf{r}_A,\mathbf{s})G_0^*(\mathbf{r}_B,\mathbf{s})}{G_0(\mathbf{r}_B,\mathbf{s})}\, d\mathbf{s}}_{D^3_{AB}} . \qquad (4.12)
\end{aligned}$$

Following the interpretation of Chapter 3, the term D^1_{AB} recovers $G_0(\mathbf{r}_A,\mathbf{r}_B)$ and $G_0^*(\mathbf{r}_A,\mathbf{r}_B)$, which are the causal and acausal unperturbed impulse responses for waves excited at $\mathbf{r}_B$ and recorded at $\mathbf{r}_A$. The term D^2_{AB} yields $G_S(\mathbf{r}_A,\mathbf{r}_B)$ that describes causal scattered waves propagating from $\mathbf{r}_B$ to $\mathbf{r}_A$. Recovering $G_S(\mathbf{r}_A,\mathbf{r}_B)$ from D^2_{AB} is the objective of deconvolution interferometry with the purpose of imaging scattered waves. The last term in equation 4.12 describes a spurious arrival that arises from the *clamped point* boundary condition imposed by deconvolution interferometry (Chapter 3).

As noted above, using deconvolution according to equation 4.11 to process SWD data does not require an independent estimate of the drill-bit source function. This is the first and main difference between deconvolution interferometry and the majority of correlation-based methods used in SWD data processing. Apart from being an alternative method for treating data from standard SWD experiments, interferometry by deconvolution would be particularly useful when pilot records are either unavailable or are poor estimates of the drill-bit excitation function. Poletto and Miranda (2004) provide examples of when pilot recordings yield unreliable estimates of the drill-bit

source function. This is the case, for example, when transmission along the drill-string is weak, when the drilling well is deep (in the order of several thousands of feet), or when the drilling well is deviated or when two or more nearby wells are drilling simultaneously with the well that is equiped with pilot sensors. From the standpoint of removing the excitation function, none of these cases is an issue for deconvolution interferometry, as they are for pilot deconvolution. This is because equation 4.11 holds regardless of the complexity of the excitation (equation 6.1).

As in interferometry methods based in correlation (Schuster et al., 1994; Yu and Schuster, 2004), knowledge of the drill-bit position $\mathbf{s}$ is not necessary for the processing of SWD data by deconvolution interferometry. The only requirement for the successful application of deconvolution interferometry is that the drill-bit must occupy the stationary source locations that give rise to targeted scattered waves propagating between the receivers (Chapter 3; Snieder et al, 2006). Analogously to the method originally proposed by Schuster et al. (2004) for the imaging of drill-bit noise, it is possible to use deconvolution interferometry to reconstruct primary arrivals from free-surface ghost reflections.

So far we have only discussed SWD processing and deconvolution interferometry for acoustic media. Now we extend some of these concepts to elastic media, with the objective of applying interferometry by deconvolution to multicomponent data. The conclusions drawn in our previous discussions on removal of the drill-bit source function, pilot deconvolution and deconvolution interferometry also hold for elastic media. Here, the goal is to understand what is the result of combining different receiver components when performing deconvolution interferometry. We start by defining $G^{(i,k)}(\mathbf{r}_A, \mathbf{s})$ as the elastic frequency-domain impulse response excited by the k-th component of the source at $\mathbf{s}$, and recorded by the i-th component of the receiver

at $\mathbf{r}_A$. For our purposes it is not necessary to specify whether the Green's functions $G^{(i,k)}$ pertain to stress or to strain waves (Wapenaar, 2004; Wapenaar and Fokkema, 2006). We refer to component orientations according to the 1-, 2- and 3-directions in Figure 4.1. Next, we take the deconvolution

$$D_{A^iB^j} \;=\; \frac{u^{(i,k)}(\mathbf{r}_A,\mathbf{s})}{u^{(j,k)}(\mathbf{r}_B,\mathbf{s})} \;=\; \frac{G^{(i,k)}(\mathbf{r}_A,\mathbf{s})\,G^{(j,k)*}(\mathbf{r}_B,\mathbf{s})}{\left|G^{(j,k)}(\mathbf{r}_B,\mathbf{s})\right|^2}\,, \tag{4.13}$$

where $u^{(i,k)} = W\,G^{(i,k)}$ is the recorded data. As in equation 4.11, the source function W cancels. It follows from equation 4.13 that $D_{A^iB^j}$ is the deconvolution of the i-th component of the receiver at $\mathbf{r}_A$ with the j-th component of the receiver at $\mathbf{r}_B$. We treat $G^{(i,k)}$ as the superposition of the unperturbed wavefield $G_0^{(i,k)}$ and the scattered waves $G_S^{(i,k)}$ (as in Chapter 3). The source integral of equation 4.13 can be expressed in the same three-term form of equation 4.12. We call $D^2_{A^iB^j}$ the elastic term analogous to D^2_{AB}. The is term can be expressed as

$$\begin{aligned} D^2_{A^iB^j} \;&=\; \int_{\sigma_1} \frac{G_S^{(i,k)}(\mathbf{r}_A,\mathbf{s})G_0^{(j,k)*}(\mathbf{r}_B,\mathbf{s})}{\left|G_0^{(j,k)}(\mathbf{r}_B,\mathbf{s})\right|^2}\,d\mathbf{s} \\ &\approx\; \mathcal{K}\,G_S^{(i,j)}(\mathbf{r}_A,\mathbf{r}_B)\,. \end{aligned} \tag{4.14}$$

where $\mathcal{K}$ is a constant. Following the reasoning given by Chapter 3 in interpreting equation 4.12, $\left|G_0^{(j,k)}(\mathbf{r}_B,\mathbf{s})\right|^2$ is a slowly varying function of $\mathbf{s}$, and its source average effectively gives a constant. The phase of the integrand in equation 4.14 is controlled by the numerator (Chapter 3). In equation 4.14, σ_1 is a segment of Σ that contains the stationary source locations that give rise to the desired waves in $G_S^{(i,j)}(\mathbf{r}_A,\mathbf{r}_B)$ (Chapter 3 and 2007b). Analogously to D^2_{AB} (Chapter 3), the term $D^2_{A^iB^j}$ yields causal scattered waves that propagate from $\mathbf{r}_B$ to $\mathbf{r}_A$. Equation 4.14 states that the

scattered waves described by $G_S^{(i,j)}(\mathbf{r}_A, \mathbf{r}_B)$ are excited by j-th component of a pseudo-source at $\mathbf{r}_B$ and are recorded by the i-th component of the receiver at $\mathbf{r}_B$. As in the acoustic case (equation 4.12), the scattered waves in the second line of equation 4.14 are the objective of interferometry.

According to the Green's function representation of Wapenaar and Fokkema (2006), the full elastodynamic reconstruction of $G^{(i,j)}(\mathbf{r}_A, \mathbf{r}_B)$ using cross-correlations requires a summation over the index k when integrating over sources, and the separation of P- and shear-wavefields at the surface of integration. Draganov et al. (2006) validate the elastodynamic interferometric reconstruction described by Wapenaar and Fokkema (2006) with a numerical example for a heterogeneous model. Although deconvolution interferometry (Chapter3) has not been formally extend to elastic media, we expect that the elastodynamic reconstruction of $G_S^{(i,j)}(\mathbf{r}_A, \mathbf{r}_B)$ by deconvolution interferometry also requires a summation over the index k. Note that in equation 4.14, we do not perform a summation over the index k as in the approach by Wapenaar and Fokkema (2006). In practice, this means that the integral in the first line of equation 4.14 only yields a partial reconstruction of $G_S^{(i,j)}(\mathbf{r}_A, \mathbf{r}_B)$ (second line of equation 4.14). In the case of single-scattered waves reconstructed from the interference of transmission and reflection responses (such as the data examples we provide in this paper), the partial reconstruction of $G_S^{(i,j)}(\mathbf{r}_A, \mathbf{r}_B)$ by the use of equation 4.14 can yield events with correct kinematics but distorted amplitudes (Draganov et al., 2006). As we discuss here with our field data example, a kinematically-consistent reconstruction of single-scattered waves using equation 4.14 is sufficient for the structural delineation of fault reflectors at the San Andreas fault zone (Chapter 5).

It is known that the deconvolution of any signal with itself results in a delta function ($\delta(t)$) in the time domain. For the acoustic case in equation 4.11, this is

accomplished by setting $\mathbf{r}_A = \mathbf{r}_B$, which in turn gives the zero-offset trace in deconvolution interferometry. In Chapter 3 we show that the time-domain zero-offset response in deconvolution interferometry is given by $G(\mathbf{r}_B, \mathbf{r}_B, t) = \delta(t)$ in arbitrary media. Since deconvolved waves satisfy the same homogeneous wave equation as the original waves (Snieder et al., 2006b), spurious arrivals are generated by deconvolution interferometry to cancel scattered waves that arrive at zero-offset at nonzero times. This represents the effect of an extra boundary condition in deconvolution interferometry experiments: the point $\mathbf{r}_B$ behaves, for the *particle velocity* impulse response, like a *clamped point* in the medium (see discussion in Chapter 3) In our elastic case, setting $\mathbf{r}_A = \mathbf{r}_B$ and $i = j$ in equation 4.13 results in unity, this translates to the time-domain condition

$$D_{B^i B^i}(t) = \delta(t)\,. \tag{4.15}$$

This condition does not hold if the receivers at $\mathbf{r}_B$ and $\mathbf{r}_A$ measure different field quantities, i.e., one receiver measures stress while the other measures strain. Equation 4.15 holds for arbitrarily inhomogeneous and anisotropic media. The condition in equation 4.15 sets a different type of boundary condition than those discussed by Chapter 3 for the acoustic case. While deconvolution interferometry *clamps* the point $\mathbf{r}_B$ for $t \neq 0$ in acoustic media, in elastic media only the i-th component of the wavefield deconvolution is clamped for $t \neq 0$. Clarifying the physical meaning of the boundary condition imposed by deconvolution interferometry in elastic media is beyond the scope of this paper, and is the subject of future research.

Analogously to interferometry by correlation (Wapenaar and Fokkema, 2006; Draganov et al., 2006), it follows from equations 4.13 and 4.14 that the orientation of the pseudo-source in deconvolution interferometry is dictated by the choice of component of the receiver at $\mathbf{r}_B$ that is used for deconvolution. The choice of com-

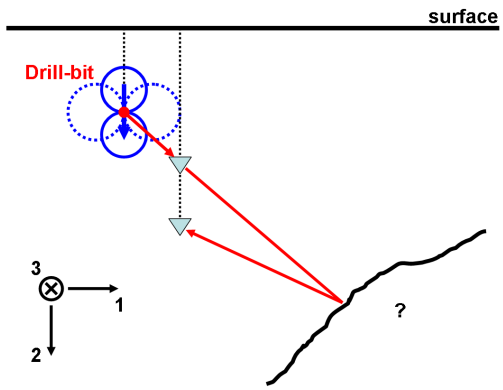

Figure 4.1. Illustration of drill-bit interferometry in elastic media. The red dot indicates a drill-bit position that yields a stationary contribution to waves that propagate between the receivers (light blue triangles). Red arrows shows the raypaths of pure-mode stationary arrivals. The blue arrow represents the oscillatory point-force excitation that describes the drill-bit source function. Solid and dashed blue circles denote the P- and S-wave radiation patterns, respectively. These radiation patterns follow the description of drill-bit radiation by Poletto (2005a). Receiver components, numbered 1 through 3, are oriented according to the vectors in the lower left-hand corner of the Figure. The medium consists of a homogeneous and isotropic half-space with an irregular reflector

ponent of the receiver at $\mathbf{r}_A$ controls the orientation of the recording component in the interferometric experiment. From elastic wave theory (Aki and Richards, 1980), the analysis of point-source radiation shows that a single source component generates impulse responses in all three receiver components, depending on the medium properties and on the source/receiver geometry. Because deconvolved waves satisfy the same homogeneous wave equations as the original experiment (Snieder et al., 2006b), the radiation pattern of the pseudo-source synthesized from deconvolution interferometry is controlled by the radiation pattern of the original physical experiment.

In SWD experiments, the drill-bit can be approximately described by an oscillatory force oriented in the local direction of the well (Rector and Hardage, 1992; Poletto, 2005a). Figure 4.1 portrays a schematic 2D representation of the drill-bit far-field radiation pattern in homegeneous and isotropic media. The radiation pattern shown in Figure 4.1 is similar to the point-force radiation pattern (Aki and Richards, 1980), except that the amount of drill-bit energy that converts into shear-waves (mostly SV-waves) is considerably larger than that from a traditional point-force source (Rector and Hardage, 1992; Poletto, 2005a). In Figure 4.1, we depict a drill-bit and instrumented well geometry that is consistent with the SAFOD case study, which we discuss in one of the next Sections. The receiver that acts as a pseudo-source in Figure 4.1 radiates waves according to the its recorded transmitted wavefield (see red arrows in the Figure). The wave modes and polarizations of the transmitted waves are dictated by the bit radiation pattern and the source/receiver geometry (Poletto, 2005a; Aki and Richards, 1980). The physical excitation in Figure 4.1 is associated to a vertically-oriented drill-bit point-force, whose radiation pattern (Rector and Hardage, 1992; Poletto, 2005a) is illustrated in the Figure. According to the geometry and bit radiation pattern in Figure 4.1, the direct waves recorded by the

top receiver are P- and S-waves polarized in the source/receiver plane. Hence, using the same notation as in equations 4.13 through 4.14 and assuming the receivers measure only the far-field response, interferometry in the context of Figure 4.1 recovers $G_S^{(i,2)}(\mathbf{r}_A, \mathbf{r}_B)$. Also, the response $G_S^{(i,2)}(\mathbf{r}_A, \mathbf{r}_B)$ is zero for $i = 3$ because SH-wave excitation (polarized in the 3-direction) from a drill-bit source is negligible in the conditions of Figure 4.1. From the drill-bit radiation pattern, we see that waves propagating along the stationary path depicted by Figure 4.1 (red arrows) carry both P- and shear-wave energy. The discussion surrounding Figure 4.1 illustrates how the radiation properties of the pseudo-source recovered from interferometry depend on the drill-bit excitation in SWD experiments. This dependence is model-dependent, and becomes more complicated with the introduction of heterogeneity and anisotropy.

4.4 Subsalt numerical example

The drill-bit imaging numerical experiment we present here is conducted with the 2D *Sigsbee* salt model (Figure 4.2). In this experiment, we place a long 100-receiver downhole array below the salt canopy, in a 45^o deviated well. The first receiver is placed at $x = 14630$ m and $z = 4877$ m , and the last receiver is at $x = 16139$ m and $z = 6385$ m. The receivers are evenly spaced; and x and z translate to the lateral and depth coordinates in Figure 4.2, respectively. The borehole array records the drilling noise from a vertical well placed at $x = 14478$ m (Figure 4.2). The drill-bit noise is recorded for a drill-bit depth interval that ranges from $z = 4572$ m to $z = 6705$ m. The objective of this numerical experiment is to show interferometry can recover, from drill-bit noise, up-going single-scattered waves that propagate between the receivers, such as the one represented by the raypath in Figure 4.2 (represented by the dashed arrow). The up-going scattered waves recovered by interferometry of drill-bit noise

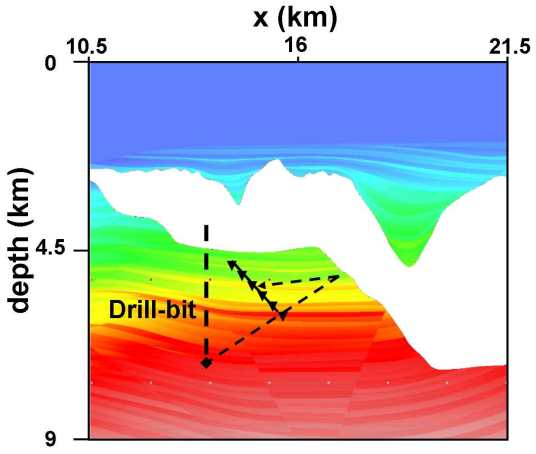

Figure 4.2. Structure of *Sigsbee* model and schematic acquisition geometry of the drill-bit experiment. The colors in the model denote acoustic wavespeed. The dashed black line indicates a well being drilled, which excites waves in the medium. The waves are recorded in a deviated instrumented well, inclined 45° with respect to the vertical direction. The solid line with triangles represents the instrumented well. The dashed arrow illustrates a stationary contribution to singly reflected waves that can be used to image the salt flank from the drilling noise.

can be used to image the *Sigsbee* structure from below.

To replicate drill-bit wave excitation in the numerical experiment, we first modeled 200 evenly-spaced shots within the drilling interval of interest. These shots were modeled by an acoustic finite difference method (Claerbout, 1985). Next, we convolved the shots with a 60 second-long model of the drill-bit excitation (Figure 4.3). The model for the drill-bit excitation is that of a roller-cone bit (Polleto, 2005a). We add band-limited noise (see Figure 4.3) to the model by Poletto and Miranda (2004) to make the drill-bit signal wide-band. Similar to the numerical example in Poletto and Miranda (2004), the bit and drilling parameters we used in our model are listed in the caption of Figure 4.3. The excitation function in Figure 4.3 represents the portion of the drilling energy that is radiated in the rock formation (Poletto 2005a,

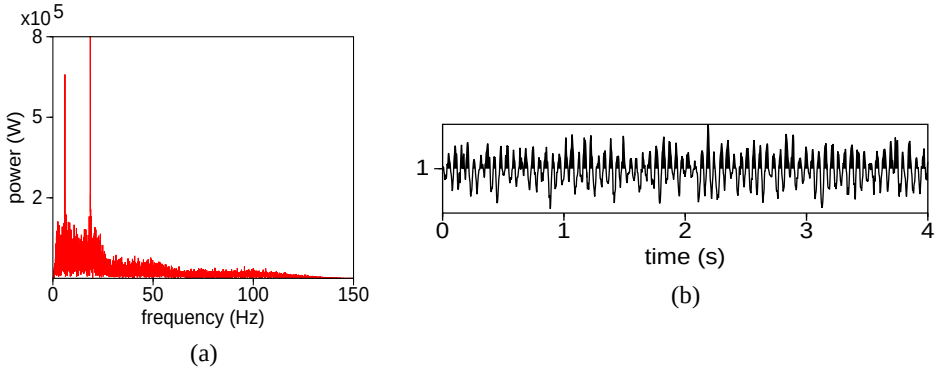

Figure 4.3. Numerical model of the drill-bit excitation. (a) shows the power spectrum of the drill-bit source function. Note that although it is wide band, the power spectrum of the source function in (a) has pronounced peaks that correspond to vibrational drilling modes. (b) is the drill-bit source function in the time-domain. We show only the first 4 s of the 60 second-long drill-bit source function used in the modeling. The assumed drill-bit is a tri-cone bit an outer diameter of 0.35 m, an inner diameter of 0.075 m and a density of 7840 kg/m^3. Each cone is comprised of three teeth rows as in the example by Poletto and Miranda (2004). Drill-string P-wave velocity is of 5130 m/s. The drilling was modeled with a weight on bit of 98 kN, torque on bit of 6 kNm, 60 bit revolutions per minute, a rate of penetration of 10 meters per hour and four mud pumps with a rate of 70 pump strikes per minute.

Poletto and Miranda, 2004).

Figure 4.3a shows the power spectrum of the modeled bit signal, while Figure 4.3b shows a portion of the drill-bit source function in the time-domain. As discussed in the previous Section, the time-domain drill-bit excitation has a narrow-band character (Figure 4.3b) because the source power spectrum is dominated by vibrational drilling modes (Poletto, 2005a; Poletto and Miranda, 2004). This behavior is also present in the data recorded by the borehole receivers. The common receiver gather from receiver 50 in Figure 4.4a shows that the simulated data is dominated by the character of the drill-bit excitation function (Figure 4.3b). The records in Figure 4.4a depict a moveout that characterizes the direct-wave arrival from the drill-bit. The weak events

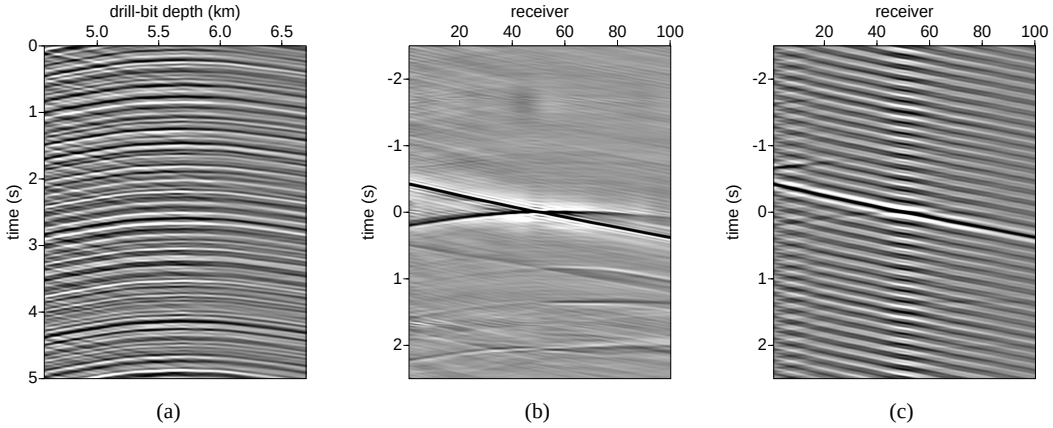

Figure 4.4. (a) Synthetic drill-bit noise records at receiver 50. Only 5 s out of the 60 s of recording time are shown. The narrow-band character of the records is due to influence of specific drilling modes (Figure 4.3a). (b) Deconvolution-based interferometric shot gather with the pseudo-source located at receiver 50. (c) Pseudo-shot gather resulting from cross-correlation with same geometry as (b). Receiver 1 in (a) and (b) is the shallowest receiver of the borehole array (Figure 4.2).

with positive slopes in the left-hand portion of Figure 4.4a are salt-bottom reflections from when the drill-bit is close to the bottom of the salt (see geometry in Figure 4.2).

Interferometry of recorded data such as in Figure 4.4a results in pseudo-shot gathers as in Figures 4.4b and c. The use of deconvolution interferometry as shown in the left-hand side of equation 4.12 (Chapter 3) for a fixed $\mathbf{r}_B$ at receiver 50 results in Figure 4.4b. The pseudo-shot gather in Figure 4.4c is obtained from correlation interferometry (equation 6.2; e.g., Draganov et al., 2006) for the same geometry as Figure 4.4b. Although both Figures 4.4b and c represent waves excited by a pseudo-source at receiver 50, the wavefield in Figure 4.4b is approximately impulsive, while the data in Figure 4.4c is dominated by the autocorrelation of the drill-bit source function. Because the excitation function is canceled in deconvolution interferometry (Chapter 3; equation 4.11), the pseudo-source in Figure 4.4 is impulsive. The

source power spectrum in equation 4.2 results, in the time-domain, in the dominant reverberation in the pseudo-shot generated by correlation (Figure 4.4c). When pilot sensors are available, pilot deconvolution methods (e.g., Rector and Marion, 1991; Poletto and Miranda, 2004) can be employed to remove the source autocorrelation from data such as in Figure 4.4c (equation 4.10).

Many of the features of the deconvolution pseudo-shot gather in Figure 4.4b are explained by the theory presented by Chapter 3; the interferometric shot gather generated by deconvolutions shows causal and acausal direct waves, and causal scattered arrivals. According to Chapter 3, the zero-offset trace obtained by deconvolution interferometry is a band-limited delta function at $t = 0$. This can also be observed in Figure 4.4 for the trace at receiver 50 (i.e., the zero-offset trace). The presence of this delta function at zero-offset imposes the so-called *clamped point* boundary condition in acoustic media (Chapter 3). Because of this boundary condition, the gather in Figure 4.4 contains spurious arrivals. The visual identification of these arrivals in the gather is not straightforward because the recorded wavefield is complicated, given the model complexity (Figure 4.2). These spurious arrivals, however, typically do not translate into image artifacts (Chapter 3).

Given the acquisition geometry in this numerical experiment (Figure 4.2), there is a point, to the left-hand side of the receivers, where drill-bit position aligns with the array direction. This drill-bit position samples a source stationary point for the direct waves that travel between the receivers. At this stationary position, the drill-bit excites waves that travel straight down the receiver array. These waves are responsible for the recovery of the direct-wave events with positive slopes in Figure 4.4. With the drilling geometry shown in Figure 4.2 the drill-bit never reaches a position where it aligns with the receivers to the right-hand side of the array. Therefore, the drill-

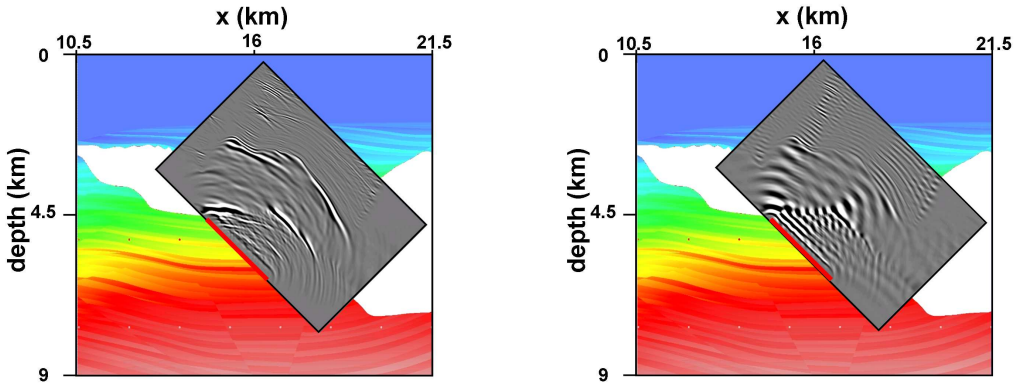

(a) (b)

Figure 4.5. Images obtained from drill-bit noise interferometry. The images, in grey scale, are superposed on the Sigsbee model in Figure 4.2. Panel (a) is the image obtained from shot-profile wave-equation migration of pseudo-shot gathers generated from deconvolution interferometry (such as in Figure 4.4b). The image in (b) is the result of migrating correlation-based interferometric shot gathers. The red lines in the images represent the receiver array.

bit does not sample a stationary source point that emits waves that travel directly upward along the receiver array. Hence, the direct-wave events with negative slopes in the pseudo-shot gather (Figure 4.4b) have a distorted curved moveout instead of the correct linear moveout shown by the direct waves that have positive slopes. A similar phenomenon was observed by Mehta et al. (2006), who show that the distortions caused by poor source sampling over stationary source positions can be attenuated by tapering the ends of the integrand in equation 6.2.

We generate interferometric shot gathers such as the ones in Figures 4.4b and c for pseudo-sources at each of the receivers in the array. This yields 100 pseudo-shots, which are recorded by the 100-receiver array. We use shot-profile wave-equation migration to image the interferometric data. The migration is done by wavefield extrapolation with the spilt-step Fourier method (Biondi, 2006). The wavefield extrapolation is done in a rectangular grid conformal to the receiver array, where the extrapolation steps are taken in the direction perpendicular to the array. Figure 4.5 displays the images obtained from migrating the pseudo-shot gathers from deconvolution interferometry (Figure 4.5a), and from the correlation-based method (Figure 4.5b).

In interferometric experiments, the image aperture is dictated by the geometry of the receiver array (red lines in Figure 4.5). The positioning of physical sources that are used in interferometry along with the medium properties control the actual subsurface illumination that is achieved by interferometry. When the sources completely surround the receivers, the interferometric pseudo-source radiates energy in all directions, similarly to a real physical source (Wapenaar and Fokkema, 2006; Larose et al., 2006). When the physical excitation generated by the sources is one-sided (Wapenaar, 2006; Chapter 3), pseudo-source radiation is uneven. Therefore, that the subsurface illumination in the images in Figure 4.5 is controlled by the illumina-

tion given by the original drill-bit/receiver geometry. In our case, the illumination given by interferometric shots is different from that obtained by placing real physical sources at the receiver locations; hence, the resulting image from these active shots would be different, in terms of illumination, from those in Figure 4.5. This is an important distinction between the imaging interferometric pseudo-shots and imaging actual shots placed at the receiver locations. We have to make this distinction because the physical sources in the experiment (Figure 4.2) do not constitute the closed surface required for equations 6.2 and 4.12 to hold.

Comparing the images in Figure 4.5 with the Sigsbee model in Figure 4.2, shows that the image from deconvolution interferometry (Figure 4.5a) provides a better representation of the subsurface structure than does the image from correlation interferometry (Figure 4.5b). The salt reflectors (top and bottom) are better resolved in in Figure 4.5a than they are in Figure 4.5b. Also, it is possible to identify subsalt sediment reflectors in Figure 4.5a which are not visible in Figure 4.5b. The reflectors in Figure 4.5a are well resolved because deconvolution interferometry successfully suppresses the drill-bit source function when generating pseudo-shot gathers (Figure 4.4). The image from deconvolution interferometry does not present severe distortions due to the spurious arrivals characteristic of deconvolution pseudo-shot gathers (Chapter 3). As discussed by Chapter 3, these spurious events typically do not map onto coherent reflectors on shot-profile migrated images like the one in Figure 4.5a. The image from correlation interferometry (Figure 4.5b) portrays a distorted picture of the Sigsbee structure (Figure 4.2) because the correlation-based pseudo-shot gathers are dominated by the power spectrum of the drill-bit excitation (Figure 4.4c; equation 6.2). The narrow-bandcharacter of the drill-bit source (Figures 4.3b, 4.4a and 4.4c) is responsible for the "ringy" appearance of the image in Figure 4.5b.

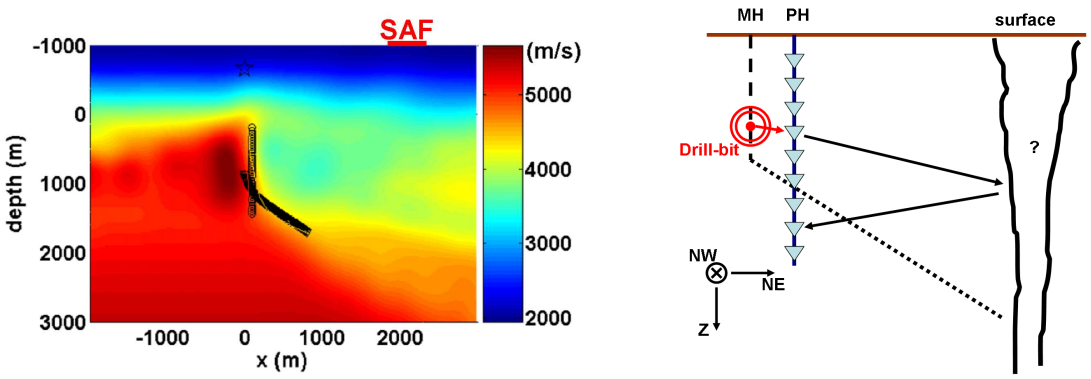

(a) (b)

Figure 4.6. Panel (a) shows the large-scale structure of the P-wave velocity field (velocities are colorcoded) at Parkfield, CA. The circles in (a) indicate the location of the sensors of the SAFOD pilot-hole array used for the recording of drilling noise. The SAFOD MH is denoted by the triangles. The location of the SAFOD drill site is depicted by the star. Depth is with respect to sea level, the altitude at SAFOD is of approximately -660 m. Panel (b) shows the schematic acquisition geometry of the downhole seismic-while-drilling (SWD) SAFOD dataset. Receivers are indicated by the light-blue triangles. The structures outlined by black solid lines to the right-hand side of the figure represent a target fault. As indicated by (b), receivers are oriented in the Z-(or downward vertical), NE- and NW-directions. (b) also shows a schematic stationary path between the drill-bit and two receivers. Both panels represent Southwest to Northeast (from left to right) cross-sections at Parkfield.

Drill-bit imaging technology based on pilot recordings (e.g., Rector and Marion, 1991; Haldorsen et al., 1994; Poletto and Miranda, 2004) provides images that are accurate representations of subsurface geology, such as the image in Figure 4.5a. In the context of SWD, deconvolution interferometry is an alternative processing methodology that does neither require an independent estimate of the drill-bit source function, nor any assumptions of wave propagation within the drill-string. We present the Sigsbee SWD numerical example with the intention of modeling a situation where pilot recordings are absent or would yield a poor representation of the drill-bit excitation. Our numerical example also demonstrates that deconvolution interferometry can also be used for passive drill-bit imaging, where no knowledge about the drill-bit position is required.

4.5 SAFOD drill-bit data

The San Andreas Fault Observatory at Depth (SAFOD) is located at Parkfield, CA. Its objective is to actively study the San Andreas Fault (SAF) zone from borehole data, as well as to monitor the fault zone activity. SAFOD consists of two boreholes, the Pilot-Hole (PH) and the Main-Hole (MH). The geometry of the PH and MH relative to the to surface trace of the SAF is displayed in Figure 4.6a. The data we analyze consists of the noise excited by the drilling of the MH, recorded by the 32-receiver array permanently placed in the PH. The geologic context of this experiment and the full interpretation of the results we show here, along with active-shot seismic data, are presented in Chapter 5. We focus here on the use of deconvolution interferometry to obtain an image of the SAF, and on the differences between the deconvolution- and correlation-based approaches in the processing of the SAFOD SWD data.

The main objective of the SAFOD borehole SWD experiment is to provide broad-

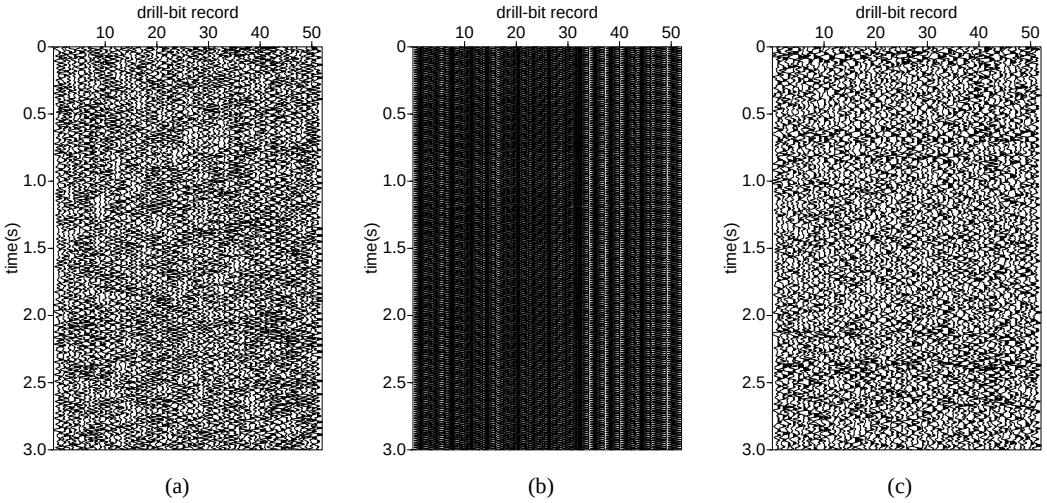

Figure 4.7. Drill-bit noise records from the SAFOD Pilot-Hole. Because the drill-bit is closest to receiver 26, the data recorded at this receiver, shown by panel (a), is not contaminated by electrical noise. For the same drill-bit position, panel (b) shows the data recorded at receiver 23. Panel (c) shows the result of filtering the electrical noise from the data in panel (b). These data show the first 3 s of the full records (which are 60 s long). For the records shown here, the drill-bit position is practically constant. These data are from the vertical component of recording.

side illumination of the SAF that is not possible from surface measurements. Figure 4.6b illustrates how single reflections from the SAF can potentially be recovered by the drilling noise records measured at the SAFOD PH array. The stationary path indicated by the red and black arrows in Figure 4.6b shows that the interference between the drill-bit direct arrivals with fault-scattered waves can be used to reconstruct primary fault reflections propagating between the receivers. Because the distance between the MH and PH is only in the order of 10 meters (Boness and Zoback, 2006), the drill-bit only gives stationary contributions to waves emanating from a given receiver when drilling next to that receiver. This is an important consideration in identifying which portion of the recorded data is useful for processing (see below).

The acquisition of the SAFOD PH drill-bit noise records began in June 2004, and continued until late August 2004 (Taylor et al., 2006). The MH intersected the PH on July 15$^{\text{th}}$ (Figure 4.6a). The drill-bit noise recorded after the MH crossed the PH is not of interest for our interferometry purposes because, unlike the drill-bit positions illustrated by Figure 4.6b, it does not yield stationary contributions that give primary fault reflections that propagate between the receivers. Due to field instrumentation issues (S. T. Taylor, 2006; personal communication), most of the data recorded by the PH array before July 15$^{\text{th}}$ consists of electrical noise only. A window of approximately 20 hours prior to the intersection of the PH by the MH coincides with the portion of the PH data for which the instrumentation problem was fixed. The data acquired within this window are used in the analysis we show here.

According to the MH drilling records, the depth interval that was sampled by the usable drill-bit data extends from approximately 350 m to 450 m (in the scale in Figure 4.6a). We use the data recorded in this interval to generate interferometric shot records. Within the 350-450 m bit interval, the drill-bit passes by the PH receiver 26.

Since the stationary contributions of the sources to recovering primary reflections from the SAF only occur when the bit is next to a receiver, the data recorded by receiver 26 in the depth interval of 350-450 m can be used as the filter for interferometry. This translates to setting $\mathbf{r}_B$ in equations 6.2, 4.12 or 4.13 to the coordinates of receiver 26. Hence, out of the 32 receivers of the SAFOD PH array, it is only possible to create interferometric shot gathers with a pseudo-source at receiver 26.

A small portion of the recorded data is shown in Figure 4.7. The data in Figure 4.7a are from the vertical component of receiver 26, while the data in Figures 4.7b and c correspond to receiver 23. Since the records shown in Figure 4.7 are subsequent recordings of the drill-bit noise of 1 minute duration (of which only the first 3 s are shown in Figure 4.7), the drill-bit position for the records in the Figure is practically constant. The data recorded by receiver 26 shown in Figure 4.7a are low-pass filtered to preserve signal up to 75 Hz. A similar filter, preserving frequencies up to 55Hz, is applied to the original data from receiver 23 in Figure 4.7b, resulting in the data in Figure 4.7c. The data recorded by receiver 23 (Figure 4.7b) is heavily contaminated by electrical noise, at frequencies of 60, 120 and 180 Hz. This electrical noise is practically negligible in the data from receiver 26, as shown by Figure 4.7 where the 60 Hz monochromatic oscillation cannot be seen. Because the bit is close to receiver 26, the drilling noise is louder than the electrical noise in Figure 4.7a. After low-pass filtering, the data from receiver 23 (Figure 4.7c) shows a similar character to that from receiver 26 (Figure 4.7a). As discussed in previous sections (and illustrated by Figure 4.3), the SAFOD drill-bit noise data shows a narrow-band character, typical of the vibrational modes from drilling. The drilling of the SAFOD MH was done with a roller-cone bit.

A critical issue with the processing of the SAFOD SWD data is that pilot records

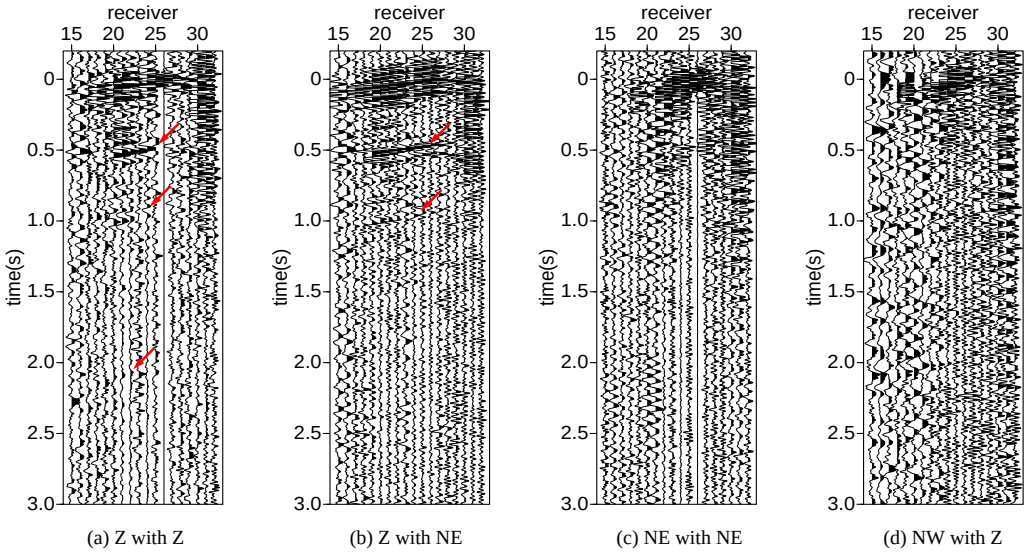

Figure 4.8. Pseudo-shot gathers from deconvolution interferometry. In these gathers, receiver 26 acts as a pseudo-source. Each panel in the Figure is the result of deconvolving different combinations of receiver components: the deconvolution of the Z- with Z-components yields (a), Z- with NE-components give (b), NE- with NE-components result in (c), and NW- with Z-components yield (d). Physically, panel (a) shows waves recorded by the vertical component for a pseudo-shot at receiver 26, excited by a vertical point-force. (b) is also the vertical component for a pseudo-shot at PH-26, but unlike the wavefield in (a), it represents waves excited by a point-force in the NE-direction. Likewise, (c) pertains to both excitation and recording in the NE-direction, while waves in (d) are excited by a vertical point-force and are recorded in the NW-direction. The red arrows show reflection events of interest. Note that receiver 32 is the shallowest receiver in the SAFOD PH array (Figure 4.6). Receiver spacing is of 40 m. The component orientations we use here are the same as those in Figure 4.6b.

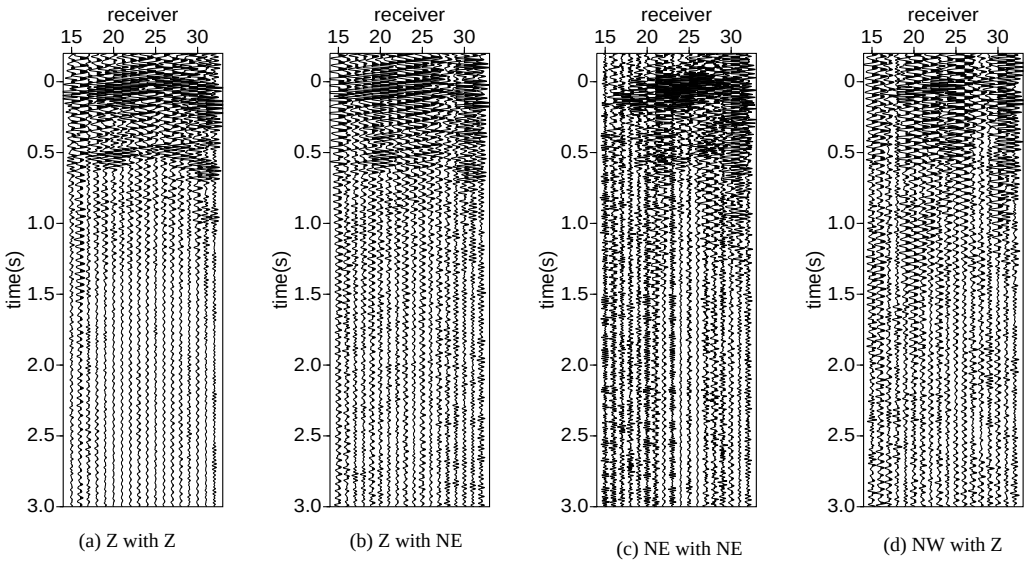

Figure 4.9. Pseudo-shot gathers from correlation interferometry. Here, each panel is associated to the correlation of the same receiver components as in the corresponding panels in Figure 4.8. The physical interpretation of excitation and recording directions is the same as for Figure 4.8. Unlike the data in Figure 4.8, the source function in these data is given by the autocorrelation of the drill-bit excitation.

are not available. Drill-string accelerometers were not placed in the SAFOD rig until August 2004 (Taylor et al., 2006), after the acquisition of the SAFOD PH data we process here. Since no pilot records are available, pilot-based SWD processing (Rector and Marion, 1991; Haldorsen et al., 1994; Poletto and Miranda, 2004) cannot be applied to the PH drill-bit data. Thus, these data are a natural candidate for the application of deconvolution interferometry. Figure 4.8 shows four pseudo-shot gathers derived from deconvolution interferometry using different combinations of receiver components (see equations 4.13 through 4.14). We only display the traces for receivers 15 through 32 in Figure 4.8 because electric noise in receivers 1-14 prevents the recovery of coherent signals. Before computing the pseudo-shots in Figures 4.8 and 4.9, all data were low-passed to preserve frequencies up to 55 Hz. For the interferometry, we divide each minute-long record into two 30-second long traces. With approximately 20 hours of recording time, the resulting traces in the pseudo-shot records are the result of stacking in the order of 2000 deconvolved or correlated traces (see equations 6.2 and 4.12). For a discussion on our numerical implementation of deconvolution, see Appendix A.

The panels in Figure 4.8 show that combining different components in deconvolution interferometry yields different waveforms. Scattered arrivals, indicated by red arrows, can be identified in Figures 4.8a and b, but not in c and d. The first reason for the difference between the results in the four panels of the Figure lies in equations 4.13 through 4.14. According to these equations, deconvolving data recorded in the i-component with data recorded by the j-component results in the interferometric impulse response recorded by the i-component and excited by the j-component. This means that the data in Figure 4.8a represents a vertical excitation at receiver 26 recorded by the vertical component at all receivers. Likewise, Fig-

ure 4.8b represents a vertical excitation and the recording of data in the Northeast direction (NE-component). Similar interpretations follow for the other two panels in the Figure, and are given in the Figure caption.

In Section 4.3.2, we discuss the influence of the drill-bit radiation properties on the radiation pattern of the pseudo-source synthesized by interferometry. The radiation characteristics of the pseudo-source together with signal-to-noise ratio in different recording components of the receiver away from the drill-bit (and from receiver 26) is also responsible for the differences between the panels of Figure 4.8. Because coherent arrivals can be seen in Figures 4.8a and b, two conclusions can be drawn. First, the signal-to-noise ratio in the vertical component (Z-component) of the receivers is sufficiently high to record scattered waves. Second, Figure 4.8a shows that the recorded drill-bit direct wave has nonzero polarization in the Z-direction. This is caused by the fact that the pseudo-source radiation is controlled by the radiation pattern of the bit (Section 4.3.2), and this case most of the energy radiated by the bit is polarized in the vertical direction.

Since Figure 4.8b shows coherent events (indicated by red arrows) that are reconstructed from energy recorded by the Northeast component, it follows that the direct-wave response from the bit excitation has a nonzero polarization component in the NE-direction as well. In these data, receiver 26 records drill-bit direct waves polarized both in the Z- and NE-directions because the receiver is in the bit's near-field (the PH and MH are a few meters apart). The measured near-field response to an excitation in the Z-direction (the drilling direction is close to vertical) is polarized both in the vertical and in-plane horizontal components (Aki and Richards, 1980; Tsvankin, 2001). The waves scattered from the SAF have far-field polarization because the fault zone is approximately 2 km away from the PH. The lack of scattered

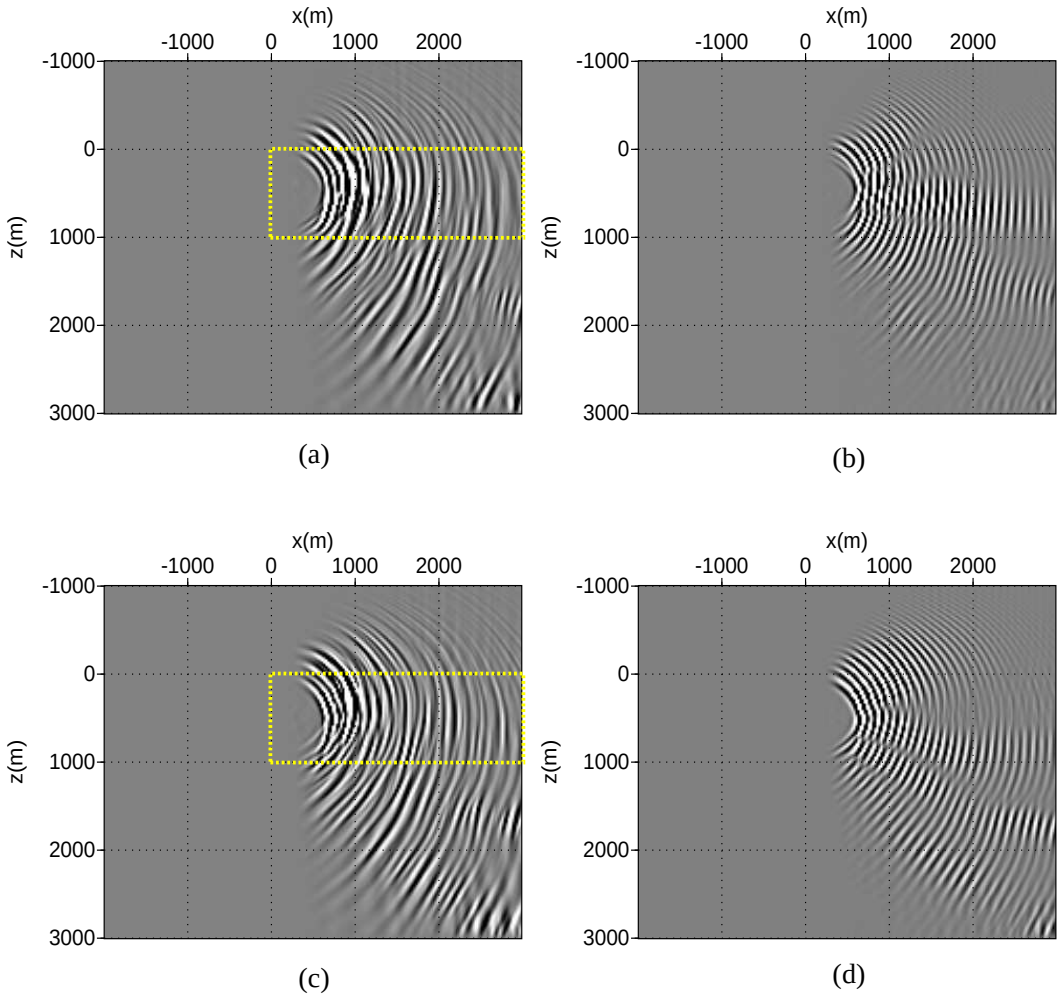

Figure 4.10. Shot-profile wave-equation images of interferometric shot gathers with a pseudo-source at receiver 26. The left panels are the result migrating pseudo-shot gathers from deconvolution interferometry while the panels on the right result from cross-correlation. The migration of the data in Figure 4.8a and b gives panels (a) and (c), respectively. Analogously, panels (b) and (d) are obtained from migrating the data in Figures 4.9a and b. The yellow boxes outline the subsurface area that is physically sampled by P-wave reflections. The data were migrated with the velocity model in Figure 4.6a.

signals in Figures 4.8c and d are mostly have a poor signal-to-noise ratio in the the Northeast and Northwest components (NE- and NW-components) of the receivers far from the bit.

The zero-offset trace (the trace at receiver 26) in Figures 4.8a and c is a band-limited delta function centered at $t = 0$. This is a demonstration of the deconvolution interferometry boundary condition in equation 4.15. The acoustic counterpart of this boundary condition generates introduces spurious arrivals in the pseudo-shot gathers (Chapter 5). In Figure 4.8a, we do not observe pronounced spurious arrivals associated with the scattered events (marked by red arrows). As highlighted in Section 4.3.2, the boundary condition in equation 4.15 does not have the same physical meaning as in the acoustic case (Chapter 3). A thorough understanding of the physical meaning of equation 4.15 is beyond the scope of this paper.

The pseudo-shot gathers in Figure 4.8 were generated by deconvolution interferometry while the ones in Figure 4.9 are the result of correlation interferometry (e.g., Wapenaar, 2004; Draganov et al., 2006). Analogously to the observations made in the previous Section, the correlation-based interferometric shot gathers (Figure 4.9) are influenced by the autocorrelation of the drill-bit source function, giving them a monochromatic appearance. The scattered events seen in Figures 4.8a and b cannot be identified in Figures 4.9a and b. In a more standard SWD processing routine, the autocorrelation of the source function could be removed from the data in Figure 4.9 by means of pilot deconvolution (Rector and Marion, 1991; Poletto and Miranda, 2004). We reiterate that this type of processing is not possible in our case because pilot records are not available.

Together with geologic information from the MH data and with an active shot acquired by sensors in the MH, in Chapter 5 we associate the event arriving with a

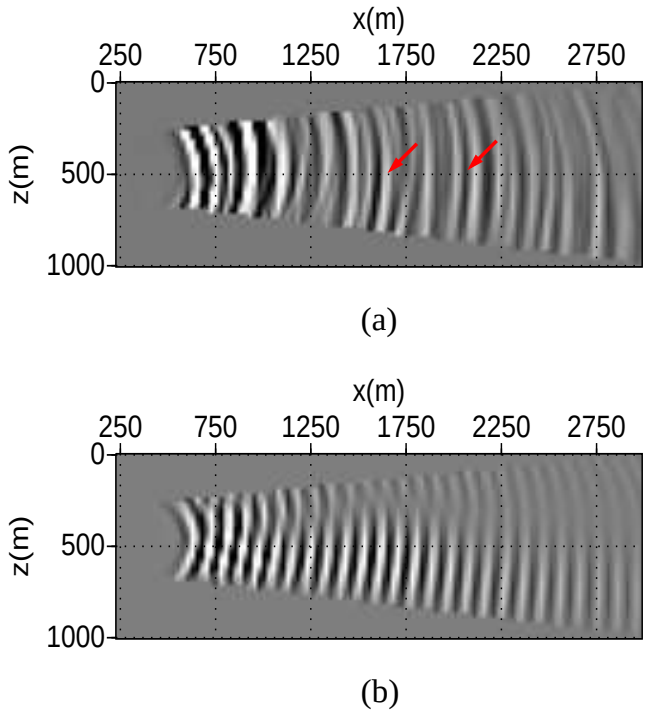

Figure 4.11. Final images from the interferometry of the SAFOD drill-bit noise recordings. The image in (a) is the result of stacking the images from deconvolution interferometry in Figures 4.10a and c. The right-hand side arrow shows the location of San Andreas Fault reflector. The other arrow highlights the reflector associated to a blind fault zone at Parkfield. The stack of the images from correlation interferometry in Figures 4.10b and d gives the image in (b). We muted the portion of the stacked images that is not representative of physical reflectors. The area of the image in (a) and (b) corresponds to the area bounded by yellow boxes in Figure 4.10.

zero-offset time of approximately $t = 1.0$ s (second arrow from top) in Figures 4.8a and b to the primary P-wave reflection from the SAF. The event at 0.5 s (marked by top arrow) is the reflection from a blind fault zone that was intercepted by the SAFOD MH (Solum et al., 2006; Boness and Zoback, 2006). The bottom arrow in Figure 4.8a indicates a an event with approximately 2.0 s of zero-offset time that whose slope is determined by shear-wave velocity. We interpret this arrival as a pure-mode shear-wave reflection from the SAF. Since only the pseudo-shots in Figures 4.8a and b present physically meaningful arrivals, we only show migrated images from these two panels.

The migration of the pseudo-shot data was done with the same methodology as in the Sigsbee numerical example. We use shot-profile migration by wavefield extrapolation (Biondi, 2006), where the extrapolation steps are taken in the horizontal coordinate away from the SAFOD PH (Figure 4.6). Migrated images are shown in Figure 4.10. The images of the pseudo-shots from deconvolution interferometry (left panels) show reflector-like features that cannot be identified on the images from correlation interferometry (right panels). The images from correlation-based pseudo-shots have a narrow-band character that is similar to that of the pseudo-shots themselves, caused by the presence of the autocorrelation of the drill-bit excitation function (Figure 4.9). This is the same phenomenon we show in the images from the Sigsbee model (Figure 4.5), with the difference that the Sigsbee images are produced from 100 pseudo-shots. Because the SAFOD images result from migrating a single shot, the reflectors are curved toward the edges of the images (top and bottom of images in Figure 4.10) due to effect of the migration operator and the relatively small aperture of the receiver array used to reconstruct the data.

The final image from the SAFOD SWD data was obtained by stacking the top

images with the bottom ones in Figure 4.10. We do this with the intention of enhancing the reflectors that are common in both images. The final SAFOD images are shown in Figure 4.11. Figure 4.11 only shows the portion of the images that yield physically meaningful reflectors, which is highlighted by the yellow rectangles in Figures 4.10a and c. The image from deconvolution interferometry (Figure 4.11a) shows reflectors that cannot be seen in the image from correlation interferometry (Figure 4.11b). In Chapter 3 we show that the reflector at $x \approx 2000$ m indicated by the right arrow coincides with the contact of the SAF with metamorphic rocks to the Northeast. The reflector at $x \approx 1600$ m coincides with a possibly active blind fault zone at Parkfield. The observations made in Chapter 5 are based on the data we present here together with active-shot data measured at the MH and with fault intersection locations from the MH (Solum et al, 2006; Boness and Zoback, 2006).

4.6 Discussion and conclusions

We present the method of interferometry by deconvolution, described by Chapter 3, as an alternative to the processing of seismic-while-drilling (SWD) data. In these types of datasets, the signature of the drill-bit source function complicates the recovery of the subsurface response (e.g., Poletto and Miranda, 2004). Most SWD processing methods rely on the so-called pilot sensors to obtain an independent estimate of the drill-bit excitation that is used to remove the drill-bit source function (Rector and Marion, 1991; Haldorsen et al., 1994; Poletto and Miranda, 2004). Here, we review SWD methods based on pilot recordings in the context of seismic interferometry by cross-correlations (e.g., Poletto and Miranda, 2004; Draganov et al., 2006). The method of deconvolution interferometry is capable of recovering the subsurface response from SWD data without the need for an independent estimate of the drill-bit

excitation. Additionally, the knowledge about the drill-bit position is not a requirement for the application of interferometry (see also Schuster et al., 2004), as it is for other SWD applications (e.g., Poletto and Miranda, 2004). Interferometry requires, however, that the drill-bit must sample the source stationary points that give rise to the target scattered waves (Chapter 3; Snieder et al, 2006).

Extending concepts presented by Chapter 3, we discuss the application of deconvolution interferometry in elastic media. With physical arguments we state that the interferometric response obtained by the deconvolution of the i-component of a given receiver by the j-component of another receiver results in single-scattered waves that propagate between these two receivers. These waves are the impulse response from a j-oriented point-force excitation at one of the receivers, recorded by the i-component at the other receiver. Because the deconvolved data satisfies the same wave equation as the original physical experiment, the radiation properties of the drill-bit (Poletto, 2005a) determine the radiation pattern of the pseudo-source synthesized by interferometry. In the case of receivers positioned far from the drill-bit and highly heterogeneous media, deconvolution interferometry can potentially extract a response that is closer to a full elastic response, as discussed by Wapenaar and Fokkema (2006).

Our numerical experiment with the *Sigsbee* model seeks to reproduce a passive subsalt SWD experiment where pilot recordings are absent. Using modeled drill-bit noise (Poletto, 2005a), we produce images of the Sigsbee salt canopy from the receiver array sitting below the salt. The image from deconvolution interferometry provides a reliable representation of the structure in the model because the deconvolution removes the drill-bit excitation function from the data. When distorted by the dominant vibrational modes of the drill-bit source function, the image from correlation interferometry gives a poorer representation of the model structure when compared

with the deconvolution image. The choice of the Sigsbee model shows the feasibility of the passive application of drill-bit imaging in subsalt environments. SWD typically is not done in such environments because the wells are deeper than they are onshore, and the transmission through the drill-string is weaker which makes rig pilot records unreliable estimates of the drill-bit excitation (Poletto and Miranda, 2004). Additionally, many subsalt wells are drilled with PDC bits, which radiate less energy than the roller-cone bit (Poletto, 2005a). The signal from PDC bits is thus difficult to measure from the surface or from the sea bottom. This difficulty can be overcome with downhole receiver arrays, as in our example. Although we used a model for a roller-cone bit, we expect results of deconvolution interferometry of noise records from PDC bits (Poletto 2005a) to be similar to ours .

Using field data acquired at the Pilot Hole of the San Andreas Fault Observatory at Depth (SAFOD), we validate the method of deconvolution interferometry in recovering the impulse response between receivers from drill-bit noise records. The SAFOD SWD data are ideal for the application of deconvolution interferometry because pilot recordings are not available. From interferometry by deconvolution, we synthesize scattered waves that propagate from receiver 26 toward the other receivers that are not visible in pseudo-shot gathers from correlation interferometry. Single-scattered P-waves were obtained mostly by the deconvolution of the vertical component of recording of the PH receivers, with the vertical and Northeast components of receiver 26. Shot-profile migration of the interferometric shots generated by deconvolution yield coherent reflectors. From the images presented here together with active-shot data and fault intersection locations from the MH, in Chapter 5 we identify the San Andreas Fault reflector as well as a possibly active blind fault at Parkfield, CA. Their conclusions rely on the processing we describe here, where interferometry by

deconvolution plays an important role in imaging the fault reflectors (Chapter 3).

More than just an alternative to processing SWD data as it is typically acquired, deconvolution interferometry opens possibilities for using passive measurements of drill-bit or rig noise for imaging. Poletto (2005b) provides a thorough comparison between drill-bit and conventional seismic sources. The fact that seismic interferometry techniques do not require knowledge about the source position allows for pseudo-acquisition geometries that cannot be accomplished by standard SWD experiments. The geometries in of the Sigsbee and SAFOD datasets presented in this paper are examples of non-conventional acquisition that can be treated by interferometric techniques. The use of the free-surface ghosts to reconstruct primary reflections that propagate between receivers (Schuster et al., 2004; Yu et al., 2004) is another example where deconvolution interferometry can also be applied. Interferometry of internal multiples (Chapter 6) can potentially be accomplished from SWD as well. The passive imaging from working drill-bits could help in the monitoring of fields in environmentally sensitive areas, where active seismic experiments are compromised. These areas now become more of a concern as the search for unconventional reservoirs increases. One such area is the Tempa Rossa field in Italy (D'Andrea et al., 1993). While active seismic activity in this field is hindered by environmental regulations, its future production is expected to reach 50000 oil barrels per day. Environment-friendly seismic monitoring of oil fields like Tempa Rossa could potentially be accomplished with recordings of the field's drilling activity and with deconvolution interferometry.

4.7 Acknowledgements

This research was financed by the NSF (grant EAS-0609595) and by the sponsors of the Consortium for Seismic Inverse Methods for Complex Structures at the

Center for Wave Phenomena. Tom Taylor (Duke University; presently at VS Fusion) provided us with the SAFOD data, and his help was vital in identifying which portion of the data could be used in our processing. Peter Malin (Duke University) gave us the orientations of the PH receivers. The velocity model we used to migrate the data was given to us by Andres Chavarria (P/GSI). The equipment and acquisition of the SAFOD SWD data were donated by Schlumberger. We thank Flavio Poletto for visiting CWP during the 2006 Sponsor Meeting, when he kindly shared his expertise in drill-bit noise processing with us. I.V. thanks Doug Miller and Jakob Haldorsen (both Schlumberger) for discussions about SWD processing and deconvolution interferometry.

Chapter 5

BROADSIDE IMAGING OF THE SAN ANDREAS FAULT[1]

5.1 Summary

The San Andreas Fault Observatory at Depth provides perhaps the most comprehensive set of data on the structure and dynamics of the San Andreas fault. We use two independent experiments recorded by the seismometer arrays of the SAFOD Pilot and Main Holes to resolve the localized structure of the San Andreas fault zone and of an intermediate fault zone at depth. From Pilot Hole recordings of the drilling noise coming from the Main Hole, we reconstruct the waves that propagate between the Pilot Hole sensors and use them to image the fault zone structure. The use of correlated drilling noise leads to a high-resolution image of a major transform fault zone. Another independent image is generated from the detonation of a surface explosive charge recorded at a large 178-sensor array placed in the Main Hole. The images reveal the San Andreas fault as well as an active blind fault zone that could potentially rupture. This is confirmed by two independent methods. The structure and the activity of the imaged faults is of critical importance to understanding the current stress state and activity of the San Andreas fault system.

[1]Submitted to Nature.

5.2 The SAFOD project

The San Andreas Fault Observatory at Depth (SAFOD) was conceived to closely study and monitor the earthquake dynamics and structure of the San Andreas Fault (SAF) at Parkfield, CA (http://www.icdp-online.de/sites/sanandreas/index/index.html). Characterizing the structure and dynamics of the SAF strike-slip system is crucial for understanding the geodynamics of transform plate boundaries and their associated seismicity. In particular, the SAF at Parkfield has historically been seismically active, with seven catalogued earthquakes of magnitude six approximately (Bakun and McEvilly, 1984; Roeloffs and Langbein, 1994); the latest one occurred in September 2004 (Kerr, 2006).

Consisting of a vertical borehole, the Pilot Hole (PH), and of a deviated well that intersects the SAF, the Main Hole (MH), SAFOD is designed to sample and monitor the SAF system from within the subsurface at Parkfield. Together with surface observations, data from SAFOD already contributed greatly to the understanding of the SAF system at Parkfield. Figure 5.1a is a scaled schematic cartoon that summarizes and connects results from several publications that analyze data from the SAFOD site. Much of the information on the surface geology and on the basement and sedimentary structures at Parkfield comes from geologic mapping (Rymer et al., 2003) and from surface refraction (Catchings et al., 2003) and reflection (Hole et al., 2001; Catchings et al., 2003) seismic data. The lateral delineation of the Salinian granite to the SW of the SAF has also been inferred from magnetotelluric (Unsworth et al., 2000; Unsworth and Bedrosian, 2004) measurements and from joint inversion of gravity and surface seismic data (Figure 5.1b; Roecker et al., 2004; and Thurber et al., 2004). Analysis of PH rock samples (Solum et al., 2004) and of their in-situ physical properties (Boness and Zoback, 2004) helped determine the lithology and

the stress state around the PH. Likewise, recent studies of rock samples from drilling (Solum et al., 2006) and well-logs (Boness and Zoback, 2006) from the MH have shed light on the subsurface geology along the SAFOD MH. It was not until 2006 that the SAFOD MH first intersected the SAF (Figure 5.1a), and the upcoming coring of the SAF system during the Phase 3 drilling of the MH (summer 2007) promises to bring important information on the internal composition of the SAF.

Previous to the drilling of the SAFOD MH, microseismic events along with surface active-shots recorded at the PH seismometer array were used to make some of the first images of the SAF at depth (Chavarria et al., 2003) which also contributed much to our understanding of the subsurface geology at Parkfield (Figure 5.1a). As a continuation of the subsurface imaging at Parkfield, we use drilling noise recorded at the PH and an active-shot experiment recorded at the SAFOD MH to obtain high-resolution images of the SAF system between depths of 0 to approximately 1.5 km (from sea level; this corresponds to approximately 0.6 to 2.1 km from the surface). These images help to resolve the wave-scattering structures associated to the SAF as well as at least one other heavily faulted zone between the SAFOD drilling site and the SAF. Images such as the ones we present here are critical for the development of detailed models of the SAF plate and earthquake dynamics.

5.3 Imaging the SAF from passive and active seismic data

The SAFOD data we use were acquired in two experiments. The first experiment was carried out in July 2004, when the SAFOD PH receiver array (Figure 5.1b) was switched on to constantly monitor the drilling noise during the early stages of the drilling of the SAFOD MH. We used the drill-bit noise recordings of the SAFOD PH array to create an image of the SAF. In a second independent experiment, conducted

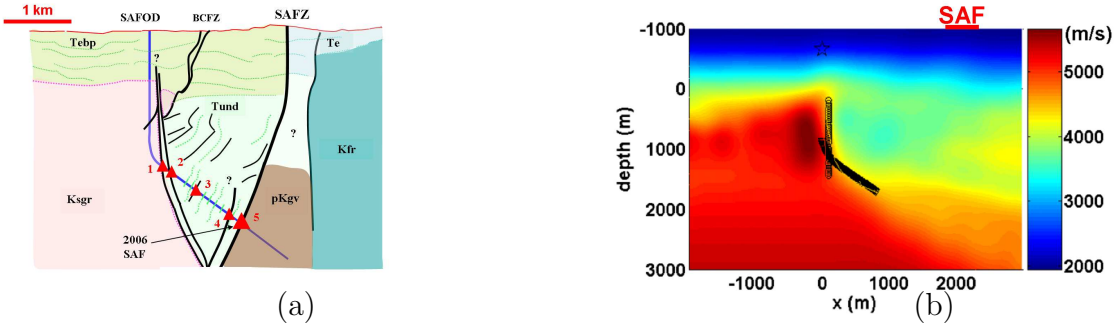

(a) (b)

Figure 5.1. Panel (a) shows our current knowledge of the structure of the San Andreas fault system at Parkfield, CA. The main geologic formations are indicated by different colors and by their corresponding acronyms, these are: the Tertiary Ethegoin (Te), Tertiary Ethegoin-Big Pappa (Tebp), Tertiary undifferentiated (Tund), Cretaceous Franciscan rocks (Kfr), Cretaceous Salinian Granite (Ksgr), and the pre-Cretaceous Great Valley (pKgv). The SAFOD main-hole (MH) is indicated by the blue solid line. Black solid lines in (a) represent faults. BCFZ refers to the Buzzard Canyon Fault zone. The areas where the finer-scale structure of the SAF system were unknown are indicated by question marks. The red triangles, numbered 1 through 5, show approximate locations of intersections of the MH with major zones of faulting (Solum et al., 2006). Triangle number 5 represents the point where the MH penetrated the SAF in 2006. Panel (b) shows the large-scale structure of the P-wave velocity field (velocities are colorcoded) that approximately corresponds to the schematic representation in (a). The circles in (b) indicate the location of the sensors of the SAFOD pilot-hole array used here for the recording of drilling noise. The SAFOD MH array, used in the active-shot experiment, is indicated by the triangles. The location of the active shot is depicted by the star. Depth is with respect to sea level, the altitude at SAFOD is of approximately −660 m.

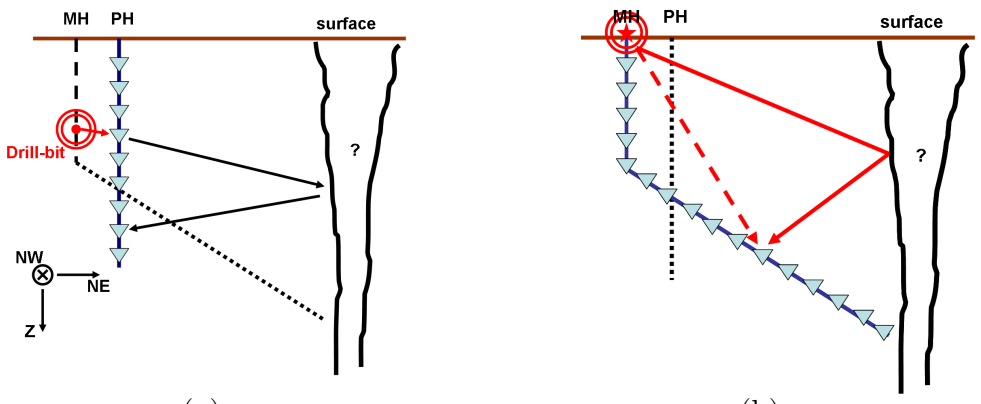

(a) (b)

Figure 5.2. Schematic acquisition geometries of SAFOD data. Receivers are indicated by the light-blue triangles. The structures outlined by black solid lines to the right-hand side of the figure represent a target fault. (a) shows the acquisition geometry of the downhole seismic-while-drilling (SWD) dataset. It consists of multiple 60 second-long recordings of drill-bit noise excited at different depths, recorded at 32 3-component receivers in the PH. As indicated by (a), receivers are oriented in the Z-(or downward vertical), NE- and NW-directions. (a) also shows a schematic stationary path between the drill-bit and two receivers. Interferometry recovers only the portion of the propagation path represented by black arrows in (a). The active-shot geometry in (b) is comprised of 178 3-component receivers placed in the MH. The dashed red arrow in (b) represents all waves that propagate towards the NE (right-hand side of the figure), while the solid red line represents all waves going toward SW (left-hand side of (b)). The inclination of the deviated portion of the MH is of about 45° with respect to the vertical. The receiver components of the SAFOD MH array are co-oriented with those of the PH array, whose orientations are shown in (a).

in 2005, a large 178-receiver array was placed in the SAFOD MH (Figure 5.1b) to record the active shooting of an 80-pound explosive charge placed at the surface near the SAFOD MH. We also used this shot record to image the SAF. These two experiments differ not only on the geometry of the data acquisition (i.e., source and receiver positioning), but also in the physical character of the excitation that generates the recorded waves. To account for the differences between the PH and the MH data, we applied different processing to each dataset and to subsequently produce the images. Figure 5.2 provides schematic representations of the data acquisition geometry for the PH drill-bit noise recordings and for the MH active-shot experiment.

To create an image of the SAF zone from the drill-bit noise records we rely on the concept of seismic interferometry (Curtis et al., 2006; Larose et al., 2006). Interferometry recovers the response between any two receivers in an arbitrarily heterogeneous and anisotropic medium as if a source was placed at one of the receiver locations(Lobkis and Weaver, 2001; Snieder et al., 2006). We only briefly highlight the issues of interferometry that are of particular concern to the processing of the SAFOD PH drilling noise records.

Typically, interferometry makes use of cross-correlations between recorded data to recover waves propagating between receivers (Lobkis and Weaver, 2001). By doing so, the recovered receiver response includes an average of the power spectra of the excitations(Lobkis and Weaver, 2001, Snieder et al., 2006). Removing the contribution of the source power spectrum is an issue when recovering signals from drill-bit noise because in this case the wave-generation mechanism is constantly active, and the spectrum is heavily dominated by specific vibration modes associated to the drilling process (Poletto and Miranda, 2004). An example of this behavior from SAFOD PH-array records can be found in Figure 5.4a.

It is possible, however, to remove the drill-bit source signature from drilling noise records (Poletto and Miranda, 2004). The standard industry practice is to estimate the drill-bit signature by placing accelerometers on the drill-stem (Poletto and Miranda, 2004; Rector and Marion, 1991). This estimate is then used to extract the drill-bit noise signature from the cross-correlations of the recorded data, leaving only the approximate impulse response of the Earth (Lobkis and Weaver, 2001; Poletto and Miranda, 2004). Following this accelerometer-based approach, drill-bit imaging has been previously applied to surface recordings of MH drilling noise at Parkfield (Taylor et al., 2005). In our case, such accelerometer recordings are not available. As an alternative to interferometry by cross-correlations, we used an interferometry technique based on deconvolutions (Chapter 3). This technique synthesizes the response between receivers from incoherent excitations as if one of the receivers acted as a pseudo-source, while canceling the effect of the drill-bit source signature without the need for drill-stem accelerometers.

In Figure 5.3a we show the result from processing approximately 17 hours of drilling noise records into a shot record with a pseudo-source at receiver PH-26. With the pseudo-source centered at 0 s, PH-26 acts as the pseudo-shot responsible for the excitation of waves (Chapter 3). Figure 5.3a shows the direct wave that propagates from receiver PH-26 and is recorded at the other receivers. The reflection events highlighted in Figure 5.3a are caused by faults in the SAF system. The data in Figure 5.3a represents waves excited by a vertically-oriented force (see Figure 5.4). In addition, we are also able to recover the excitation at receiver PH-26 associated to a Northeast-oriented force (see Figure 5.4c). The SAFOD interferometric image we will discuss here is a product from imaging the pseudo-shots at PH-26 excited by forces oriented both in the vertical and in the Northeast (NE) directions.

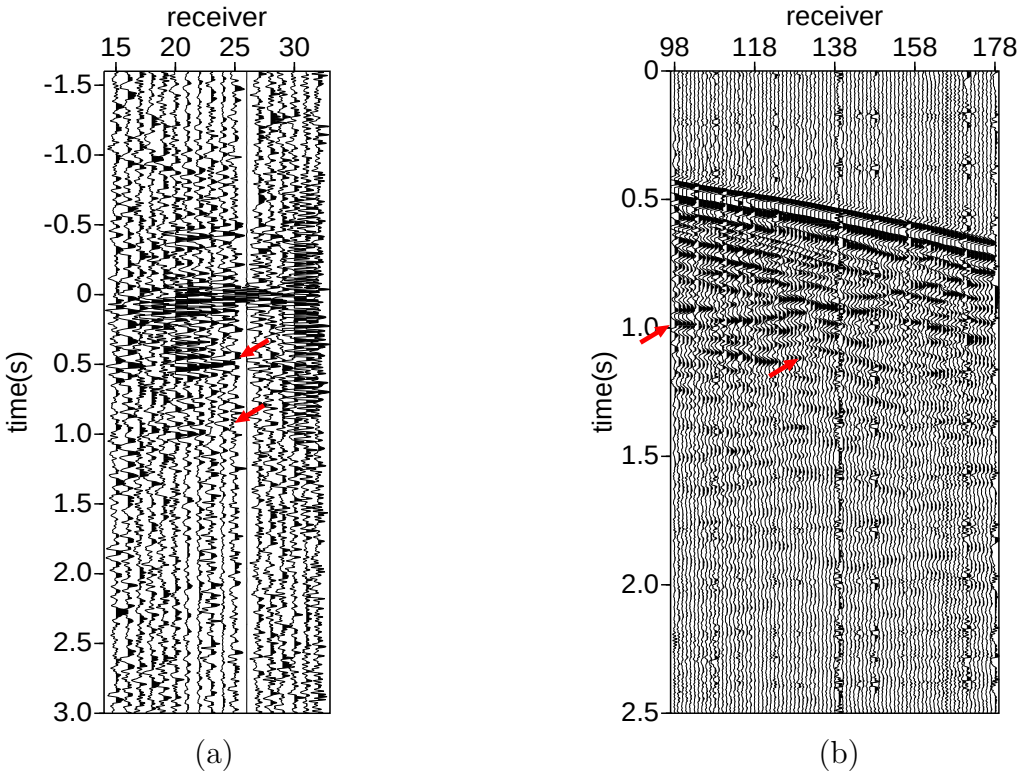

(a) (b)

Figure 5.3. (a) Vertical component of the interferometric shot gather for a pseudo-shot position at pilot-hole receiver PH-26. Red arrows indicate reflections of interest. The reflection event that arrives at approximately 1.0 s at receiver PH-24 is interpreted to correspond to a P-wave reflection from the SAF zone. Due to the noise levels, only a subset of the 32 receivers of the PH array is sensitive to the incoming signals from the SAF zone. (b) Data recorded by the vertical component of motion in the SAFOD MH array from the active-shot experiment. The red arrows indicate two left-sloping events that are associated to P-wave reflections from faults within the SAF system.

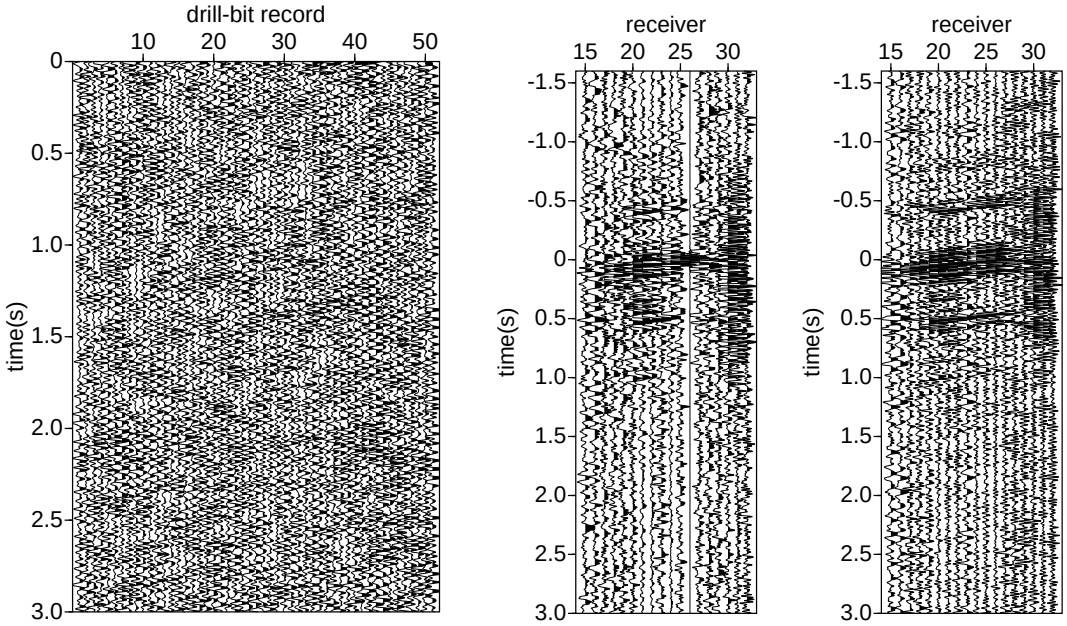

(a) (b) (c)

Figure 5.4. (a) Short samples of sequential recordings of drilling noise from the receiver PH-26. The visually monochromatic character of the records is due to drilling vibrational modes. (b) Vertical component of the interferometric shot gather for a pseudo-shot position at pilot-hole receiver PH-26. The recording at (b) represents waves excited by a vertical point-force. (c) is also the vertical component for a pseudo-shot at PH-26, but unlike the wavefield in (b), it represents waves excited by a point-force in the NE-direction. The complicated character of the drilling noise in (a) is attenuated by the interferometry procedure that produces the data in (b) and in (c). Note that receiver PH-32 is the shallowest receiver in the SAFOD PH array (see Figure 1b in main text).

Unfortunately, out of almost two months of recording drilling noise at the PH array, only about a day and a half of the data is useable for interferometry purposes due to data acquisition problems. Within this time window, the drill-bit is closest to receiver PH-26 (the distance between the MH and PH at that depth is of only a few meters). It is at this drill-bit position that we find the most prominent contribution from the waves excited by the drill-bit for the reconstruction of the waves that propagate between receiver PH-26 and the remaining receivers. We refer to this point as a stationary position for the drill-bit source (Snieder et al., 2006). To recover signals propagating between receivers, it is necessary to have physical sources at the stationary points that link a pair of receivers to a target reflector (Snieder et al., 2006). The only drill-bit stationary point sampled within the good-quality PH records recovers waves that emanate from receiver PH-26. This restriction limits the area of the SAF zone from which we can produce a physically meaningful image to the area shown in Figure 5.6a.

The shot gather from the SAFOD MH active-shot experiment (Figure 5.3b) shows a reflection as a left-sloping event arriving at main-hole receiver MH-98 at approximately 1.0 s (indicated by the top-most arrow). Another weaker left-sloping event that arrives at approximately 1.2 s at receiver MH-98 (lower-most arrow) is associated with a P-wave reflection from the SAF zone. Since the receivers MH-98 to MH-178 are in the deviated, deeper-most portion of the SAFOD MH (see Figure 5.1b), right-sloping events are mostly associated with right-going waves, whereas left-sloping events are associated with left-going waves (see also Figure 5.2b). This observation only holds for a subset of the receivers of the large 178-receiver MH array: the ones which lie in the deviated portion of the MH. These would be receivers MH-98 through MH-178 (Figure 5.3b), whose locations are shown in Figure 5.1b. For the purpose

of imaging the SAF system from the MH array, it is important to discern between right- and left-going waves in the data because fault reflection information for this acquisition geometry is predominantly contained in left-going waves. With frequency-wavenumber filtering (Biondi, 2006), we extract only the left-sloping events from Figure 5.3b. We use only these events to image the SAF zone.

The process of mapping data such as in Figure 5.3 into a subsurface image (Figure 5.6) is what we refer to as *imaging* or *migration*. Imaging typically requires a velocity model of the subsurface; the one we use is shown in Figure 5.1b. This model was estimated from surface seismic tomography (Thurber et al., 2004). We do the imaging of the PH and MH data (Figure 5.3) with two different methodologies. For imaging from the PH data we use the technique of shot-profile migration by wavefield extrapolation (Biondi, 2006). The wavefield extrapolation is done by the split-step fourier phase-shift plus interpolation method. The MH active-shot data in Figure 5.3b is imaged by *reverse-time migration* (Biondi, 2006).

5.4 High-resolution images and the SAF

The images from the SAFOD PH and MH arrays are shown in Figures 5.6a and b (also in Figures S3a and b). The interferometric image from PH array (Figures 5.6a and S3a) provides a different area of "illumination" of the subsurface than the active-shot image from the MH array (Figures 5.6b and S3b). This is a consequence of the differences in the acquisition geometry of these two experiments. The images displaying all subsurface positions corresponding to the velocity model in Figure 5.1b are shown in the support Figure 5.5. A numerical model was build for the MH active-shot data to aid us in understanding what is the subsurface area that could be illuminated by the active-shot experiments, as well as what would be the character of

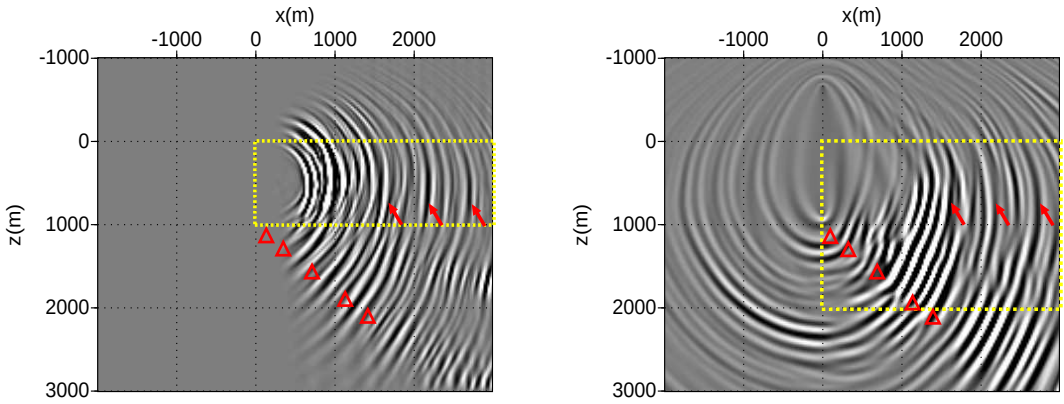

(a) (b)

Figure 5.5. (a) Image obtained from stacking the results of migrating the SAFOD interferometric shot gathers in Figures S5.4c and d. After migrating only the left-going waves from the SAFOD MH active-shot data (Figure 2b in main text), we obtain the image in (b). The red arrows point to features that are common to both images. These features are the same as indicated by the red arrows and numbers 1 through 3 in main-text Figure 3. The dashed yellow boxes in (a) and in (b) highlight the portions of the images that are shown in main-text Figures 3a and 3b, respectively. Both yellow boxes in fact represent the subsurface area that is physically sampled by P-wave reflections, which in turn depends on the acquisition geometry of each experiment (see Figure S5.2). The red triangles show the approximate locations where the SAFOD MH intersected major fault zones (see main text Figure 1b). Distances in the x-axis in (a) and (b) are with respect to the location of the SAFOD drill site at the surface. The surface trace of the SAFz is at approximately $x = 2000$ m.

image artifacts caused by waves diffracted by the Salinian granite. From the portion of the synthetic image that showed physically meaningful reflectors we chose the area of illumination of the SAFOD MH image in Figure 5.6b. The support Figure 5.7 shows the results from the numerical modeling of the SAFOD MH active-shot data.

Since both images are built from single-shot data (a pseudo-shot in the PH interferometric data and the active-shot in the MH data), they are prone to artifacts associated with the limited illumination (Biondi, 2006). Additionally, the method of interferometry by deconvolutions may produce image artifacts (Chapter 3). It is thus critical to establish which reflectors in the images in Figure 5.6 (and in Figure 5.5) pertain to actual faults or interfaces in the subsurface.

We rely on two independent criteria to gain insight into which reflectors in Figure 5.6 (and in Figure 5.5) represent real faults and/or interfaces. The first criterion is based on the consistency of events between different images. Note that all of the available images were generated from independent experiments. In our case, on one hand we have the drilling noise recordings at the PH array, and on the other hand we have the the active-shot MH data. The images from Chavarria et al. (2003) (Figure 5.6) come from PH recordings of both surface active shots and microseismicity from the SAF. Not only were the data in these three experiments different, but also the corresponding images were generated by distinct methodologies. Consequently, reflectors that are consistent in two or more images are likely to be representative of actual subsurface structures.

The second criterion for interpreting reflectors in Figure 5.6 is the correlation between the location of fault zone intersections at the SAFOD main-hole (Solume et al., 2006) and the position of reflectors which are consistent in two or more images. The position of the five main fault zones intersected by the MH are shown schemat-

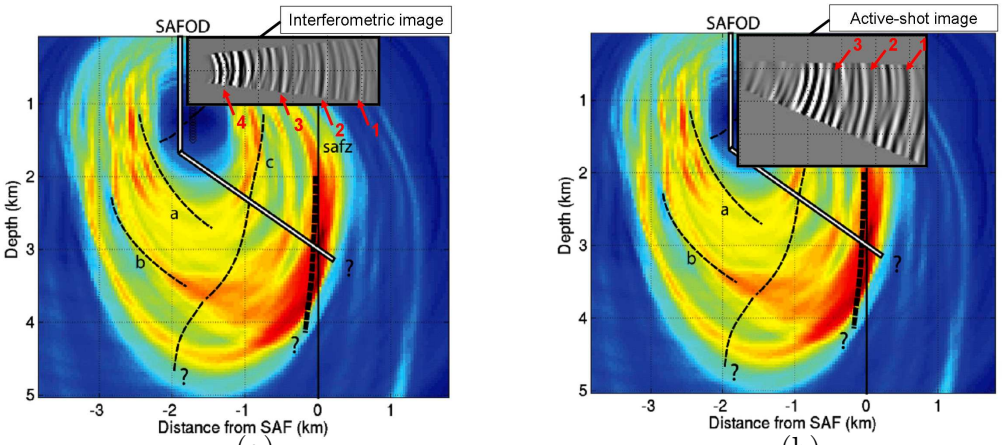

Figure 5.6. Images from the drill-bit noise recordings and from the active-shot experiment (in grey-scale, outlined by black-boxes). These images are overlayed on the result obtained from Chavarria et al. (2003). The overlay in (a) is the interferometric image from the SAFOD PH array, compiled after synthesizing drilling noise records into a pseudo-shot at the location of receiver PH-26. (b) shows an overlay of the image obtained from reverse-time imaging of the active-shot recorded at the SAFOD MH. The arrows mark the most prominent reflectors in the images. The reflectors numbered 1 through 3 coincide in both images. Reflectors 2 and 3, and possibly 4 are associated with fault zones. The SAF zone is visible at reflector 2 in both images. The location of the SAFOD MH in the background color images is schematic, since the MH was drilled after the work by Chavarria et al. (2003) was published. See also Figures S3a and S3b for the full images from the drill-bit noise recordings and active-shot data.

ically in Figure 5.1a and are superposed on the full images from the SAFOD PH and MH arrays in the support Figure 5.5. The comparison between MH fault intersections (Solum et al., 2006;Boness and Zoback, 2006) and reflectors in the images (Figure 5.5) is not always straight forward because the subsurface area illuminated by the images does not coincide with the MH well-path. Despite this difficulty, we provide our interpretation of the correlation between the MH fault intersections and imaged reflectors based on the overlay of these data (Figure 5.5) and on our current conceptual geologic model of the subsurface at SAFOD (Figure 5.1a).

In the interferometric image from the PH drilling noise records (Figure 5.6a) we highlight four distinct reflection events. The events 1 through 3 coincide both in the interferometric and active-shot images (Figures 5.6a and b, respectively; see support also Figure 5.5). Reflector 2 (Figure 5.6) is associated with the SAF, because its lateral position coincides with the lateral position of the surface trace of the SAF (marked by a vertical solid line at 0 km in the background images in Figure 5.6). In both the PH and MH images, the position of reflector 2 is consistent with the scattering zone associated with the SAF zone from Chavarria et al. (2003). Even though our images of the SAF (reflector 2, Figure 5.6) do not illuminate the fault all the way to its point of intersection with the SAFOD MH, the change in dip of the SAF in the active-shot image at approximately 1100 m depth is consistent with the intersection of the MH with fault zone 4 (Figures 5.1a and S3b). Since the anomaly that represents the SAF in the image by Chavarria et al. (2003) is caused by direct-wave energy coming from microseismicity within the SAF, the relative positioning between the SAF reflector in the MH active-shot image and the corresponding reflector in the background image suggests that reflector 2 may be due to P-wave energy scattered at the contact of the Franciscan rocks to the NE with the SAF zone to the SW

(Solum et al., 2006; Boness and Zoback, 2006). The PH interferometric and MH active-shot images resolve structures larger than approximately 75 to 100 m in size, presenting higher resolution when compared to the previous images of the SAF at Parkfield (Hole et al., 2003; Chavarria et al., 2003). The geometry of our experiments (especially of the PH drill-bit records) is ideal for the broad-side imaging of the SAF, complementing the previous Parkfield experiments (Hole et al., 2003; Chavarria et al., 2003).

Although the reflector 1 is consistent between the PH interferometric image and the MH active-shot image, we do not associate it to any known faults. The reason for this is that there is no surface trace of a fault at the location of reflector 1; nor has a major fault zone yet been intersected by the SAFOD MH after the SAF. If reflector 1 is indeed an artifact produced from the imaging procedures applied to both the PH and the MH data, it was not reproduced by the numerical modeling of the SAFOD MH data. Since the modeling in Figure 5.7 was acoustic (accounting only for P-wave propagation), reflector 1 could be due to erroneous imaging of recorded P-to-S converted waves. Note that our imaging procedures also assume that the medium is acoustic, so any recorded converted waves will be imaged as artifact reflectors placed farther than their P-wave counterparts. This, we believe, is what happens to reflector 1; a P-to-S converted reflection perhaps related to the SAF P-wave reflector at reflector 2 (Figure 5.6).

The fact that reflector 4 can only be seen in the PH interferometric image is not necessarily inconsistent with the MH image because even if the reflector pertained to a physical event, its location makes it mostly invisible for the MH active-shot image (the reflector is located between the shot and most of the receivers in the MH array). The location of reflector 4 in Figure 5.5a suggests a possible correspondence with the

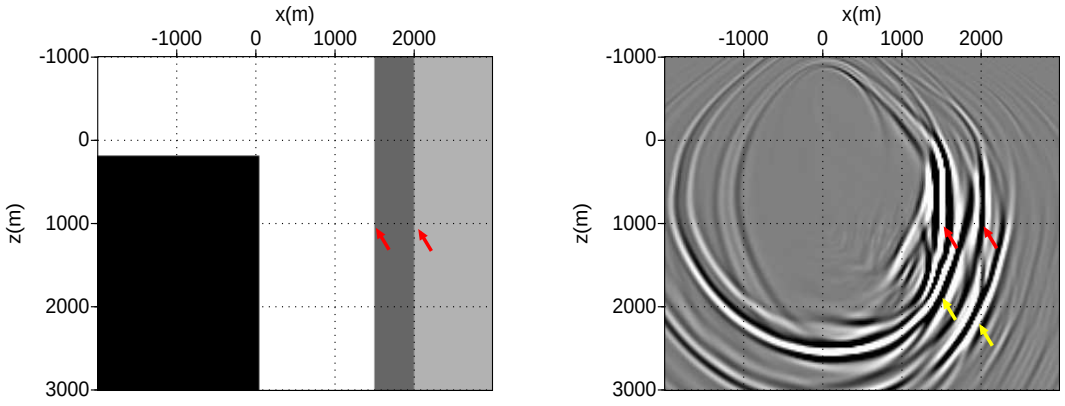

(a) (b)

Figure 5.7. Acoustic numerical modeling of the SAFOD MH active-shot data. (a) shows the structure of the reflectivity model used to generate the synthetic data. The velocity model used is the same as the one used for imaging (Figure 1b in main text). The black block in the reflectivity model in (a) represents the Salinian granite (see Figure 1a in main text), whereas the grey structures to the left of the model generate two vertical fault-like features. After applying the same imaging procedure as for the field SAFOD MH data (Figure 5.5), we end up with the image in (b). The red arrows mark the position of the target reflectors both in the model (a) and in the image (b). The reflections of waves generated by the diffraction of energy in the corner of the granite block appear as image artifacts (marked by yellow arrows). Without the numerical model, these artifacts could potentially be misinterpreted as dipping fault structures. The objective of the numerical modeling is not to closely replicate all features of the data (Figure 2b in main text). Instead, the objective of the model is two-fold: it helps us understand which portion of the subsurface is "illuminated" by P-wave reflections in the active-shot experiment, and it gives us an idea of how P-waves that are diffracted and/or guided by the granite structure may appear in the image.

SAFOD MH intersection with fault zone number 2 (Figures 5.1a and S3a). If such a correspondence is true, then reflector 4 is likely to represent the contrast between the Salinian granite and the sediments, which is bordered by fault zone 2 (Figure 5.1a).

Reflector 3 in Figure 5.6 is also associated with a fault zone. It is present in both the PH interferometric and in the MH active shot images, and its location coincides with the scattered energy observed by Chavarria et al. (2003) in their P-wave migration images (see Figure 3C and 3B of their paper). We associate this reflector with fault intersection number 4 (Figure 5.1a) in the SAFOD MH array (Solum et al., 2006; Boness and Zoback, 2006). The location of the fault intersection is close to the portion of the fault illuminated by the MH active-shot image (see Figure 5.5b). Also, the fault image dips in the SW direction towards the point of intersection between the SAFOD MH and fault number 4 (Figures 5.1a and S3b). The location of this fault zone at reflector 3 coincides with a well-resolved localized cluster of microseismic events detected both by surface records (Nadeau et al., 2004) and by the PH array (Oye et al., 2004). The images in Figure 5.6 show considerably higher resolution than the previous images from Chavarria et al. (2003) in imaging the intermediate fault zone corresponding to fault number 4 (Figure 5.1a). The imaging of this intermediate fault zone (and its subsequent intersection at the SAFOD PH) is important to the understanding of the structure of the SAF system, especially because there is no trace of this fault system at the surface. Since it is a blind fault (Yeats and Hutfile, 1995; Talebian et al., 2004), determining the activity status of fault 3 is critical in assessing its seismogenic risk. The existence of this feature interpreted from two independent observations provides the basis for a better fault zone understanding and its hazard assessment. Unknown blind faults have been the cause of major fatal earthquakes, such as the 1994 Northridge earthquake (Yeats and Hutfile, 1995) and

the 2003 Bam earthquake in Iran (Talebian et al., 2004).

The dip of the SAF reflector and of the intermediate fault reflector support the interpretation of the SAF system being structurally characterized by a flower structure (Figure 5.1a). Previous surface seismic profiling also suggested the presence of intermediate fault zones (Hole et al., 2001) such as the one confirmed here. It remains to be understood whether this intermediate faulting is associated with the same flower structure as the SAF, potentially representing an earlier trace or an active branch of the SAF, or if these secondary faults belong to a separate flower structure (Chavarria et al., 2003). According to Solum et al. (2006), well casing deformation was only observed at fault intersection 5 (associated to the SAF, Figure 5.1a). The other four fault zones showed no signs of fault activity since so far there was no casing deformation associated to them. If the imaged intermediate fault zone (reflector 3, Figure 5.6) is indeed an inactive fault zone, it might well represent an earlier trace of the SAF. On the other hand, the clusters of microseismic activity previously observed (Nadeau et al., 2004; Oye et al., 2004) are likely associated to the imaged blind fault zone (reflector 3, Figure 5.6), which suggests that this fault zone is likely to be an active part of the current SAF system.

Other important factors for understanding fault activity and seismogenic potential are fault zone mineralogy, fluid content and pore-pressure. It has been previously suggested that there may be high-pressured fluids within the SAF zone at Parkfield (Unsworth et al., 2000; Unsworth and Bedrosian, 2004; Chavarria et al., 2003). Both the SAF reflector and reflector 3 in Figure 5.6 are consistent with the lateral positioning of the known low resistivity anomaly inferred by magnetotelluric soundings at Parkfield (Unsworth et al., 2000; Unsworth and Bedrosian, 2004). Indeed, the analysis of the inferred fault material from the SAF and from the imaged interme-

diate fault zone (Solum et al., 2006) shows a high concentration of clay minerals, which are typically associated with low resistivity materials and with fluid-rich rocks. Furthermore, the analysis of rocks from the deeper SAF Solum et al. (2006) also showed the presence of serpentine, a mineral that could potentially generate fluid seals within the SAF leading to the creation of high-pressured fluid pockets inside the fault (Unsworth et al., 2000; Unsworth and Bedrosian, 2004). From the available seismic data, it is not yet possible to determine if the observed fault reflections are caused by fault-trapped fluids, by the contrast in material properties across the faults (Solum et al., 2006) or by a combination of these factors.

Nonetheless, the understanding of the structure of the SAF system has gained much from the imaging from the PH drill-bit noise and the MH active-shot experiments conducted at SAFOD. Our current images from these experiments not only provide better resolution in the structural definition of the faults within the SAF, but were also played a decisive role in the characterization of a blind fault zone between the SAFOD PH and the SAF. The high-resolution structural characterization of the SAF system is critical to the understanding of fault-growth and earthquake mechanics at Parkfield. The results we present here prove that imaging from noise can be crucial for illuminating complex fault zones in areas where observations from active experiments are insufficient. With the help of further continuous coring and analysis of fault material from the SAFOD MH Phase 3 drilling (to be conducted Summer 2007), the nature of the observed fault reflections will be perhaps better understood.

5.5 Acknowledgements

This research was supported through grant EAS-0609595 of the NSF. We also acknowledge the partial support of the sponsors of the Seismic Inverse Methods for

Complex Structures consortium at the Center for Wave Phenomena, Colorado School of Mines. Schlumberger donated the equipment and funds for the acquisition of PH drill-bit data. Paulsson Geophysical Services, Inc. (P/GSI), acquired and donated the MH active-shot data. We thank Peter Malin (Duke University) for intermediating the data exchange, and for providing the orientation of the Pilot Hole receivers.

Chapter 6

TARGET-ORIENTED INTERFEROMETRY – IMAGING INTERNAL MULTIPLES IN SUBSALT VSP DATA[1]

6.1 Summary

Seismic interferometry has become a technology of growing interest for imaging borehole seismic data. We demonstrate that interferometry of internal multiples can be used to image targets above a borehole receiver array. We use an interferometry technique, based on representation theorems for perturbed media, that targets the reconstruction of specific primary reflections from multiply reflected waves. In this *target-oriented* interferometry approach, we rely on shot-domain wavenumber separation to select the directions of waves arriving at a given receiver. We provide a description of this method along with two conceptual applications, and compare it to other approaches to seismic interferometry. Using a numerical Walk-Away VSP experiment recorded by a subsalt borehole receiver array in the *Sigsbee* salt model, we use the interference of internal multiples to image the salt structure from below. In this numerical example, the interferometric image that targets internal multiples reconstructs the bottom and top salt reflectors above the receiver array, as well as subsalt sediment structure between the array and the salt. Because of the limited source summation in this interferometry example, the interferometric images show artifact reflectors within the salt body. We apply this method to a field Walk-Away

[1]Submitted to Geophysics.

VSP from the Gulf of Mexico. With the field data, we demonstrate that the choice of shot-domain wavenumbers in the target-oriented interferometry procedure controls the wavenumbers in the output pseudo-shot gathers. Target-oriented interferometric imaging from the 20-receiver array recovers the top of salt reflector that is consistent with surface seismic images. The interferometric images of the subsalt sediments below the array shows a dip discrepancy with the active-shot WAW image. These differences are attributed to the presence of artifacts in both images, as well as to differences in shot/receiver geometry and uncertainties in the velocity model. The best images from the field data are obtained from deconvolution interferometry, because the pseudo-shots generated by cross-correlation contain the autocorrelation of the air gun source function.

6.2 Introduction

Most of exploration seismic imaging is done from surface seismic records. In areas of high structural complexity (e.g., near salt bodies), borehole seismic data may give detailed subsurface information that cannot be obtained from surface seismic data. Hornby et al. (2005) give an example where Walk-Away VSP data acquired in a subsalt receiver array are used to image sediments below salt that are invisible with surface seismic data. Another example is given by Grech et al. (2003), who use Walk-Away VSP data to image geologic features in a complex compressional tectonic setting where surface seismic is compromised.

Current techniques in the field of seismic interferometry (Curtis et al., 2006; Schuster and Zhou, 2006) open possibilities for innovative uses of borehole seismic data, because seismic interferometry reconstructs waves that propagate between receivers as if one of them acted as a source. Hence, with interferometry, it is possible

to "create" pseudo-acquisition geometries that differ from the original physical experiments. Schuster et al. (2004) used the concept of interferometry to migrate free-surface reflections from Reverse VSP data. The Virtual Source method of Bakulin and Calvert (2004, 2006) is used to image beneath a complex overburden from borehole sensors placed in a horizontal well with no knowledge of the overburden model parameters. In Chapters 4 and 5 we use drill-bit noise recordings along with a deconvolution interferometry method to perform the broad-side imaging of the San Andreas fault at Parkfield, CA. In the context of salt flank imaging, Willis et al. (2006) presented a numerical example demonstrating that diving waves can be used for the interferometric imaging of near-vertical salt reflectors. Xiao et al. (2006) present a model-based interferometric method to image transmitted P-to-S waves that can be used for salt flank imaging.

Here, we use internal multiples in interferometry to reconstruct primary reflections. This type of interferometry is applicable, for example, to the imaging of structures located above a borehole receiver array using data from standard Walk-Away VSP geometries. Such an interferometric imaging technique can be used to image salt and subsalt structures from borehole receivers placed beneath the target reflectors. Although no knowledge of model parameters is necessary for the interferometry of internal multiples, this method relies on wavefield separation to select waves propagating in specific directions between receivers (Chapter 2). For this reason, we refer to this method as *target-oriented* interferometry. Apart from being suitable to image features above the receiver array, target-oriented interferometry can also be tailored to image below the array. In that case, our method is analogous to the Virtual Source applications of Bakulin and Calvert (2006) and Mehta et al. (2007a). Bakulin and Calvert (2006) rely on the isolation of a window around the direct arrival to separate

the down- from the up-going waves. A similar wavefield separation is done by Mehta et al. (2007a) using dual-wavefield summation. Our wavefield separation procedure is based on selecting the directions of waves incoming at the receivers according to their shot-domain wavenumbers. The interferometric imaging of features below the receiver array using up- and down-going wavefield separation (Bakulin and Calvert, 2006; Mehta et al., 2007a) can be justified by the one-way reciprocity theorems derived by Wapenaar et al. (2004). Such one-way theorems, however, cannot be used for the interferometry of up-going internal multiples (excited by sources at the surface) to reconstruct down-going single scattered waves. We use these waves to image salt features from subsalt borehole arrays. To perform the interferometry of internal multiples we rely on the two-way representation theorems for perturbed media derived in Chapter 2.

Imaging from multiples has been proposed by other authors in different contexts than we present here. Weglein and co-workers (2003, 2006) propose model-independent imaging based on an inverse scattering series approach. Berkhout and Verschuur (2006) compare the convolution-based multiple elimination methods (SRME) to cross-correlation interferometry, and propose a weighted cross-correlation method to construct primary reflections from surface-related multiples. With an approach similar to that of Berkhout and Verschuur (2006), Hargreaves (2006) provides a field data example of imaging from multiples in a shallow water environment. Although these methods are not restricted to the processing surface seismic data, they are not designed for targeting specific arrivals or portions of the image space. This is one of the objectives of the interferometry method we describe here. Furthermore, the methods of Berkhout and Verschuur (2006) and Hargreaves (2006) focus on surface-related multiples, whereas we focus on the imaging of internal multiples.

We first describe how to manipulate recorded wavefields to generate interferometric data that targets specific arrivals, using the representation theorems of Chapter 2. Throughout this description, we give conceptual examples of the application of target-oriented interferometry to image above and below the receiver array. Next, we use the *Sigsbee* salt model to create a numerical subsalt Walk-Away VSP experiment. With these synthetic data, we compare images from target-oriented interferometry with those obtained from interferometry of the full recorded wavefields. Finally we validate the use of internal multiples in the imaging of subsalt features from a field Walk-Away VSP data acquired in the Gulf of Mexico. We use the field data to give a detailed account of the effect of target-oriented interferometry in the pseudo-shot gathers, as well as in the context of correlation-based and deconvolution-based (Chapter 3) interferometry.

6.3 Target-oriented interferometry

In this section, we describe how to use interferometry to target the illumination of specific regions in the subsurface. We decompose the recorded data in the frequency domain as (Chapters 2 and 3)

$$u(\mathbf{r}_A, \mathbf{s}, \omega) = W(\mathbf{s}, \omega) \left[G_0(\mathbf{r}_A, \mathbf{s}, \omega) + G_S(\mathbf{r}_A, \mathbf{s}, \omega) \right] ; \tag{6.1}$$

where $\mathbf{s}$ and $\mathbf{r}_A$ are source and receiver locations, respectively, and ω is the angular frequency. The recorded data u is given by the superposition of the unperturbed impulse response G_0 and its perturbation G_S (Chapters 2 through 4). The function $W(\mathbf{s}, \omega)$ describes the excitation at $\mathbf{s}$. Here, we assume that the medium perturbations that give rise to G_S are localized within the support of a volume $\mathbb{P}$ (Figure 6.1). To generate interferometric data (Lobkis and Weaver, 2001; Wapenaar et al., 2004;

Draganov et al., 2006), we cross-correlate the data measured at $\mathbf{r}_A$ (equation 6.1) with the data recorded at $\mathbf{r}_B$ and integrate over the sources $\mathbf{s}$, which gives (e.g., Curtis et al., 2006; Larose et al., 2006)

$$\oint_{\Sigma} u(\mathbf{r}_A, \mathbf{s}, \omega) u^*(\mathbf{r}_B, \mathbf{s}, \omega)\, d\mathbf{s} \;=\; \langle |W(\mathbf{s}, \omega)|^2 \rangle \left[G(\mathbf{r}_A, \mathbf{r}_B, \omega) \;+\; G^*(\mathbf{r}_A, \mathbf{r}_B, \omega) \right] , \qquad (6.2)$$

when the integration is done over a closed surface Σ as illustrated by Figure 6.1. According to this equation, interferometry reconstructs $G(\mathbf{r}_A, \mathbf{r}_B, \omega)$ (and its acausal version), which is the response measured at $\mathbf{r}_A$ as if the source is placed at $\mathbf{r}_B$ (Wapenaar et al., 2004; Bakulin and Calvert, 2004). Note that G in equation 6.2 is the perturbed impulse response given by $G = G_0 + G_S$ (equation 6.1). Equation 6.2 is valid for arbitrarily heterogeneous media. For our purposes, it is convenient to assume that both the unperturbed and perturbed portions of the medium (see Figure 6.1) are heterogeneous. Also, multiple scattering may occur both in the unperturbed and perturbed regimes (e.g., Figure 6.1a). The objective in our experiments, however, is to image only G_S: the waves scattered within the perturbation volume $\mathbb{P}$ (Figure 6.1). These waves are included in the recovered response $G(\mathbf{r}_A, \mathbf{r}_B, \omega)$ in equation 6.2. Since the pseudo-source at $\mathbf{r}_A$ in equation 6.2 radiates energy in all directions, directly separating G_S from G in right-hand side of equation 6.2 may not be straightforward because waves in G_0 and G_S can have similar apparent wavenumbers (i.e., it is difficult to determine if an arrival comes from above or below the array). This is a common problem, for example, for free-surface multiple suppression in OBC data (Mehta et al., 2007a). To overcome this problem with borehole seismic data, we propose a method to manipulate the recorded wavefields before interferometry, producing pseudo-sources that radiate most of the energy in a single preferential direction. This

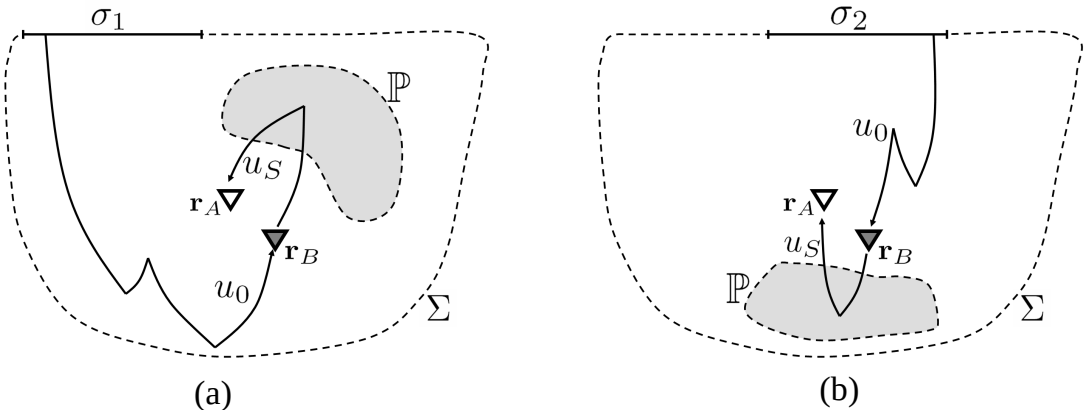

Figure 6.1. Geometry of the perturbation approach to target-oriented interferometric imaging. A large volume is bounded by the surface Σ, that contains medium perturbations that are restricted to the volume $\mathbb{P}$ (indicated by the grey-shaded areas). Closed surfaces are denoted by the dashed lines. In both panels, u_0 are unperturbed wavefields, while u_S are wavefield perturbations due to scattering within the volume $\mathbb{P}$. The solid lines illustrate stationary wave-paths. Two receivers, located at $\mathbf{r}_A$ and $\mathbf{r}_B$, are represented by triangles. The grey triangle denotes the receiver that acts as a pseudo-source in the interferometric experiments. When the target is imaging medium perturbations above the receivers, as in panel (a), I rely on waves excited by sources over the surface σ_1 (solid black line). In panel (b), interferometry targets the reconstruction of up-going scattered waves from below the receivers. In this case, I consider only waves generated by sources on the surface σ_2. These Figures are extended after Chapter 2.

direction is chosen such that the resulting interferometric data reconstructs only the desired waves G_S.

An alternative form of interferometry that targets the extraction of the wavefield perturbation $G_S(\mathbf{r}_A, \mathbf{r}_B, \omega)$, measured at $\mathbf{r}_A$ and excited by a pseudo-source at $\mathbf{r}_B$ is (Chapter 2)

$$\int_{\sigma_i} u_S(\mathbf{r}_A, \mathbf{s}, \omega) u_0^*(\mathbf{r}_B, \mathbf{s}, \omega)\, d\mathbf{s} \;\; \approx \;\; \langle |W(\mathbf{s}, \omega)|^2 \rangle\, G_S(\mathbf{r}_A, \mathbf{r}_B, \omega)\,; \tag{6.3}$$

where the integration over sources is no longer conducted over the closed surface Σ, but rather over a part of it, denoted by σ_i (e.g., σ_1 or σ_2 in Figure 6.1) which is the $i-$ th chosen segment of Σ. There are two important differences between equations 6.2 and 6.3 (Chapter 2). First, the integrand in the left-hand side of equation 6.2 contains the correlation of perturbed wavefields u whereas in the integrand in equation 6.3 we correlate the unperturbed wavefield $u_0(\mathbf{r}_B, \mathbf{s}, \omega)$ with the wavefield perturbation $u_S(\mathbf{r}_A, \mathbf{s}, \omega)$ (which alone does not satisfy the wave equation). Second, on the right-hand side of equation 6.2 we recover the causal and acausal wavefields $G(\mathbf{r}_A, \mathbf{r}_B, \omega)$, while equation 6.3 recovers only the causal part of the wavefield perturbation $G_S(\mathbf{r}_A, \mathbf{r}_B, \omega)$.

In order for equation 6.3 to hold, the sources over σ_1 must sample the stationary points that yield the desired events in $G_S(\mathbf{r}_A, \mathbf{r}_B, \omega)$ (Snieder et al, 2006; Chapter 3). Equation 6.3 is approximate because we neglect a volume integral that accounts for the effect of medium perturbations that lie in the stationary path of unperturbed waves (Chapter 2). The volume integral that is not present in equation 6.3 can indeed be neglected by selecting waves from u_0 whose path does not go through the perturbation volume $\mathbb{P}$ (Chapter 2). Below we describe a method that selects waves in u_0 by wavefield separation.

The truncation of the surface integral (Wapenaar, 2006; Chapter 3) can lead to a nonzero error in the wavefield reconstructed interferometry (Wapenaar, 2006; Chapter 3). This may cause amplitude and phase distortions (Wapenaar, 2006; Chapter 3), and can introduce spurious arrivals (Snieder et al., 2006; Chapter 3). Here, we consider only sources over σ_i since they are the ones that sample the stationary source points of the arrivals of interest (see below). Because stationary source points of other arrivals that are not of interest are not sampled along σ_i, these arrivals are not

reconstructed by equation 6.3.

The objective of the methodology we present is to use interferometry to target the reconstruction of scattered waves G_S for a particular geometry of the receiver array and the region we desire to image (represented by the perturbation volume $\mathbb{P}$). Figure 6.1 presents two scenarios in which we perform target-oriented interferometry. In the first scenario, in Figure 6.1a, the portion of the medium we wish to image (the volume $\mathbb{P}$) is above the receivers. To image the perturbations within $\mathbb{P}$ in Figure 6.1a we rely on up-going scattered waves u_0 that generate down-going wavefield perturbations u_S. An example of these arrivals is shown by the arrows in Figure 6.1a. The stationary source points for the desired waves in Figure 6.1a are located along σ_1. Our second scenario, in Figure 6.1b, consists of a target perturbation volume $\mathbb{P}$ that is below the receivers. In this case, we use for interferometry down-going unperturbed waves u_0 and up-going wavefield perturbations u_S. This scenario is the same as in earlier applications of the Virtual Source method (Bakulin and Calvert, 2006; Mehta et al., 2007a). Typically, in active seismology experiments, sources are only available over the surface of the Earth (or of the Ocean, in marine experiments). For this reason, we assume in the experiments in Figure 6.1 that sources are only available on the top portion of the surface Σ.

To perform target-oriented interferometry according to equation 6.3, we select specific arrivals in u_0 and u_S (Figure 6.1) with a two-step procedure. The first step, as explained above, is to select the portion of the surface Σ that contains the stationary source points that correspond to the arrivals of interest. In the example in Figure 6.1a, interferometry recovers the desired perturbations $u_S(\mathbf{r}_A, \mathbf{r}_B, \omega)$ from the sources over σ_1; while sources over σ_2 help recover the perturbations in Figure 6.1b. Note that it is not necessary to know the shot coordinates, as long the waves radiated by the shots

come from the surface segment σ_i. We choose the segment σ_i based on the relative position of the receivers and the portion of the surface we wish to image (volume $\mathbb{P}$). For example, the sources over σ_1 excite direct waves that propagate downward and rightward in Figure 6.1a, that once reflected in the unperturbed medium are recorded as the up-going waves u_0 that are illustrated in the figure. In the case of Figure 6.1b, the sources over σ_2 are the ones that radiate energy directly down towards the receivers, being thus suitable for reconstructing the desired scattered perturbations from interferometry (see also Bakulin and Calvert, 2006; and Mehta et al., 2007a). The second step in selecting the portions of the recorded wavefields that are used for interferometry consists of wavenumber filtering and is discussed next.

The raw data recorded at the receivers for the sources over the chosen source segment σ_i are the total wavefields u (equation 6.1). To do target-oriented interferometry using equation 6.3, it is necessary to separate the wavefields u_0 and u_S from the recorded perturbed wavefields u (equation 6.1). Here, we separate u_0 and u_S from u according to the direction of the incoming waves at a given receiver. The direction of incoming waves, in the time-domain, can be inferred from the slopes of the arrivals in the recorded shot gathers (i.e., for a fixed source and multiple receivers). In the frequency-wavenumber domain, these slopes translate to the apparent shot-domain wavenumbers, which we refer to as k_s. The choice of which wavenumbers to use at $\mathbf{r}_A$ and $\mathbf{r}_B$ varies from one experiment to another (see Figures 6.1 and 6.2).

Figure 6.2a describes the wavefield separation necessary to target the imaging of scatterers above the receiver array, as in Figure 6.1a. In this case, keeping the negative shot-domain wavenumbers at $\mathbf{r}_B$ (left-hand side of Figure 6.2a) defines $u_0(\mathbf{r}_B, \mathbf{s}, \omega)$ (equation 6.3), which contains mostly up-going incoming waves. This ensures that the pseudo-source at $\mathbf{r}_B$ (see equation 6.3) radiates mostly up-going energy. For

the receivers that record the interferometric data, represented by $\mathbf{r}_A$, the choice of incoming wave direction depends on the relative positioning between a given receiver and the pseudo-source at $\mathbf{r}_B$. If the receiver is above the pseudo-source (top cartoon on right-hand side of Figure 6.2a), waves with $k_s < 0$ give $u_S(\mathbf{r}_A, \mathbf{s}, \omega)$ (see equation 6.3). For $\mathbf{r}_A$ below $\mathbf{r}_B$, we use waves with $k_s > 0$ to extract $u_S(\mathbf{r}_A, \mathbf{s}, \omega)$. The interferometry of the wavefields separated according to Figure 6.2a is suitable for targeting the imaging of structures above the receivers as in Figure 6.1a because it generates a pseudo-shot gather that radiates energy towards the upper-right corner of the model.

To image below the receiver array, as in Figure 6.1b, wavefield separation can be done according to Figure 6.2b. For the pseudo-source at $\mathbf{r}_B$, we select the down-going incoming waves $u_0(\mathbf{r}_B, \mathbf{s}, \omega)$ excited by the sources over σ_2 (Figure 6.1b) by preserving arrivals with $k_s > 0$ (left-hand cartoon in Figure 6.2b). Keeping waves with $k_s < 0$ at the recording receivers in the interferometry experiment yields $u_S(\mathbf{r}_A, \mathbf{s}, \omega)$ (right-hand cartoon in Figure 6.2b). This criterium for the extraction of $u_S(\mathbf{r}_A, \mathbf{s}, \omega)$ from $u(\mathbf{r}_A, \mathbf{s}, \omega)$ is the same for receivers that are either above or below the pseudo-source. For that reason we represent by $\mathbf{r}_A$ receivers that are both above and below $\mathbf{r}_B$ in Figure 6.2b. After wavefield separation as in Figure 6.2b, using $u_S(\mathbf{r}_A, \mathbf{s}, \omega)$ and $u_0(\mathbf{r}_B, \mathbf{s}, \omega)$ for different $\mathbf{r}_A$ positions results in a pseudo-shot gather that radiates energy down toward the perturbation volume $\mathbb{P}$ (Figure 6.1b). As mentioned above, the case of Figure 6.1b is also the objective of the Virtual Source method (Bakulin and Calvert, 2006; Mehta et al., 2007a). These studies rely on wavefield separation techniques that are different from ours. Bakulin and Calvert (2006) window the data in the time-domain receiver gathers, using a small window containing the direct arrival as u_0, and the remainder of the data as u_S. Along with windowing, Mehta et al. (2007a) use a method based on the summation of vertical and hydrophone

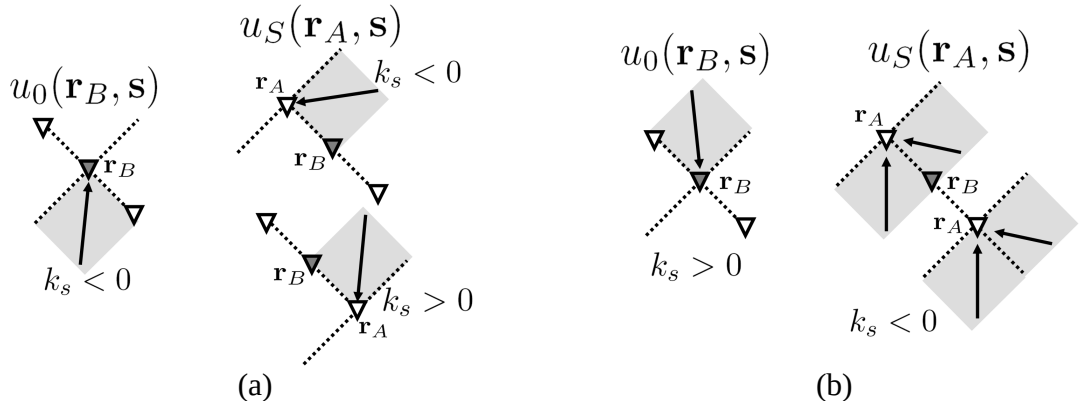

Figure 6.2. Examples of wavefield separation for target-oriented interferometry. The wavefield u_0 and the perturbation u_S are extracted from the recorded perturbed wavefield u by wavefield separation. Wavefield separation is implemented by wavenumber filtering (e.g., by $f-k$ filtering) in the shot domain. Receivers are represented by triangles. The receiver that acts as a pseudo-source (located at $\mathbf{r}_B$) is indicated by the grey triangles. The arrows indicate the direction of waves arriving at the receivers. The directions parallel and perpendicular to the receiver line define a coordinate frame indicated by the dashed lines. In this coordinate frame, k_s is the shot-domain wavenumber of a given recorded wave. Panel (a) illustrates the separation of wavefields necessary for target-oriented interferometric imaging in the context of Figure 6.1a. This is one particular choice of pseudo-sources that radiate energy towards the upper right-hand portion of the medium above the array. The wavefield separation in panel (b) is designed for the imaging experiment in Figure 6.1b. This procedure can be thought in terms of selecting a portion of the *Ewald sphere* (Ewald, 1962).

components in 4-component ocean bottom cable (OBC) data to separate down- from up-going wavefields, and treat them as u_0 and u_S, respectively.

Target-oriented interferometry using wavefield separation by shot-domain wavenumber as shown in the examples in Figure 6.2 can be adapted to remote sensing geometries other than those illustrated by Figure 6.1. The choice of which sources to use and how to separate waves at $\mathbf{r}_A$ and $\mathbf{r}_B$ (equation 6.3) varies with each particular case. Although no specific knowledge about the model is required by equation 6.3, a priori information about relative location of the image target and the receiver array helps determining an appropriate set of source locations σ_i and as well which wavenumbers to use. The result of target-oriented interferometry can also be explained through the concept of the *Ewald Construction* (Ewald, 1962). Used in particle physics, with applications in crystallography and electronic microscopy, the Ewald Construction shows explicitly the relationship between incident and diffracted wavenumbers through the *Ewald sphere* (Ewald, 1962). The wavenumber selection at $\mathbf{r}_B$ corresponds to the rotation of the Ewald sphere around the origin of its reciprocal space (Ewald, 1962), which translates into exploring different excitation directions. Selecting the wavenumbers at $\mathbf{r}_A$ results on selecting a subset of possible diffractions from the Ewald sphere.

While our method can be applied to a variety of geometries, we discuss the examples in Figures 6.1 and 6.2 because they are applicable to the data examples we provide. Although the data from interferometry carries the average source power spectra (see equations 6.2 and 6.3), it is possible, in principle, to remove the effect of the excitation function from the reconstructed data. When estimates of the power spectra of the source function are available, these can be used to extract the impulse response from interferometry (Wapenaar and Fokkema, 2006; Mehta et al., 2007a).

Interferometry by deconvolution (Chapter 3) is an option for reconstructing an

interferometric impulse response when estimates of the source power spectra are not available. In particular, deconvolution interferometry can be more effective than its correlation-based counterpart in reconstructing impulsive pseudo-sources when the input excitation consists of a complicated, unknown waveform (Chapters 3 and 4). This is the case when the excitation is comprised of waves coming from the Earth's subsurface (Snieder and Şafak, 2006; Mehta et al., 2007b). This may also be the case when using internal multiples to do interferometry. Note, for example, that the excitation recorded by $\mathbf{r}_B$ in Figure 6.1a consists of a superposition of primaries and, to a lesser extent, of higher-order multiples. Consequently, the signal corresponding to this excitation can be a complicated incoherent function. Here, apart from using correlation interferometry, we rely on a deconvolution interferometry method (Chapter 3) to create impulsive images from our data examples. Although in this Section we describe target-oriented interferometry with cross-correlations, the wavefield separation procedure is the same when using deconvolutions (Chapter 3). In the next two Sections we describe numerical and field data examples of target-oriented interferometric imaging in subsalt environments.

6.4 Numerical example

We present an example that consists of a subsalt Walk-Away (WAW) VSP numerical experiment using the *Sigsbee* velocity model. The purpose of this numerical example is to use the subsalt WAW VSP data to image the Sigsbee salt canopy from below by using the interference of internal multiples, analogous to the example in Figure 6.1. Figure 6.3 illustrates the model as well as the experiment. The experiment simulates the recording of shots placed 500 ft deep, at 100 evenly-spaced receivers in a deviated borehole (Figure 6.3). The first receiver is placed at $x = 48000$ ft and at a

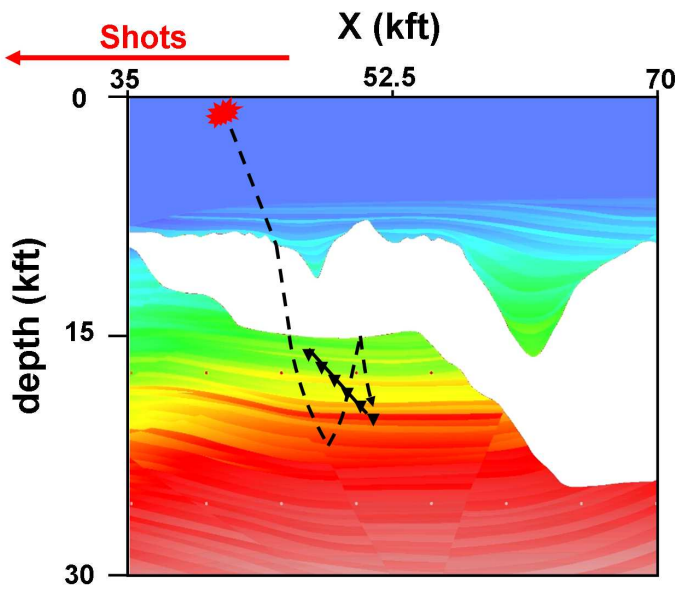

Figure 6.3. Geometry of the numerical experiment with the *Sigsbee* model. The figure displays the model structure, colorcoded by acoustic wavespeed. A receiver array with 100 sensors is set beneath the salt body, in a 45° inclined borehole (solid line with triangles). Shots are placed in a horizontal line 500 ft below the water surface, and extend laterally towards the left-hand side of the receiver array, as indicated by the red arrow. Interferometry is used to image the salt with the receiver array by reconstructing down-going primary reflections propagating between the receivers from internal multiples. The wavepath of one such multiple is indicated by the dashed black arrow.

depth of 16000 ft; while the lateral and depth coordinates of the last receiver are 52950 ft and 20950 ft, respectively. The shots start at $x = 10000$ ft with a shot interval of 125 ft. The source waveform consists of a Ricker wavelet with 12 Hz peak frequency. In our experiments, we consider shots placed from $x = 10000$ ft to $x = 53500$ ft (this corresponds to the surface σ_1 in Figure 6.1a).

Interferometric images using the full recorded data (with no wavefield separation) are shown in Figure 6.4. The imaging in these examples is done by wavefield extrapolation in a slant coordinate system that conforms with the receiver array. Wavefield

extrapolation is done by the Split-step Fourier Phase-shift-plus-interpolation method (Biondi, 2006). Figure 6.4a is generated using cross-correlation interferometry while Figure 6.4b is obtained from deconvolution interferometry after source summation (Chapter 3). Although the source function is suppressed by deconvolution interferometry (Figure 6.4b), the difference between the images in Figure 6.4 is not substantial because the original source function is a band-limited pulse. Significant differences between correlation- or deconvolution-based interferometric images exist when the source excitation is complicated and poorly known (see next Section; and also Chapter 3). The images in Figure 6.4 show an accurate reconstruction of the salt canopy, especially towards the right-hand side of the model where the salt flanks are dipping. Above the receiver array, the imaged salt is characterized by reflectors that are weak compared to the dipping salt flanks. The images of the sediments between the salt the receiver array are distorted and do not reproduce the horizontal bedding of the model (Figure 6.3).

After applying the target-oriented interferometry method based on wavefield separation illustrated by Figure 6.2a, we obtain the images in Figure 6.5. We adapted the wavefield separation in Figure 6.2a to include also positive numbers recorded at $\mathbf{r}_A$ above $\mathbf{r}_B$. This ensures the array in the interferometric experiment also records wave that come from directly above the receivers. Note that although the original source and receiver geometry is the same for the images in Figures 6.4 and 6.5 is the same, the portion of the model illuminated by these two sets of images is substantially different. As discussed in the previous Section, the pseudo-sources reconstructed by target-oriented interferometry are designed to radiate energy upward (Figures 6.1a and 6.2a). Hence, the images in Figure 6.5 illuminate the model predominantly in the area above the receiver array. These images show bright reflectors at the

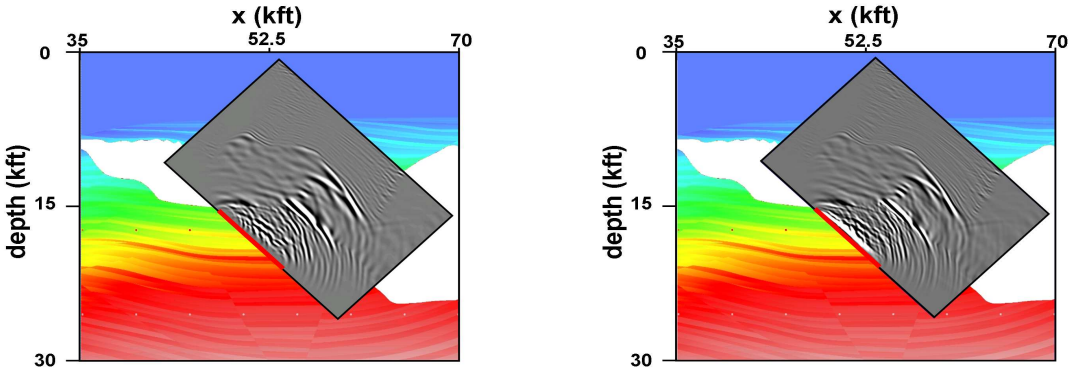

Figure 6.4. Images obtained from interferometry of the data acquired in the numerical experiment (Figure 6.3). The images, in grey scale, are superposed on the velocity model from Figure 6.3. The images are based on cross-correlation interferometry (panel a), and on deconvolution interferometry (panel b). I used the full wavefield recorded at the receivers to reconstruct the interferometric shot gathers from which these images are obtained.

bottom and top salt above the array, which appear as dim reflectors in the images in Figure 6.5. Figure 6.5 shows that the target-oriented interferometric images recover the structure of the subsalt sediments which are not seen in Figure 6.4. The reflector that corresponds to the dipping top salt (right-hand side of images in Figure 6.4) is not present in the images in Figure 6.5. This reflector is absent in the target oriented interferometric images because it is imaged in Figure 6.4 from reflections reconstructed from diving waves that arrive at the receiver array with positive shot-domain wavenumbers. Since the wavefield separation builds the filter u_0 from $k_s < 0$, reflectors from such diving waves are not present in Figure 6.5.

As in Figure 6.4, there is little difference between the image obtained from correlation interferometry and the one from deconvolution interferometry (Chapter 3). This is because the excitation function used in the modeling is a band-limited pulse (see above). There are artifact reflectors within the salt that appear more strongly

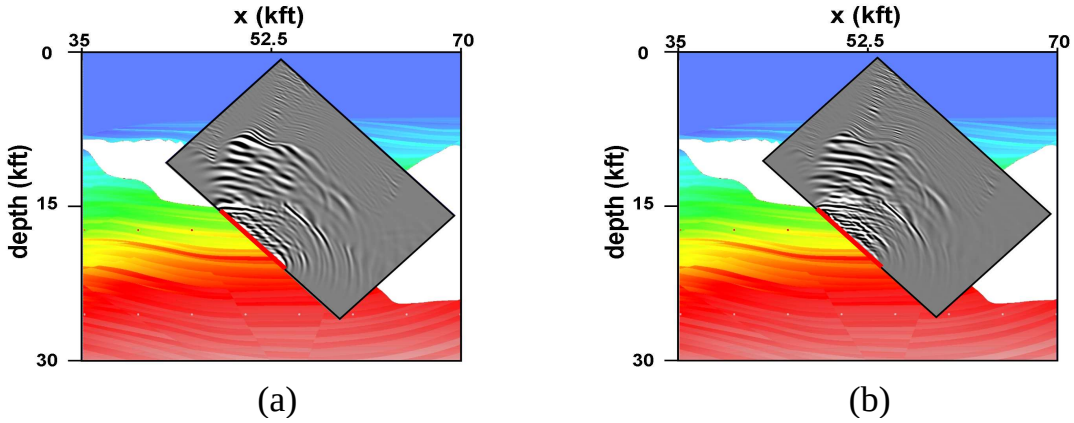

Figure 6.5. Images obtained from target-oriented interferometry of the Sigsbee Walk-Away VSP data (Figure 6.3). Target-oriented interferometry is implemented with the wavefield separation approach described in Figure 6.2a, adapted to include waves arriving from directly above the receivers. As in Figure 6.4, the image in (a) is obtained from cross-correlation interferometry and the image in (b) from deconvolution interferometry. The reflectors in these images come from single-reflections reconstructed by interferometry mostly from internal multiples. This numerical experiment is analogous to that shown in Figure 6.1a.

in Figure 6.5 than in Figure 6.4. These artifacts come from the spurious arrivals introduced by truncation of the surface integral in interferometry (Snieder et al., 2006; Wapenaar, 2006; Chapter 3). Along with the reflections of interest, these spurious arrivals are enhanced by the wavefield separation procedure (Figure 6.2a). With this numerical example, we illustrate the effect of designing interferometric sources that illuminate a particular portion of the model. We discuss the result of target-oriented interferometry in the pseudo-shot gathers using the field data examples in the next Section.

6.5 Gulf of Mexico subsalt VSP data

The field Walk-Away VSP data we present here was acquired by BP in the Gulf of Mexico, and has been previously used to image subsalt sediments by Hornby et

al. (2005). The experiment geometry, shown in Figure 6.6, is similar to that of the numerical example we discuss in the previous Section. In the Gulf of Mexico data, the data was recorded by an array of 20 three-component receivers located below the salt canopy, in a well deviated from the vertical by approximately 40^o (Figure 6.6a). The top-most receiver has coordinates $x = 0$ ft and $depth = 21516$ ft; and the bottom receiver is at $x = 910$ ft and $depth = 23180$ ft. Figure 6.6b shows the shot-receiver geometry in plane-view (the N-axis in the Figure points toward the geographic North). Here, we refer to the receivers in the array, from top to bottom, as Receivers 1 through 20.

Our objective with these field data is to demonstrate the target-oriented interferometry technique as in the examples in Figures 6.1 and 6.2. Using the Sources A (Figure 6.6b) and wavefield separation according to Figure 6.2a, we image the subsurface above the array, as illustrated by Figure 6.1a. The Sources B, along with the wavefield separation described in Figure 6.2b, yields an interferometric image targeted at the medium below the array that is shorter than that of the Sigsbee numerical example, analogously to Figure 6.1b. With a 20-receiver array that is shorter than that in the numerical example (see previous Section), interferometry generates 20 pseudo-shot gathers, each recorded by 19 receivers. Because the receiver array is short (Figure 6.6a), the interferometric images have a small aperture compared to the active-shot images from surface seismic or from the WAW VSP data (Hornby et al., 2005).

We show the data recorded by the vertical component of motion of Receiver 1 for all the shots (Figure 6.6b) in Figure 6.7a. After separating waves with negative wavenumbers in the shot domain ($k_s < 0$; see Figure 6.2), and sorting the data recorded by Receiver 1, we obtain the gather in Figure 6.7b. Keeping the positive

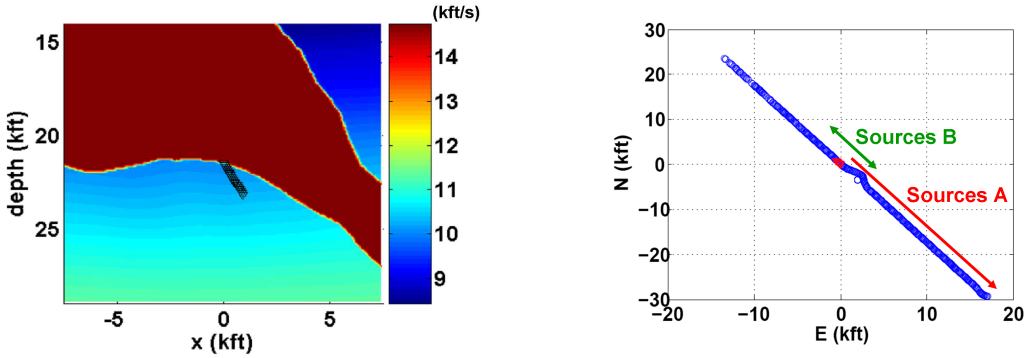

Figure 6.6. Geometry and acquisition of the Walk-Away VSP field data. The velocity model derived from surface seismic is shown in (a). Receivers are placed in a deviated Ill below the salt canopy, as indicated by the black triangles in (a). A plane view of the shot-receiver acquisition geometry is given by (b). Shot positions are denoted by blue circles, while receiver locations are represented by red triangles. In panel (b), the coordinate frame is centered on the location of the shallowest receiver. **N** is distance oriented toward the North; **E** is Eastward oriented. The orientation of the velocity profile in (a) coincides with that of the WAW line in (b). The lateral distance in (a) is also measured with respect to the location of the shallowest receiver, along the direction of the acquisition plane. The arrows in (b) indicate which sources are used for controlling the illumination of the interferometric data. Sources A (in red) correspond to the sources over σ_1 in the experiment in Figure 6.1a. Sources B (in green) are the ones that contribute to imaging below the array (source over σ_2; Figure 6.1b).

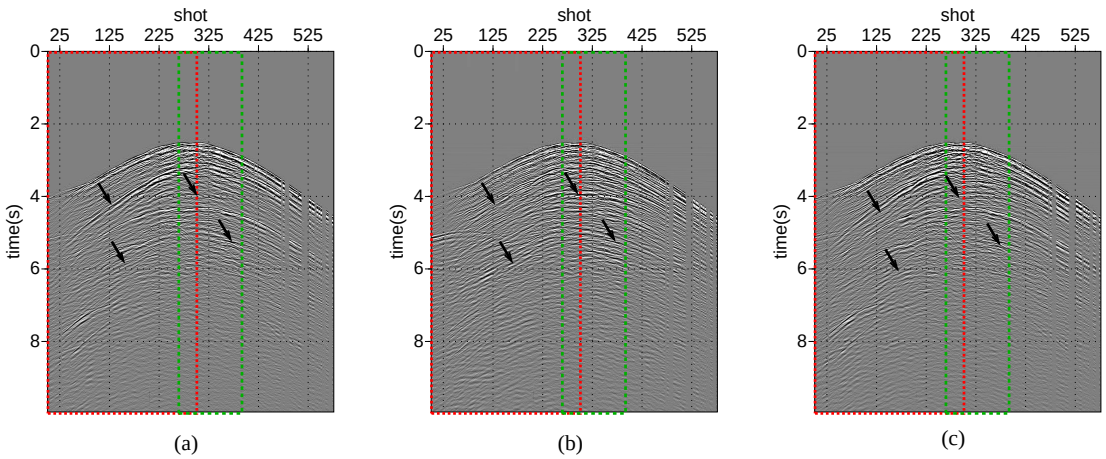

Figure 6.7. The effect of wavefield separation on receiver gathers from field data. The original data recorded at receiver 1 (shallowest receiver in Figure 6.6a) is shown in panel (a). The receiver gather in panel (b) only contains waves with $k_s < 0$ (see Figure 6.2). The data in (c) come from the positive wavenumbers in the shot domain ($k_s > 0$). The black arrows highlight portions of the data for which wavefield separation has a visible effect. The red box outlines the portion of the data that corresponds to Sources A (Figure 6.6b), while the data inside the green box is excited by Sources B.

wavenumbers in the shot-gathers ($k_s > 0$) yields the receiver gather in Figure 6.7c. By comparing Figures 6.7a and 6.7b (see arrows in the Figures), we observe that the wavefield recorded at Receiver 1 for $k_s < 0$ (Figure 6.7b) differs from the original record (Figure 6.7a). On the other hand, the receiver gather with only $k_s > 0$ in Figure 6.7c is similar to the gather in Figure 6.7a. The fact that the gather with $k_s > 0$ is more similar to the original recorded data than the gather with $k_s < 0$ suggests that the recorded data is dominated by waves with $k_s > 0$. This is because the receiver array is below the sources and the salt, so the direct wavefield and some of its interactions with salt are recorded by the receivers as down-going waves, for which $k_s > 0$.

After wavefield separation, whose effect is illustrated by Figure 6.7, we generate pseudo-shot gathers at all receiver locations. Interferometric shot gathers with the pseudo-shot at Receiver 10 are shown in Figures 6.8 and 6.9. The pseudo-shot gathers in Figure 6.8 are produced from correlation interferometry, as in equations 6.2 and 6.3. In Figure 6.9, we use deconvolution interferometry where deconvolution is done after stacking over sources (Chapter 3). This method consists on deconvolving each pseudo-shot from correlation interferometry with its zero-offset trace. Hence, each panel in Figure 6.9 is the result of taking the data in the corresponding panel from Figure 6.8 and deconvolving it with its trace at Receiver 10 (Chapter 3). We show the data from Receiver 10 because, since it is the receiver in the middle of the array, it illustrates best the effect of target-oriented interferometry in the pseudo-shot gathers.

The data in Figures 6.8a and 6.9a are reconstructed using all sources (Figure 6.6b), along with both positive and negative shot-domain wavenumbers. The pseudo-shot gathers in Figures 6.8a and 6.9a contain both positive and negative wavenumbers in the pseudo-shot domain. Note that the pseudo-shot in Figure 6.8a is dominated by positive wavenumbers. This is because the energy in receiver data (Figure 6.7) is dominated by the down-going waves with $k_s > 0$ (see discussion above). The moveout character (i.e., the pseudo-shot wavenumbers) varies between the three panels in Figures 6.8 and 6.9. Figures 6.8b and 6.9b, the pseudo-shot data has positive wavenumbers for receivers that lie below Receiver 10 (Receivers 11 through 20), and negative wavenumbers for the receivers lying above Receiver 10 (Receivers 1 through 9). This is a consequence of the choice of k_s used to separate the wavefield perturbations u_S (see Figure 6.2a). Using $k_s < 0$ for $\mathbf{r}_A$ above $\mathbf{r}_B$, results in negative pseudo-shot wavenumbers for the receivers above Receiver 10 (Figures 6.8b and 6.9b). Likewise, taking $k_s > 0$ for $\mathbf{r}_A$ below $\mathbf{r}_B$ results in positive pseudo-shot wavenumbers

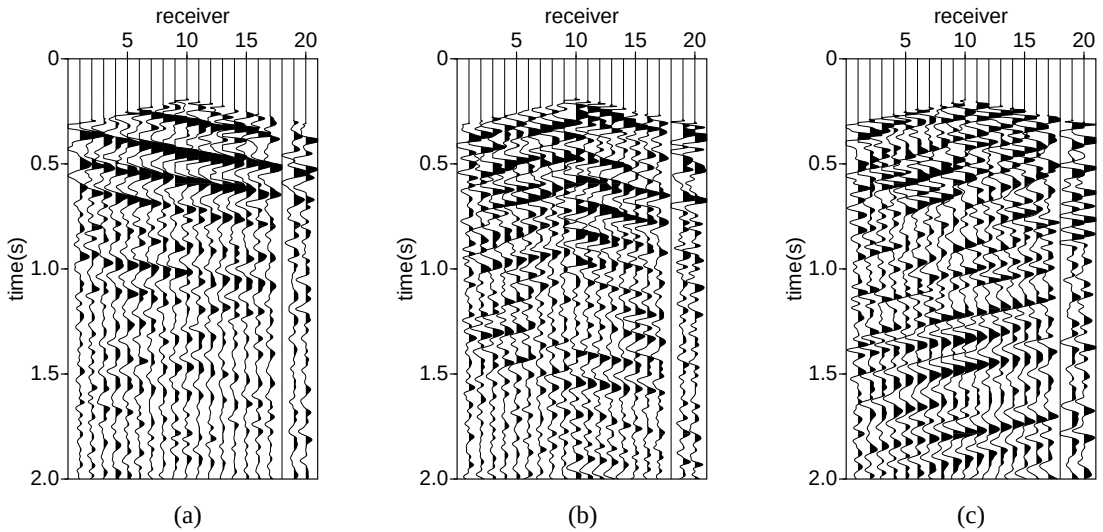

Figure 6.8. Interferometric shot gathers with pseudo-shot at receiver 10, reconstructed with correlation interferometry. The pseudo-shot gather in (a) results from correlating the full wavefields from all sources (Figure 6.6b). After performing wavefield separation according to Figure 6.2a and using the data from Sources A for interferometry, gives the pseudo-shot gather in (b). Panel (c) comes from the interferometry of the data from Sources B, after wavefield separation as in Figure 6.2b. All data are muted for the removal of the direct wave.

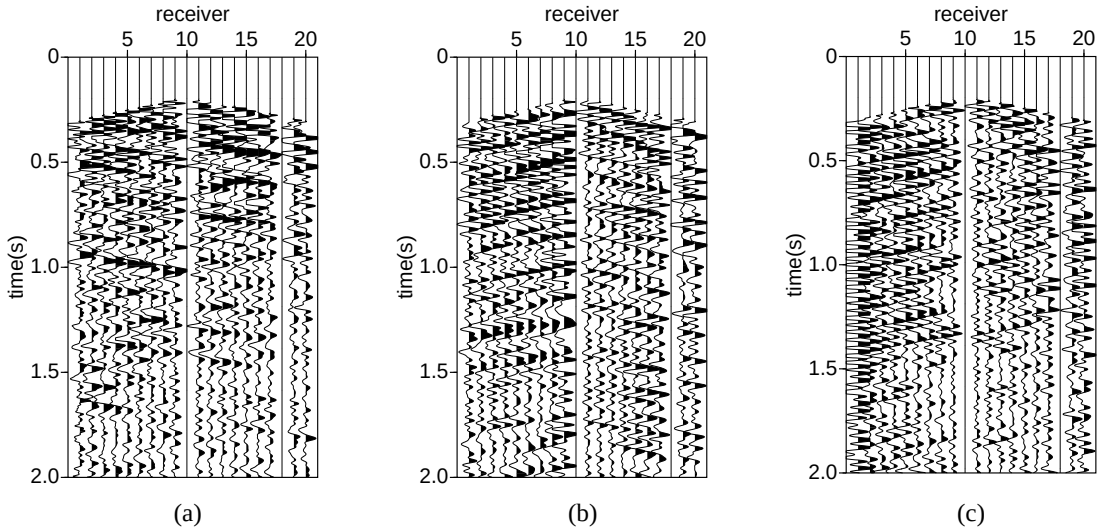

Figure 6.9. Pseudo-shot gathers from deconvolution interferometry. The input data in panels (a), (b) and (c) is the same as that in Figures 6.8a, b and c, respectively. The data in (a) is reconstructed from the full wavefield from all sources (Figure 6.6b). Sources A (Figure 6.6b) along with wavefield separation according to Figure 6.2a are used to obtain the gather in (b). When applying the wavefield separation in Figure 6.2b to Sources B, I get the data in (c) after deconvolution interferometry.

at the receivers that are lower than Receiver 10. The slopes in the pseudo-shot gathers are thus controlled by the recorded shot-domain wavenumbers at the receivers in the interferometric experiment (see Figure 6.2). Because of this, the choice of $k_s < 0$ for the separation of u_S (Figure 6.2b) in Figures 6.8c and 6.9c results in only negative pseudo-shot wavenumbers. Comparing panels b and c with panel a in Figures 6.8 and 6.9 shows how wavefield separation by shot-domain wavenumbers (Figure 6.2) can be used to target specific arrivals in the data reconstructed by interferometry.

Unlike the numerical example in the previous Section, the data obtained from deconvolution interferometry is wider-band compared to that resulting from correlation interferometry (compare panels in Figure 6.8 with those of Figure 6.9). The data reconstructed by deconvolution interferometry is impulsive while correlation interferometry produces pseudo-shots that have the imprint of the autocorrelation (Chapter 3; Wapenaar and Fokkema, 2006). In our case, the wavefield in the field data was generated by marine air gun sources. Hence, the data in Figure 6.8 contains the autocorrelation of the air gun source function while the data in Figure 6.9 does not. Mehta et al. (2007a) also observed the presence of this autocorrelation in the interferometry of marine OBC data. In their case the autocorrelation excitation was removed with an independent estimate of the air gun source function. Here, we rely on deconvolution interferometry (Chapter 3) to reconstruct impulsive pseudo-shot data (Figure 6.9) because an estimate of the air gun autocorrelation is not available.

We migrate all pseudo-shot gathers using shot-profile reverse-time migration (Baysal et al., 1983). Each of the panels in Figure 6.10 is the result of stacking the migrated images from pseudo-shots placed at every receiver in the array. The middle panels in Figure 6.10 are from pseudo-shots designed to radiate energy upward (see Figure 6.2a). Because of this, the images in Figure 6.10b and e have brighter ampli-

tudes above the array, compared to Figures 6.10a and d. Although the pseudo-sources that result in Figures 6.10b and e radiate energy upward (Figure 6.2), the salt above the array reflects much of the radiated energy downward. This explains the image artifacts below the receiver array in Figure 6.10b and e. Furthermore, since wavefield separation is done by *f-k* filtering, the small aperture of the array introduces a bias in the wavefield separation. This bias can yield *cross-talk* (e.g., Wapenaar and Fokkema, 2006) between waves propagating in different directions and that contributes to energy below the array in Figure 6.10b and e. The right-hand panels in Figure 6.10 are from interferometric sources that radiate energy downward (Figure 6.2b). This results in images (Figures 6.10c and f) that have most of the energy concentrated below the array. Panels a and d in Figure 6.10 result from migrations with the velocity model in Figure 6.6a.

We removed the top of salt (i.e., replaced sediment above the salt with salt velocity) in the upper right-hand corner of Figure 6.6a to generate the images in the middle and right-hand panels in Figure 6.10. The absence of the salt top in the velocity model ensures that top salt reflectors are not artifacts introduced by the salt/sediment contrast in the model. The influence of the bottom salt velocity contrast can be seen in all images in Figure 6.10 where the reflectors in the lower right-hand quadrant of the images terminate abruptly. The image aperture in Figure 6.10 is controlled by the geometry of the receiver array, since receivers act both as sources and receivers in interferometry. Thus, since the array is relatively small (Figure 6.6a), the circular patterns in the images are artifacts of the migration operator where the subsurface is not sampled by specular reflections.

To facilitate the interpretation of the interferometric images in Figure 6.10 we isolate the portions of the subsurface that are physically sampled by the images in Fig-

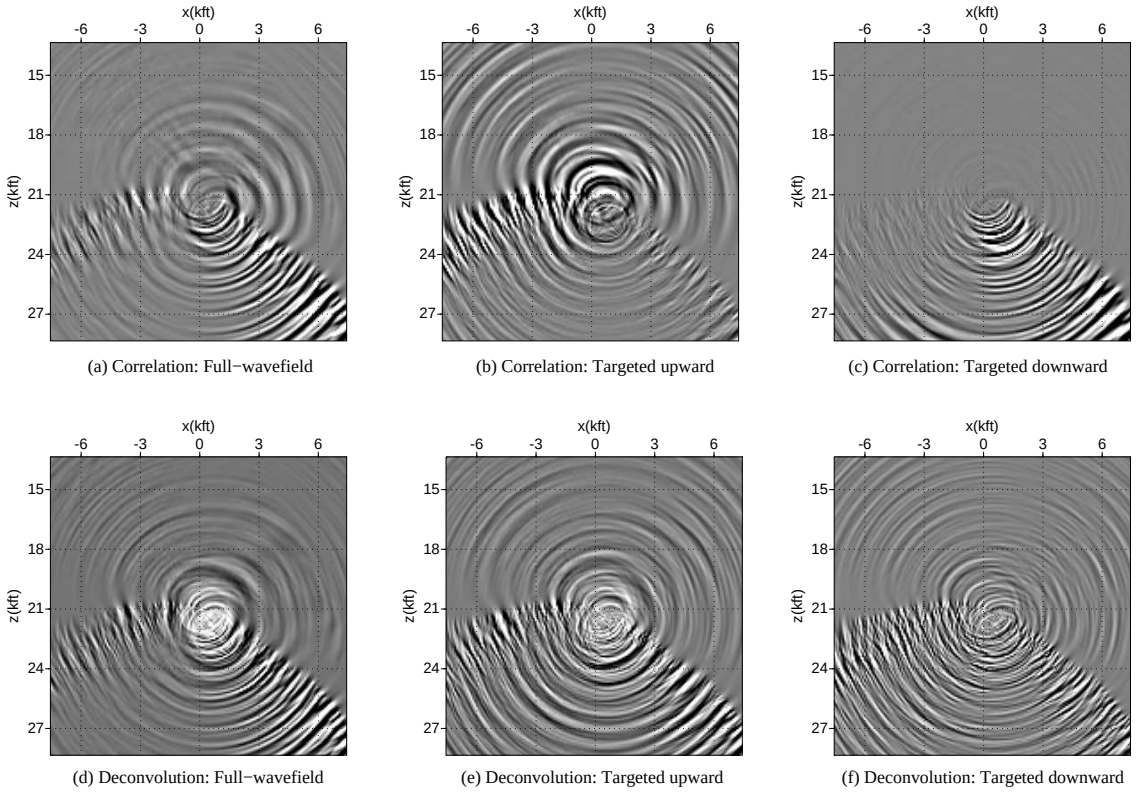

Figure 6.10. Comparison between images after reverse-time migration, with and without target-oriented interferometry. The images are the result of stacking the shot-profile migrations of the pseudo-shots at every receiver. The images in the left-hand panels (a and c) correspond to using all sources and the full wavefield for interferometry; the images in the center panels (b and e) are from pseudo-sources that radiate energy upward (as in Figure 6.1a; wavefield separation is done according to Figure 6.2a). The images in (c) and (f) are the result of reverse-time migration of pseudo-sources designed to radiate energy downward (see also Figures 6.1b and 6.2b). Images on the top panels result from correlation interferometry, and the bottom images are obtained with deconvolution interferometry. The images correspond to the same portion of the subsurface shown by the model in Figure 6.6a. Image aperture is controlled by the geometry of the receiver array (Figure 6.6a).

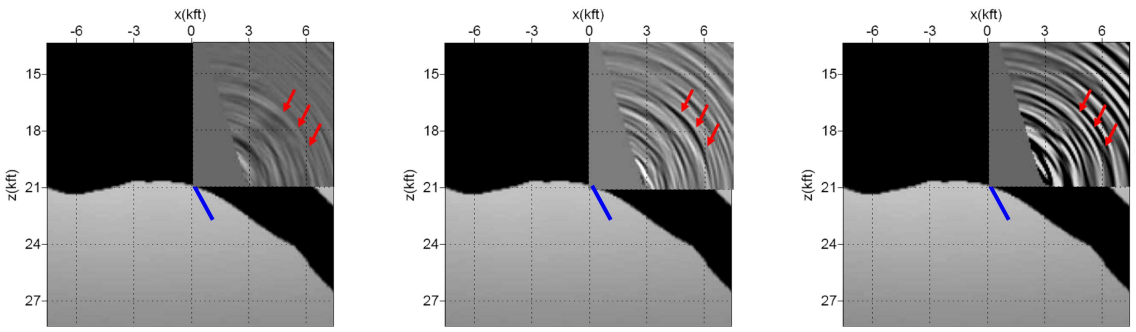

Figure 6.11. Interferometric images of the upper-right portion of the subsurface above the receiver array (see Figure 6.6a). The images are superposed on the velocity model estimated from surface seismic data. The blue line represents the receiver array. The image in (a) is extracted from Figure 6.10d and corresponds to using the full wavefield from all sources in seismic interferometry. The images in (b) and (c) are targeted at reflectors above the array (see Figures 6.1a and 6.2a). The images in panels (a) and (b) are from deconvolution interferometry (extracted from Figures 6.10d and e, respectively); and the image in (c) is from correlation interferometry (Figure 6.10b). The red arrows indicate the top of salt interpreted from surface seismic (Figure 6.6a).

ures 6.11 and 6.12. For spatial reference, we superpose the interferometric images over the velocity model estimated from surface seismic data (background in Figures 6.11 and 6.12) and indicate the position of the receiver array (blue line). The image from deconvolution-based target-oriented interferometry (Figure 6.11b) recovers the reflector corresponding to the top of salt inferred from surface seismic. This reflector is not visible in Figures 6.11a and 6.11c. Wavefield separation (see Figure 6.2a) is necessary to separate the events that illuminate the top salt reflector in Figure 6.11b. Although Figure 6.11c is also a product of target-oriented interferometry, the top salt reflector is obscured by the autocorrelation of the air gun source function, mapped onto the image. The image in Figure 6.11b comes from deconvolution interferometry, where the pseudo-shots are approximately impulsive and result in an impulsive image (Chapter 3).

The images in Figure 6.12 show how wavefield separation in interferometry can be used to image beneath the receiver array. This application is analogous to the Virtual Source method by Bakulin and Calvert (2006) and by Metha et al. (2007). Our images of the subsalt sediments illuminate predominantly the subsurface portion near the salt bottom. The sediments immediately below the array could not be imaged by interferometry, unlike the cases of Bakulin and Calvert (2006) or Mehta et al. (2007a). This happens because the salt canopy, immediately above the receiver array, acts as a major wave guide. As such, the salt directs most of the down-going energy from the sources at the surface, along the salt-sediment interface. This phenomenon accounts for the fact that subsalt reflectors in Figure 6.12b and d are only illuminated close to the bottom of the salt. As with Figure 6.11, the target-oriented image from deconvolution interferometry, Figure 6.12b, provides the best image of the subsalt sediments. Note that the subsalt reflectors in Figures 6.12a and c have a circular pattern characteristic of the migration operator. Instead, the reflectors in Figure 6.12b are better focussed, with a flatter character, and it differs in dip from the images in panels a and c. The reasoning for which the image in Figure 6.11b is superior to a and c is the same as given in our discussion about Figure 6.11 (see above).

When comparing the interferometric image of the subsalt sediments (Figure 6.13a) with the 2D WAW VSP image (Figure 6.13b; Hornby et al., 2005) we find that the sediment dips are different between these two images. Since the subsalt illumination is poor, as seen in the interferometric images and in the surface seismic data (Hornby et al., 2005), the differences in the experiment geometry account for some of the differences in the images in Figure 6.13. In the interferometry experiment, the source/receiver array is relatively small and the reflectors are close to the array, so the

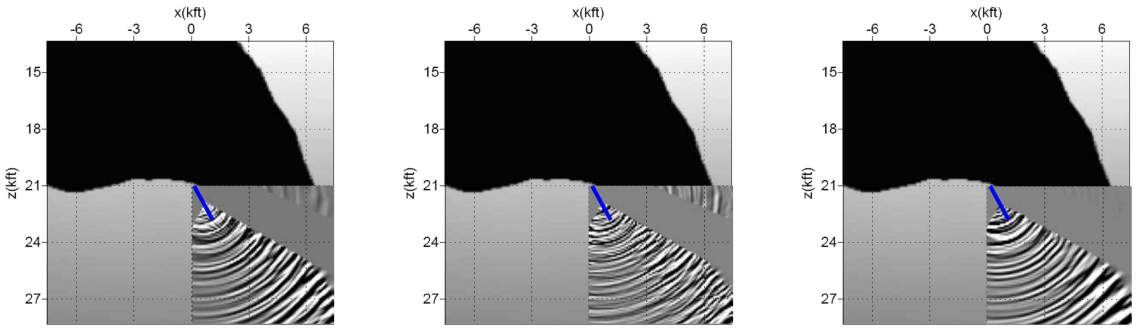

Figure 6.12. Interferometric images of the lower-right portion of the subsurface below the receiver array (blue line). As in Figure 6.11, the images are superposed on the velocity model from surface seismic (Figure 6.6a). The image in (a) is obtained from interferometry of the data with no wavefield separation, using all available sources. Interferometry is designed to target the reflectors below the array (see Figures 6.1b and 6.2b) in the images in (b) and in (c). The images in (a) and (b) are the result of deconvolution interferometry while the image in (c) comes from correlation interferometry. The images in (a), (b) and (c) are extracts from Figures 6.10d, f, and c, respectively.

migration operator artifacts in Figure 6.13a have a more circular shape compared to those in Figure 6.13b. The operator artifacts in Figure 6.13b look flatter than those in Figure 6.13a because the sources are placed far from the receivers at the sea surface. Also, the images in Figure 6.13 illuminate different portions of the subsurface because the shot/receiver geometry is different. Nonetheless, for the correct velocity model both images should display similar structures were their illumination zones coincide. The difference in the dips of subsalt reflectors close to the salt bottom may be related to uncertainties in the velocity model estimated from surface seismic. This is difficult to settle given the size of the receiver array and the poor illumination below the salt.

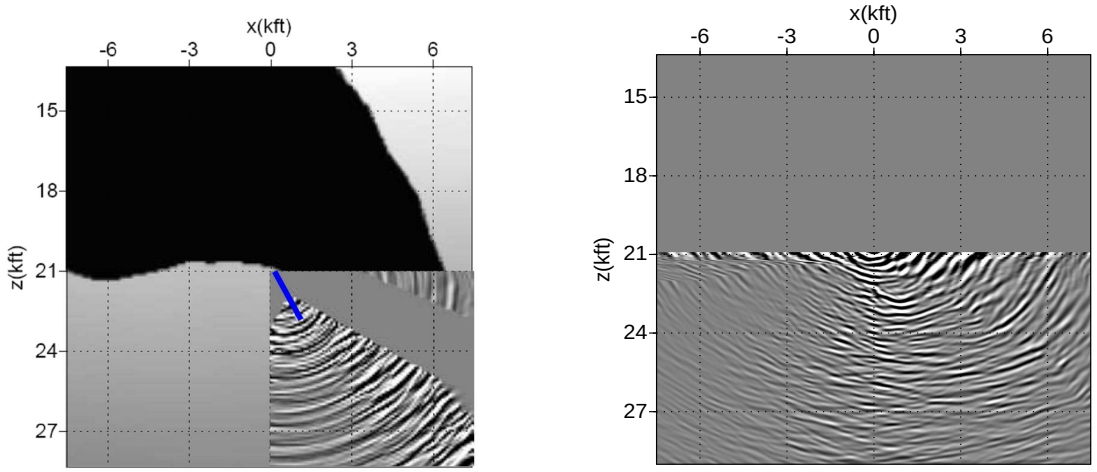

Figure 6.13. Comparison between subsalt images from interferometry, in panel (a), and (b) from active-shot migration of the full Walk-Away VSP data (see Figure 6.6b for the geometry). Panel (a) is the same as the Figure 6.12b. The image in panel (b) is the result of migration by wavefield extrapolation (Hornby et al., 2005), and only images below the receiver array.

6.6 Discussion and conclusions

We present an interferometry technique based on wavefield separation in the shot-domain that targets the reconstruction of specific arrivals in the interferometric shot gathers. We promote that this target-oriented interferometry technique can be used to reconstruct single-reflected waves from internal multiples. Such a reconstruction can be applied, for example, to the imaging of subsalt features above receiver arrays in subsalt in Walk-Away VSP experiments. Our target oriented interferometry technique is based upon two-way representation theorems derived for acoustic perturbed media in Chapter 2. The application of the technique consists in manipulating the recorded data to separate unperturbed waves at the receiver that acts as a pseudo-source, and wavefield perturbations at the receivers that record the interferometric experiment. We separate these wavefields according to the directions of the waves incoming at a given receiver; i.e., according to the shot-domain wavenumber. We discuss the application of target-oriented interferometry to image the medium above a receiver array as well as below the array.

Using the *Sigsbee* salt model, we illustrate how interferometric illumination can be controlled using wavefield separation along with the appropriate choice of sources to be included. The numerical experiment consists of a large-offset Walk-Away VSP recorded at a deviated 100-receiver array placed below the salt. Seismic interferometry with no wavefield separation yields an image of the salt body which is well defined in the dipping salt flanks to the right-hand side of the array. These reflectors are mainly sampled by diving waves, analogously to the numerical experiment by Willis et al. (2006). The images obtained from target-oriented interferometry recover the reflectors at the top and base of salt located immediately above the receiver array. These images also recover a portion the subsalt sediment structure that cannot be

retrieved by the interferometry of the full recorded wavefields. In the Sigsbee example, the target-oriented interferometry procedure reconstructs down-going single-scattered waves from up-going internal multiples recorded in the original experiment.

We also use a field Walk-Away VSP data acquired in the Gulf of Mexico (Hornby et al., 2005) to test the target-oriented interferometry method. The data were recorded in a 20-receiver subsalt array in a deviated well. The acquisition geometry is similar to that of the Sigsbee numerical experiment. With the field data, we illustrate that the choice of shot-domain wavenumbers, at the receivers that record the interferometric data, controls the wavenumbers in the pseudo-shot gathers. This phenomenon can be explained using Ewald's diffraction sphere (Ewald, 1962), where the choice of diffracted wavenumbers dictates which portion of the scatterers will be imaged. Because the air gun excitation in the field data is not impulsive, we rely on deconvolution interferometry after source summation (Chapter 3) to reconstruct impulsive pseudo-shot data. Interferometric shot gathers generated from correlation interferometry show an imprint of the air gun autocorrelation that also maps onto the image domain. When an independent estimate of the air gun autocorrelation is available, it can be deconvolved directly from the correlation-based pseudo-shot gathers (Mehta et al., 2007a). Using wavefield separation to design pseudo-shots that radiate energy upward, we image the top of salt from the receiver array using recorded internal multiples. This top of salt reflector is not reproduced by the image from interferometry of the full recorded wavefields. Furthermore, we use the subsalt VSP data to demonstrate how interferometry can be manipulated to target the subsurface below the array. The interferometric image of subsalt reflectors and the active-shot image from the WAW VSP show events with differing dips. This difference can in part be accounted by the differences in the recording geometry and subsalt illumi-

nation between the two experiments. Additionally, we note that the velocity model used to produce these images was estimated from surface seismic. The WAW VSP, and especially the interferometric data are more sensitive to local perturbations in the subsalt velocities near the array than the surface seismic data. Hence, an "acceptable" velocity model for the imaging of surface seismic data may not be adequate for the imaging of the WAW VSP and the interferometric data. It is thus possible that the differences between the WAW VSP and interferometric images are caused by the uncertainty in the velocity model estimated from surface seismic.

The target-oriented interferometry technique we discuss here is approximate. Its first approximation lies in the truncation of the source integration in the generation of the pseudo-shot gathers. This truncation leads to the introduction of spurious events that behave like multiples (Snieder et al. 2006; Wapenaar, 2006; Chapter 3). Some of these spurious multiples may be mapped onto coherent reflectors in the interferometric images. We observe this in the Sigsbee numerical VSP experiment, where the spurious multiples are imaged as artifact reflectors within the salt body. Our interferometry procedure is also approximate because it neglects a volume integral of the medium perturbations required by the interferometry method in perturbed media (Chapter 2). This approximation leads to the reconstruction of interferometric shots that are kinematically correct but with distorted amplitudes. Therefore, target oriented interferometry as we present here is suitable mostly for structural imaging.

Wavefield separation of shot-domain wavenumbers to construct pseudo-shot gathers that radiate the energy downward is similar to the Virtual Source method by Bakulin and Calvert (2006). Bakulin and Calvert (2006) perform wavefield separation by windowing the data to separate the direct arrival from the rest of the data. Their method, based on separating the direct arrival, practically eliminates unwanted

spurious events, but can only be applied to image below the array and requires picking the data. Also using the Virtual Source method, Mehta et al. (2007a) separate up- from down-going waves using dual-field (4-component) measurements in OBC data. The wavefield separation method by Mehta et al. (2007a) could potentially be applied to different imaging geometries, such as for the imaging with internal multiples as we propose here. That would require that the VSP data were acquired with dual-field sensors.

The interferometric experiments we present in this paper are not necessarily restricted to active-shot VSP experiments and P-wave imaging. The same experiments could be conceived in the context of passive seismic measurements (e.g., Draganov et al., 2006) or in the interferometric imaging of drill-bit noise records (Poletto and Miranda, 2004; Chapter 4). Wapenaar (2004) and Draganov et al. (2006) present a methodology to recover elastic pseudo-shot records using seismic interferometry. Likewise, target-oriented interferometry can be potentially designed to recover multicomponent subsalt pseudo-shot records. Such records, along with surface seismic data, can help in better understanding the local physical structure in subsalt environments. This understanding may come in the form of more realistic models of the subsalt velocity field that incorporate anisotropy as well as lateral parameter variations. Finally, we advocate the importance of utilizing long receiver arrays in the acquisition of data that is to be used for interferometry. As in the Sigsbee numerical example, long receiver arrays can help in obtaining interferometric images with a wide image aperture: each receiver added to an array contributes with a source and a receiver to the interferometry experiment.

6.7 Acknowledgements

This research was financed by the NSF (grant EAS-0609595) and by the sponsors of the Consortium for Seismic Inverse Methods for Complex Structures at the Center for Wave Phenomena. We thank BP for giving us the filed VSP data and for allowing the publication of the results. We thank Francis Rollins, Jianhua Yu, Qiang Sun and Scott Michell (all BP) for useful discussions and suggestions.

Chapter 7

CONCLUSION AND FUTURE RESEARCH

Since the main Chapters (Chapters 2 through 6) consist of stand-alone articles, I present the main conclusions of each Chapter in the Chapters themselves (e.g., in their corresponding Discussion Conclusions section). Therefore, the objective of this last Chapter is not to repeat the content presented in the main Chapters, but to provide a brief general conclusion to this dissertation and to suggest future research paths of the research developed here.

The reciprocity theorems in Chapter 2 offer general formulations than can be used for interferometry, scattering-based imaging, and inversion for acoustic waves. As discussed within Chapter 2, such theorems can potentially be directly applied not just to geophysics, but also in ocean acoustics, laboratory ultrasonics and medical imaging. Here I treat reciprocity theorems for perturbed acoustic waves, and an important next step for this research which will be pursued in the near future is to extend these theorems to a wider class of physical phenomena. This generalization would be analogous to that proposed by Wapenaar et al.(2006) and Snieder et al. (2007), who propose reciprocity theorems that describe elastodynamic and electromagnetic wave propagation in lossy media, diffusion, and advection, as examples. Another important aspect of Chapter 2 is its connection to the scattering problem, which can lead to extensions of the equations I present through the use of scattering series formulations (e.g., Lippmann, 1956; de Hoop, 1996). This connection suggests that the equations in Chapter 2 can be tailored, through scattering series formulations,

for other applications such as inverse-scattering imaging (Weglein et al., 2003) or multiple suppression (Weglein et al. 2003; Malcolm et al., 2007). Furthermore, it is possible that once reciprocity theorems for perturbed media are generalized for other physical phenomena (similarly to Wapenaar et al., 2006; and Snieder et al., 2007), there may also be scattering-like series formulations that describe phenomena such as diffusion and advection.

The generalization of the reciprocity theorems in perturbed media (Chapter 2) to other physical systems can potentially lead to the extension of deconvolution interferometry (Chapter 3) to other systems; for example, to elastic and electromagnetic waves, and of diffusion. Deconvolution interferometry for electromagnetic waves could find applications in, for example, radio telescopy. Given that interferometry by correlations is well understood for elastic wave propagation (e.g., Wapenaar, 2004; Wapenaar and Fokkema, 2006; Draganov et al., 2006), one of the most natural extensions of Chapter 2, and therefore of deconvolution interferometry, is to account for elastodynamic waves. Although I provide a heuristic elastic application of deconvolution interferometry in Chapter 4, modifying the theory in Chapter 3 to account for elastic waves is a necessary extension for processing seismic data. As I discuss in Chapter 3, in light of work such as that of Loewenthal and Robinson (2000) and Amundsen (2001), the use of deconvolutions may play an important in devising interferometry techniques that preserve amplitude properties of the recorded data that allow the estimation of subsurface reflectivity. Interferometry by deconvolution as presented by Chapter 3 can be potentially be adapted into an inverse interferometry procedure, where the deconvolution filters are designed to meet chosen criteria for the output interferometric experiments.

Deconvolution interferometry (Chapter 3) is particularly useful for data where

waves are excited by long, incoherent and poorly known source functions. This makes interferometry by deconvolution equally suitable both for active and passive seismic imaging. In Chapter 4, I show that deconvolution interferometry can be used for the passive imaging of drilling noise, without the need for independent estimates of the drill-bit source function. The imaging of seismic-while-drilling data by deconvolution interferometry is a novel method that can be applied the passive monitoring of oilfields (e.g., the Valhall field in the North Sea), or to the imaging of oilfields in environmentally sensitive areas where the acquisition of standard surface seismic is limited (e.g., Tempa Rossa field, Italy). Apart from passive imaging, deconvolution interferometry can be useful for monitoring structures. Snieder and Şafak (2006) provide a 1D example of how deconvolution interferometry can be used to extract the impulse response of a building from earthquake records. This type of interferometry can also be applied to monitoring the integrity of working engines, bridges, off-shore platforms or producing wells.

In the context of studying the San Andreas fault with SAFOD data, the geological interpretation of the results I present in Chapter 5 can be revised after the coring of the SAFOD Main Hole, which will be conducted during Summer 2007 in the Phase III of the SAFOD drilling project. A key question that remains to be addressed concerns the physical cause of the reflectors I observe in Chapter 5: the reflections could be caused by the contrast of physical properties across the fault (e.g., due to geology), by the physical properties within the faults (e.g., fluid infill, overpressure, etc.), or by a combination of these factors. More work can also be done with an extensive microseismicity dataset acquired with a 80-receiver array in the SAFOD Main Hole (J.A. Chavarria, personal communication, 2006). The application of interferometry to these data can add to the knowledge of the earthquake dynamics of the San Andreas

fault zone at Parkfield. Chapters 4 and 5 demonstrate the potential of interferometry for reconstructing images of subvertical faults; the particular use of deconvolution may lead to the extraction of fault reflectivity properties from interferometric images.

In Chapters 4 and 6 I show perturbation-based interferometry can play an important role in localized imaging in subsalt environments. Chapter 4 implicitly suggests that the use of permanent subsalt borehole sensors can be useful in locally monitoring subsalt reservoirs by the use of interferometry on passive data. Note that these passive data may consist of drilling and rig noise as well as microseismic events. The target-oriented interferometry method, discussed in Chapter 6, is an important step toward imaging particular desired events. In the application I describe in Chapter 6, the imaging of internal is accomplished with the target-oriented interferometry, which depends on the theory presented in Chapter 2. The interferometry approach in Chapter 6 can in principle be adapted to image any chosen direction in multiply scattering media, and can be applied to multicomponent seismic data and electromagnetic waves. Interferometry as presented in Chapter 6 can be extended to recover single-scattered converted and pure-mode shear waves from internal multiples. This application depends on the proper formal extension of deconvolution interferometry for elastic waves. Together with surface seismic data, interferometry experiments such as in Chapters 4 and 6 can, in principle, aid in locally constraining anisotropic subsalt velocity models, since they add information in terms of depth constraint (provided by the borehole receiver array), propagation paths that differ from those in surface seismic data, and pure-mode shear-wave information in off-shore acquisitions.

REFERENCES

[1] K. Aki and P.G. Richards. Quantitative seismology. *Freeman Co., San Francisco*, 1980.

[2] L. Amundsen. Elimination of free-surface related multiples without need of the source wavelet. *Geophysics*, 66:327-341, 2001.

[3] P. Armstrong, L. Nutt and R. Minton. Drilling Optimization Using Drill-bit Seismic in the Deepwater Gulf of Mexico. *IADC/SPE Drilling Conference*, IADC/SPE 59222, 2000.

[4] A. Bakulin and R. Calvert. Virtual source: new method for imaging and 4D below complex overburden. *Soc. Explor. Geophys. Expand. Abs.*, 2477–2480 , 2004.

[5] A. Bakulin and R. Calvert. The virtual source method: Theory and case study. *Geophysics*, 71:SI139-SI150, 2006.

[6] W.H. Bakun and T.V. McEvilly. Recurrence models and Parkfield, California earthquakes. *J. Geoph. Res.*, 89:3051–3058, 1984.

[7] E. Baysal, D.D. Kosloff, and J.W. Sherwood. Reverse-time migration. *Geophysics*, 48:1514-1524, 1983.

[8] A. Bennia and N.S. Nahman. Deconvolution of causal pulse and transient data. *IEEE Transactions on Instrumentation and Measurement*, 39:933–939, 1990.

[9] A.J. Berkhout and D.J. Verschuur. Estimation of multiple scattering by iterative inversion, Part I: Theoretical considerations. *Geophysics*, 62:15861595, 1997.

[10] A.J. Berkhout and D.J. Verschuur. Imaging of multiple reflections. *Geophysics*, 71:SI209-SI220, 2006.

[11] B. Biondi. 3D Seismic Imaging. *Investigations in Geophysics, 14, Society of Exploration Geophysicists*, 240 pages, 2006.

[12] N. Bleistein and R.A. Handelsman. Asymptotic expansions of integrals. *Dover, New York*, 1975.

[13] N. Bleistein, J.K. Cohen and. J.W. Stockwell Jr. Mathematics of Multidimensional Seismic Imaging, Migration, and Inversion. *Springer, New York*, 2001.

[14] N.L. Boness and M.D. Zoback. Stress-induced seismic velocity anisotropy and physical properties in the SAFOD Pilot Hole in Parkfield, CA. *Geophys. Res. Let.*, 31:L15S17, 2004.

[15] N.L. Boness and M.D. Zoback. A multiscale study of the mechanisms controlling shear velocity anisotropy in the San Andreas Fault Observatory at Depth. *Geophysics*, 71:F131–F146, 2006.

[16] R.D. Catchings, M.R. Goldman, M.J. Rymer, G. Gandhok, and G.S. Fuis. Data Report for the Main Line of the PSINE Seismic Survey Across the San Andreas Fault and the SAFOD Site Near Parkfield, California. *USGS Open-file Report*, 03-04:30, 2003.

[17] R.D. Catchings, M.J. Rymer, and M.R. Goldman. Subsurface Structure of the San Andreas Fault Zone Near SAFOD From High-resolution Seismic Images. *Geophys. Res. Abs.*, 5:07861, 2003.

[18] J.A. Chavarria, P. Malin, R.D. Catchings and E. Shalev. A look inside the San Andreas fault at Parkfield through vertical seismic profiling. *Science*, 302:1746–1748, 2003.

[19] J.F. Claerbout. Synthesis of a layered medium from its acoustic transmission response. *Geophysics*, 33:264–269, 1968.

[20] J.F. Claerbout. Imaging the Earth's Interior. *Blackwell Publishing*, 1985.

[21] R.W. Clayton and R.A. Wiggins. Source shape estimation and deconvolution of teleseismic body waves. *Geophys. J. R. Astron. Soc.*, 47:151–177, 1976.

[22] R. Courant and D. Hilbert. Methods of Mathematical Physics. *Wiley-Interscience*, Vols. I and II, 1989.

[23] A. Curtis, P. Gerstoft, H. Sato, R. Snieder and K. Wapenaar. Seismic interferometry - turning noise into signal. *The Leading Edge*, 25:1082–1092, 2006.

[24] S. D'Andrea, R. Pasi, G. Bertozzi and P. Dattilo. Geological model, advanced methods help unlock oil in Italy‘s Apennines. *Oil and Gas Journal*, 91:53–57, 1993.

[25] A. de Hoop. Time-domain reciprocity theorems for acoustic wave fields in fluids with relaxation. *J. Acoust. Soc. Am.*, 84:1877–1882, 1988.

[26] M. de Hoop. Generalization of the Bremmer coupling series. *J. Math. Phys.*, 37:3246-3282, 1996.

[27] A. Derode, E. Larose, M. Campillo, and M. Fink. How to estimate the Greens function of a heterogeneous medium between two passive sensors? Application to acoustic waves. *Appl. Phys. Lett.*, 38:3054-3056, 2003.

[28] D. Draganov, K. Wapenaar and J. Thorbecke. Synthesis of the reflection response from the transmission response in the presence of white noise sources. *65th Annual International Meeting, EAGE, Extended Abstracts*, P218, 2003.

[29] D. Draganov, K. Wapenaar and J. Thorbecke. Seismic interferometry: Reconstructing the earths reflection response. *Geophysics*, 71:SI61-SI70, 2006.

[30] P.P. Ewald. Fifty years of X-Ray Diffraction. *Intl. U. Crystall.*, Section 15.3, page 250, 1962.

[31] J.T. Fokkema and P.M. van den Berg. Seismic applications of acoustic reciprocity. *Elsevier Service Publishing Co.*, 1993.

[32] M. Fink. Time-reversal acoustics in complex environments. *Geophysics*, 71:SI151-SI164, 2006.

[33] K. Gödel. On Fomally Undecidable Propositions of Principia Mathematica and Related Systems. *translated by B. Meltzer and introduced by R.B. Braithwaite (1998)*, URL: http://www.ddc.net/ygg/etext/godel, 1930.

[34] G.D. Gopen and J.A. Swan. The science of scientific writing. *American Scientist*, 78:550–558, 1990.

[35] J.B.U. Haldorsen, D.E. Miller and J.J. Walsh. Walk-away VSP using drill noise as a source. *Geophysics*, 60:978-997, 1994.

[36] D. Halliday, A. Curtis, D. van Mannen and J. Robertsson. Interferometric surface wave (ground roll) isolation and removal. *submitted to Geophysics*, 2007.

[37] N. Hargreaves. Surface multiple attenuation in shallow water and the construction of primaries from multiples. *Soc. Explor. Geophys. Expand. Abs.*, 2689–2692, 2006.

[38] F. Hettlich. Frechet derivatives in inverse obstacle scattering. *Inverse Problems*, 14:209–210, 1998.

[39] J.A. Hole, R.D. Catchings, K.C. St. Clair, M.J. Rymer, D. A. Okaya, and B. J. Carney. Steep-Dip Seismic Imaging of the Shallow San Andreas Fault Near Parkfield *Science*, 294:1513–1515, 2001.

[40] E. Holvik and L. Amundsen. Elimination of the overburden response from multicomponent source and receiver seismic data, with source designature and decomposition into PP-, PS-, SP-, and SS-wave responses. *Geophysics*, 70:S43-S59, 2005.

[41] B. Hornby, T. Fitzpatrick, F. Rollins, H. Sugianto, C. Regone. 3D VSP used to image near complex salt structure in the deep water Gulf of Mexico. *EAGE 67th Conference & Exhibition Extended Abstracts*, E022, 2005.

[42] R. A. Kerr. Parkfield keeps secrets after long awaited quake. *Science*, 306:206–207, 2006.

[43] V. Korneev and A. Bakulin. On the fundamentals of the virtual source method. *Geophysics*, 71:A13-A17, 2006.

[44] E. Larose, L. Margerin, A. Derode, B. van Tiggelen, M Campillo, N. Shapiro, A. Paul, L. Stehly and M. Tanter. Correlation of random wavefields: An interdisciplinary review. *Geophysics*, 71:SI11-SI21, 2006.

[45] B.A. Lippmann. Rearrangement collisions. *Physics Review*, 102:264-268, 1956.

[46] O.I. Lobkis and R.L. Weaver. On the emergence of the Green's function in the correlations of a diffuse field. *J. Acoust. Soc. Am.*, 110:3011-3017, 2001.

[47] D. Loewenthal and E.A. Robinson. On unified dual wavefields and Einstein deconvolution. *Geophysics*, 65:293–303, 2000.

[49] A. Malcolm, J. Scales and B.A. van Tiggelen. Extracting the Greens function from diffuse, equipartitioned waves. *Physical Review E*, 70:015601, 2004.

[49] A.E. Malcolm, M.V. de Hoop, and H. Calandra. Identification of image artifacts from internal multiples. *Geophysics*, 72:S123-S132, 2007.

[50] M. Malusa, F. Poletto and F. Miranda. Prediction ahead of the bit by using drill-bit pilot signals and reverse vertical seismic profiling (RVSP). *Geophysics*, 67:1169-1176, 2002.

[51] D. van Manen, A. Curtis, and J.O.A. Robertsson. Interferometric modeling of wave propagation in inhomogeneous elastic media using time reversal and reciprocity. *Geophysics*, 71:SI47-SI60, 2006.

[52] K. Mehta, R. Snieder, R. Calvert and J. Sheiman. Virtual source gathers and attenuation of free-surface multiples using OBC data:implementation issues and a case study. *Soc. Explor. Geophys. Expand. Abs.*, 2669–2673, 2006.

[53] K. Mehta, A. Bakulin, J. Sheiman, R. Calvert, and R. Snieder. Improving virtual source method by wave-field separation. *Geophysics*, in press, 2007a.

[54] K. Mehta, J. Sheiman, R. Snieder, and R. Calvert. Virtual source method applied to Mars OBC data for time-lapse monitoring. *Geophysics*, in revision, 2007b.

[55] K. Mehta, R. Snieder and V. Graizer. Extraction of near-surface properties for a lossy layered medium using the propagator matrix. *Geophys. J. Intl.*, 169:271–280, 2007c.

[56] K. Mehta, R. Snieder and V. Graizer. Down-hole receiver function: a case study. *Bull. Seism. Soc. Am.*, submitted, 2007d.

[57] D. Miller, J. Haldorsen and C. Kostov. Methods for deconvolution of unknown source signatures from unknown waveform data. *US Patent*, 4 922 362, 1990.

[58] R. Muijs, J.O.A. Robertsson and K. Holliger. Prestack depth migration of primary and surface-related multiple reflections: Part I Imaging. *Geophysics*, 72:S59-SI69, 2006.

[59] R.M. Nadeau, A. Michelini, R.A. Uhrhammer, D. Dolenc and T.V. McEvilly. Detailed kinematics, structure and recurrence of micro-seismicity in the SAFOD target region. *Geophys. Res. Let.*, 31:L12S08, 2004.

[60] H. Ohanian and R. Ruffini. Gravitation and Spacetime. *Norton & Co.,New York*, 2nd Edition, 1994.

[61] V. Oye, J.A. Chavarria and P. Malin. Determining SAFOD area microearthquake locations solely with the Pilot Hole seismic array data. *Geophys. Res. Let.*, 31:L12S10, 2004.

[62] A.M. Penrose and S.B. Katz. Writing in the Sciences: Exploring Conventions of Scientific Discourse. *Longman, Boston*, 1998.

[63] F. Poletto, F.L. Rocca and L. Bertelli. Drill-bit signal separation for RVSP using statistical independence. *Geophysics*, 65:1654-1659, 2000.

[64] F. Poletto, M. Malusa, F. Miranda and U. Tinivella. Seismic-while-drilling by using dual sensors in drill strings. *Geophysics*,69:1261-1271, 2004.

[65] F. Poletto and F. Miranda. Seismic while drilling, fundamentals of drill-bit seismic for exploration. *Handbook of Geophysical Exploration*, Vol 35, 2004.

[66] F. Poletto. Energy balance of a drill-bit seismic source, part 1: Rotary energy and radiation properties. *Geophysics*, 70:T13-T28, 2005a.

[67] F. Poletto. Energy balance of a drill-bit seismic source, part 2: Drill bit versus conventional seismic sources. *Geophysics*, 70:T29-T44, 2005b.

[68] F. Poletto and L. Petronio. Seismic interferometry with a TBM source of transmitted and reflected waves. *Geophysics*, 71:SI85-SI93, 2006.

[69] M. Porsani and B. Ursin. Mixed-phase deconvolution and wavelet estimation. *The Leading Edge*, 19:76-79, 2000.

[70] M. Porsani and B. Ursin. Direct multichannel predictive deconvolution. *Geophysics*, 72:H11-H27, 2007.

[71] L. Qu, P.S. Routh and K. Ko. Wavelet deconvolution in a periodic setting using cross-validation. *IEEE Signal Processing Letters*, 13:232-235, 2006.

[72] J.W.S. Rayleigh. The Theory of Sound, Vol II. *Dover Publications, Inc.*, 1878 (reprint 1945).

[73] J.W. Rector and B.P. Marion. The use of drill-bit energy as a downhole seismic source. *Geophysics*, 56:628-634, 1991.

[74] J.W. Rector and B.A. Hardage. Radiation pattern and seismic waves generated by a working roller-cone drill bit. *Geophysics*, 57:1319-1333, 1992.

[75] J.W. Rector. Noise characterization and attenuation in drill bit recordings. *J. Seis. Expl.*, 1:379-393, 1992.

[76] J.E. Rickett and J.F. Claerbout. Acoustic daylight imaging via spectral factorization; helioseismology and reservoir monitoring. *The Leading Edge*, 19:957–960, 1999.

[77] L.S. Rodberg and R.M. Thaler. Introduction to the Quantum Theory of Scattering. *Academic Press, New York*, 1967.

[78] S. Roecker, C. Thurber and D. McPhee. Joint inversion of gravity and arrival time data from Parkfield: New constraints on structure and hypocenter locations near the SAFOD drill site. *Geophys. Res. Let.*, 31:L12S04, 2004.

[79] E. Roeloffs and J. Langbein. The earthquake prediction experiment at Parkfield, California. *Reviews of Geophysics*, 32:315–336, 1994.

[80] P. Roux, W.A. Kuperman, and NPAL Group. Extracting coherent wave fronts from acoustic ambient noise in the ocean. *J. Acoust. Soc. Am.*, 116:1995-2003, 2004.

[81] M.J. Rymer, R.D. Catchings and M.R. Goldman. Structure of the San Andreas fault as revealed by surface geologic mapping and high-resolution seismic profiling near Parkfield, California. *Geophys. Res. Abstr.*, 5, 13:513, 2003.

[82] K.G. Sabra, P. Roux and W.A. Kuperman . Arrival-time structure of the time-averaged ambient noise cross-correlation function in an oceanic waveguide. *J. Acoust. Soc. Am.*, 117:164–174, 2004.

[83] K.G. Sabra, P. Gerstoft, P. Roux, W.A. Kuperman and M. Fehler. Surface-wave tomography from microseisms in Southern California. *Geophys. Res. Let.*, 32:L14311, 2005a.

[84] K.G. Sabra, P. Roux, A.M. Thode, G.L. DSpain, and W.S. Hodgkiss. Using ocean ambient noise for array self-localization and self-synchronization. *IEEE J. of Oceanic Eng.*, 30:338-347, 2005b.

[85] P. Sava and B. Biondi. Wave-equation migration velocity analysis – I: Theory. *Geophys. Prosp.*, 52:593–606, 2004.

[86] P. Sava. Time-shift imaging condition in seismic migration. *Geophysics*, 71:S209–S217, 2006.

[87] E. Schrödinger. Space-Time Strucutre. *Cambridge University Press*, 1950.

[88] G.T. Schuster, F. Followill, L.J. Katz, J. Yu, and Z. Liu. Autocorrelogram migration: Theory. *Geophysics*, 68:1685-1694, 2004.

[89] G.T. Schuster and M. Zhou. A theoretical overview of model-based and correlation-based redatuming methods. *Geophysics*, 71:SI103-SI110, 2006.

[90] N.M. Shapiro, M. Campillo, L. Stehly, and M.H. Ritzwoller. High-resolution surface-wave tomography from ambient seismic noise. *Science*, 307:1615-1618, 2005.

[91] Y. Shen, A.F. Sheehan, K.G. Dueker, C. de Groot-Hedlin and H. Gilbert. Mantle Discontinuity Structure Beneath the Southern East Pacific Rise from P-to-S Converted Phases. *Science*, 280:1232–1235, 1998.

[92] R. Snieder. The Role of the Born approximation in nonlinear inversion. *Inverse Problems*, 6:247–266, 1990.

[93] R. Snieder. Extracting the Green's function from the correlation of coda waves: A derivation based on stationary phase. *Phys. Rev. E.*, 69:046610, 2004.

[94] R. Snieder and E. Şafak. Extracting the building response using seismic interferometry; theory and application to the Millikan library in Pasadena, California. *Bull. Seismol. Soc. Am.*, 96:586-598, 2006.

[95] R. Snieder, K. Wapenaar and K. Larner. Spurious multiples in seismic interferometry of primaries. *Geophysics*, 71:SI111-SI124, 2006a.

[96] R. Snieder, J. Sheiman and R. Calvert. Equivalence of the virtual-source method and wave-field deconvolution in seismic interferometry. *Phys. Rev. E*, 73:066620, 2006b.

[97] R. Snieder. Retrieving the Greens function of the diffusion equation from the response to a random forcing. *Phys. Rev. E*, 74:046620, 2006.

[98] R. Snieder. Extracting the Greens function of attenuating heterogeneous acoustic media from uncorrelated waves. *J. Acoust. Soc. Am.*, in press, 2007.

[99] R. Snieder, K. Wapenaar, and U. Wegler. Unified Green's function retrieval by cross-correlation; connection with energy principles. *Phys. Rev. E*, 75:036103, 2007.

[100] J.G. Solum and B.A. van der Pluijm. Phyllosilicate mineral assemblages of the SAFOD Pilot Hole and comparison with an exhumed segment of the San Andreas Fault System. *Geophys. Res. Let.*, 31:L15S19, 2004.

[101] J.G. Solum, S.H. Hickman, D.A. Lockner, D.E. Moore, B.A. van der Pluijm, A.M. Schleicher and J.P. Evans. Mineralogical characterization of protolith and fault rocks from the SAFOD Main Hole. *Geophys. Res. Let.*, 33:L21314, 2006.

[102] M. Talebian, E.J. Fielding, G.J. Funning, M. Ghorashi, J. Jackson, H. Nazari, B. Parsons, K. Priestley, P.A. Rosen, R. Walker, and T.J. Wright. The 2003 Bam (Iran) earthquake: Rupture of a blind strike-slip fault. *Geophys. Res. Let.*, 31:L11611, 2004.

[103] A. Tarantola. Inverse Problem Theory. *Elsevier, Amsterdam*, 1987.

[104] A. Tarantola. Elements for Physics – Quantities, Qualities, and Intrinsic Theories. *Springer-Verlag, Berlin*, 2006.

[105] S.T. Taylor, P. Malin, E. Shalev, J.B.U. Haldorsen, R. Coates, and C. Stolte. Drill bit seismic imaging of the San Andreas Fault System at SAFOD. *Soc. of Expl. Geophys. Exp. Abstr.*, 24:2657–2660, 2005.

[106] D. Thompson and R. Snieder. Seismic anisotropy of a building. *The Leading Edge*, 25:1093, 2006.

[107] C. Thurber, S. Roecker, H. Zhang, S. Baher and W. Ellsworth. Fine-scale structure of the San Andreas fault zone and location of the SAFOD target earthquakes. *Geophys. Res. Let.*, 31:L12S02, 2004.

[108] J. Trampert, M. Cara and M. Frogneux. *SH* propagator matrix and Q_s estimates from borehole- and surface-recorded earthquake data. *Geophys. J. Intl.*, 112:290–299, 1993.

[109] I. Tsvankin. Seismic Signatures and Analysis of Reflection Data in Anisotropic Media. *Handbook of Geophysical Exploration*, Vol 29, 2001.

[110] D.L. Turcotte and G. Schubert. Geodynamics. *Cambridge University Press, London*, 2001.

[111] M. Unsworth, P. Bedrosian, M. Eisel, G. Ebert and W. Siripunvaraporn. Along strike variations in the electrical structure of the San Andreas Fault at Parkfield, CA. *Geophys. Res. Let.*, 27:3021–3024, 2000.

[112] M. Unsworth and P. Bedrosian. Electrical resistivity at the SAFOD site from magnetotelluric exploration. *Geophys. Res. Let.*, 31:L12S05, 2004.

[113] K. van Wijk. On estimating the impulse response between receivers in a controlled ultrasonic experiment. *Geophysics*, 71:SI79-SI84, 2006.

[114] K. Wapenaar, D. Dragonov, J. Thorbecke, and J. Fokkema. Theory of acoustic daylight imaging revisited. *72nd Annual International Meeting, SEG, Expanded-Abstracts*, 1981-1984, 2002.

[115] K. Wapenaar. Retrieving the elastodynamic Green's function of an arbitrary inhomogeneous medium by cross correlation. *Phys. Rev. Lett.*, 93:254301, 2004.

[116] K. Wapenaar, J. Thorbecke, and D. Dragonov. Relations between reflection and transmission responses of three-dimensional inhomogeneous media. *Geophys. J. Int.*, 156:179–194, 2004.

[117] K. Wapenaar. Green's function retrieval by cross-correlation in case of one-sided illumination. *Geophys. Res. Lett.*, 33:L19304, 2006.

[118] K. Wapenaar and J. Fokkema. Green's function representations for seismic interferometry. *Geophysics*, 71:SI133-SI146, 2006.

[119] K. Wapenaar, E. Slob, and R. Snieder. Unified Green's Function Retrieval by Cross Correlation. *Phys. Rev. E.*, 97:234301, 2006.

[120] R.L. Weaver and O.I. Lobkis. Ultrasonics without a source: Thermal fluctuation correlations and MHz frequencies. *Phys. Rev. Lett.*, 87:134301–1/4, 2001.

[121] R.L. Weaver and O.I. Lobkis. Diffuse fields in open systems and the emergence of the Green's function. *J. Acoust. Soc. Am.*, 116:2731–2734, 2004.

[122] G.M. Webster. Deconvolution. *Geophysics reprint series*, Vol. 1, 1978.

[123] A.B. Weglein, F.V. Araújo, P.M. Carvalho, R.H. Stolt, K.H. Matson, R.T. Coates, D. Corrigan, D.J. Foster, S.A. Shaw, and H. Zhang. Inverse scattering series and seismic exploration. *Inverse Problems*, 19:R27–R83, 2003.

[124] A.B. Weglein, B.G. Nita, K.A. Innanen, E. Otnes, S.A. Shaw, F. Liu, H. Zhang, A.C. Ramírez, J. Zhang, G.L. Pavlis, and C. Fan. Using the inverse scattering series to predict the wavefield at depth and the transmitted wavefield without an assumption about the phase of the measured reflection data or back propagation in the overburden. *Geophysics*, 71:SI125-SI137, 2006.

[125] A.N. Whitehead and B. Russell. Principia Mathematica. *Cambridge University Press*, 3 vols, Cambridge University Press, 1910, 1912, and 1913. Second edition, 1925 (Vol. 1), 1927 (Vols 2, 3). Abridged as Principia Mathematica to *56, Cambridge University Press, 1962.

[126] E.P. Wigner. The Unreasonable Effectiveness of Mathematics in the Natural Sciences. *Comm. Pure Appl. Math.*, 13:222-236, 1960.

[127] M.E. Willis, R. Lu, X. Campman, M.N. Toksöz, Y. Zhang, and M.V. de Hoop. A novel application of time-reversed acoustics: Salt-dome flank imaging using walkaway VSP surveys. *Geophysics*, 71:A7-A11, 2006.

[128] R.S. Yeats and G.J. Hutfile. The Oak Ridge fault system and the 1994 Northridge earthquake. *Nature*, 373:418–420, 1995.

[129] J. Yu, L.J. Katz, F. Followill, H. Sun and G.T. Schuster. Autocorrelogram migration: IVSPWD test. *Geophysics*, 68:297307, 2004.

[130] J. Yu and G.T. Schuster. Crosscorrelogram migration of inverse vertical seismic profile data. *Geophysics*, 71:S1-S11, 2006.

[131] X. Xiao, M. Zhou, and G.T. Schuster. Salt-flank delineation by interferometric imaging of transmitted P- to S-waves. *Geophysics*, 71:SI197-SI207, 2006.

APPENDIX A

PHYSICAL ANALYSIS OF THE DECONVOLUTION INTERFEROMETRY SERIES

According to the derivation in Section 3.3.2 of Chapter 3, the deconvolution in equation 4.11 can be expressed in series form

$$D_{AB} = \frac{C_{AB}}{|G_0(\mathbf{r}_B, \mathbf{s})|^2} \sum_{n=0}^{\infty} \left(- \frac{G_S(\mathbf{r}_B, \mathbf{s})}{G_0(\mathbf{r}_B, \mathbf{s})} - \frac{G_S^*(\mathbf{r}_B, \mathbf{s})}{G_0^*(\mathbf{r}_B, \mathbf{s})} \right)^n . \tag{A.1}$$

The objective of this appendix is to reproduce the steps and physical approximations that simplify the series in equation A.1. Let us first consider the $n = 2$ term in the summation in equation A.1, which is

$$S_2 = \left(- \frac{G_S(\mathbf{r}_B, \mathbf{s})}{G_0(\mathbf{r}_B, \mathbf{s})} - \frac{G_S^*(\mathbf{r}_B, \mathbf{s})}{G_0^*(\mathbf{r}_B, \mathbf{s})} \right)^2 \tag{A.2}$$

Substituting this term in the expansion of $|G(\mathbf{r}_B, \mathbf{s})|^{-2}$ (equation 3.13) gives, to second order in G_S,

$$\begin{aligned} |G(\mathbf{r}_B, \mathbf{s})|^{-2} \approx & \frac{1}{|G_0(\mathbf{r}_B, \mathbf{s})|^2} \left[1 - \frac{G_S(\mathbf{r}_B, \mathbf{s})}{G_0(\mathbf{r}_B, \mathbf{s})} - \frac{G_S^*(\mathbf{r}_B, \mathbf{s})}{G_0^*(\mathbf{r}_B, \mathbf{s})} \right] \\ & + \frac{1}{|G_0(\mathbf{r}_B, \mathbf{s})|^2} \left[\left(\frac{G_S(\mathbf{r}_B, \mathbf{s})}{G_0(\mathbf{r}_B, \mathbf{s})} \right)^2 + \left(\frac{G_S^*(\mathbf{r}_B, \mathbf{s})}{G_0^*(\mathbf{r}_B, \mathbf{s})} \right)^2 + 2 \frac{|G_S(\mathbf{r}_B, \mathbf{s})|^2}{|G_0(\mathbf{r}_B, \mathbf{s})|^2} \right] , \end{aligned} \tag{A.3}$$

where the very last term is zero-phase. When $|G_0|^2 >> |G_S|^2$, the zero-phase term in equation A.3 can be neglected because it does not contribute with any new arrival. Equation A.3 thus simplifies to

$$\begin{aligned} |G(\mathbf{r}_B, \mathbf{s})|^{-2} \approx & \frac{1}{|G_0(\mathbf{r}_B, \mathbf{s})|^2} \left[1 - \frac{G_S(\mathbf{r}_B, \mathbf{s})}{G_0(\mathbf{r}_B, \mathbf{s})} - \frac{G_S^*(\mathbf{r}_B, \mathbf{s})}{G_0^*(\mathbf{r}_B, \mathbf{s})} \right] \\ & + \frac{1}{|G_0(\mathbf{r}_B, \mathbf{s})|^2} \left[\left(\frac{G_S(\mathbf{r}_B, \mathbf{s})}{G_0(\mathbf{r}_B, \mathbf{s})} \right)^2 + \left(\frac{G_S^*(\mathbf{r}_B, \mathbf{s})}{G_0^*(\mathbf{r}_B, \mathbf{s})} \right)^2 \right] ; \end{aligned} \tag{A.4}$$

for which the actual contribution from $n = 2$ to the sum in equation A.1 is

$$S_2 \approx \left(\frac{u_S(\mathbf{r}_B, \mathbf{s})}{u_0(\mathbf{r}_B, \mathbf{s})} \right)^2 + \left(\frac{u_S^*(\mathbf{r}_B, \mathbf{s})}{u_0^*(\mathbf{r}_B, \mathbf{s})} \right)^2 , \tag{A.5}$$

instead of the full S_2 term in equation A.2. Applying the same rationale for the simplification of S_2 to the $n = 3$ term from the summation in equation A.1 gives

$$S_3 = \left(- \frac{G_S(\mathbf{r}_B, \mathbf{s})}{G_0(\mathbf{r}_B, \mathbf{s})} - \frac{G_S^*(\mathbf{r}_B, \mathbf{s})}{G_0^*(\mathbf{r}_B, \mathbf{s})} \right)^3 . \tag{A.6}$$

S_3 can be expressed in terms of S_2, such that

$$S_3 = S_2 \times \left(- \frac{G_S(\mathbf{r}_B, \mathbf{s})}{G_0(\mathbf{r}_B, \mathbf{s})} - \frac{G_S^*(\mathbf{r}_B, \mathbf{s})}{G_0^*(\mathbf{r}_B, \mathbf{s})} \right) . \tag{A.7}$$

Using the simplified S_2 (equation A.5) in evaluating S_3 gives

$$
\begin{aligned}
S_3 \;\approx\; & -\left(\frac{G_S(\mathbf{r}_B,\mathbf{s})}{G_0(\mathbf{r}_B,\mathbf{s})}\right)^3 - \left(\frac{G_S^*(\mathbf{r}_B,\mathbf{s})}{G_0^*(\mathbf{r}_B,\mathbf{s})}\right)^3 \\
& - \frac{|G_S(\mathbf{r}_B,\mathbf{s})|^2}{|G_0(\mathbf{r}_B,\mathbf{s})|^2}\frac{G_S(\mathbf{r}_B,\mathbf{s})G_0^*(\mathbf{r}_B,\mathbf{s})}{|G_0(\mathbf{r}_B,\mathbf{s})|^2} - \frac{|G_S(\mathbf{r}_B,\mathbf{s})|^2}{|G_0(\mathbf{r}_B,\mathbf{s})|^2}\frac{G_S^*(\mathbf{r}_B,\mathbf{s})G_0(\mathbf{r}_B,\mathbf{s})}{|G_0(\mathbf{r}_B,\mathbf{s})|^2}
\end{aligned}
\tag{A.8}
$$

The last two terms of S_3 in the above equation are not zero-phase. Note also that despite being nonzero phase, the phase of these terms is the same of other terms of lower order. For example, the term $\left(|G_S|^2 / |G_0|^4\right) G_S\, G_0^*$ has the same phase as the integrand in the D_{AB}^2 term in equation 4.12, but with weaker amplitude and opposite polarity. Because they do not result in new arrivals and have weak amplitudes, we drop the last two terms in equation A.9 and reduce S_3 to

$$
S_3 \;\approx\; -\left(\frac{G_S(\mathbf{r}_B,\mathbf{s})}{G_0(\mathbf{r}_B,\mathbf{s})}\right)^3 - \left(\frac{G_S^*(\mathbf{r}_B,\mathbf{s})}{G_0^*(\mathbf{r}_B,\mathbf{s})}\right)^3 . \tag{A.9}
$$

Any S_n term of the summation in equation A.1 can be written in terms of S_{n-1} in the same form of equation A.7. Analogously to equation A.9, any S_n will yield four terms from which two terms can be dropped according to the same rationale we use to neglect the last two terms in equation A.9. Thus, by induction, the summation in equation A.1 simplifies to

$$
\sum_{n=0}^{\infty}\left(-\frac{G_S(\mathbf{r}_B,\mathbf{s})}{G_0(\mathbf{r}_B,\mathbf{s})} - \frac{G_S^*(\mathbf{r}_B,\mathbf{s})}{G_0^*(\mathbf{r}_B,\mathbf{s})}\right)^n \;\approx\; 1 + \sum_{n=1}^{\infty}(-1)^n\left[\left(\frac{G_S(\mathbf{r}_B,\mathbf{s})}{G_0(\mathbf{r}_B,\mathbf{s})}\right)^n + \left(\frac{G_S^*(\mathbf{r}_B,\mathbf{s})}{G_0^*(\mathbf{r}_B,\mathbf{s})}\right)^n\right] . \tag{A.10}
$$

Using this simplified summation in the deconvolution series gives

$$D_{AB} \approx \frac{C_{AB}}{|G_0(\mathbf{r}_B,\mathbf{s})|^2}\left(1+\sum_{n=1}^{\infty}(-1)^n\left[\left(\frac{G_S(\mathbf{r}_B,\mathbf{s})}{G_0(\mathbf{r}_B,\mathbf{s})}\right)^n+\left(\frac{G_S^*(\mathbf{r}_B,\mathbf{s})}{G_0^*(\mathbf{r}_B,\mathbf{s})}\right)^n\right]\right). \quad (A.11)$$

The term-by-term expansion of the equation above is such that for any given value of n, the terms

$$D_{AB,\text{terms}} = (-1)^n\left(\frac{G_S^*(\mathbf{r}_B,\mathbf{s})}{G_0^*(\mathbf{r}_B,\mathbf{s})}\right)^n\left(\underbrace{G_0(\mathbf{r}_A,\mathbf{s})G_S^*(\mathbf{r}_B,\mathbf{s})}_{C_{AB}^2}+\underbrace{G_S(\mathbf{r}_A,\mathbf{s})G_S^*(\mathbf{r}_B,\mathbf{s})}_{C_{AB}^4}\right) \quad (A.12)$$

cancel, for $n+1$, with the terms

$$D_{AB,\text{terms}} = (-1)^{n+1}\left(\frac{G_S^*(\mathbf{r}_B,\mathbf{s})}{G_0^*(\mathbf{r}_B,\mathbf{s})}\right)^{n+1}\left(\underbrace{G_0(\mathbf{r}_A,\mathbf{s})G_0^*(\mathbf{r}_B,\mathbf{s})}_{C_{AB}^1}+\underbrace{G_S(\mathbf{r}_A,\mathbf{s})G_0^*(\mathbf{r}_B,\mathbf{s})}_{C_{AB}^3}\right); \quad (A.13)$$

which in the limit $n \to \infty$ leaves only the contribution of the causal ratio G_S/G_0 to D_{AB} in equation A.11. The cancelation of the terms proportional to the acausal ratio G_S^*/G_0^* (highlighted by equations A.12 and A.13) is responsible for the absence of acausal terms having the same phase as C_{AB}^3 and C_{AB}^4 (equation 3.4) in deconvolution interferometry (equation 4.12). Because of these successive cancelations, we arrive to

$$\begin{aligned} D_{AB} \approx \frac{G_0(\mathbf{r}_A,\mathbf{s})G_0^*(\mathbf{r}_B,\mathbf{s})}{|G_0(\mathbf{r}_B,\mathbf{s})|^2} &+ \frac{G_S(\mathbf{r}_A,\mathbf{s})G_0^*(\mathbf{r}_B,\mathbf{s})}{|G_0(\mathbf{r}_B,\mathbf{s})|^2} \\ &+ \frac{C_{AB}}{|G_0(\mathbf{r}_B,\mathbf{s})|^2}\sum_{n=1}^{\infty}(-1)^n\left(\frac{G_S(\mathbf{r}_B,\mathbf{s})}{G_0(\mathbf{r}_B,\mathbf{s})}\right)^n, \end{aligned} \quad (A.14)$$

which, in compact form, gives

$$D_{AB} \approx \frac{G(\mathbf{r}_A, \mathbf{s})}{G_0(\mathbf{r}_B, \mathbf{s})} + \frac{C_{AB}}{|G_0(\mathbf{r}_B, \mathbf{s})|^2} \sum_{n=1}^{\infty} (-1)^n \left(\frac{G_S(\mathbf{r}_B, \mathbf{s})}{G_0(\mathbf{r}_B, \mathbf{s})} \right)^n . \tag{A.15}$$

We present this approximate deconvolution series as a tool to identify the most prominent events within the integrand of the deconvolution interferometry integral (equation 3.10). Equation A.14 is also useful in the description of the kinematics of deconvolution interferometry terms, as we discuss in the main text. If one seeks to describe the result of deconvolution interferometry with a more accurate dynamic behavior, the original series in equation A.1 is more appropriate.

APPENDIX B

STATIONARY-PHASE EVALUATION OF LEADING ORDER TERMS OF THE DECONVOLUTION INTERFEROMETRY SERIES

The wavefields shown in Figure 3.3 can be described by the ray-geometric impulse responses

$$\begin{aligned} u_0(\mathbf{r}_{A,B},\mathbf{s}) &= G_0(\mathbf{r}_{A,B},\mathbf{s}) = -\frac{e^{ik\left|\mathbf{r}_{A,B}-\mathbf{s}\right|}}{4\pi\left|\mathbf{r}_{A,B}-\mathbf{s}\right|}, \text{ and} \\ u_S(\mathbf{r}_{A,B},\mathbf{s}) &= G_S(\mathbf{r}_{A,B},\mathbf{s}) = -r\frac{e^{ik\left(\left|\mathbf{r}^{sr}_{A,B}-\mathbf{r}_{A,B}\right|+\left|\mathbf{s}-\mathbf{r}^{sr}_{A,B}\right|\right)}}{4\pi\left(\left|\mathbf{r}^{sr}_{A,B}-\mathbf{r}_{A,B}\right|+\left|\mathbf{s}-\mathbf{r}^{sr}_{A,B}\right|\right)}; \end{aligned} \quad \text{(B.1)}$$

where $\mathbf{r}^{sr}_{A,B}$ are the specular reflection points for the receiver-source pairs $(\mathbf{r}_{A,B},\mathbf{s})$. G_0 and G_S are the far-field acoustic Green's functions we use to describe u_0 and u_S, respectively. In our model, $\mathbf{s}=(x,y,z=0)$ and $\mathbf{r}_{A,B}=(x_{A,B},y_{A,B}=0,z_{A,B})$. The distances in the phases and denominators in equation B.1 can be expressed in terms of the corresponding ray-lengths in Figure 3.3. Using the Green's functions in equation B.1 to express D^1_{AB} (equation 4.12) we get

$$D^1_{AB} = \frac{1}{(4\pi L_B)^2}\int\frac{e^{ik(L_A-L_B)}}{L_A L_B}dxdy\,, \quad \text{(B.2)}$$

where $\varphi = ik\left(L_A-L_B\right)$ is the phase of the integrand. The source position that gives a stationary contribution to the integral in equation B.2 satisfies

$$0 = \frac{\partial \varphi}{\partial y} = \frac{y}{L_A} - \frac{y}{L_B} \; ; \tag{B.3}$$

and

$$0 = \frac{\partial \varphi}{\partial x} = \frac{x - x_A}{L_A} - \frac{x - x_B}{L_B} = \sin \psi_A - \sin \psi_B \; , \tag{B.4}$$

where ψ_A and ψ_B is the angle defined between the direct wave and the vertical at receivers A and B. It follows from equations B.3 and B.4 that the stationary point for the source in the D^1_{AB} term satisfies (Snieder et al., 2006)

$$\psi_A = \psi_B = \psi \qquad \text{and} \qquad y = 0 \; . \tag{B.5}$$

It is expected that the stationary contribution for all terms comes from sources at $y = 0$ because $y_{A,B} = 0$ and the model is a flat reflector in a homogeneous and isotropic medium. The condition $\psi_A = \psi_B$ (equation B.5) states that the stationary source is the one that sends a direct wave which is first recorded at $\mathbf{r}_B$ and goes straight to $\mathbf{r}_A$. This is the same stationary condition as for the C^1_{AB} term of Snieder et al. (2006).

To approximate the integral in equation B.2 with the stationary-phase method we must evaluate, at the stationary point, the second derivatives

$$\begin{aligned} \frac{\partial^2 \varphi}{\partial x^2} &= \frac{z_A^2}{L_A^3} - \frac{z_B^2}{L_B^3} = \frac{z_A^2}{L_A^2} \frac{1}{L_A} - \frac{z_B^2}{L_B^2} \frac{1}{L_B} \\ &= \cos^2 \psi \left(\frac{1}{L_A} - \frac{1}{L_B} \right) \; , \end{aligned} \tag{B.6}$$

and

$$\frac{\partial^2 \varphi}{\partial y^2} = \frac{L_A^2}{L_A^3} - \frac{L_B^2}{L_B^3} = \frac{1}{L_A} - \frac{1}{L_B} \, . \tag{B.7}$$

Based on these second derivatives, the stationary-phase approximation (Bleistein and Handelsman, 1975) to equation B.2 is

$$D_{AB}^1 = \frac{n}{(4\pi L_B)^2} \frac{1}{(4\pi)^2} \frac{\exp\left(ik\left(L_A - L_B\right)\right)}{L_A L_B} \quad \times e^{-i\pi/4} \sqrt{\frac{2\pi}{k}} \frac{1}{\sqrt{\cos^2\psi \left(\frac{1}{L_B} - \frac{1}{L_A}\right)}} \times e^{-i\pi/4} \sqrt{\frac{2\pi}{k}} \frac{1}{\sqrt{\frac{1}{L_B} - \frac{1}{L_A}}} \, , \tag{B.8}$$

where $k = \frac{\omega}{c}$. At the stationary source point, where $\psi_A = \psi_B$, the distance $L_A - L_B$ is equivalent to the distance $|\mathbf{r}_A - \mathbf{r}_B|$. Thus, in the stationary-phase approximation, D_{AB}^1 is given by

$$D_{AB}^1 \; = \; \frac{nc}{32\pi^2 \, L_B^2 \, cos\psi} \, \frac{G_0(\mathbf{r}_A, \mathbf{r}_B)}{(-i\omega)} \, . \tag{B.9}$$

From the derivation above, the stationary-phase evaluation of D_{AB}^1 is completely analogous to the evaluation of C_{AB}^1 (equation 3.4) in Snieder et al. (2006). Since the same occurs with the term D_{AB}^2, we refrain from reproducing the steps of its stationary-phase approximation in this paper, and refer the readers to Snieder et al. (2006) for these steps.

APPENDIX C

SHORT NOTE ON DECONVOLUTION

Our numerical application of deconvolution is based on the so-called *water level* deconvolution (Clayton and Wiggins, 1976), given by

$$D_{AB} = \frac{u(\mathbf{r}_A, \mathbf{s})}{u(\mathbf{r}_B, \mathbf{s})} = \frac{u(\mathbf{r}_A, \mathbf{s})\, u^*(\mathbf{r}_B, \mathbf{s})}{|u(\mathbf{r}_B, \mathbf{s})|^2 + \epsilon \langle |u(\mathbf{r}_B, \mathbf{s})|^2 \rangle}, \tag{C.1}$$

where $\langle |u(\mathbf{r}_B, \mathbf{s})|^2 \rangle$ is an average of the power spectrum of the data measured at $\mathbf{r}_B$. The factor ϵ is a free-parameter that we choose by visually inspecting the output of the deconvolution in equation C.1. When ϵ is too large, the denominator becomes a constant and the result of the deconvolution approximates the result of cross-correlation (equation 4.2). When ϵ is too small the deconvolution becomes unstable. An optimal value of ϵ results in the desired deconvolved trace with weak random noise associated to the water level regularization (Clayton and Wiggins, 1976).

There are other deconvolution approaches that yield better results than the water-level deconvolution method. For deconvolution references in the exploration geophysics literature, we refer to the article collection edited by Webster (1981) and to the work of Porsani and Ursin (Porsani and Ursin, 2000; Porsani and Ursin, 2007). In the signal processing field, the work of Bennia and Nahman (1996) and Qu et al. (2006) are examples of deconvolution methods that are relevant to SWD processing.